



Universiteit
Leiden
The Netherlands

Models of the ISM in galaxy centers

Meijerink, Rowin

Citation

Meijerink, R. (2006, November 8). *Models of the ISM in galaxy centers*. Retrieved from <https://hdl.handle.net/1887/4971>

Version: Corrected Publisher's Version

License: [Licence agreement concerning inclusion of doctoral thesis in the Institutional Repository of the University of Leiden](#)

Downloaded from: <https://hdl.handle.net/1887/4971>

Note: To cite this publication please use the final published version (if applicable).

**MODELS OF THE ISM
IN
GALAXY CENTERS**

MODELS OF THE ISM IN GALAXY CENTERS

Proefschrift

ter verkrijging van
de graad van Doctor aan de Universiteit Leiden,
op gezag van de Rector Magnificus Dr. D.D. Breimer,
hoogleraar in de faculteit der Wiskunde en
Natuurwetenschappen en die der Geneeskunde,
volgens besluit van het College voor Promoties
te verdedigen op woensdag 8 november 2006
te klokke 16.15 uur

door

Rowin Meijerink

geboren te Enschede in 1978

Promotiecommissie

Promotor: Prof. dr. F.P. Israel

Co-promotor: Prof. dr. M.C. Spaans (Kapteyn Astronomical Institute)

Referent: Prof. dr. A.G.G.M. Tielens (NASA Ames Research Center, USA)

Overige leden: Prof. dr. E.F. van Dishoeck
Dr. M.R. Hogerheijde
Prof. dr. V. Icke
Dr. P.P. van der Werf
Prof. dr. P.T. de Zeeuw

Voor mijn ouders

Cover: "The alchemist" by Sir William Fettes Douglas (1822 - 1891)

Contents

1	General introduction	1
1.1	Galaxy building blocks	1
1.1.1	Dust	1
1.1.2	Gas	1
1.2	Extreme environments in Galaxy Centers	2
1.3	This thesis	4
1.3.1	Part I	4
1.3.2	Part II	4
1.3.3	Part III	5

Part I: Dust in M51

2	Introduction	9
3	A sub-millimeter exponential disk in M 51	13
3.1	Observations and data reduction	14
3.1.1	Sky noise and background removal	15
3.1.2	Total flux density	18
3.2	Contamination by J=3-2 CO line emission	19
3.3	The diffuse disk	19
3.3.1	The Monte Carlo radiation transfer code RADMC	19
3.3.2	Adopted disk structure	21
3.4	Results and analysis	22
3.4.1	M 51 stellar parameters	22
3.4.2	Disk parameter determination	22
3.4.3	Dust mass and gas-to-dust ratio	26
3.5	Summary	26
4	The spiral structure of M 51 at 850 μm	29
4.1	Observations	30
4.2	Contamination by in-band $J = 3 - 2$ CO line	30
4.3	Morphological comparison to other wavelengths	33
4.3.1	Arm I (Inner Southern arm)	34
4.3.2	Arm II (Inner Northern arm)	34

4.4	The dust column density	35
4.5	The atomic and molecular mass	36
4.6	The CO to H ₂ conversion factor	41
4.7	Discussion	43
4.8	Conclusions	44

Part II: PDR and XDR models

5	Code description	49
5.1	Introduction	50
5.2	The Photon-dominated Region model	50
5.2.1	Heating processes	52
5.2.2	Cooling processes	56
5.2.3	Chemistry	60
5.3	The X-ray dominated region model	64
5.3.1	Energy deposition rate per hydrogen nucleus	65
5.3.2	Heating processes	65
5.3.3	Cooling processes	67
5.3.4	Chemistry	68
6	PDR and XDR comparison	75
6.1	Introduction	76
6.2	PDR test models	76
6.2.1	Heating	76
6.2.2	Cooling	77
6.2.3	Temperature structure	79
6.2.4	Chemistry	79
6.3	XDR test models	81
6.3.1	Heating	81
6.3.2	Cooling	81
6.3.3	Temperature structure	83
6.3.4	Chemistry	84
6.4	Conclusion	85
7	Comparison to other PDR codes	95
7.1	Introduction	96
7.2	Description of the Benchmark Models	96
7.2.1	PDR Code Characteristics	96
7.2.2	Benchmark Frame and Input Values	98
7.3	Results	100
7.4	Concluding remarks	102
7.4.1	Meijerink & Spaans code	102
7.4.2	All codes	102

Part III: Model applications

8	A grid of PDR and XDR models	107
8.1	Introduction	108
8.2	'Standard' clouds	108
8.3	Surface temperatures	110
8.4	Fine-structure lines	112
8.4.1	[SiIII] 35 μm /[CII] 158 μm intensity ratio	112
8.4.2	[OI] 63 μm /[CII] 158 μm intensity ratio	116
8.4.3	[FeII] 26 μm /[CII] 158 μm intensity ratio	117
8.4.4	[CI] 369 μm /[CI] 609 μm intensity ratio	117
8.5	Rotational lines	118
8.5.1	CO rotational lines	118
8.5.2	High J -CO rotational transitions	123
8.5.3	^{13}CO rotational lines	125
8.5.4	$^{13}\text{CO}/\text{CO}$ ratios	126
8.5.5	[CI] 609 $\mu\text{m}/^{13}\text{CO}(2-1)$ ratio	126
8.5.6	HCN rotational lines	128
8.5.7	HCN/CO line intensity ratios	130
8.5.8	HCO^+ rotational lines and HCN/ HCO^+ line intensity ratios	133
8.5.9	HNC/HCN ratios	135
8.5.10	SiO and CS	136
8.6	Column density ratios	137
8.6.1	CN/HCN column density ratio	137
8.6.2	CH/HCN column density ratios	139
8.6.3	CH^+ /HCN column density ratios	140
8.6.4	HCO/HCO^+ column density ratios	142
8.6.5	$\text{HOC}^+/\text{HCO}^+$ column density ratios	143
8.6.6	NO/CO column density ratios	143
8.6.7	$\text{N}_2\text{H}^+/\text{CO}$ column density ratios	144
8.7	Summary and outlook	144
9	Irradiated ISM: Discriminating between Cosmic Rays and X-rays	157
9.1	Introduction	158
9.2	PDR and XDR models	158
9.3	Chemical and thermal structure	160
9.4	CO line intensities and ratios	160
9.5	[CI] 609 $\mu\text{m}/^{13}\text{CO}(2-1)$ ratios	161
9.6	HCN/CO and HCN/ HCO^+ ratios	161
9.7	Conclusions	162
10	Interpretation of observed sub-mm emission of nearby galaxies	167
10.1	Introduction	168
10.2	Observations	168
10.3	Angular scales and their consequences	169

10.4	Comparison to model ratios	169
10.4.1	CO ratios	169
10.4.2	[CI] $609\mu\text{m}/^{13}\text{CO}(2-1)$	175
10.4.3	HCN/HCO ⁺ ratios	175
10.4.4	HCN/CO ratios	175
10.4.5	HNC/HCN ratios	176
10.4.6	CS ratios	177
10.5	Comparison to Galactic PDRs	177
10.6	X-ray versus FIR emission	177
10.7	Discussion	178
10.7.1	Individual galaxies	178
10.7.2	General remarks	181
11	Highlights & Outlook	195
11.1	Identification of diagnostics	195
11.2	Model extensions	197
11.3	Future observatories	198
	References	199
	Nederlandse Samenvatting	207
	Syatu pisi fu na buku in Sranan	213
	Curriculum Vitae	219
	Nawoord	221

CHAPTER 1

General introduction

1.1 Galaxy building blocks

The baryonic matter in a galaxy comprises gas, dust and stars. The gas consists of atoms and molecules while dust takes the form of silicate and carbonaceous solids. Stars are present with masses between 0.01 and 100 times the mass of the sun. There are about 100 billion stars in our galaxy, which make up roughly 90 percent of the visible mass. The other 10 percent consists of gas and dust, and is generally called the interstellar medium (ISM) or circumstellar medium (CSM). These percentages may be different in other galaxies. We can find this ISM under a very broad range of conditions. The densities range from ~ 0.1 to over 10^{10} cm^{-3} , and the temperatures from 10 to 10^6 K. Most of the galaxy volume is filled with very low density gas ($\sim 0.1 \text{ cm}^{-3}$). In regions, where stars are formed, the gas has contracted due to gravitational instabilities, and densities range between $10^4 - 10^6 \text{ cm}^{-3}$. Planetary nebulae, representing the last phase of evolution for intermediate-mass stars, have low densities ($10 - 100 \text{ cm}^{-3}$), but can attain very high temperatures (10^4 K). Very high densities $10^8 - 10^{10} \text{ cm}^{-3}$ and moderate temperatures 10 – 300 K are found in proto-planetary disks. Although we speak about very high densities, on earth this is about the best vacuum we can achieve.

1.1.1 Dust

Dust particles have a very broad range in sizes, from about 10\AA to $0.25\mu\text{m}$, and therefore have very different properties. Although we know that dust consists of silicate and amorphous grains, the exact composition and structure of dust is not very well understood, and also changes when it is exposed to different influences. We know that, although dust particles make up only 1 percent of the mass of the ISM, they provide most of the extinction at optical and ultraviolet wavelengths. Accurate extinction curves are hard to derive, and often vary from line of sight to line of sight. Dust also provides a very important heating source of the gas. It heats the gas through photo-electric emission and gas-dust collisions. Dust is also the host for a very important reaction, namely the formation of H_2 , since the gas phase reaction rate for the formation of H_2 is very slow.

1.1.2 Gas

Gas in galaxies consists for the largest part of hydrogen (~ 90 percent) and helium (~ 8.5 percent). The other ~ 1.5 percent are called metals by the astronomers, and are heavier elements such as carbon, nitrogen and oxygen. Depending on impinging flux and density,

gas clouds obtain a thermal and chemical structure, emitting all kinds of atomic fine-structure and molecular (e.g., H_2 , CO , HCN and H_2O) rotational and vibrational lines. The lines are emitted in the (sub)-millimeter range of the spectrum, and can be observed with telescopes such as the James Clerk Maxwell Telescope (JCMT), and the Institute de Radio Astronomie Millimétrique (IRAM) 30m telescope. For every set of conditions, a different set of line intensities and line intensity ratios is obtained, and these provide, therefore, excellent probes to estimate the physical properties of the gas.

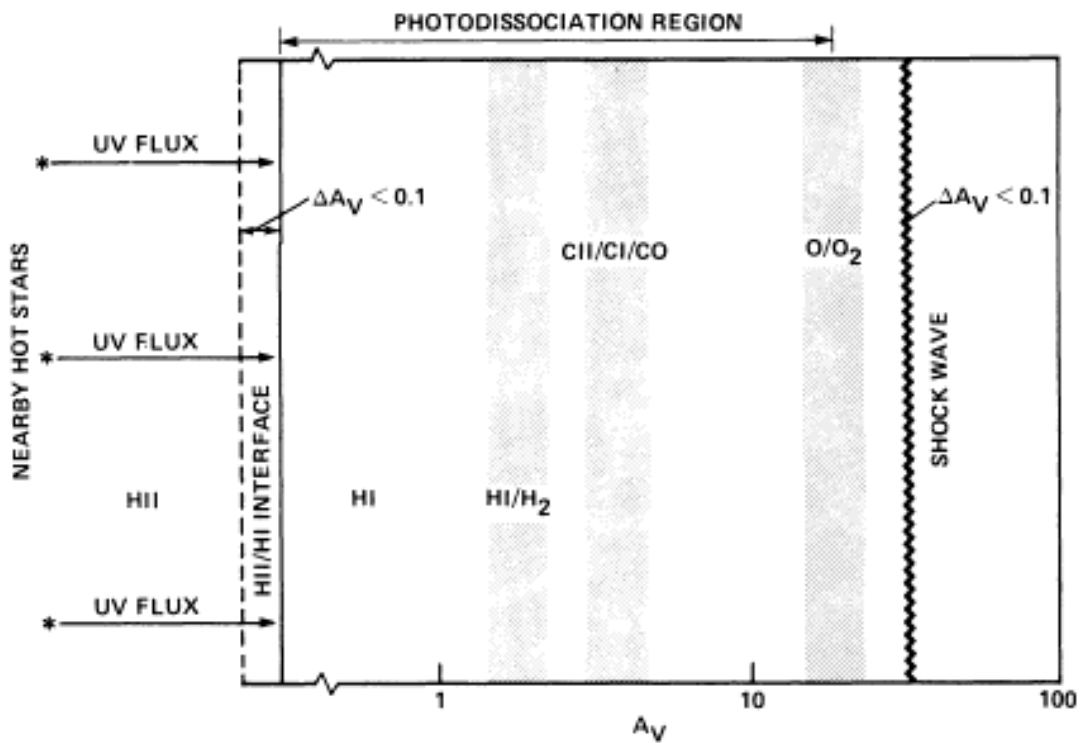


Figure 1.1: Schematic overview of a Photon Dominated Region (Tielens & Hollenbach 1985).

1.2 Extreme environments in Galaxy Centers

Our planetary system orbits at about a distance of 8 kpc from the center of the galaxy. The number of stars per unit volume is low, given that the closest star is at a distance of 1.3 pc (4.2 light years). However, in the center of a galaxy the stellar density and the average gas density are much higher than in the Solar Neighborhood. Therefore, the center of a galaxy is more efficient at converting interstellar gas into stars, and as a consequence the average interstellar radiation field is much more intense. Strong radiation is not only provided by newly formed stars, but also by the often present central black hole, when it accretes nearby gas and stars. Although strong radiation may be produced, galaxy centers are often very obscured in the optical, since the higher dust content of galaxy centers can provide extinctions ranging between 10 and 100 magnitudes. In the sub-millimeter

	High H_X/n	$H/H_2 \sim 0.01$	Low H_X/n
H	H	$H/H_2 \sim 0.01$	H_2
T	$T \sim 10^4 \text{ K}$	$T \sim 2000 \text{ K}$	$T < 200 \text{ K}$
C, C ⁺	C ⁺ , C	C, C ⁺	CO, C, C ⁺
O	O	O	O, OH, O ₂ , H ₂ O
X_e	$X_e \sim 10^{-2} - 10^{-1}$	$X_e \sim 10^{-3} - 10^{-2}$	$X_e < 10^{-3}$
Fe ⁺	Fe ⁺	Fe ⁺	Fe ⁺ , Fe

Figure 1.2: Schematic overview of an X-ray Dominated Region (Maloney et al. 1996).

range, dust opacities are very low, and tracers such as CO, HCN, and HCO⁺ provide excellent diagnostics. We will model these lines with Photon Dominated Regions (PDRs, Tielens & Hollenbach 1985) and X-ray Dominated Regions (XDRs, Maloney et al. 1996). PDRs are regions irradiated by far-ultraviolet (FUV: $6 < E < 13.6 \text{ eV}$) photons, which are produced by O and B stars in star-bursts. Generally, we express the impinging flux between $6 < E < 13.6 \text{ eV}$ in units of G_0 , the Habing (1969) average interstellar radiation field. XDRs are regions exposed to X-ray ($1 < E < 100 \text{ keV}$) photons, coming from accreting black hole environments. These PDRs and XDRs are extensively discussed in Chapters 5 and 6, with their chemical structure in summarized Fig. 1.1 and 1.2. The PDR, with a modest ionization degree of $< 3 \times 10^{-4}$, exhibits a clear stratified structure in important interstellar species as H & H₂ and C⁺, C & CO, whereas the XDR, with electron abundances as large as 10^{-1} , has a chemical structure where these species can co-exist. These properties, studied in this thesis, lead to unique interstellar diagnostics that distinguish the effects of massive stars (FUV photons) and an accreting black hole (X-rays) on the central regions of galaxies.

1.3 This thesis

1.3.1 Part I

In Chapter 2, we give an introduction to observations of dust in galaxies. We discuss some of the important results, the problems which have been encountered, and the uncertainties.

In Chapter 3, we show a 850 μm map of the interacting spiral galaxy M 51, which has been observed with the JCMT. It shows well-defined spiral arms, closely resembling the structures seen in CO and HI emission. However, most of the 850 μm emission originates in an underlying exponential disk, a component that has not been observed before in a face-on galaxy at these wavelengths. The scale-length of this disk is 5.45 kpc, which is somewhat larger than the scale-length of the stellar disk, but somewhat smaller than that of atomic hydrogen. Its profile cannot be explained solely by a radial disk temperature gradient but requires the underlying dust to have an exponential distribution as well. This reinforces the view that the sub-mm emission from spiral galaxy disks traces total hydrogen column density, i.e. the sum of H_2 and HI. A canonical gas-to-dust ratio of 100 ± 26 is obtained for $\kappa_{850} = 1.2 \text{ g}^{-1} \text{ cm}^2$, where κ_{850} is the dust opacity at 850 μm .

In Chapter 4, we determine the surface density of the dust and molecular gas and the CO-to- H_2 conversion factor in the spiral arms of M 51. The dust surface density is obtained from the 850 μm emission. Using the dust surface density, for each point in the disk the surface density of the gas can be derived under the assumption that the gas-to-dust ratio has the same radial dependence as the metallicity, as measured by the fractional abundance of oxygen. By comparing these gas surface densities with the observed total gas density from 21-cm neutral hydrogen observations and CO observations of the molecular gas, we can determine the CO-to- H_2 conversion factor as function of position within the galaxy. The central total hydrogen-gas-to-dust-mass ratio is found to be 60. The resulting CO-to- H_2 conversion factor is consistent with other independent determinations in M51 and shows a radial gradient.

1.3.2 Part II

In Chapters 5 and 6, we present a far-ultraviolet (PDR) and an X-ray dominated region (XDR) code. We include and discuss thermal and chemical processes that pertain to irradiated gas. An elaborate chemical network is used and a careful treatment of PAHs and H_2 formation, destruction and excitation is included. For both codes we calculate four depth-dependent models for different densities and radiation fields, relevant to conditions in star-burst galaxies and active galactic nuclei. A detailed comparison between PDR and XDR physics is made for total gas column densities between $\sim 10^{20}$ and $\sim 10^{25} \text{ cm}^{-2}$. We show cumulative line intensities for a number of fine-structure lines (e.g., [CII], [OI], [CI], [SiII], [FeII]), as well as cumulative column densities and column density ratios for a number of species (e.g., CO/H_2 , CO/C , HCO^+/HCN , HNC/HCN). The comparison between the results for the PDRs and XDRs shows that column density ratios are almost constant up to $N_{\text{H}} = 10^{22} \text{ cm}^{-2}$ for XDRs, unlike those in PDRs. For example, CO/C in PDRs changes over four orders of magnitude from the edge to $N_{\text{H}} = 10^{22} \text{ cm}^{-2}$. The CO/C and CO/H_2 ratios are lower in XDRs at low column densities and rise at $N_{\text{H}} >$

10^{23} cm^{-2} . At column densities $N_{\text{H}} \leq 10^{22.5} \text{ cm}^{-2}$, HNC/HCN ratios are lower in XDRs too, but they show a moderate increase to values > 1 at higher N_{H} .

In Chapter 7, we present a comparison between independent computer codes that model the physics and chemistry of photon dominated regions (PDRs). A number of benchmark models are calculated, covering low and high gas densities n and far ultraviolet intensities χ (FUV: $6 < E < 13.6 \text{ eV}$). χ is in units of the Draine (1978) average interstellar radiation field, where $\chi = G_0/1.71$. The benchmark models are computed in two ways: one set assuming constant temperatures, thus testing the consistency of the chemical network and photo-reactions, and a second set determining the temperature self-consistently by solving the thermal balance, thus testing the modeling of the heating and cooling mechanisms accounting for the detailed energy balance throughout the clouds. Our goal is to understand the mutual differences in the PDR codes and their effects on the physical and chemical structure of the model clouds, and to converge the output of different codes to a common solution. We identify a number of key processes that govern the chemical network and which are treated differently in the various codes, such as the contribution of PAHs to the electron density or the temperature dependence of the dissociation of CO by cosmic ray induced secondary photons, and formulate and define a proper common treatment. By understanding the impact of the PDR geometry we agree on how to compare the results from spherical and plane-parallel PDR models. As a result from the benchmark calculations we establish a comprehensive set of reference models for ongoing and future PDR modeling. We conclude that the benchmark results from the PDR code, which is described in Chapters 5 and 6, compare very well with the results obtained by other participating codes.

1.3.3 Part III

In Chapter 8, numerical models are constructed from the codes, which are presented in Chapters 5 and 6, in order to determine the physical conditions that pertain to molecular gas close to the sources of radiation, which are often found in nuclei of active galaxies. These models iteratively determine the thermal and chemical balance of molecular gas that is exposed to X-rays (1-100 keV) and far-ultraviolet radiation (6-13.6 eV), as a function of depth. We present a grid of XDR and PDR models that span ranges in density ($10^2 - 10^{6.5} \text{ cm}^{-3}$), irradiation ($10^{0.5} - 10^5 G_0$ and $F_X = 1.6 \times 10^{-2} - 160 \text{ erg cm}^{-2} \text{ s}^{-1}$) and column density ($3 \times 10^{21} - 1 \times 10^{25} \text{ cm}^{-2}$). Predictions are made for the most important atomic fine-structure lines, e.g., [CII], [OI], [CI], [SiII], and for molecular species like HCO^+ , HCN, HNC, CS and SiO up to $J = 4$, CO and ^{13}CO up to $J = 16$, and column densities for CN, CH, CH^+ , HCO, HOC^+ , NO and N_2H^+ . We find that surface temperatures are higher (lower) in PDRs compared to XDRs for densities $> 10^4$ ($< 10^4$) cm^{-3} . For the atomic lines, we find that, largely due to the different XDR ionization balance, the fine-structure line ratios of [SiII] $35 \mu\text{m}/[\text{CII}] 158 \mu\text{m}$, [OI] $63 \mu\text{m}/[\text{CII}] 158 \mu\text{m}$, [FeII] $26 \mu\text{m}/[\text{CII}] 158 \mu\text{m}$ and [CI] $369 \mu\text{m}/[\text{CI}] 609 \mu\text{m}$ are larger in XDRs than in PDRs, for a given density, column and irradiation strength. Similarly, for the molecular lines, we find that the line ratios HCN/HCO^+ and HNC/HCN , as well as the column density ratio CN/HCN , discriminate between PDRs and XDRs. In particular, the HCN/HCO^+ 1-0 ratio

is < 1 (> 1) for XDRs (PDRs) if the density exceeds 10^5 cm^{-3} and if the column density is larger than 10^{23} cm^{-2} . For columns less than $10^{22.5} \text{ cm}^{-2}$ the XDR HCN/HCO⁺ 1-0 ratio becomes larger than one, although the individual HCN 1-0 and HCO⁺ 1-0 line intensities are weaker. For modest densities, $n = 10^4 - 10^5 \text{ cm}^{-3}$, and strong radiation fields ($> 100 \text{ erg s}^{-1} \text{ cm}^{-2}$), HCN/HCO⁺ ratios can become larger in XDRs than PDRs as well. Also, the HCN/CO 1-0 ratio is typically smaller in XDRs, and the HCN emission in XDRs is boosted with respect to CO only for high (column) density gas, with columns in excess of 10^{23} cm^{-2} and densities larger than 10^4 cm^{-3} . Furthermore, CO is typically warmer in XDRs than in PDRs, for the same total energy input. This leads to higher CO $J=N+1-N$ /CO 1-0, $N \geq 1$, line ratios in XDRs. In particular, lines with $N \geq 10$, like CO(16-15) and CO(10-9) observable with HIFI/Herschel, discriminate very well between XDRs and PDRs. This is crucial since the XDR/AGN contribution will typically be of a much smaller (possibly beam diluted) angular scale and a 10-25% PDR contribution can already suppress XDR distinguishing features involving HCN/HCO⁺ and HNC/HCN. For possible future observations, column density ratios indicate that CH, CH⁺, NO, HOC⁺ and HCO are good PDR/XDR discriminators.

The ISM of active galaxy centers is exposed to a combination of cosmic ray, FUV and X-ray radiation. In Chapter 9, we apply PDR models to this ISM with both ‘normal’ and highly elevated ($5 \times 10^{-15} \text{ s}^{-1}$) cosmic ray rates and compare the results to those obtained for XDRs. Our existing PDR-XDR code is used to construct models over a $10^3 - 10^5 \text{ cm}^{-3}$ density range and for $0.16-160 \text{ erg s}^{-1} \text{ cm}^{-2}$ impinging fluxes. An elevated cosmic ray rate leads to larger high J ($J > 10$) CO PDR ratios, but these are always exceeded by the corresponding XDR ratios. The [CI] $609 \mu\text{m}/^{13}\text{CO}(2-1)$ line ratio is boosted by a factor of a few in PDRs with $n \sim 10^3 \text{ cm}^{-3}$ exposed to a high cosmic ray rate. At higher densities ratios become identical irrespective of cosmic ray flux, while XDRs always show elevated [CI] emission per CO column. The HCN/CO and HCN/HCO⁺ line ratios, combined with high J CO emission lines, are good diagnostics to distinguish between PDRs under either low or high cosmic ray irradiation conditions, and XDRs. Hence, we conclude that the HIFI instrument on Herschel, which can detect these CO lines, will be crucial in the study of active galaxies.

In Chapter 10, we assess the presence of star-forming regions, active galactic nuclei, and enhanced cosmic ray rates in the centers of nearby galaxies through molecular emission of HCN, HCO⁺, HNC, CO, ¹³CO, CS and [CI]. We use the grid of PDR and XDR models calculated in Chapter 8, where density, impinging FUV and X-ray flux, and column density are varied for homogeneous slabs. We derive the (high cosmic ray) PDR and XDR components for individual galaxies, and define a diagnostic diagram, which can be applied to other galaxies, e.g., (U)LIRGS, as well. In general, we find that XDRs or elevated cosmic ray PDRs are necessary to explain CO(2-1)/CO(1-0) and [CI]/¹³CO(2-1) ratios, which are tracing the diffuse part of the ISM. In particular, we find that NGC 1068, often viewed as a pure AGN, needs a dense PDR component.

In Chapter 11, we conclude with an outlook. We discuss possible model extensions, which will be needed to interpret observations from future telescopes, such as Herschel and ALMA. We suggest some possible diagnostic molecules (when accurate collision rates become available) for future observations.

Part I
Dust in M 51

CHAPTER 2

Introduction

The determination of the dust content in galaxies, especially in relation to the total gas mass, has been a subject of discussion for several decades. In the 1980s, *IRAS* measurements seem to imply relatively high gas-to-dust-mass ratios for spiral galaxies, ranging from $M(\text{H}_2)/M_{\text{dust}} = 450 \pm 270$ (Young et al. 1986) to 570 ± 50 (Young et al. 1989) and $M(\text{HI} + \text{H}_2)/M_{\text{dust}} = 1080 \pm 70$ (Devereux & Young 1990). These values are very much larger than the Galactic value of about 100 originally proposed by Spitzer (1978). At least part of the discrepancy is caused by *IRAS*' lack of sensitivity to cold dust ($T_{\text{dust}} < 25$ K), as it operated in the far-infrared (FIR: $\lambda=10\text{-}100 \mu\text{m}$) only. *IRAS* thus misses a possibly large fraction of the total dust amount, emitting radiation mostly in the (sub)-millimeter range ($\lambda = 0.1 - 1.0$ mm).

In the 1990s, telescopes operating at longer wavelengths obtain new insights. Instruments such as the Sub-millimeter Common Bolometer Array (SCUBA) at the James Clerk Maxwell Telescope (JCMT), the Infrared Space Observatory (ISO), and other bolometer arrays find evidence for a significant contribution by relatively cold dust. Observations in a number of well-studied galaxies show that the typical temperatures of the dust are in the range of $15 < T_{\text{dust}} < 25$ K (e.g., NGC 891: Guélin et al. 1993; M 51: Guélin et al. 1995; NGC 4631: Braine et al. 1995; NGC 891: Alton et al. 1998; NGC 891: Israel et al. 1999; NGC 3079: Stevens & Gear 2000; NGC 6946: Alton et al. 2002). In general, a fit of the SEDs in these galaxies requires the presence of both warm and cold dust. By contrast, in our Galaxy these components of the ISM are typically resolved allowing for single temperature SED fits.

Next, Dunne et al. (2000) observe 104 galaxies from the *IRAS* Bright Galaxy Sample as part of the SCUBA Local Universe Galaxy Survey (SLUGS) and find an average dust temperature of $T_{\text{dust}} = 35.6 \pm 4.9$ K when fitting a single-component SED to the 60, 100 and 850 μm fluxes. The average gas-to-dust-mass ratio for this sample is 581 ± 43 , similar to the values derived from *IRAS* measurements a decade earlier and still much larger than the value of, e.g., 160 for our Galaxy found by Sodroski et al. (1994) based on *COBE* data at 140 and 240 μm . However, Dunne et al. (2000) fit single dust temperatures to the galaxies as a whole although their ISM is probably a composite of unresolved colder and warmer components as was found for the individual galaxies in the earlier studies. Commenting on this possibility, Dunne et al. (2000) state that if a cold dust component of 20 K is assumed to be present the derived dust masses would be 1.5-3.0 times higher and the gas-to-dust-mass ratios correspondingly lower and closer to the Galactic value.

Popescu et al. (2002) perform a survey with ISO in the Virgo cluster. After fitting two component SED models to the 60, 100 and 170 μm fluxes, they find that the *IRAS* determinations of the dust mass in these galaxies should be raised by a factor of 6-13.

They obtain a median temperature of 18 K for the cold dust component, in good agreement with the range of values from the sub-mm telescopes. Stevens et al. (2005) analyze 14 nearby spiral galaxies, and fit two-temperature models. Their mean gas-to-dust-mass ratio is 120 ± 60 , very similar to that in our own Galaxy.

Based on these recent results, it thus appears likely that other galaxies have global gas-to-dust-mass ratios similar to that of our Galaxy and the perceived earlier discrepancy is caused by an insensitivity of the observations to the presence of an ubiquitous cold dust component. Direct observations of this cold dust component, however, often lack resolution or are carried out in highly inclined systems revealing little about its detailed distribution within the galaxies.

The spatial distribution of dust and its relation to other components of the ISM is best studied in face-on systems, but at sub-mm wavelengths surface brightnesses are typically low. This particularly hampers the search for diffuse emission from inter-arm regions. Another more specific problem is that, e.g., the SCUBA field-of-view (2.3 arcmin) is small compared to the angular size of the disks of nearby galaxies, requiring a scan-map type of observing mode. For SCUBA this way of observing raises a few complications, because of its requirement to chop on-source while scanning, which results in the individual observations lacking sensitivity on spatial scales corresponding to the used chop-throw. By combining observations with different chop-throws one can minimize this problem, but the largest-scale features remain poorly determined, including the total flux density. The example of NGC 6946 is illustrative. Little diffuse emission in the inter-arm region is seen by Alton et al. (2002) in the 850 μm map. Consequently, they state that "relatively little is known about how the dust is distributed with respect to the spiral arms and, in particular, whether inter-arm grain material is prevalent or not". The gas-to-dust-mass ratios they find range from 60 in the center to about 100 in the outer part of the galaxy (see Fig. 8 in their paper). Comparing their observations to the CO and HI 21cm line emission, they find a good correlation between the 850 μm emission and the CO emission and no correlation between the sub-mm emission and the atomic gas. This contrasts with their observations of the edge-on spiral NGC 891 (Alton et al. 1998) where they find the global radial profile of the 850 μm to follow the CO emission in the inner region but at larger radii to follow the atomic gas, suggesting an overall correlation with the total gas density.

At resolutions much lower than those provided by the JCMT, the cold dust in galaxies has been mapped with ISO in the far-infrared (Haas et al. 1998; Popescu et al. 2002; Hippelein et al. 2003; Tuffs & Gabriel 2003; Popescu & Tuffs 2003). These observations confirm the ubiquitous presence of cold dust below 20 K first observed by Chini et al. (1986) and indicate that the cold dust component is smoothly distributed over the disk and heated by the diffuse interstellar radiation field (Hippelein et al. 2003; Xu et al. 1994). Alton et al. (2001) report evidence for diffuse inter-arm dust in SCUBA observations of NGC 7331. For a recent discussion of 'dusty disks' see also Bianchi (2004).

M 51 is a well studied, face-on interacting spiral galaxy at an assumed distance of 9.7 Mpc. It is well known for its strong CO emission, but contrary to NGC 6946 its density-wave and spiral arms are well-organized and prominent, showing a high contrast in the radio continuum (see e.g. Tilanus & Allen 1991; 1989). The distribution of cold

dust in the nuclear region of M 51 has been mapped at 1.2 mm by Guélin et al. (1995), who notes a close correlation with CO line emission. Our current 850 μm observations (Fig. 3.1) show that its dust emission is exceptionally strong. The spiral arms are clearly distinguished, but there is also a substantial amount of emission from an extended diffuse disk. To our knowledge, such a submillimeter disk has not been clearly identified in any other galaxy, but in view of the ISO observations discussed previously it may be a common component of spiral galaxies. In Chapter 3 we explore the nature and properties of this diffuse disk. In Chapter 3 we focus on the spiral arms. We determine the dust surface density from the 850 μm in the spiral arms and compare this to other tracers of the ISM. Using the dust surface density, at each point the surface density of the gas can be derived with the assumption that the gas-to-dust ratio has the same radial dependence as the metallicity, as measured by the fractional abundance of oxygen. By comparing these gas surface densities with the observed total gas density from 21-cm neutral hydrogen observations and CO observations of the molecular gas, we can determine a radial profile for CO-to-H₂ conversion factor, X. This way of determining the X-factor is independent from most other methods used in previous studies (c.f., Israel et al. 2006; Guélin et al. 1995; Nakai & Kuno 1995).

CHAPTER 3

A sub-millimeter exponential disk in M 51

A 850 μm map of the interacting spiral galaxy M 51 shows well-defined spiral arms, closely resembling the structures seen in CO and HI emission. However, most of the 850 μm emission originates in an underlying exponential disk, a component that has not been observed before in a face-on galaxy at these wavelengths. The scale-length of this disk is 5.45 kpc, which is somewhat larger than the scale-length of the stellar disk, but somewhat smaller than that of atomic hydrogen. Its profile cannot be explained solely by a radial disk temperature gradient but requires the underlying dust to have an exponential distribution as well. This reinforces the view that the sub-mm emission from spiral galaxy disks traces total hydrogen column density, i.e. the sum of H_2 and HI. A canonical gas-to-dust ratio of 100 ± 26 is obtained for $\kappa_{850} = 1.2 \text{ g}^{-1} \text{ cm}^2$, where κ_{850} is the dust opacity at 850 μm .

R. Meijerink, R.P.J. Tilanus, C.P. Dullemond, F.P. Israel, and P.P. van der Werf, 2005
Astronomy & Astrophysics, Volume 430, pp. 427–434

3.1 Observations and data reduction

M 51 was observed at $850\ \mu\text{m}$ and $450\ \mu\text{m}$ in the spring of 1998 and 1999 at the JCMT¹ using the Submillimeter Common User Bolometer Array (SCUBA: Holland et al. 1999). In order to map a $13.5' \times 13.5'$ region around M 51, the camera was used in scan-map mode during which it scanned at a rate of $3''$ per second across the field, while the secondary was chopped with a frequency of 7.8 Hz in right ascension or in declination to cancel atmospheric signal variations as well as bolometer DC fluctuations. This uses the revised version of the Emerson-Klein-Haslam algorithm proposed by Emerson (1995). The scan angle across the field, $(15.5 \pm 60^\circ)$, was chosen such that the resulting image is fully sampled. The total integration time was about 20 hours spread over 6 nights.

To restore the brightness distribution of the source, the chop must be deconvolved from the observed map by using a division in the Fourier plane (Jenness et al. 2000). The Fourier transform (FT) of the chop is a sine wave with zeroes at the origin and at harmonics of the inverse chop throw. The initial observations used chop throws of 20, 30, and 65 arcsecs. To minimize regions of low weight (close to zeroes) in the Fourier plane we later added throws of 44 and 68 arcsecs. Each individual observation was flat-fielded, corrected for atmospheric opacity, and de-spiked. For each of the 10 different chop configurations the individual maps were co-added. Next, the resulting 10 maps were Fourier-transformed, weighted, and coadded. The coadded image was transformed back to yield the finished image. This is the standard reduction for SCUBA scan-map observations as implemented in the SCUBA User Reduction Facility software (SURF: Jenness & Lightfoot 1998).

The data were flux-calibrated using Mars and the secondary standards HL Tau and CRL 618. In the final image, the beam-size at $850\ \mu\text{m}$ is about $15''$ (FWHM). The calibrated image is shown in Fig. 3.1 and has an overall rms of ~ 9 mJy/beam. The inconspicuous source to the north is the nucleus of NGC 5195. The familiar spiral pattern is clearly visible and can be traced over a large fraction of the disk. This is quite unlike the sub-mm continuum observations of other face-on spirals, which in general lack the sensitivity to trace the arms outside the inner region. The morphology of the arms resembles in detail the one seen in CO emission (Aalto et al. 1999; Wielebinski et al. 1999), and we will address the contamination of the continuum emission by in-band line emission in Sect.3.

Remarkably, the $850\ \mu\text{m}$ emission from M 51, showing the distribution of the cool dust, is dominated by a diffuse exponential disk, a component that has not been directly imaged before at sub-mm wavelengths and with a high resolution in a face-on spiral. The $450\ \mu\text{m}$ observations also show spiral structure and an extended disk. In part because of the difficulty in deriving an accurate flux calibration and the poorer image quality we do not discuss further the $450\ \mu\text{m}$ data in this paper.

¹The James Clerk Maxwell Telescope is operated by the Joint Astronomy Centre on behalf of the Particle Physics and Astronomy Research Council of the United Kingdom, the Netherlands Organization for Scientific Research and the National Research Council of Canada

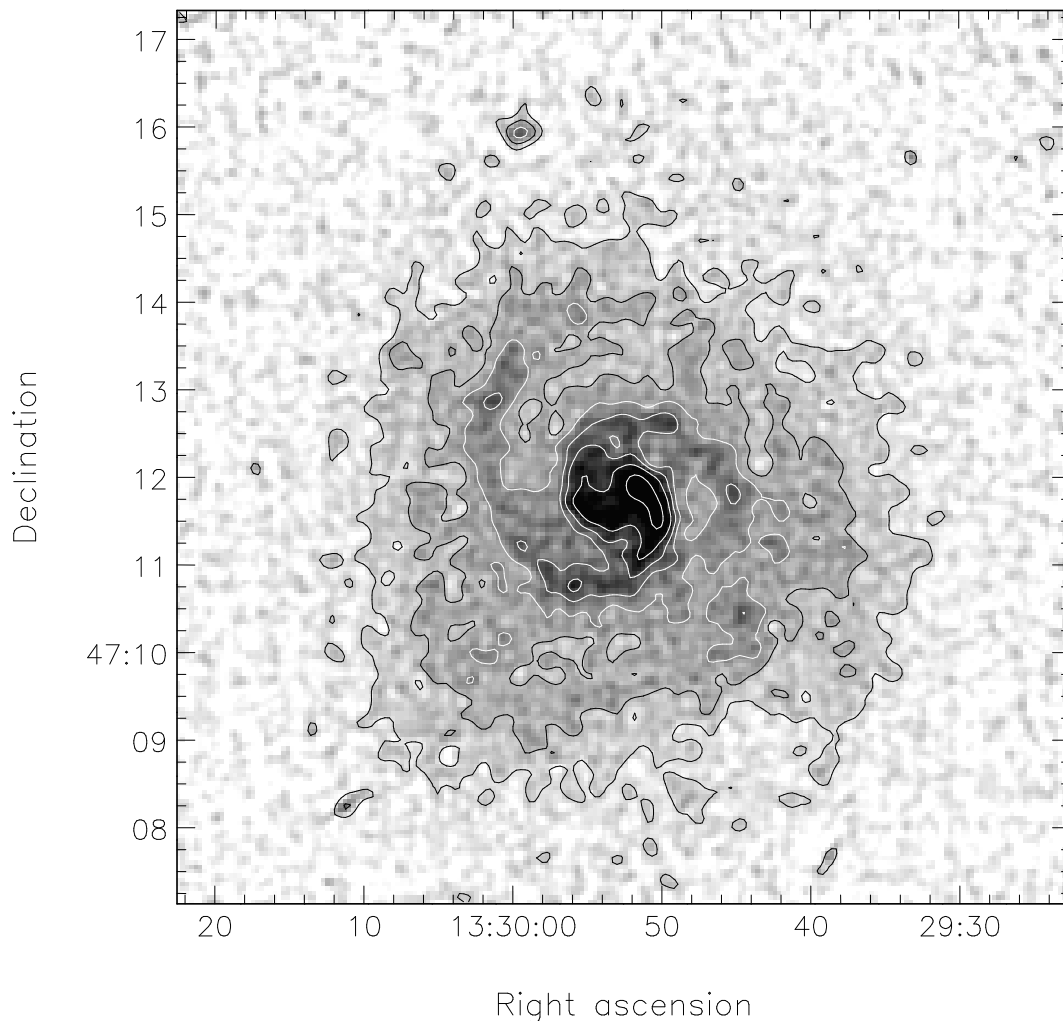


Figure 3.1: SCUBA calibrated and background-corrected $850 \mu\text{m}$ grey-scale image of M 51 with $850 \mu\text{m}$ contour superimposed. The contour levels are 13.5 ($=1.6 \sigma$), 27, 40.5, 58.5, 72, 90 and 117 mJy/beam. 13.5 mJy/beam corresponds to 2.6 MJy sr^{-1} . This image clearly shows the extended $850 \mu\text{m}$ disk. The small source to the north is the nucleus of NGC 5195.

3.1.1 Sky noise and background removal

Analyzing extended structures in SCUBA scan maps is a delicate process. While there is no doubt about the reality of the exponential disk, careful processing is required for reliable parameter extraction. There are a number of reasons for this.

First, while regions of low weight have been minimized through the use of many different chop configurations, the zero near the origin of the Fourier plane cannot be suppressed. This results in a poor determination of the largest-scale features in the map, including the total flux density. The effect is similar to that caused by missing short spacings in radio interferometry observations and it has a similar effect on the background.

Second, chopping removes noise due to sky fluctuations with a frequency compara-

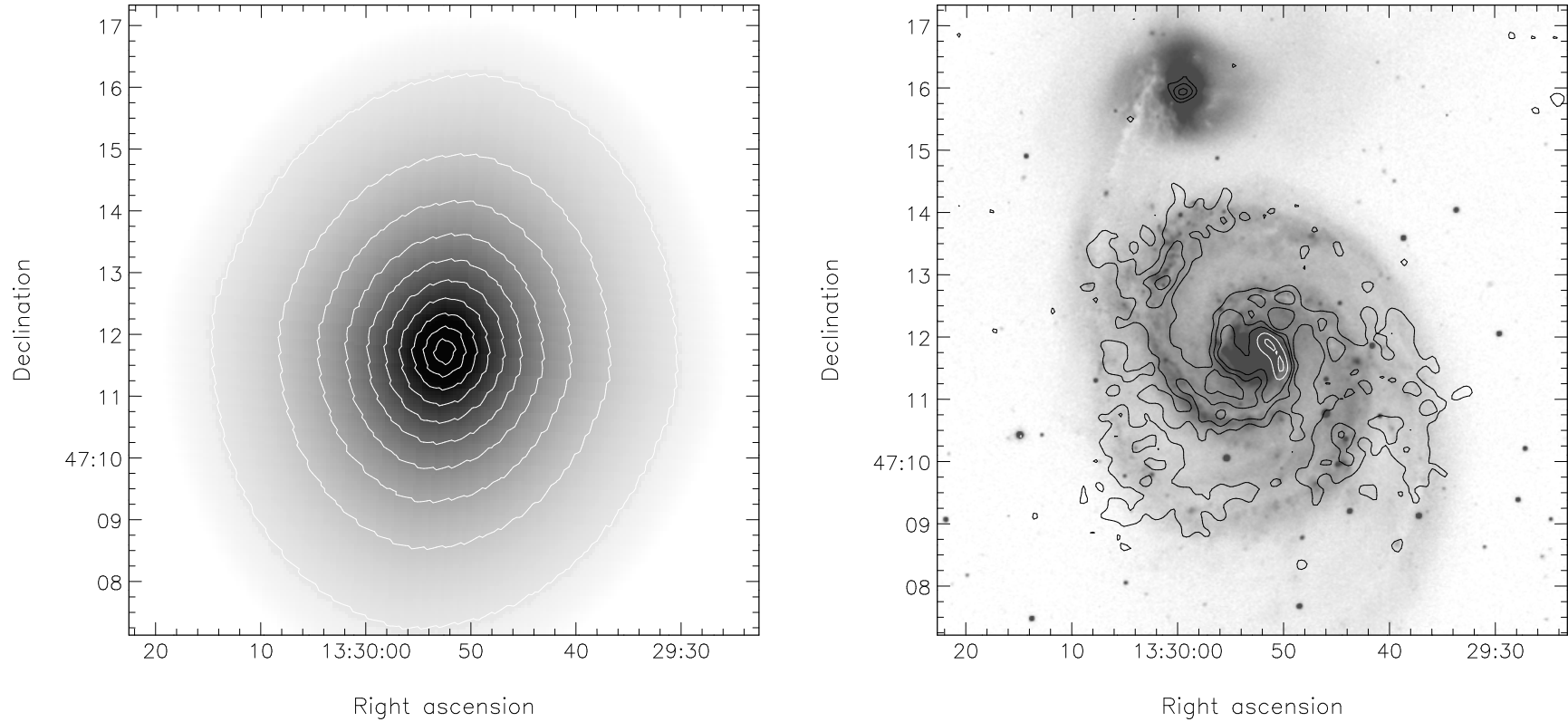


Figure 3.2: Left: Fitted exponential disk subtracted from the total $850\ \mu\text{m}$ emission as shown in Fig. 3.1. Contour steps are $6\ \text{mJy/beam}$ ($1.15\ \text{MJy sr}^{-1}$). The maximum intensity of the disk is $66\ \text{mJy/beam}$ with a major axis scale-length of $1.95'$. Right: Contours of $850\ \mu\text{m}$ in M 51 after subtraction of the exponential disk superimposed on a 6400\AA optical image (Tilanus et al. 1988). Contour levels are 12 ($=1.5\ \sigma$; $2.3\ \text{MJy sr}^{-1}$), 24, 36, 56 and $72\ \text{mJy/beam}$. The image shows the centroid of the $850\ \mu\text{m}$ emission to be located along the inner edges of the spiral arms and the optical dust lanes.

Table 3.1: Galaxy parameters

M 51	
Type ^a	SAS(s)bcp
Radio Centre:	
R.A. (B1950) ^b	13 ^h 27 ^m 46.3 ^s
Decl.(B1950) ^b	+47°27'10''
R.A. (J2000) ^b	13 ^h 29 ^m 52.7 ^s
Decl.(J2000) ^b	+47°11'42''
V_{LSR}^c	+464 km s ⁻¹
Inclination i^c	20°
Position angle P^c	170°
Distance D^d	9.7 Mpc
Scale	21''/kpc
Scale-lengths (disk):	(arcsec) (kpc)
B ^e	92.8±9.4 4.36±0.45
I ^e	81.2±7.0 3.81±0.33
R ^e	80.4±6.1 3.77±0.29
K ^e	87.1±6.8 4.09±0.32
Effective radius (bulge):	(kpc)
B ^f	0.94±0.72
V ^f	0.98±0.52
R ^f	1.07±0.57
I ^f	1.06±0.50

Notes to Table 3.1:

^a RSA (Sandage & Tammann 1987)

^b Turner & Ho (1994)

^c Tully (1974)

^d Sandage & Tammann (1975)

^e Beckman et al. (1996)

^f Laurikainen & Salo (2001)

ble to the chop frequency. It cannot remove the effect of a sky signal which is steadily increasing or decreasing during the scan, i.e., a slowly and monotonically varying component in the sky. In such situations the ‘on’ minus ‘off’ will always leave a small residual sky signal. We have used the standard SURF option, *scan_rlb*, to subtract a linear baseline from each bolometer scan fitted to the outer 2 arcmin on each side of the scan. While this significantly improves the flatness of the background, it will leave any ripples that may be due to *non-linear* variations of the sky during each scan. To improve further the sky-noise removal we have used the SURF routine *calcsky* (Jenness & Lightfoot 1998), which is similar to the *remsky* routine used for non-raster data. A detailed discussion of these methods is beyond the scope of the paper, but while *scan_rlb* relies on the fact that there

is no source signal at the edges of the map, *calcsky* makes use of the fact that (a component of) the sky noise is correlated across the bolometer array during each integration step. The application of both methods improves the flatness of the background without changing the overall appearance of the image.

Nevertheless, even with the application of the above, relatively objective, methods, background artifacts remain, likely because of the missing Fourier zero. This is a common feature of SCUBA scan maps. We use an iterative procedure to correct the image which involves subtracting an inclined exponential (the diffuse disk), un-sharp masking and blanking of the remaining source signal (arms, nucleus), followed by a polynomial plane fit and convolution to obtain a smooth, large-scale representation of the background. The operations are done using the finished co-added image. While comparable to the procedure used by e.g. Alton et al. (2002), it is subjective in nature. As guidelines we use the following assumptions: the background is flat and the inter-arm emission originates from the diffuse disk only.

The exponential diffuse disk will be discussed separately in section 4: we fit a scale-length of $1.95'$, perhaps fortuitously the same as found for the 20 cm ‘base’ disk (Tilanus et al. 1988), the inclination and position angle as in Table 3.1, and fit a peak of 66 mJy/beam. Across the disk of the galaxy the fitted background approximates a linear slope of -12 ± 10 mJy/beam: from -2 in the south to -22 in the north. The mean level of -12 mJy/beam corresponds to (minus) 9% of the 132 mJy/beam peak in the raw map. By inspecting the resulting inter-arm regions (Fig. 3.2) we estimate the local background to be accurate to a level of about ± 2 mJy/beam or about $\pm 5\%$ of the typical knots in the arms. Given the overall rms in the image of 9 mJy/beam, this uncertainty is about four times larger than the statistical uncertainty of the mean over the areas inspected. Fig. 3.1 shows the calibrated observations after correction for the low-level large-scale background fluctuations.

3.1.2 Total flux density

Using an aperture of $8'$, which just excludes the nucleus of NGC5195, we find an integrated flux of 14.5 ± 1.1 Jy. The uncertainty quoted indicates the range of values found when varying the aperture from $7.4'$ to $10'$, not the uncertainty resulting from the background variations. To estimate the latter we inspect the variation of the mean level in $2.5'$ square regions around M 51, similar to the size of the nucleus and inner arms. This variation is about 0.5 mJy/beam and can serve as an indication of the quality of the background correction where it is applied to regions already largely free from emission. By contrast we note that the ± 2 mJy/beam uncertainty of the background in the inter-arm regions, as mentioned in the previous section, is positive in the south and negative in the north, suggesting that the uncertainty of the zero level taken over the whole of the disk of M 51 is less than 2 mJy/beam. Based on these considerations we adopt an overall uncertainty in the background level of 1.5 mJy/beam, which corresponds to 1 Jy when summed over the $8'$ aperture. Finally, we need to add a 10% uncertainty in the flux of the calibrators at sub-mm wavelengths. Treating the various uncertainties as statistical errors, we derive a total $850 \mu\text{m}$ flux for M 51 of 15 ± 2 Jy. This value includes the contribution from line emission within the passband of SCUBA’s $850 \mu\text{m}$ filter, a topic which will be

discussed in the next section.

3.2 Contamination by J=3-2 CO line emission

The broad passband of the SCUBA instrument includes the wavelength of the $J=3-2$ ^{12}CO line. Thus, at any point in the map the continuum emission measured by SCUBA is, in principle, contaminated by CO line emission. In order to investigate the extent of the contamination we obtained with the JCMT in spring 2001 a set of CO(3-2) spectra across both inner arms of M 51 and supplemented these with archived spectra of the nuclear region. In the arms, the CO line contribution can be up to 30-40 percent of the observed continuum emission *after subtraction of the exponential disk*. Thus, a substantial fraction of the arm morphology seen in the SCUBA map directly results from contaminating line emission. Because of the apparently close correspondence between CO and dust emission on a global scale (Guélin et al. 1995), the effect is mostly quantitative and does not change the overall morphology of the arms qualitatively. The $J=3-2$ emission from the inter-arm regions is weak and in individual pointings does not exceed the noise in the measurements. In the center of M 51 we find an upper limit of 12 per cent (3σ) to any line contribution to the *emission from the fitted disk*. Consequently, we may assume either a constant CO contribution at any level below 12 per cent, or a maximum contribution of 12 per cent at the center decreasing to zero at the outer edge. These two possibilities thus define lower and upper limits, respectively, to the $850\mu\text{m}$ emission scale-length.

3.3 The diffuse disk

We have separated emission in the diffuse disk from arm emission by subtracting an inclined exponential disk and making the assumption that the inter-arm emission originates from the diffuse disk only (see also section 2.1). The best fit to the data is given by an exponential disk with a maximum intensity of 66 mJy/beam, and a major axis intensity scale-length of $1.95'$, corresponding to a linear scale-length of 5.45 kpc at the assumed distance of M 51. As $1 \text{ MJy sr}^{-1} = 5.22 \text{ mJy/beam}$, the maximum intensity $66 \text{ mJy/beam} = 12.7 \text{ MJy sr}^{-1}$. The subtracted exponential disk and the arm emission are shown in Fig. 3.2. The global parameters adopted for M 51, such as the distance, inclination, and position angle, are given in Table 3.1.

The apparent existence of a diffuse exponential disk raises further interesting questions. What kind of dust distribution can account for such a disk: an exponential dust distribution at a constant temperature, a constant dust distribution with a temperature gradient, or both an exponential distribution *and* a temperature gradient? What is the dust mass in proportion to the amount of gas?

3.3.1 The Monte Carlo radiation transfer code RADMC

To answer these questions, we have modeled the observed emission using a modified version of the axi-symmetric Monte Carlo code RADMC (see Dullemond & Dominik 2004).

This continuum radiative transfer code is based on the method of Bjorkman & Wood (2001) and Lucy (1999), but adapted to suit the purpose of this paper. The basic idea of this method is as follows. The input luminosity of the system comes from the population of stars in the galaxy. At every location in the galaxy this is represented by a wavelength-dependent source function with the spectral shape of the local stellar population. Integrated over wavelength and over space this source function yields the total intrinsic bolometric luminosity of the galaxy. Each spatial cell represents a certain fraction of this luminosity, dependent on the spatial distribution of the stars. And within such a cell each wavelength interval represents again a fraction of this luminosity, depending on the local spectral shape of the stellar population. In this way each space-wavelength cell represents a well-defined fraction of the total input energy into the problem.

The total input luminosity is now evenly divided over N_{phot} photon packages. These packages are launched into the galaxy at random angles from randomly chosen space-wavelength cells, where the probability for each space-wavelength cell to launch this photon is proportional to the fraction of the total input luminosity represented by that cell. Each photon package is launched and performs a random walk through the computational domain until it eventually escapes to infinity. After that, the next photon package is launched.

As these photon packages travel through the computational domain they can experience scattering and absorption events. A scattering event merely changes the direction of the photon package, but an absorption-reemission event can also change its wavelength. The probability function for this random wavelength is $dP(\lambda)/d\lambda \sim \partial B_\lambda(T)/\partial T$, where T is the local dust temperature at the moment the photon package enters the cell. The dust temperature changes during the simulation, increasing with the number of photon packages that have entered the cell. Each photon package travelling through a cell increases the ‘energy’ of the cell proportionally to the energy of the photon package, the length l of the path through the cell and the opacity of the cell at that wavelength. The temperature of the cell is increased after each passage in such a way that the total dust emission of the cell $4\pi \int_0^\infty \rho_{\text{dust}} \kappa_\lambda B_\lambda(T) d\lambda \times V_{\text{cell}}$ (where V_{cell} is the cell volume) equals the sum of all contributions $\rho_{\text{dust}} \kappa_\lambda l L_{\text{tot}}/N_{\text{phot}}$ of all photons that have so far passed through the cell.

The increase in the energy of the cell happens each time a photon travels through the cell, while a discrete scattering or absorption-reemission event (which changes the direction and/or wavelength of a photon package) occurs only at random locations along the path of the photon package. This random location is chosen to be at an optical depth of $\tau = |\log(\text{ran}(i_{\text{seed}}))|$ away from the last discrete event, where $\text{ran}(i_{\text{seed}})$ is a random number between 0 and 1.

Once all the photons have been launched and have left the system, the dust temperature and scattering source function at every location in the galaxy have been determined. Modulo random fluctuations this should be the correct temperature and scattering source term distribution. Now we use a ray-tracing code (part of the radiative transfer package RADICAL (Dullemond & Turlola 2000)) to produce the desired images and/or spectra. But to verify whether this temperature and scattering source term distribution is indeed the correct solution, RADMC has been tested in two ways. First, we have verified that flux is conserved to a high level of precision ($< 1\%$) by making spectra at many incli-

nation angles and integrating over wavelength and inclination to obtain the total output luminosity. Since the spectra are produced using a ray-tracing code, and not by counting the outgoing photon packages (as is the case for the Bjorkman & Wood code), this energy conservation is not numerically guaranteed, and therefore represents a good check on the self-consistency. The code has also been tested against many other codes in a 2-D radiative transfer comparison project (Pascucci et al. 2004).

3.3.2 Adopted disk structure

We assume that the stellar distribution consists of two components, the exponential disk and the bulge. For the bulge we use a Hubble profile (Reynolds 1913; Hubble 1930), which models the stellar emissivity as:

$$\begin{aligned} \mathcal{L}(R, z) &= \mathcal{L}_{\text{disk}} \exp\left(-\frac{R}{h_s} - \frac{|z|}{z_s}\right) \\ &+ \mathcal{L}_{\text{bulge}}(1 + B^2)^{-3/2} \end{aligned} \quad (3.1)$$

in which B is given by the expression:

$$B = \frac{[R^2 + (z/(b/a))^2]^{-3/2}}{R_e} \quad (3.2)$$

where R and z are cylindrical coordinates, $\mathcal{L}_{\text{bulge}}$ and $\mathcal{L}_{\text{disk}}$ bulge and disk emissivities at the center of the galaxy, respectively, h_s and z_s the respective stellar scale-lengths and scale-heights, R_e the effective bulge radius and b/a the minor/major axial ratio.

We explore both exponential and constant dust distributions. The parameterization to describe the exponential dust distribution is the same as that used for NGC 891 by Xilouris et al. (1998):

$$\rho(R, z) = \rho_c \exp\left(-\frac{R}{h_d} - \frac{|z|}{z_d}\right) \quad (3.3)$$

with ρ_c being the central dust density, h_d the dust distribution scale-length and z_d the dust distribution scale-height. A constant dust distribution is obtained from the same expression by putting the scale-length at infinity.

Extinction coefficients are obtained from the model described by Draine & Lee (1984). We consider four different silicate-to-graphite ratios in the grains, 0.5:0.5, 0.4:0.6, 0.3:0.7 and 0.2:0.8. The particle sizes a are set between 0.005 and 0.25 μm with a size distribution proportional to $a^{-3.5}$. Our modeling does not include either polyaromatic hydrocarbons (PAH's) or very small dust particles. Although these particles dominate the mid-infrared emission at e.g. 10–20 μm , their contribution to sub-millimeter emission at 850 μm is expected to be negligible (see, e.g., Li & Draine 2001).

The spectral energy distribution of the stars is taken from the models calculated by Bruzual & Charlot (1993). Specifically, we use the model for a continuously star-forming galaxy with a star-forming rate of $10^{-10} M_{\odot}/\text{yr}$ per unit solar mass, assuming a galaxy

age of 10 Gyr. We verify that decreases in the assumed age to 5 Gyr or even 1 Gyr do not cause significant changes in the parameters needed to fit the 850 μm radial profile. The dust temperature rises marginally, causing a small change in the dust surface density. The latter, however, is much more influenced by the uncertainty in the total luminosity.

3.4 Results and analysis

3.4.1 M 51 stellar parameters

First, the scale-length of the stellar emission must be determined as accurately as possible, because it dominates determinations of the scale-length of the 850 μm dust emission. The stellar emissivity of M 51 has been extensively studied by Beckman et al. (1996) who determined both arm and inter-arm scale-lengths in the B , R , I and K photometric bands, where they did not correct for extinction. Their inter-arm results are summarized in Table 3.1. Emission in the R and I bands predominantly traces old stars which are distributed more or less homogeneously throughout the disk. We use these bands to determine the scale-length of the stellar emission. As this emission is susceptible to dust attenuation, we have taken extinction into account as well. Starting with an initial estimate of the intrinsic scale-length of the stars, the radiation transfer code computes a value for the attenuated scale-length of the stars, which was then compared with the observations.

The M 51 bulge effective radius has not been determined. However, as it does not dominate the radial profile, we use a value of 1.03 kpc characteristic of similar galaxies (Laurikainen & Salo 2001), also summarized in Table 3.1.

Unlike the scale-length of the exponential star distribution, the scale-heights of both the stellar disk and the dust are in effect degenerate: model and data do not provide useful constraints. For instance, a wide range of stellar scale-heights yields almost identical 850 μm emission profiles. Dust temperatures are marginally affected, requiring some changes in the 10 – 100 μm wavelength range of the spectrum. We keep the ratio h_s/z_s identical to that found in NGC 891 (Xilouris et al. 1998). Obviously, as long as the face-on optical depth is kept constant the sub-millimeter emission does not change perceptibly either when we vary the dust scale-height. When we increase dust scale-heights from 0.25 to 0.35 kpc, temperatures change by no more than 1-2 degrees.

In order to determine the total luminosity of M 51, we integrate the UV (OAO), visual and far-infrared (IRAS) flux densities as provided in the NASA/IPAC Extragalactic Database, the 170 μm point as given by Tuffs & Gabriel (2003) and our 850 μm point. We find a luminosity of $L_{\text{tot}} = 1.1 \times 10^{11} L_{\odot}$, which corresponds to a star formation rate of a few $M_{\odot}\text{yr}^{-1}$, with an estimated uncertainty of about 30%. Of this total luminosity, about 5% originates in the bulge and the remaining 95% in the exponential disk.

3.4.2 Disk parameter determination

Even if the stellar luminosity and the CO contamination are known, the stellar scale-height, z_s , and the dust scale-height, z_d , are degenerate. Adopting values as outlined in the

previous section, we explore the parameter space over three variables: (i) the total amount of dust, which scales with the central face-on optical depth $\tau_{V,f}$ integrated from infinity to the galaxy center, (ii) the scale-length of the dust distribution h_d , and (iii) the scale-length of the stellar disk h_s , since the observed scale-length is attenuated by dust. These variables are uniquely determined when the stellar luminosity and the CO contamination are known. Since this is not the case, we identify combinations of parameters that best reproduced the observed $850 \mu\text{m}$ radial profile.

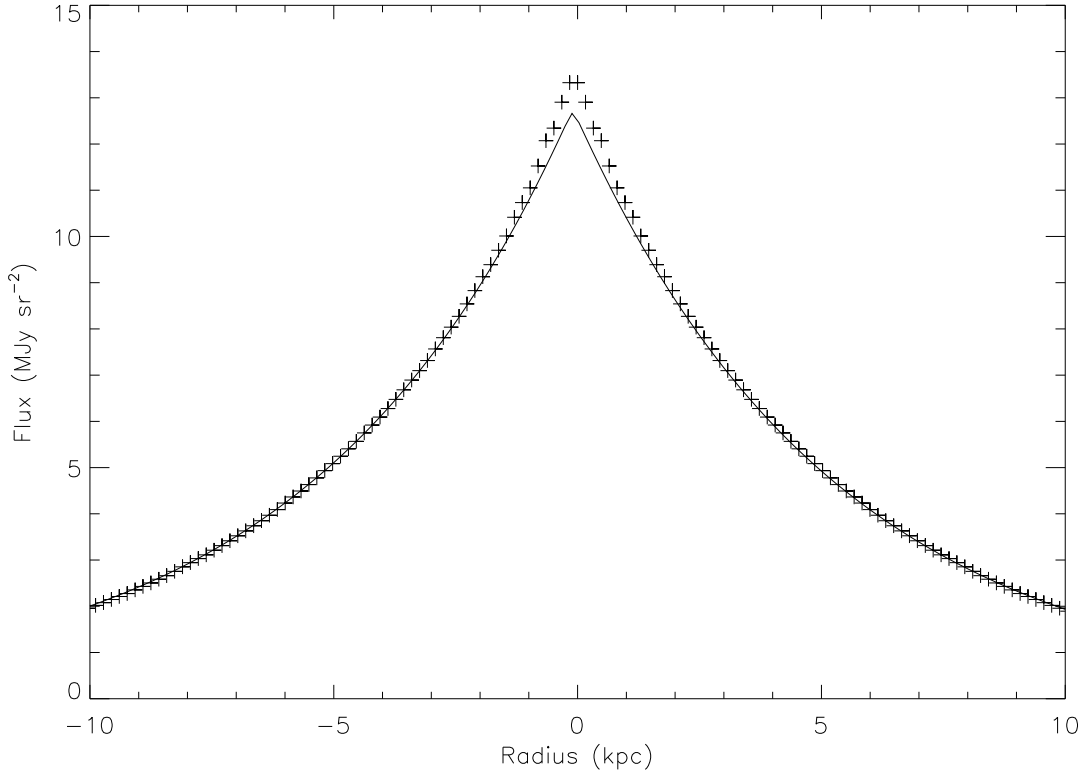


Figure 3.3: The model exponential disk (crosses) compared to the actual emission of the M 51 disk (solid line), for $h_d = 7.65$ kpc, $h_s = 3.15$ kpc, $L = 1.1 \cdot 10^{11} L_\odot$, $\tau_{V,f} = 4.35$ and no CO contamination.

We have summarized the model results in Table 3.2. An example of a fit is shown in Fig. 3.3. Note that the model gives a poor fit in the very center. This is caused by the presence of the bulge in the model which provides additional dust heating, hence more sub-millimeter emission in the center. We only subtract the disk component from the observed emission.

In Fig. 3.4 we show the required face-on central optical depth for a range of total galaxy luminosities and CO contributions. For a luminosity $L_{\text{tot}} = 1.1 \times 10^{11} L_\odot$ these optical depths $\tau_{V,f}$ range from 3.7 (assuming 12% CO contamination) to 4.4 (zero contamination). Inclusion of the luminosity uncertainty increases this to a slightly larger range $\tau_{V,f}$ 3.4–4.8. The high optical depth derived here is consistent with the typically higher values derived from far-infrared and sub-mm compared to optical observations (see, e.g.,

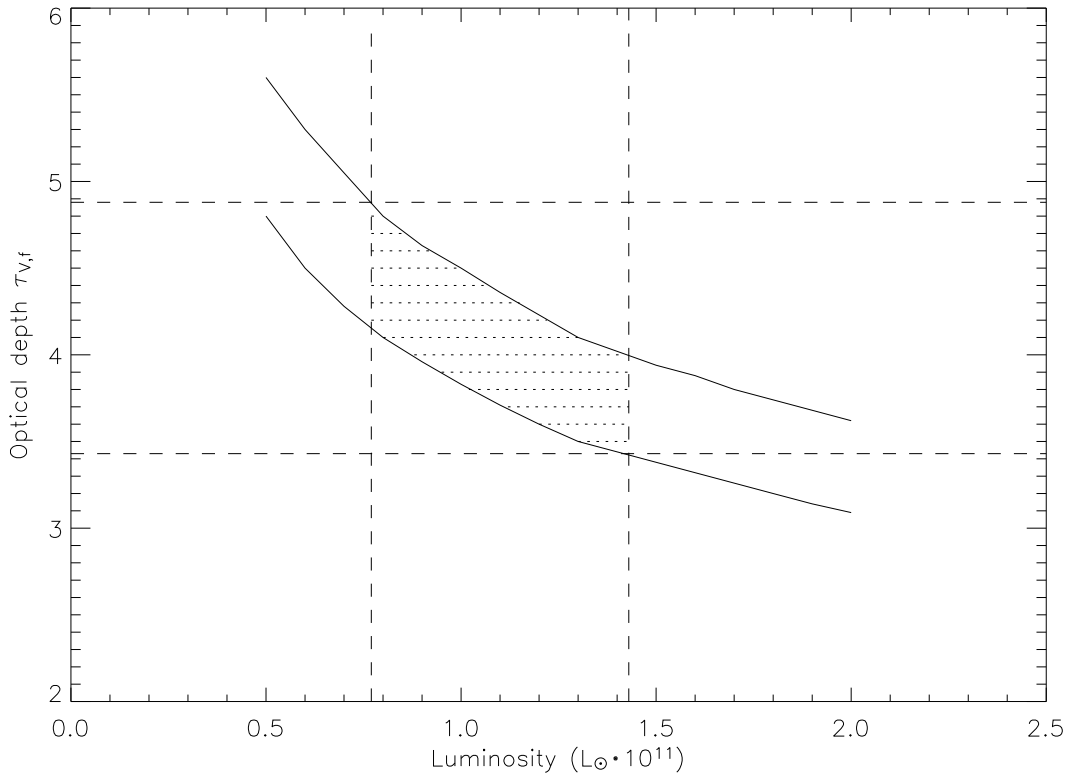


Figure 3.4: Resulting optical depth for different luminosities assuming either zero CO contamination (upper line) or an omnipresent maximum 12 per cent contamination (lower line). The shaded area shows the possible solutions.

Table 3.2: Model results

CO contamination	No	Maximal	Variable
h_s (kpc)	3.15	3.15	3.15
h_d (kpc)	7.65	7.65	8.65
$\tau_{V,f}$ ($L = 0.8 \cdot 10^{11} L_\odot$)	4.8	4.1	4.2
$\tau_{V,f}$ ($L = 1.1 \cdot 10^{11} L_\odot$)	4.4	3.7	3.7
$\tau_{V,f}$ ($L = 1.4 \cdot 10^{11} L_\odot$)	4.0	3.4	3.5

Bianchi 2004). Popescu et al. (2000) find a value of 3.1 for NGC 891. In this case, however, arm and interarm emission are fitted simultaneously. The associated scale-lengths vary likewise. For instance, as long as the CO contamination is constant with radius, we find a dust scale-length $h_d = 7.65$ kpc and a stellar scale-length $h_s = 3.15$ kpc. On the other hand, if the CO contamination is maximal (12%) at the center and minimal (zero) at a radius of 10 kpc, we obtain a slightly larger scale-length $h_d = 8.65$ kpc. The scale-length h_s remains the same within the uncertainties. The value of h_d is somewhat smaller than the scale-length of atomic hydrogen. The value of h_d is comparable to a scale-length of

9 ± 1 kpc that we derive for the atomic hydrogen outside 6 kpc (Tilanus & Allen 1991).

In addition to a radial density gradient, we also find a radial temperature gradient because the stellar scale-length is much smaller than the dust scale-length, i.e., the stars are more centrally concentrated than the dust. Radial temperature profiles for the average grain size at position $z = 0$ kpc are shown in Fig. 3.5. When the dust scale-length is larger, we also see a steeper temperature gradient throughout the galaxy. The small fluctuations in the Fig. 3.5 profile are artifacts due to statistical noise.

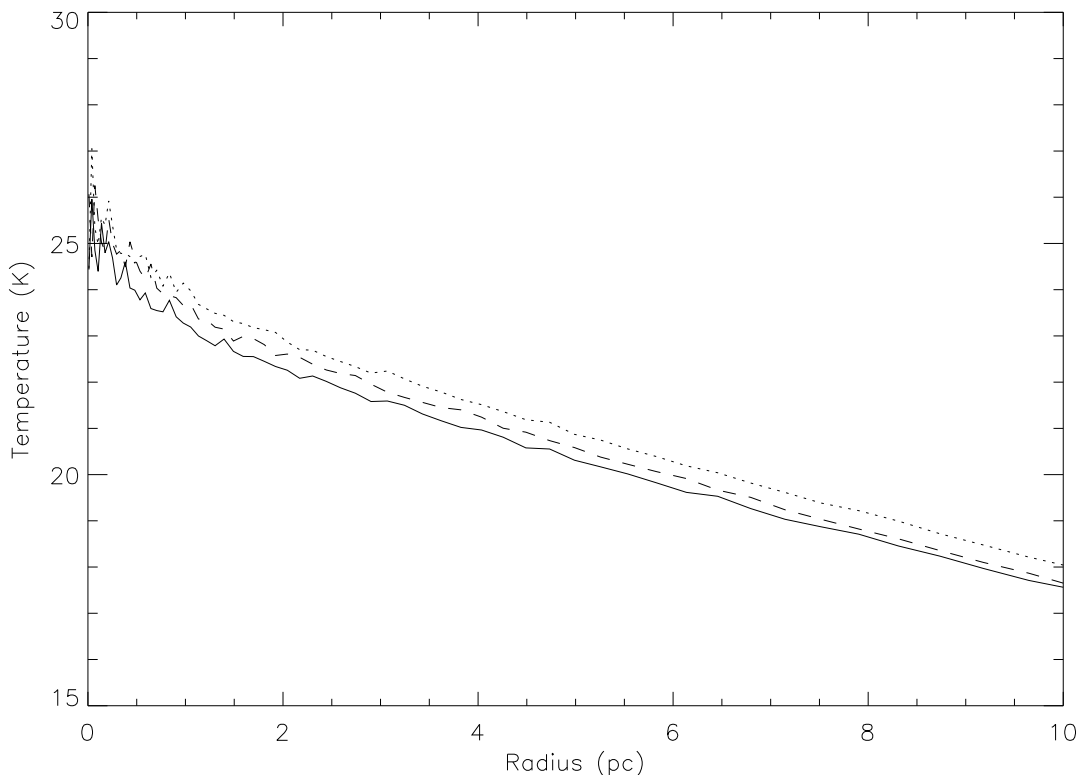


Figure 3.5: Radial temperature profile for a total luminosity for M 51 of $L = 1.1 \cdot 10^{11} L_{\odot}$. The solid line denotes zero CO contamination, the dotted line a maximum 12 per cent contamination, and the dashed line a contamination decreasing from maximum in the center to zero at the outer edge of M 51.

The good fit of the $850 \mu\text{m}$ profile provided by exponential distributions with finite scale-lengths already suggests that the M 51 disk is hard to explain in terms of a radially constant density distribution. We nevertheless attempt to force such a fit, and find that this can only be done if the M 51 stellar scale-lengths are more than an order of magnitude smaller than actually found. Thus, a constant density distribution may be ruled out with confidence. An exponential density distribution of the cold dust is required to explain to observed exponential $850 \mu\text{m}$ disk.

SCUBA sub-mm observations of the edge-on spiral NGC 891 suggest that the cold dust distribution traces the total hydrogen column density, i.e., molecular hydrogen in the

central regions and neutral hydrogen at larger radii (Fig. 5 in Alton et al. 2000). Subsequent far-infrared observations by Popescu & Tuffs (2003) have shown that the cold dust emission traces the neutral hydrogen into the extended HI disk. The current observations of M 51, showing an exponential dust density distribution, a close association with the molecular hydrogen in the central region, and comparable scale-lengths of the dust and HI distributions at larger radii further reinforce the suggestion that the cold dust is correlated with the total hydrogen column density in galaxies.

3.4.3 Dust mass and gas-to-dust ratio

Once the density and temperature profiles are determined we may, in principle, determine the radial dust mass distribution. In Fig. 3.6 we show the surface mass densities as a function of radius for a graphite and silicate ratio of 0.5:0.5. The peak dust surface densities are 0.90 (no CO contribution) and 0.77 M_{\odot}/pc^2 (12 percent CO). The central gas (HI + H₂ + He) surface density is $\Sigma_{\text{gas}} = 60 M_{\odot}\text{pc}^{-2}$ (Israel et al. 2006), with an estimated uncertainty of 25-30%. This results in a gas-to-dust ratio of 73 ± 17 .

In this dust mixture, we have a dust emission coefficient of $\kappa_{850} = 0.9 \text{ g}^{-1}\text{cm}^{-2}$. However, the actual value of κ_{850} is rather uncertain. James et al. (2002) used SCUBA observations to derive a value $\kappa_{850} = 0.7 \pm 0.2 \text{ g}^{-1}\text{cm}^{-2}$ but their data show a spread in values for individual galaxies of a factor of two. Worse, Alton et al. (2000) find a three times higher value for the galaxy NGC 891, whereas Agladze et al. (1996) in the laboratory come to a value about two times higher than that of James et al. (2002).

We can make an estimate of κ_{850} in M 51. When we increase the fraction of graphite in the grains, a higher value for the dust emission coefficient is obtained. With a higher dust emission coefficient, the surface mass density is lower. For $\kappa_{850} = 1.2 \text{ g}^{-1}\text{cm}^{-2}$, the peak surface densities as shown in Fig. 3.6 will be 0.65 (no CO contribution) and 0.56 (12 percent CO). In Table 3.3, gas-to-dust ratios are shown for four different gas mixtures and for a luminosity of $L = 1.1 \cdot 10^{11} L_{\odot}$. A canonical gas-to-dust ratio of 100 ± 26 is obtained with a dust emission coefficient $\kappa_{850} = 1.2 \text{ g}^{-1}\text{cm}^{-2}$, somewhat less than twice the value found by James et al. (2002).

Table 3.3: Gas to dust-ratios

silicate:graphite	$\kappa_{850} (\text{g}^{-1}\text{cm}^{-2})$	dust:gas
0.5:0.5	0.9	73 ± 17
0.4:0.6	1.0	82 ± 21
0.3:0.7	1.1	91 ± 24
0.2:0.8	1.2	100 ± 26

3.5 Summary

1. SCUBA 850 μm observations of M 51 show a well-delineated spiral structure superimposed on a prominent extended exponential base disk.

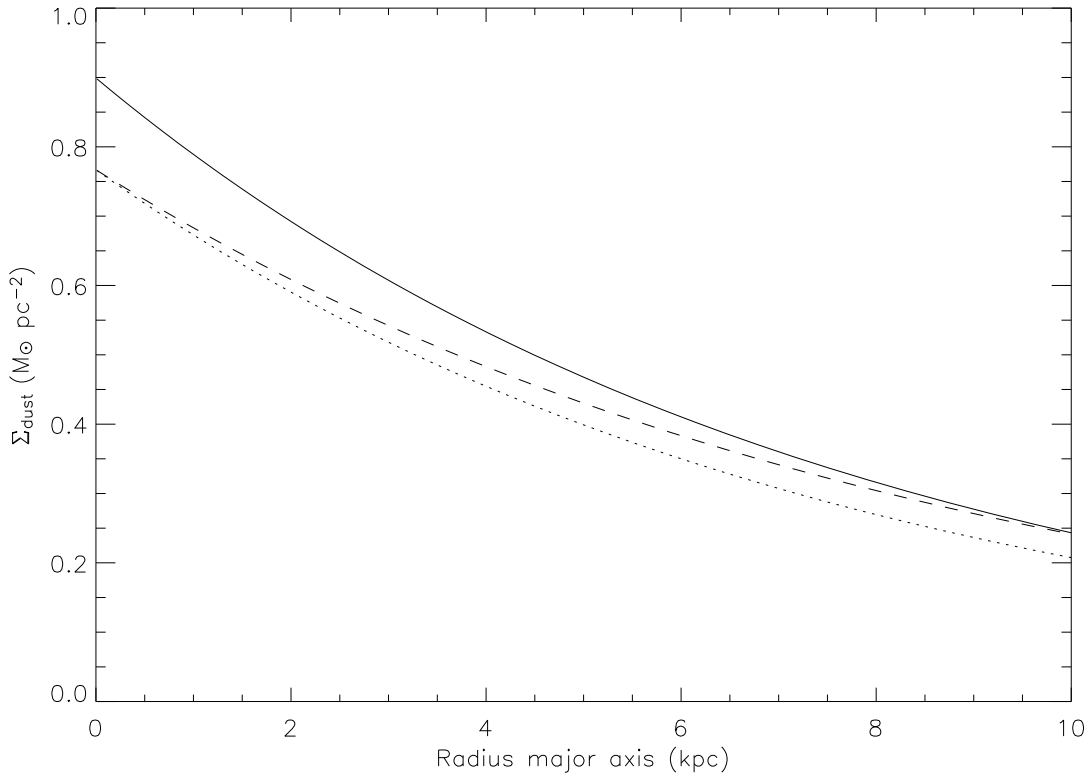


Figure 3.6: The dust surface density profiles for a silicate-to-graphite ratio of 0.5:0.5 and $\kappa_{850} = 0.9 \text{ g}^{-1} \text{ cm}^2$; no CO contribution (solid line), 12 percent CO contribution (dotted line) and decreasing CO contribution (dashed line).

2. The observed base disk is evidence for an underlying exponential density distribution of cold dust in M 51. This reinforces the suggestion that the cold dust in spiral galaxies traces the total hydrogen density, i.e. the sum of H_2 and HI
3. While throughout M 51 a radial temperature gradient occurs, because the stars are more centrally concentrated than the dust, this gradient by itself cannot be the origin of the exponential nature of the observed $850 \mu\text{m}$ disk.
4. A reasonable estimate of the dust emission coefficient, based on a canonical gas to dust ratio of 100 ± 26 , is $\kappa_{850} = 1.2 \text{ g}^{-1} \text{ cm}^2$.
5. We find a stellar scale-length h_s of 3.15 kpc and a dust scale-length h_d that ranges from 7.65 to 8.65 kpc.
6. We find a typical central face-on optical depth $\tau_{V,f} = 4.0$.

Acknowledgements

This research has made use of the NASA/IPAC Extragalactic Database (NED) which is operated by the Jet Propulsion Laboratory, California Institute of Technology, under contract with the National Aeronautics and Space Administration. We want to thank Eric Bell for a helpful discussion about dust opacities. RT thanks Ron Allen and Leo Blitz for an invigorating discussion on the nature of the exponential dust disk. We also thank S. Bianchi and the referee, R.J. Tuffs, for their insightful comments and helpful suggestions which have improved this paper.

CHAPTER 4

The spiral structure of M 51 at 850 μm

We will determine the surface density of the dust and molecular gas and the CO-to-H₂ conversion factor in the spiral arms of M 51. The dust surface density is obtained from the 850 μm emission. Using the dust surface density, for each point in the disk the surface density of the gas can be derived with the assumption that the gas-to-dust ratio has the same radial dependence as the metallicity, as measured by the fractional abundance of oxygen. By comparing these gas surface densities with the observed total gas density from 21-cm neutral hydrogen observations and CO observations of the molecular gas, we can determine the CO-to-H₂ conversion factor as function of position within the galaxy. The central total hydrogen-gas-to-dust-mass ratio is found to be 60. The resulting CO-to-H₂ conversion factor is consistent with other independent determinations in M51 and shows a radial gradient.

R. Meijerink, R.P.J. Tilanus, F.P. Israel, and P.P. van der Werf, 2005
Astronomy & Astrophysics, submitted

4.1 Observations

M 51 was observed at 850 μm in the spring of 1998 and 1999 at the JCMT¹ using Submillimeter Common User Bolometer Array (SCUBA: Holland et al. 1999). The instrument was used in scan-map mode in order to map the $13.5' \times 13.5'$ field around M 51. The scan angle across the field ($15.5 \pm 60^\circ$), was chosen in such way that the resulting image is fully sampled. The total integration time was about 20 hours spread over 6 nights. The initial observations used chop throws of 20, 30 and 65 arcsec, later throws of 44 and 68 were added. We use the standard reduction for SCUBA scan-map observations as implemented in the SCUBA User Reduction Facility Software (SURF: Jenness & Lightfoot 1998). A detailed description of the data reduction is given in Sect. 2 of Meijerink et al. (2005). The observations show the presence of an extended cold-dust disk (Sect. 4 of Meijerink et al. (2005)). In order to isolate the emission of the spiral arms we remove the contribution of the extended disk by subtracting an inclined exponential. The resulting 850 μm emission from the spiral arms in M 51 is shown in Fig. 3.1.

4.2 Contamination by in-band $J = 3 - 2$ CO line

The broad passband of the SCUBA instrument at 850 μm includes the wavelength of the $J = 3 - 2$ ^{12}CO line. Thus, at any point in the map the continuum emission measured by SCUBA is, in principle, contaminated by CO line emission. Such contamination is negligible for the diffuse disk in the inter-arm region (Meijerink et al. (2005)). This is not the case in the spiral arms, which contain a large amount of CO emission that can account for up to half of the observed 850 μm emission.

In order to correct for the line emission in the SCUBA observations, we need the $J = 3 - 2$ ^{12}CO intensity distribution in M 51. Unfortunately, the largest map available covers a $70'' \times 140''$ area in the central part of M 51 (Israel et al. 2006), which is only a small part of the complete 850 μm map. Kramer et al. (2005) recently concluded, however, that the CO(3-2)/CO(2-1) ratio measured at $80''$ resolution is fairly constant at three widely spread pointings, namely 0.76 at ($0'', 0''$), 0.75 at ($-84'', -84''$) and 0.76 at ($+72'', +84''$), respectively, relative to the center of M 51 as given in Table 3.1. This suggests the use of a large-extent, scaled $J = 2 - 1$ ^{12}CO map to correct for the contribution of the $J = 3 - 2$ line emission. Such a map fortunately is available.

García-Burillo et al. (1993) mapped the $J = 2 - 1$ ^{12}CO line emission in M 51 with the IRAM 30m telescope. They covered an area of $3' \times 3'$ and produced a fully sampled map (i.e. with steps of $6''$) at an angular resolution of $12''$ (FWHM). We convolve this map to the $15''$ (FWHM) resolution of the JCMT observations. After correcting for the beam efficiencies of $\eta_{mb} \approx 0.55$ (IRAM 230 GHz) and $\eta_{mb} \approx 0.63$ (JCMT 345 GHz), we calculated an average CO(3-2)/CO(2-1) ratio of 0.72 in the area covered by the map of Israel et al. (2006). This ratio is in excellent agreement with the values found by Kramer et al. 2005 and was used to subtract a scaled version of the $J = 2 - 1$ ^{12}CO map from the

¹The James Clerk Maxwell Telescope is operated by the Joint Astronomy Center on behalf of the Particle Physics and Astronomy Research Council of the United Kingdom, the Netherlands Organization for Scientific Research and the National Research Council of Canada

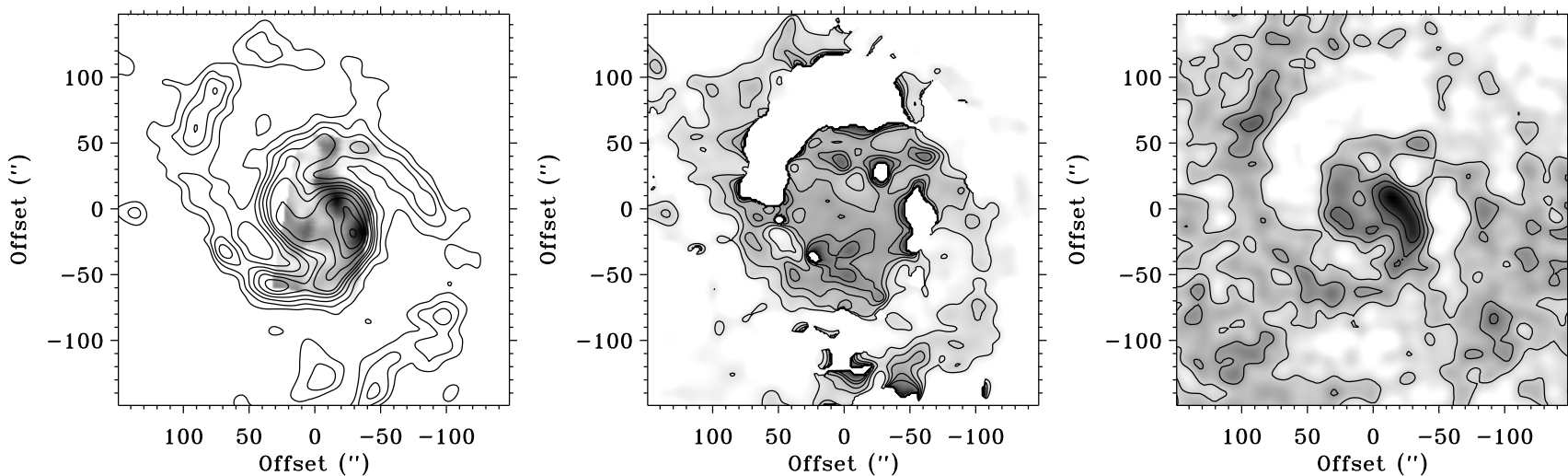


Figure 4.1: Correction of the SCUBA $850\ \mu\text{m}$ emission for in-band CO(3-2) line-emission. The maps shown have been deprojected for an inclination angle of 20° . *Left:* CO(2-1) contours (García-Burillo et al. 1993) overlaid on the CO(3-2) (Israel et al. 2006) emission map. *Center:* Amount of the correction (percent of observed): The contours are at: 10, 20, 30, 40, and 50 percent. *Right:* The $850\ \mu\text{m}$ spiral arm continuum emission corrected for the in-band CO emission. The contours are at: 10, 20, 30, and 40 mJy/beam.

observed $850\ \mu\text{m}$ map to correct for in-band CO line emission.

Fig. 4.1 shows the CO(2-1) contours overlaid on the CO(3-2) map (*left*), after de-projection according to the parameters given in Table 3.1. The *center* panel shows the percentage contamination of in-band line emission based on the scaled $J = 2 - 1\ ^{12}\text{CO}$. The *right* panel shows the $850\ \mu\text{m}$ emission in the spiral arms after correcting for the contaminating CO line emission. We find the largest correction in the center (up to 50 percent). The overall morphology of the $850\ \mu\text{m}$ map, however, did not change significantly, which indicates a close correlation between the CO and dust.

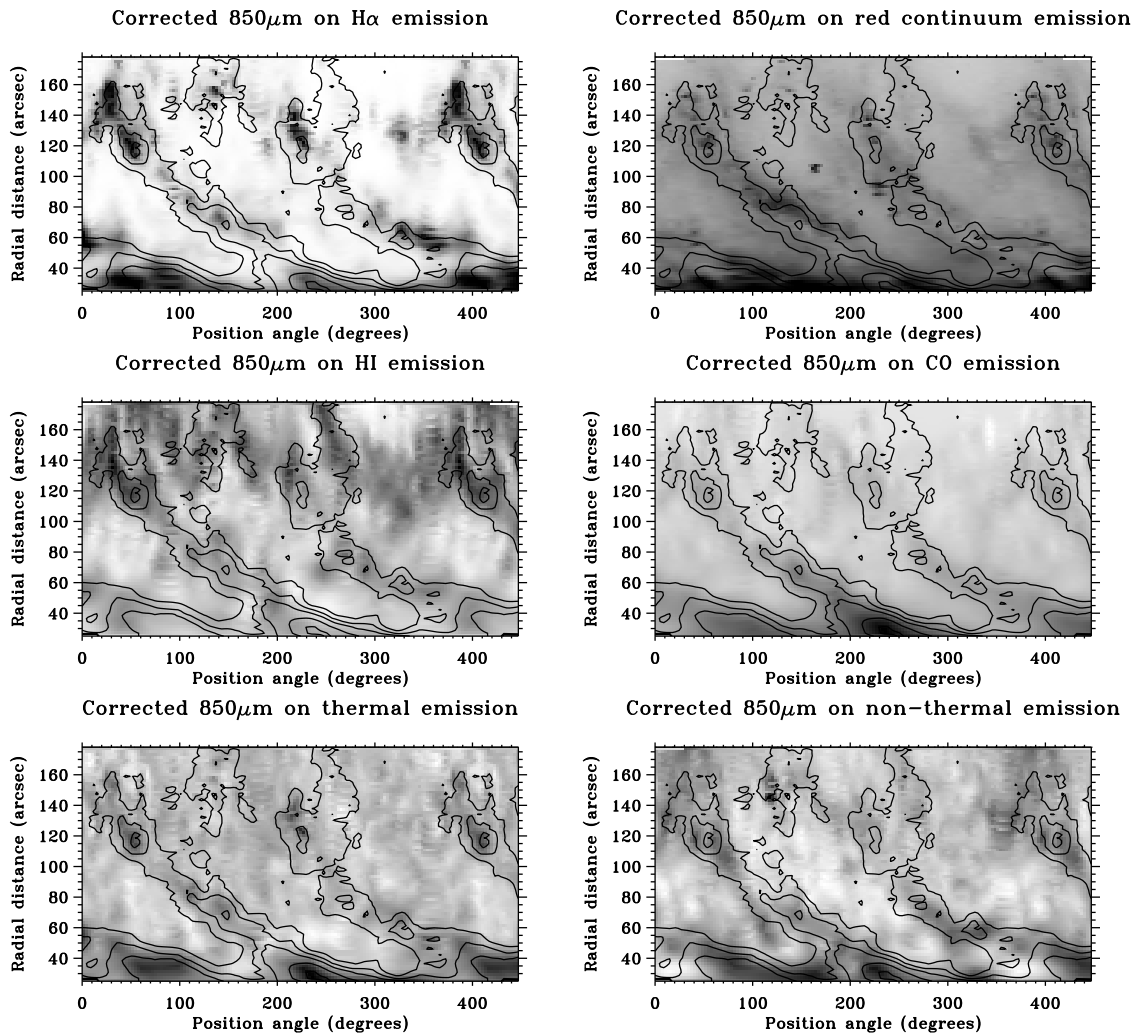


Figure 4.2: These figures show the $850\ \mu\text{m}$ emission in the spiral arms, corrected for in-band line emission, overlaid on various other tracers of the spiral structure: *Top left*: $\text{H}\alpha$, *top right*: red continuum, *center left*: HI 21 cm, *center right*: $J=2-1\ ^{12}\text{CO}$, *bottom left*: thermal, and *bottom right*: non-thermal continuum emission, respectively.

Table 4.1: Data sets used for comparison to 850 μm emission

Data set	Reference	Resolution (")
6400Å red cont.	van der Hulst et al. (1988)	9
H α	Tilanus et al. (1988)	9
$J = 2 - 1$ ^{12}CO	García-Burillo et al. (1993)	12
HI 21 cm line	Rots et al. (1990)	13
6 cm (thermal)	Tilanus et al. (1988)	8
20 cm (non-th.)	Tilanus et al. (1988)	8

4.3 Morphological comparison to other wavelengths

Now that we have corrected the 850 μm emission for contamination from the in-band CO(3-2) line emission, we are in a position to make a morphological comparison of the distribution of the cold dust with other components of the ISM (see Table 4.1).

We convolved all data to the 15" FWHM resolution of our data set (except for the red, 6400Å continuum image), and deprojected the images adopting the parameters as listed in Table 3.1. We found it convenient to convert the different data sets to polar-coordinates (R, θ), where θ runs counterclockwise like the position angle (PA) and R is the distance in arcsec from the center. Fig. 4.2 show the 850 μm sub-mm emission overlaid on the other data sets. We define Arm I as the arm seen from a PA of 0 to 200 degrees and Arm II as seen from 250 to 400 degrees in the polar coordinates plot. Arm I and II correspond to the the inner southern arm and inner northern arm, respectively.

The top row of Fig. 4.2 shows the 850 μm emission as it compares to the H α emission from the HII regions around newly-formed massive, young stars (*left*), and the red continuum emission outlining the dust lanes and the broad stellar arms (*right*). The middle row shows a comparison with the HI 21 cm, tracing the atomic gas (*left*) and CO line emission, tracing molecular hydrogen (*right*). The bottom rows shows the radio continuum emission. The thermal emission (*left*) is closely coincident with the HII regions and the H α emission. On the other hand Tilanus et al. (1988) found that the non-thermal emission is seen very near the dust lanes and conclude that it is associated associated with spiral shocks.

The polar plots show that there is a minimum in the 850 μm emission in both arms at radial distance between 80" and 100" from the center. This is the same region, where we find a transition from predominantly molecular hydrogen (CO) and atomic hydrogen (HI 21 cm). In the literature, this region is often associated with the 4/1 resonance (Aalto et al. 1999; Rand 1993).

The pitch angle of Arm II is smaller in the center and becomes larger than Arm I in the outer part of the galaxy. The pitch angle of Arm I is more or less constant. The arms are clearly distorted, probably by the interaction with NGC 5195 north of M 51. As a result, the properties of the two arms are quite distinct. Below, we briefly discuss the arms separately and a comparison is made.

4.3.1 Arm I (Inner Southern arm)

- This arm is very well defined at 850 μm and shows two extended bright regions flanking the aforementioned minimum at $90''$. The intensity of these regions is 1.5 times larger than the brightest peaks in Arm II.
- The ridge of 850 μm emission is coincident with the main dust lane inside the minimum.
- The broad optical stellar arms are coincident with the arms at 850 μm . We identified two bright regions at a radius of $80''$ and $120''$, which are located at a slightly larger radius, than those seen at 850 μm . In the inner part, a dust lane is obscuring the optical emission.
- The CO spiral arm emission shows the same extent as the 850 μm emission in the inner part of the galaxy. In the outer part, a small CO peak is seen, at the same place where 850 μm shows a peak, but the CO emission is much less extended.
- The HI 21 cm emission is not very well associated with the spiral arms seen at 850 μm . Small emission peaks in the inner part are not coincident with those seen in the sub-mm. In the outer part, there is also HI emission in the inter arm region.
- The $\text{H}\alpha$ emission is located inside the 850 μm arms but associated with the bright emission regions at 850 μm . The emission region in the outer part is more extended than that in the inner part. The emission of $\text{H}\alpha$ in the inner part is shifted to somewhat larger radii compared to the brightest emission at 850 μm , which was also seen in the optical continuum.
- The non-thermal emission regions are located inside the 850 μm arm, but shifted toward a smaller radius.
- There are compact thermal radio emission peaks in the bright emission regions at 850 μm . They do not coincide with the CO emission emission, but correlate well with the HII regions (Tilanus et al. 1988) in the outer regions.

4.3.2 Arm II (Inner Northern arm)

- This arm is well-defined in the inner part of the galaxy, but more poorly in the outer part. The peak emission is lower than in Arm I.
- The optical arm is shifted to a larger radius compared to 850 μm . The optical dust lane does not correspond to bright peaks in the sub-millimeter dust emission.
- The CO emission is less strong compared to Arm I, but CO peaks are located at the 850 μm emission peaks.
- The HI 21 cm emission is somewhat stronger compared to Arm I and correlates somewhat better with bright peaks at 850 μm , especially at larger radii.

- Unlike in Arm I, the H α emission peaks do not correlate with the peaks seen at 850 μm . The H α emission regions are shifted to larger radius compared to 850 μm arm. The same is seen for the thermal emission.
- In the inner part, the non-thermal emission peaks are located inside the 850 μm arm.

4.4 The dust column density

From the corrected 850 μm continuum emission for CO(3-2) line contamination, we can derive a dust column density distribution, using:

$$\Sigma_{\text{dust}} = \frac{I_{\nu}}{\kappa_{\nu} B_{\nu}(T_{\text{dust}})}, \quad (4.1)$$

where I_{ν} is the intensity, κ_{ν} is the dust opacity, and $B_{\nu}(T_{\text{dust}})$ is the Planck intensity function. The dust temperature can be determined from two specific intensity maps, at the same resolution, but at two different wavelength points ν_1 and ν_2 . In that case, the recursive relation for the dust temperature T_{dust} is given by:

$$\frac{I_{\nu_1}}{I_{\nu_2}} = \frac{\kappa_{\nu_1} B_{\nu_1}(T_{\text{dust}})}{\kappa_{\nu_2} B_{\nu_2}(T_{\text{dust}})}. \quad (4.2)$$

We used the 60 and 100 μm intensity maps of M 51 from the ISO Data Archive for the determination of the dust temperature. We did not use 850 μm since the sub-mm range is in the Rayleigh-Jeans limit where the shape of the spectrum is not sensitive to the temperature. But the exclusive use of the 60 and 100 μm also has a drawback in that we have to assume that the same dust is emitting at both frequencies. Components of different temperature influence the two frequency points in different ways. It is possible, that a warm dust component is present. When such a component is present, the dust temperature will be overestimated at 850 μm . The adoption of too high a temperature will result in an underestimation of the dust mass. It is possible to rewrite Eq. 4.2 to a direct equation for T_{dust} :

$$T_{\text{dust}} = \frac{h(\nu_1 - \nu_2)}{k \ln((\nu_1/\nu_2)^{3+n} (I_{\nu_2}/I_{\nu_1}) + C_T)} \quad (4.3)$$

where C_T is a correction factor given by:

$$C_T = \left(1 - \left(\frac{\nu_1}{\nu_2}\right)^{3+n} \left(\frac{I_{\nu_2}}{I_{\nu_1}}\right)\right) \exp(-h\nu_2/kT_{\text{dust}}) \quad (4.4)$$

The emissivity coefficient n originates from the frequency dependent mass absorption coefficient, $\kappa_{\nu} \propto \nu^n$. Chini et al. (1984a,b) found that the integrated emission of cool galaxies has index $n = 2$ and warmer galaxies has $n = 1$. We take $n = 1.5$, but take into account that there is an uncertainty in n of $\Delta n = \pm 0.5$. This results in a relative uncertainty in the temperature of $\Delta T/T = 10\%$. For the reduction of the ISO maps, we used the P32 reduction tools (Peschke & Schulz 2002) and subtracted a uniform background

from both maps by determining the average flux after masking M51 and its companion. Finally, we deprojected the maps adopting the parameters as listed in Table 3.1 and convolved the 60 μm map from a resolution of 50.3'' (FWHM) to 83.9'' (FWHM), which is the resolution of the 100 μm map. The temperatures in the resulting temperature map, Fig. 4.3, range from 25 to 35 K. The south-east part has a slightly higher temperature than the north-west part of M 51, by about 5 K. The inter-arm regions show somewhat higher temperatures than the spiral arms. Devereux & Young (1992) analyzed the 60 and 100 μm measurements from IRAS. They found dust temperatures between 27 and 33 K. They state, however, that including the KAO 170 μm measurement from Smith (1982) implies that 90 percent of the dust should have a temperature $T_{\text{dust}} < 16$ K. Hippelein et al. (1996) found dust temperatures of about 30 to 33 K by using the 60, 100 and 175 μm measurements by ISO. The ISO 175 μm flux is, however, much lower than the KAO flux found by Smith (1982). This makes the very cold dust component as derived by Devereux & Young (1992) uncertain.

For the opacity we used the value $\kappa_{850} = 1.2 \text{ cm}^2/\text{g}$ as found in Meijerink et al. (2005) from Monte Carlo simulations. The actual value is very uncertain as illustrated by the spread in values derived by other authors. James et al. (2002) found an average value of $\kappa_{850} = 0.7 \pm 0.2 \text{ cm}^2/\text{g}$ in a sample of galaxies with a scatter by a factor of two. Alton et al. (2000) found a three times higher value for NGC 891 and Agladze et al. (1996) came up with a laboratory value about two times higher than that of James et al. (2002). For the moment we adopt a factor of two uncertainty in this value. Therefore, the derived surface densities from Eq. 4.1 as shown in Figs. 4.4 and 4.5 are also uncertain by a factor of two. For the spiral arms, we find that the peak dust surface density is $0.68 \text{ M}_{\odot}\text{pc}^{-2}$. This increases to $1.33 \text{ M}_{\odot}\text{pc}^{-2}$, when considering both the spiral arms and the diffuse disk. For the disk alone we would find a somewhat lower peak dust surface density than we derived in Meijerink et al. (2005). There we derived somewhat lower temperatures for the disk, which resulted in a higher dust mass. We will compare these results to the gas surface densities in the following sections.

4.5 The atomic and molecular mass

In order to compare the retrieved dust surface density to gas tracers, we first need to derive the HI surface density. We will use this result to determine the H_2 surface density. The atomic gas surface density is retrieved from the 13'' resolution map described by Rots et al. (1990). The map is deprojected and convolved to 15'' resolution for a proper comparison to the 850 μm emission. The column density of neutral atomic hydrogen can be derived from the brightness temperature by using $N(\text{HI}) = 1.823 \times 10^{23} I(\text{HI})$ (Kraus 1966, p.374). We find an average surface density $\Sigma(\text{HI}) = 3.0 \text{ M}_{\odot}\text{pc}^{-2}$ in the inter-arm region. This is subtracted to obtain the atomic surface density in the spiral arms, which is shown in Fig. 4.4. In Fig. 4.5 the total surface density is shown.

A direct determination of the molecular mass in the arms is not possible, since H_2 emission is very hard to observe. This is explained by the fact that H_2 is a symmetric molecule, and, as a consequence does not contain a permanent dipole moment. Therefore,

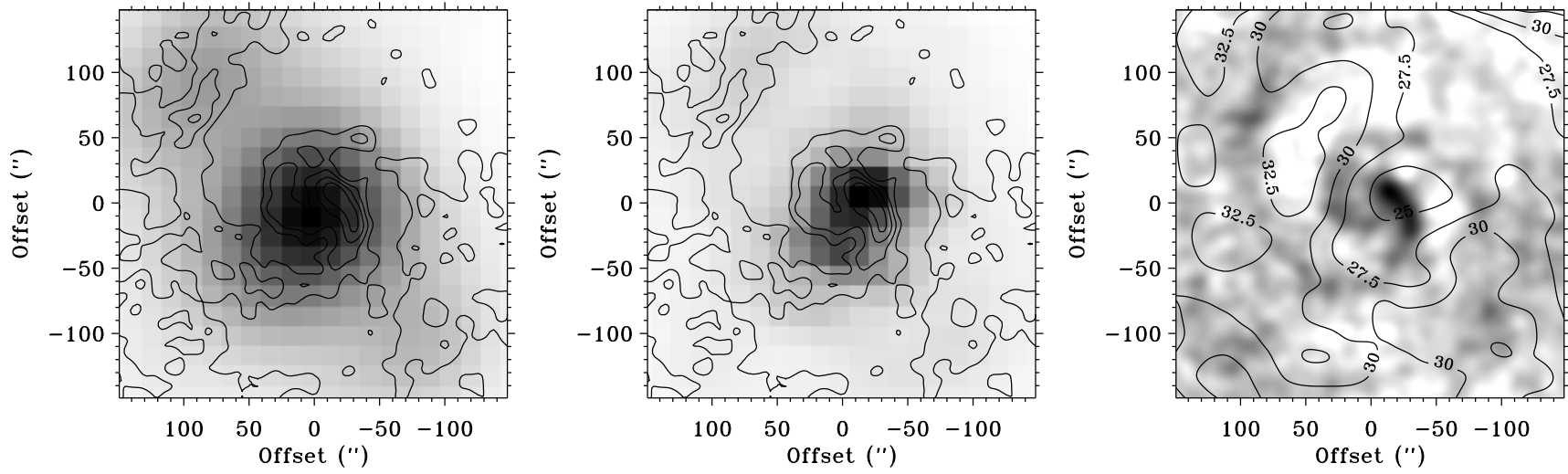


Figure 4.3: *Left*: 60 μm convolved to the 83.9'' resolution of the 100 μm map. *Center*: 100 μm at 83.9'' resolution. *Right*: Temperature contours superimposed on M51 spiral arms.

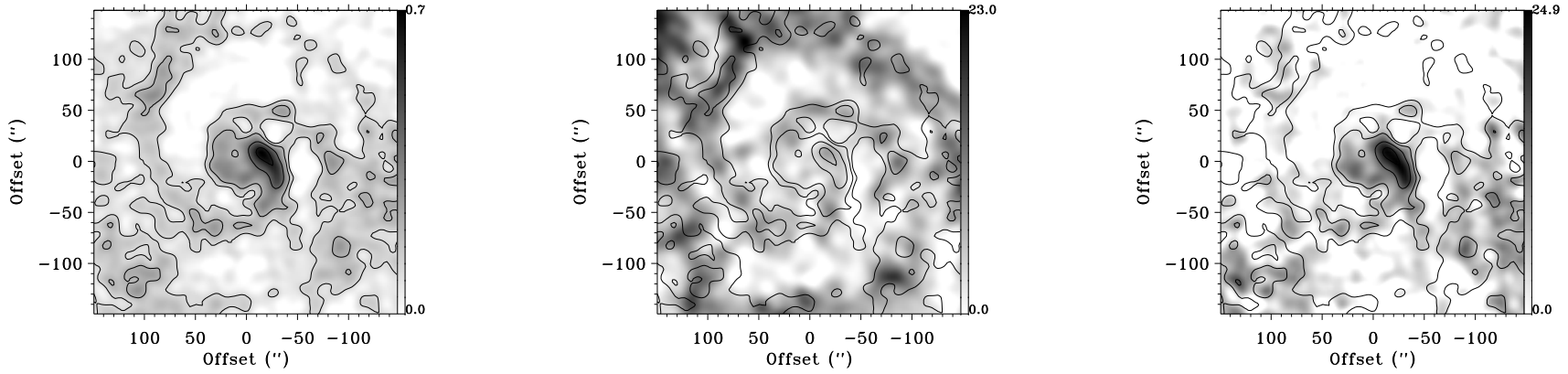


Figure 4.4: Surface density of dust (*left*), when a value of $\kappa_{850} = 1.2 \text{ cm}^2/\text{g}$ is adopted for the opacity, atomic (*center*) and molecular hydrogen (*right*) [M_{\odot}/pc^2] of the spiral arms.

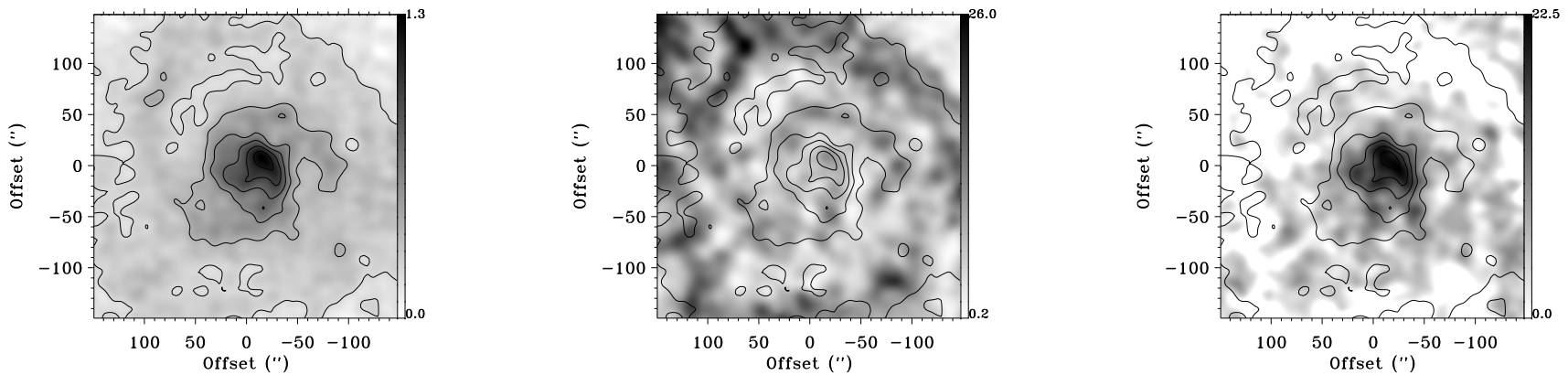


Figure 4.5: Surface density of dust (*left*), when a value of $\kappa_{850} = 1.2 \text{ cm}^2/\text{g}$ is adopted for the opacity, atomic (*center*) and molecular hydrogen (*right*) [M_{\odot}/pc^2] of the spiral arms and the diffuse disk.

H_2 does not emit permitted rotational lines. The ro-vibrational spectrum in the near-IR of H_2 can be observed. This, however, traces only the warm molecular hydrogen, which is a small part of the total amount of H_2 . Therefore, it is common to use CO emission as a tracer. A serious drawback in this method is that the conversion of CO to H_2 is not constant throughout a galaxy. For example, the conversion factor $X = N(\text{H}_2) / \int T_b dv$ in the Solar neighborhood is estimated at $1.8 \times 10^{20} \text{ cm}^{-2} / (\text{K km s}^{-1})$ (c.f. Dame et al. 2001). Based on the deficit of gamma-rays, Blitz et al. (1985) found that the conversion is several factors lower in the Galactic center. Sodroski et al. (1995) and Strong et al. (2004) confirmed this, and found a gradient throughout the galaxy. Therefore, it is not straightforward to make an estimate of the H_2 content in galaxies by using CO observations. We will use a different method as described by Israel (1997) to estimate the H_2 content of M 51. We will evaluate the molecular surface density from the HI and 850 μm surface densities in the following way:

$$\Sigma(\text{H}_2) = \Sigma_{\text{dust}} f(R) - \Sigma(\text{HI}), \quad (4.5)$$

where f is a total hydrogen-gas-to-dust-mass ratio as a function of radius. We assume that this ratio $f(R)$ is proportional to the fractional abundance of oxygen. The abundance decreases with radius. Vila-Costas & Edmunds (1992) found $12 + \log(\text{O}/\text{H}) = 9.54$ in the center and a gradient of -0.14 dex/arcmin , based on data from McCall et al. (1985), Searle (1971), Smith (1975), and Diaz et al. (1991). Zaritsky et al. (1994) found a characteristic abundance $12 + \log(\text{O}/\text{H}) = 9.23$ at $r = 2.1'$ from the center and a gradient of -0.07 dex/arcmin , but based this result only on data from McCall et al. (1985) and Diaz et al. (1991). We use the average of the two gradients, normalized to the central hydrogen-gas-to-dust-mass ratio $f(0)$.

In principle, we can find the central gas-to-dust-mass ratio $f(0)$ by looking for a place in the galaxy without CO emission. At this place the *atomic* hydrogen-gas-to-dust-mass ratio is the same as the *total* hydrogen-gas-to-dust ratio $f(R)$, when we assume that molecular hydrogen is always associated with CO. From this local $f(R)$ we can calculate the central ratio $f(0)$ by using the above mentioned normalized oxygen abundance gradient. In order to trace the CO emission, we use the $J = 2 - 1$ ^{12}CO antenna temperature map from García-Burillo et al. (1993). In the inter-arm region, we find an average emission of $T_A^* \approx 2.5 \text{ K}$. We subtract this value, when we consider the spiral arms only. Unfortunately, most of M 51 is in fact associated with CO emission. Therefore, we use a somewhat modified version from the above description. We first define two ratios. The first ratio is given by:

$$Q_{\text{HI/dust}} = \Sigma(\text{HI}) / (\Sigma_{\text{dust}} \text{norm}(R)), \quad (4.6)$$

which is the ratio between the atomic surface density, $\Sigma(\text{HI})$, and the dust surface density, Σ_{dust} . In order to correct Σ_{dust} for the gradient in the gas-to-dust-mass ratio $f(R)$, we multiplied with the normalized gas-to-dust-mass ratio $\text{norm}(R) = f(R)/f(0)$. The second ratio is given by:

$$Q_{\text{CO/dust}} = I(\text{CO}) / (\Sigma_{\text{dust}} \text{norm}(R)), \quad (4.7)$$

which is the ratio between the CO emission and the dust surface density. The dust surface density is again corrected for the gradient in the total gas-to-dust-mass ratio by multiplying with $\text{norm}(R)$.

We expect that the total gas surface density is more or less constant relative to the dust surface density corrected for the metallicity gradient, if the measured dust is a proper tracer of the total dust and the gas. $Q_{\text{HI}/\text{dust}}$ represents the part of hydrogen in atomic form, relative to dust. $Q_{\text{CO}/\text{dust}}$ is the amount CO emission, which is used as the H_2 tracer, relative to dust. This implies that there should exist a negative correlation between these defined ratios, when we make a pixel-pixel plot of these quantities. When $Q_{\text{HI}/\text{dust}}$ increases, then $Q_{\text{CO}/\text{dust}}$ should decrease. In Fig. 4.7 we have plotted $Q_{\text{CO}/\text{dust}}$ versus $Q_{\text{HI}/\text{dust}}$. We find that the ratio $Q_{\text{HI}/\text{dust}}$ is highest when $Q_{\text{CO}/\text{dust}}$ is lowest. We have fitted a linear profile through these points. The central hydrogen-gas-to-dust-mass ratio $f(0)$ is found, where $Q_{\text{CO}/\text{dust}} = 0$. We find $f(0) = 44$ when we consider the spiral arms only and $f(0) = 23$, when we use the spiral arms plus the diffuse disk. A reason for this discrepancy can be that the CO is not a proper tracer of H_2 in the inter-arm region. The transition from H to H_2 is closer to the surface of a cloud than the transition from C^+ to C to CO. When clouds are dense and have large column densities, the difference in transition is small compared to the cloud size and the transitions are closer to the surface of the cloud. When the cloud density is low, it is difficult to reach high column densities and then the difference in transition is important. This is illustrated in Fig. 4.6, where an example is given of PDR model with a semi-infinite slab geometry, with density $n = 10^{2.5} \text{ cm}^{-3}$ and radiation field $G_0 = 17$. For this model, we use the PDR code as described in Meijerink & Spaans (2005). The transition from H to H_2 is at a column $N_{\text{H}} \approx 10^{21.2} \text{ cm}^{-2}$ ($\tau_{\text{V}} \approx 1.0$), while the transition of C to CO is at $N_{\text{H}} \approx 10^{21.9} \text{ cm}^{-2}$ ($\tau_{\text{V}} \approx 4.0$). In Meijerink et al. (2005), we found a value for the central face-on optical depth of $\tau_{\text{V}} \approx 3.7$ for the disk, so it is very improbable to find shielded clouds were CO is present in large amounts.

The central hydrogen-gas-to-dust-mass ratio is derived for an assumed dust opacity of $\kappa_{850} = 1.2 \text{ cm}^2/\text{g}$. When the opacity is increased by a factor of two, the dust surface density would decrease by the same amount (Eq. 4.1). The ratio $f(R)$, however, would increase with a factor of two. Therefore, the assumed opacity does not affect the estimated molecular surface density (Eq. 4.5).

In Figs. 4.4 and 4.5, we show the estimated molecular surface density using Eq. 4.5. We use the derived central hydrogen-gas-to-dust-mass ratios, $f(0) = 44$ and $f(0) = 23$ to calculate $\Sigma(\text{H}_2)$ for the spiral arms only and the spiral arms together with the diffuse disk, respectively. When we use $f(0) = 23$ derived from the total emission of the galaxy to calculate $\Sigma(\text{H}_2)$ for the complete galaxy, we do not find a physical solution. There is too much atomic hydrogen mass subtracted in the outer parts of the galaxy, which results in a negative molecular mass. The problem is probably that we underestimate $f(0)$ in this case, since CO is probably not a good tracer of H_2 in the inter-arm region.

We also considered the possibility of a somewhat steeper gradient, throughout the galaxy. In the calculations, we assumed the total gas-to-dust-mass ratio $f(R)$ proportional to the abundance gradient in oxygen. We can also consider the possibility that $f(R)$ is proportional to the gradient in carbon. For an increasing metallicity, the ratio C/O becomes larger. As a consequence, the possibility exists that the gradient in the ratio

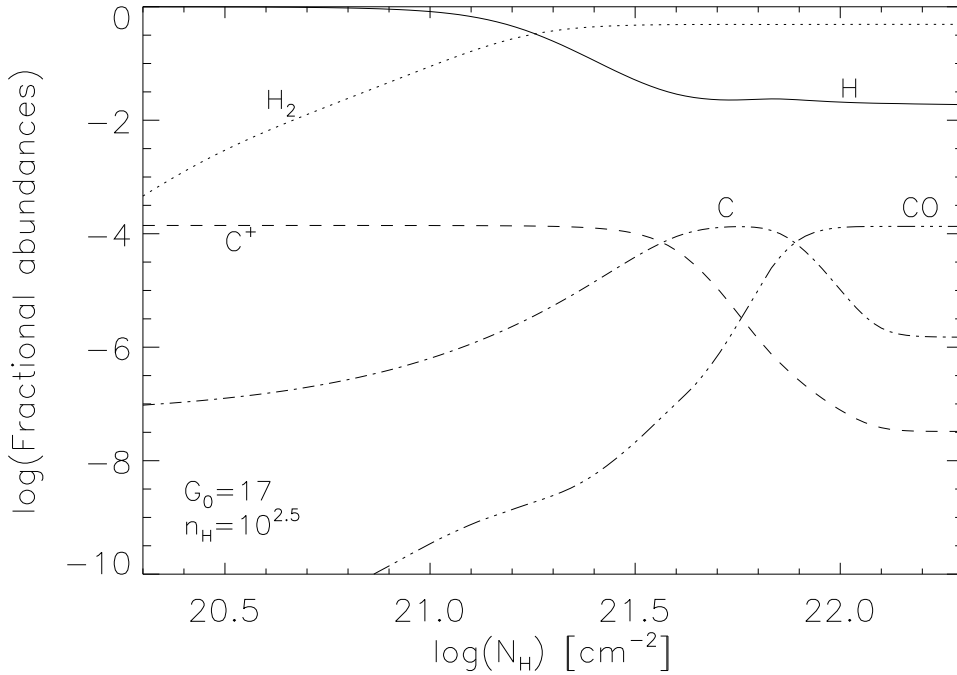


Figure 4.6: PDR with density $n = 10^{2.5} \text{ cm}^{-3}$ and $G_0 = 17$.

$f(R)$ is steeper than derived from the oxygen abundance. Unfortunately, the derived central total hydrogen-gas-to-dust-mass ratio $f(0)$ decreases in the center, when using a steeper gradient. Therefore, we still obtain a negative molecular hydrogen surface density $\Sigma(\text{H}_2)$. We conclude that it is only possible to obtain $\Sigma(\text{H}_2)$ for the spiral arms, when using this method.

The molecular mass in the arms is much more concentrated toward the center of the galaxy, while a large part is atomic in the outer spiral arms. To illustrate this, we plotted the radial atomic and molecular gas surface density for the spiral arms in Fig. 4.8. The central H₂ surface density is about half the result from Israel et al. (2006).

4.6 The CO to H₂ conversion factor

We can now derive the radial CO-to-H₂ conversion factor X in the spiral arms. We do not consider the spiral arms together with the underlying diffuse disk, due to the problems described in the previous section. We use the molecular hydrogen surface density $\Sigma(\text{H}_2)$, derived in the previous section, and the $J = 2 - 1$ ¹²CO emission map of García-Burillo et al. (1993). We want to derive the X -factor for $J = 1 - 0$ ¹²CO emission, and, therefore, we need to scale the CO emission map, for which we use the results from Kramer et al. (2005). They derived CO(2-1)/CO(1-0) ratios in three widely spread pointings, namely 0.73 at (0'' ,0''), 0.57 at (-84'' ,84'') and 0.8 at (+72'' ,+84''), respectively. We use the average ratio of the three, i.e. 0.7, in scaling the complete CO(2-1) map. The derived

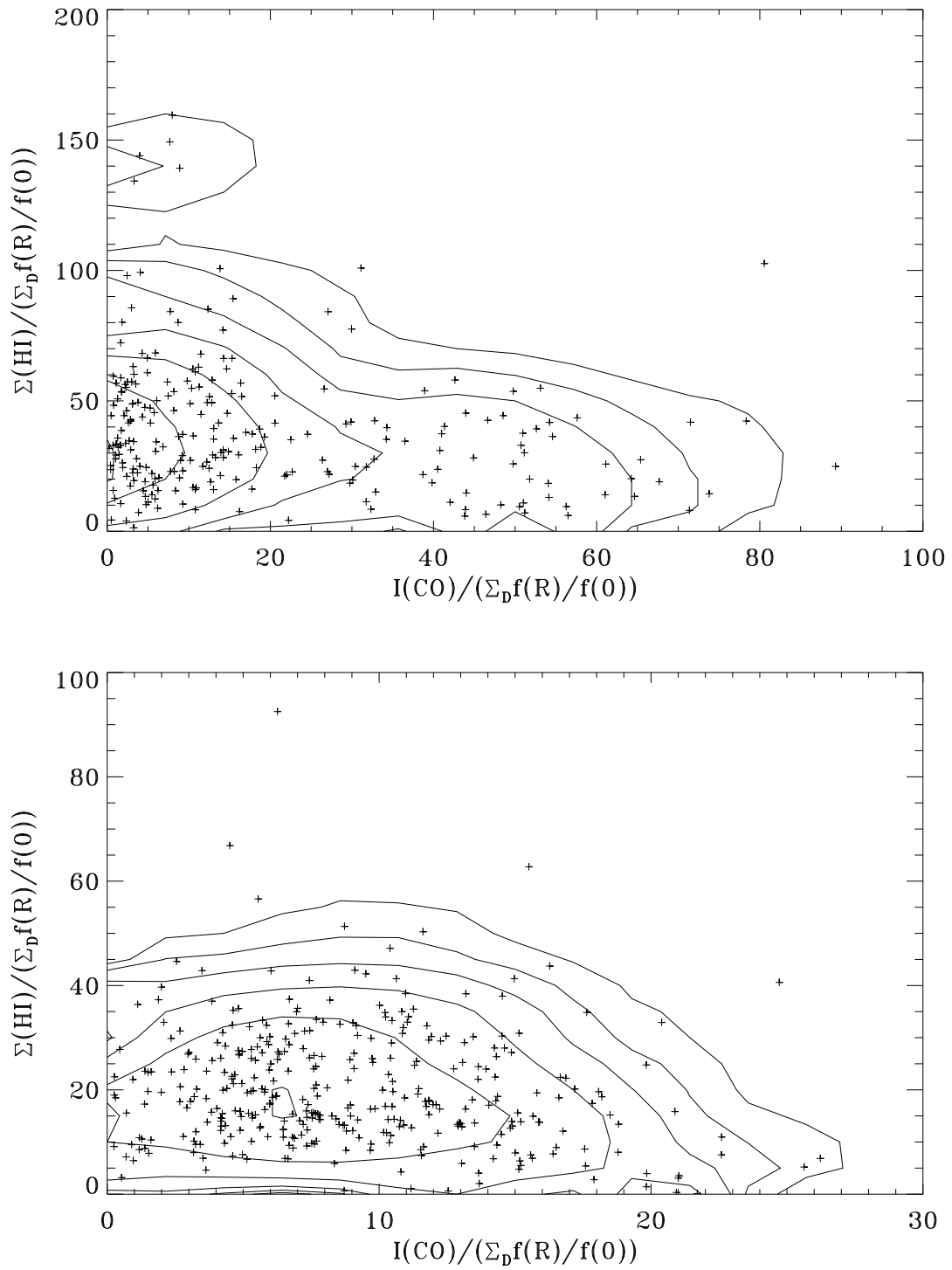


Figure 4.7: $\Sigma(\text{H}) / (\Sigma_{\text{dust}} f(\text{R}))$ vs. $I(\text{CO}) / (\Sigma_{\text{dust}} f(\text{R}))$ for spiral arms (*left*) and spiral arms + diffuse disk (*right*). The contours represent the point density.

radial dependent CO-to-H₂ conversion is plotted in Fig. 4.8. We find a gradient for the X-factor in the spiral arms throughout the galaxy, which is mostly due to the gradient in hydrogen-gas-to-dust-mass ratio. The gradient is strongly reduced when this is left out. We derive value of $0.2 \times 10^{20} \text{ cm}^{-2} / (\text{K km s}^{-1})$ in the center of M 51 to $1.3 \times 10^{20} \text{ cm}^{-2} / (\text{K km s}^{-1})$ at $140''$.

When we would have made a lower estimate of the CO emission in the inter-arms region, the radial slope of X would be somewhat less steep. The effect of this estimate is largest in the outer part, where for a $T_A^* \approx 1.5 \text{ K}$, the X factor would be 50 percent lower at $170''$.

4.7 Discussion

We derive a value for the central gas-to-dust ratio in the spiral arms of 59 (by multiplying the central ratio $f(0) = 44$ by 1.35 to include the contribution of He as well). At $2.5'$ from the center the ratio has increased by factor of two. This is much lower than the value 195-390 suggested by Dunne et al. (2000) assuming the presence of both cold and warm dust. Stevens et al. (2005) derived an average gas-to-dust ratio of 120 ± 60 for 14 nearby spirals. This is consistent with our result, and some of their galaxies have even much lower gas-to-dust ratios ($M_{\text{gas}}/M_{\text{dust}}=33$ for NGC 2903 and $M_{\text{gas}}/M_{\text{dust}}=7$ for NGC 3310) than we derive for M 51. Our results are also comparable to those found for NGC 6946 (Alton et al. 2002). We must state, however, that our ratio would possibly be decreased, when we would use a two component fit. Another factor is the dust opacity, which introduces a factor of two uncertainty in the gas-to-dust ratio.

We determine $\Sigma(\text{H}_2)$ by using the distribution of dust and $\Sigma(\text{HI})$. We find a central surface density of $\Sigma(\text{H}_2) = 13 \text{ M}_{\odot} \text{pc}^{-2}$, which is about half the average value obtained by Israel et al. (2006). The method we use works quite well in the spiral arms, but not when the complete galaxy is considered. In order to find $\Sigma(\text{H}_2)$, we first need the central gas-to-dust ratio $f(0)$. In order to find this, we need the CO emission distribution as an H₂ tracer. It seems, however, that CO might not be a good tracer of H₂ in the inter-arm region. This underestimates the gas-to-dust ratio, and, as a consequence, the H₂ surface density.

The method to determine the CO to H₂ conversion factor is independent from the method used by other authors. Israel et al. (2006) used large-velocity gradient radiative transfer models to model the observed ¹²CO and ¹³CO and to derive the H₂ column density. Nakai & Kuno (1995) used visual extinctions and the CO intensity toward 30 HII regions. Guélin et al. (1995) used the $1.2 \mu\text{m}$ emission from cold dust. Their results are over-plotted in Fig. 4.8 for comparison. The X-factor in the center of M51 has been calculated by Israel et al. (2006) and Guélin et al. (1995). They find an X-factor four times lower than the standard Milky Way value, $0.5 \pm 0.25 \times 10^{20} \text{ cm}^{-2} / \text{K km s}^{-1}$. This value is somewhat higher than the value we find in the central region of M51, which is $0.2 \times 10^{20} \text{ cm}^{-2} / \text{K km s}^{-1}$. Our results are somewhat lower than the values found by from Nakai & Kuno (1995). This might be explained by the fact that we determined the global X-factor in the arms, while Nakai & Kuno (1995) measured the X-factor in the neighborhood of HII regions. CO is easier dissociated than H₂ and this can result in a

higher X-factor.

4.8 Conclusions

1. We find prominent spiral arms at 850 μm , after correcting for the exponential disk and contamination by CO(3-2) emission.
2. We made a detailed comparison to other components of the spiral arms, which show remarkable resemblances and differences.
3. We find that the 850 μm emission correlates well with CO in the arms out to a radius of 80'' , and much more strongly with HI at radii larger than 100'' , suggesting a clear break between those two radii, apparently corresponding to a 4/1 dynamical resonance in the M 51 system.
4. In a related way, H₂ is the dominant gas component at radii less than 50'' , whereas HI is the dominant one at larger radii as expected beyond 100'' . The total gas distribution also shows a broad minimum between 50'' and 100'' .
5. The central hydrogen-gas-to-dust-mass ratio is 44, and the total gas-to-dust-ratio is 60. This is about half the value in the Solar neighborhood.
6. The method to determine the CO-to-H₂ conversion factor from the atomic and dust surface density, and CO emission turns out to give good results, but can only be applied considering the arms.
7. The CO-to-H₂ conversion factor is small in the center , $0.2 \times 10^{20} \text{ cm}^{-2} / \text{K km s}^{-1}$, and increases to $1.3 \times 10^{20} \text{ cm}^{-2} / \text{K km s}^{-1}$ at a distance of 170'' from the center. One needs to be very careful in applying a global CO-to-H₂ conversion factor to a galaxy.

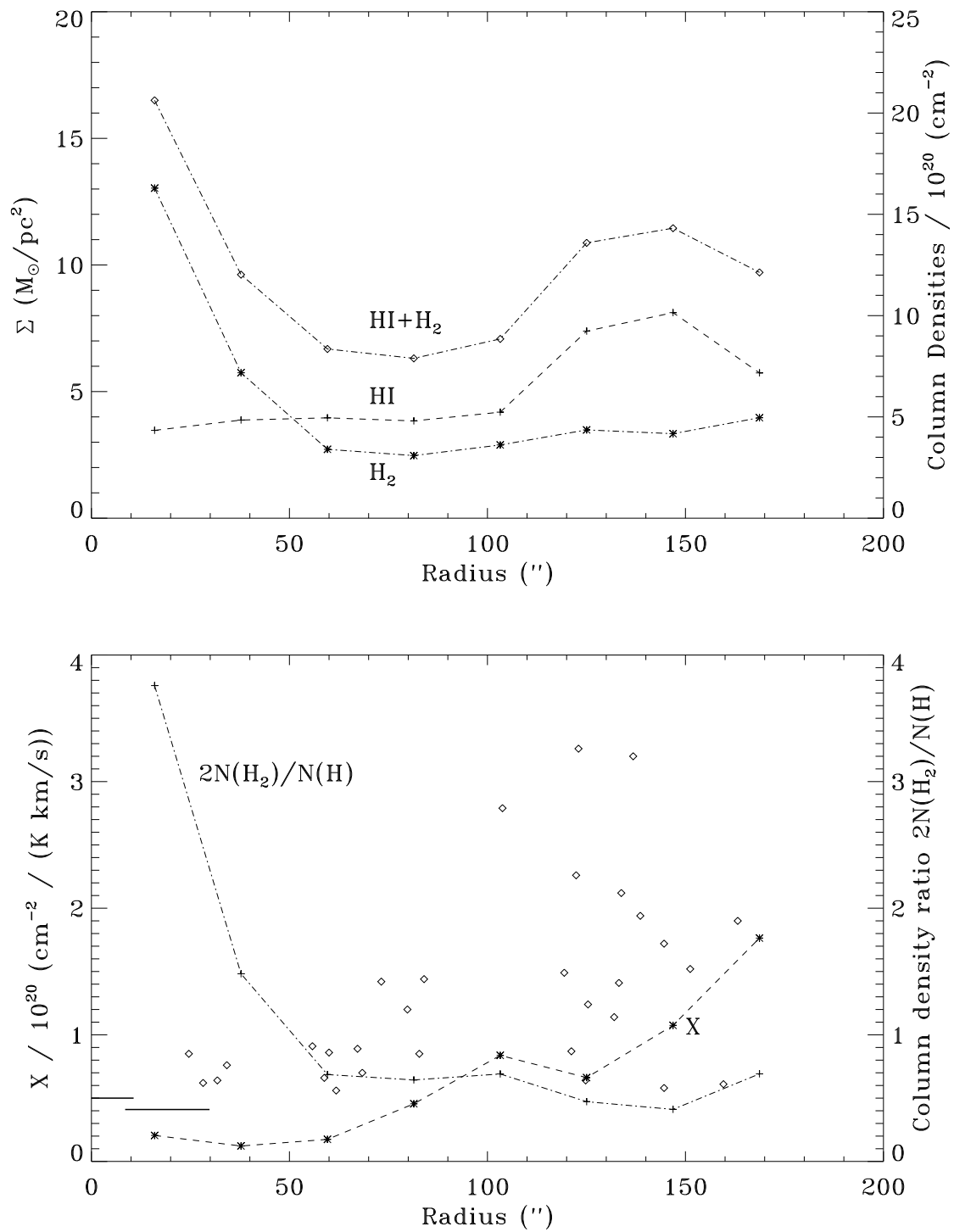


Figure 4.8: *Left*: The radial molecular, atomic and total gas surface density and column density. *Right* the column density ratio and the CO-to-H₂ conversion factor X. The results for the X factor from Nakai & Kuno (1995) are represented by the open diamonds, and from Guélin et al. (1995) and Israel et al. (2006) by the two horizontal lines.

Part II

PDR and XDR models

CHAPTER 5

Code description

Photon-dominated regions (PDRs) are regions in the interstellar medium (ISM), where the radiation field completely determines the temperature and chemical composition of the gas. These PDRs are formed under various conditions and on a range of different scales. They are found close to OB stars as well as cooler A and F stars. They are also associated with planetary nebulae, active galactic nuclei (AGN) and photo-evaporating planetary disks around newly formed stars as well as diffuse clouds. Hence, PDRs cover a wide range of astrophysical environments and trace the overall energy balance of the atomic and molecular ISM for densities of $\sim 10^2 - 10^6 \text{ cm}^{-3}$ and temperatures of $\sim 10 - 10^4$ K. The term 'PDR' is usually reserved for impinging radiation fields that peak in the FUV, while 'XDRs' (X-ray dominated regions) are formed near strong sources of X-ray emission.

Here, we present a far-ultraviolet (PDR) and an X-ray dominated region (XDR) code. We discuss the various thermal and chemical processes that pertain to irradiated gas. An elaborate chemical network is used and a careful treatment of PAHs and H_2 formation, destruction and excitation is included.

This chapter contains modified parts from:
R. Meijerink & M. Spaans, 2005
Astronomy & Astrophysics, Volume 436, pp. 397–409

5.1 Introduction

Gas clouds in the inner kpc of many galaxies are exposed to intense radiation, which can originate from an active galactic nucleus (AGN), star-burst regions or both. O and B stars dominate the radiation from star-bursts, which is mostly in the far-ultraviolet ($6.0 < E < 13.6$ eV), turning cloud *surfaces* into Photon Dominated Regions (PDRs, Tielens & Hollenbach 1985). Hard X-rays ($E > 1$ keV) from black hole environments (AGN) penetrate deep into cloud *volumes* creating X-ray dominated regions (XDRs, Maloney et al. 1996). For each X-ray energy there is a characteristic depth where photon absorption occurs. So for different spectral shapes, one has different thermal and chemical structures through the cloud. Although one source can dominate over the other energetically, (e.g., an AGN in NGC 1068 or a star-burst in NGC 253), the very different physics (surface vs. volume) require that both should be considered simultaneously in every galaxy.

In PDRs and XDRs, the chemical structure and thermal balance are completely determined by the radiation field. Therefore, PDRs and XDRs are direct manifestations of the energy balance of interstellar gas and their study allows one to determine how the ISM survives the presence of stars and AGN (Tielens & Hollenbach 1985; Boland & de Jong 1982; van Dishoeck & Black 1988; Le Bourlot et al. 1993; Wolfire et al. 1993; Spaans et al. 1994; Sternberg & Dalgarno 1995; Stoerzer et al. 1998; Spaans 1996; Bertoldi & Draine 1996; Maloney et al. 1996; Lee et al. 1996; Kaufman et al. 1999; Le Petit et al. 2002 and references therein).

PDRs and XDRs have become increasingly important as diagnostic tools of astrophysical environments with the advent of infrared and (sub-)millimeter telescopes. PDRs emit fine-structure lines of [CI] 609, [CII] 158 and [OI] 63 μm ; rotational lines of CO; ro-vibrational and pure rotational lines of H₂; many H₂O lines as well as many broad mid-IR features associated with Polycyclic Aromatic Hydrocarbons (PAHs). In PDRs, the bulk of the H₂ is converted into atomic hydrogen at the irradiated edge, CO is dissociated to neutral carbon and oxygen, and carbon is subsequently ionized to C⁺. XDRs emit brightly in the [OI] 63, [CII] 158, [SiII] 35, and the [FeII] 1.26, 1.64 μm lines as well as the 2 μm ro-vibrational H₂ transitions. The abundance of neutral carbon in XDRs is elevated compared to that in PDRs and the chemical transitions from H to H₂ and C⁺ to C to CO are smoother (Maloney et al. 1996).

In this chapter, we discuss and compare the cooling, heating and chemical processes included in the far-ultraviolet (PDR) and X-ray dominated regions (XDR) models. These codes can be used over a broad range of ambient conditions and physical scales, e.g., young stellar objects, planetary nebulae or gas outflow in galaxy clusters.

5.2 The Photon-dominated Region model

The global properties of PDRs are determined by a number of physical processes:

- Heating through photo-electric emission by dust grains and PAHs (c.f. Bakes & Tielens 1994, Weingartner & Draine 2001).

- Heating by FUV pumping of H₂, followed by collisional de-excitation (c.f. Hollenbach & McKee 1979).
- Heating by cosmic rays (c.f. Field 1969).
- Fine-structure line cooling of [CI] 609, [CII] 158, [OI] 146 and 63 μm (c.f. Tielens & Hollenbach 1985; Spaans et al. 1994).
- Molecular line cooling by warm molecular gas containing CO, H₂, H₂O, OH and CH (c.f. Neufeld et al. 1995; Spaans & Silk 2000).
- Ion-molecule reactions driven by the ionization degree of $\sim 10^{-4}$ maintained by the ionization of carbon in the FUV (c.f. Black & Dalgarno 1977; van Dishoeck & Black 1986).
- The ionization balance of atomic gas under the influence of photo-ionization reactions driven by FUV photons and counteracting recombination and charge transfer reactions with metals and particularly PAHs (c.f. Lepp & Dalgarno 1988; Bakes & Tielens 1994).

As one moves into a PDR the extinction along the line of sight increases and the impinging radiation field is attenuated. Consequently, there are two zones over which the chemical composition of the PDR changes in a fundamental way. The first fundamental change occurs at the very edge of the PDR as atomic hydrogen is converted into H₂ because the Lyman and Werner electronic bands that lead to dissociation of the H₂ molecule in the FUV become optically thick (so-called self-shielding). Deeper into the PDR, at about 3 mag of extinction, ionized carbon is quickly converted into neutral form as the FUV flux decreases due to dust absorption. C is subsequently transformed into CO, since the FUV field is reduced by grains, H₂ mutual shielding and CO self-shielding.

The first few magnitudes of extinction of the PDR are usually referred to as the radical region since many carbon hydrides and their ions, e.g., CH, CH⁺, CN, HCN, HCO⁺ (and also CO⁺), reach their peak abundance there, caused by the presence of both C⁺ and H₂ and the high ($\sim 10^2 - 10^3$ K) temperatures. Ion-molecule reactions take place that lead to the formation of a large number of different molecular species. Many of the atoms and molecules in (the radical region of) a PDR are collisionally excited at the ambient densities and temperatures, and emit brightly in the mid-IR, FIR, millimeter and sub-millimeter.

The global characteristics of any PDR are defined by a few key parameters:

- The strength of the impinging radiation field, G_0 or I_{UV} , in units of the Habing (1969) or Draine (1978) radiation field, respectively, determines the total available radiative flux at the edge of the PDR.
- The temperature and the ambient hydrogen density, $n_H = n(\text{H}) + 2n(\text{H}_2)$, sets to a large extent the pace of the chemical reactions and the excitation rates of the coolants.

- The metallicity Z , in units of the solar value Z_{\odot} , constrains the total abundances possible for carbon- and oxygen-bearing species and hence influences the chemical and thermal structure.
- The spectral shape of the impinging radiation field, parameterized by the color temperature T_{eff} for black bodies or the frequency slope for power laws, fixes the distribution of photon flux over energy.

In the next few subsections the chemical and thermal processes are discussed in more detail. In the rest of the paper we use G_0 , the Habing flux, as the normalization in which we express the incident FUV radiation field, where $G_0 = 1$ corresponds to a flux of $1.6 \times 10^{-3} \text{ erg cm}^{-2} \text{ s}^{-1}$.

5.2.1 Heating processes

Grain heating

In PDRs the photo-electric emission from (small) dust grains and PAHs is the dominant heating source. Absorption of FUV photons leads to the ejection of electrons which carry some energy of the photon away in the form of kinetic energy. This excess kinetic energy leads to heating of the gas through elastic collisions. In the past decade, it has become clear that carbonaceous interstellar grains extend into the molecular domain. These PAHs can contribute a large fraction to the total heating rate. Bakes & Tielens (1994) determined the net photo-electric heating rate and evaluated a simple analytical expression for the heating efficiency, dependent on G_0 , the kinetic gas temperature T_k and the electron density, n_e , which is given by

$$\Gamma_{\text{grain}} = 10^{-24} \epsilon G'_{0,\text{dust}} n_{\text{H}} \text{ erg cm}^{-3} \text{ s}^{-1}, \quad (5.1)$$

where the radiation field $G'_{0,\text{dust}}$ is the radiation field attenuated by dust absorption (Black & Dalgarno 1977) given by

$$G'_{0,\text{dust}} = G_0 \exp(-1.8 A_V). \quad (5.2)$$

A_V is the visual extinction at optical wavelengths caused by interstellar dust. Bohlin et al. (1978) relate the total column density of hydrogen, $N_{\text{H}} = N(\text{H}) + 2N(\text{H}_2)$ to color excess, $E(B - V)$:

$$\frac{N_{\text{H}}}{E(B - V)} = 5.8 \times 10^{21} \text{ cm}^{-2} \text{ mag}^{-1}. \quad (5.3)$$

In the literature the results of Savage et al. (1977) are often used, but in this paper only H_2 (and not HI) is taken into account. For historical reasons the radiation field attenuation is expressed in visual extinction, $A_V = 3.1E(B - V)$, and $A_V = 5.34 \times 10^{-22} N_{\text{H}}$. The heating efficiency ϵ is given by

$$\epsilon = \frac{4.87 \cdot 10^{-2}}{[1 + 4 \cdot 10^{-3}(G_0 T_k^{1/2}/n_e)^{0.73}]} + \frac{3.65 \cdot 10^{-2}(T_k/10^4)^{0.7}}{[1 + 2 \cdot 10^{-4}(G_0 T_k^{1/2}/n_e)]}. \quad (5.4)$$

The efficiency depends on the ratio $G_0 T_k^{1/2}/n_e$, which is the ratio of the ionization and recombination rates. For low $G_0 T_k^{1/2}/n_e$, grains are neutral and the heating depends linearly on the incident radiation field. For a high value of $G_0 T_k^{1/2}/n_e$, the grains are positively charged and then the heating rate is proportional to the product $n_e n_H$.

Carbon ionization heating

At the edge of the cloud, most of the carbon is singly ionized. The photo-electron energy released in an ionization is $\Delta E_C = 1.06$ eV. The ionization rate, at a certain point in the cloud, is given by $\kappa_{\text{ion}} = 1.76 G'_{0,\text{carbon}} \text{ s}^{-1}$. The heating rate due to the ionization of carbon is then given by

$$\Gamma_C = \kappa_{\text{ion}} n(\text{C}) \Delta E_C. \quad (5.5)$$

After substitution of numerical values we get the following heating rate for the local radiation field $G'_{0,\text{carbon}}$:

$$\Gamma_C = 2.79 \times 10^{-22} n(\text{C}) G'_{0,\text{carbon}} \text{ erg cm}^{-3} \text{ s}^{-1}, \quad (5.6)$$

where this time $G'_{0,\text{carbon}}$ is the radiation field attenuated by dust absorption (Black & Dalgarno 1977), carbon self-absorption (Werner 1970) and H_2 shielding (de Jong et al. 1980):

$$G'_{0,\text{carbon}} = G_0 \exp(-2.4 A_V - \tau_C - \tau b/\pi v_1^2) \times (1 + \tau b/\pi v_1^2)^{-1}, \quad (5.7)$$

where the unit-less parameters are given by

$$\tau_C = 10^{-17} N(\text{C}) \quad (5.8)$$

$$\tau = 1.2 \times 10^{-14} N(\text{H}_2) \delta v_d^{-1} \quad (5.9)$$

$$b = 9.2 \times 10^{-3} \delta v_d^{-1} \quad (5.10)$$

$$v_1 = 5 \times 10^2 \delta v_d^{-1}. \quad (5.11)$$

$N(\text{C})$ and $N(\text{H}_2)$ are the column densities of neutral carbon and molecular hydrogen and δv_d is the Doppler line width in km s^{-1} .

H₂ photo-dissociation heating

Absorption of Lyman-Werner band photons leads to the excitation of H₂. About 10% of the excitations leads to decay into the continuum of the ground electronic state (Field et al. 1966; Stecher & Williams 1967). The heating related to this dissociation is given by

$$\Gamma = 0.1 \kappa_{\text{exc.}} \langle E_{\text{diss}} \rangle, \quad (5.12)$$

where $\langle E_{\text{diss}} \rangle$ is the mean kinetic energy of the H atoms and is set to 0.4 eV (Spaans 1996). The excitation rate of H₂ is given by $\kappa_{\text{exc.}} = 3.4 \times 10^{-10} G'_{0,\text{H}_2}$, where G'_{0,H_2} is the local radiation field given by

$$G'_{0,\text{H}_2} = \beta(\tau) G_0 \exp(-2.5 A_V). \quad (5.13)$$

Self-shielding is explicitly taken into account for the excitation of H₂, by the introduction of the shielding factor $\beta(\tau)$ (see 5.2.3). After substitution of numerical values we get a heating rate of

$$\Gamma_{\text{H}_2} = 2.2 \times 10^{-23} \beta(\tau) G_0 \exp(-2.5 A_V) \text{ erg cm}^{-3} \text{ s}^{-1}. \quad (5.14)$$

H₂ collisional de-excitation heating

FUV excitation is followed by decay to ro-vibrational levels in the ground state. Collisional de-excitation leads to gas heating. This cascade process is very complicated, but we simplify this process by using a two-level approximation (see 5.2.3). The resulting heating rate is given by

$$\Gamma_{\text{H}_2} = [n(\text{H})\gamma_{10}^{\text{H}} + n(\text{H}_2)\gamma_{10}^{\text{H}_2}]n(\text{H}_2V)E_* \text{ erg cm}^{-3} \text{ s}^{-1}, \quad (5.15)$$

where the coefficients are given by Hollenbach & McKee (1979)

$$\gamma_{10}^{\text{H}} = 10^{-12} T_k^{0.5} \exp(-1000/T_k) \quad (5.16)$$

$$\gamma_{10}^{\text{H}_2} = 1.4 \times 10^{-12} T_k^{0.5} \exp(-18100/(T_k + 1200)). \quad (5.17)$$

Both of the above expression are in units of cm³ s⁻¹.

Gas-grain collisional heating

When gas and grains differ in temperature they can transfer heat through collisions. The heating rate of the gas is given by (Hollenbach & McKee 1979, 1989)

$$\Gamma_{\text{coll.}} = 1.2 \times 10^{-31} n^2 \left(\frac{T_k}{1000} \right)^{1/2} \left(\frac{100 \text{ \AA}}{a_{\text{min}}} \right)^{1/2} \times [1 - 0.8 \exp(-75/T_k)] (T_d - T_k). \quad (5.18)$$

The minimum grain size is set at $a_{\text{min}} = 10 \text{ \AA}$ and the dust temperature T_d is given by

$$T_d = (8.9 \times 10^{-11} \nu_0 G_0 \exp(-1.8 A_V) + 2.7^5 + 3.4 \times 10^{-2} [0.42 - \ln(3.5 \times 10^{-2} \tau_{100} T_0)] \times \tau_{100} T_0^6)^{0.2}, \quad (5.19)$$

based on the results of Hollenbach et al. (1991). T_0 and τ_{100} are given in equation (5.29).

Gas-grain viscous heating

Radiation pressure accelerates grains relative to the gas and the resulting drag contributes viscous heating to the gas. Grain acceleration time scales are short compared to other time scales, and therefore the grains may be considered moving at their local drift velocity, v_d . All the momentum is transferred to the gas, predominantly by Coulomb forces. For drift velocities $< 10^3 \text{ cm s}^{-1}$ (Spitzer 1978), no significant gas-grain separation takes place. In the following, we take $v_d = 10^2 \text{ cm s}^{-1}$. The heating rate is given by

$$\Gamma_{\text{visc.}} = 8\pi e^4 n_d Z_d^2 (kT_k)^{-1} (\ln \Lambda) v_d [n(C^+) G(y_{C^+}) + n_e G(y_e)], \quad (5.20)$$

where n_d is the grain volume density, Z_d is the grain charge, $n(C^+)$ and n_e are the respective C^+ and electron volume densities and the functions Λ and $G(y)$ are given by

$$\Lambda = 1.5 Z_d^{-1} e^{-3} (kT_k)^{1.5} (\pi n_e)^{-0.5} \quad (5.21)$$

$$G(y) = \frac{1}{2y^2} \left\{ \text{erf}(y) - \frac{2}{\pi^{0.5}} y e^{-y^2} \right\}, \quad (5.22)$$

where $y = v_d/v_{\text{th}}$ and v_{th} the thermal velocity of C^+ ions and electrons. $\text{erf}(y)$ is given by

$$\text{erf}(y) = \int_0^y e^{-t^2} dt. \quad (5.23)$$

Cosmic-ray heating

Cosmic ray heating is not important at cloud edges, as its energy input is exceeded by many orders of magnitude by photo-electric heating. Deeper into the cloud the FUV radiation is attenuated by dust and cosmic ray heating can become important. Glassgold & Langer (1973) and Cravens & Dalgarno (1978) calculated that the amount of heat

deposited in a molecular gas is about 8 keV per primary ionization. Then, Tielens & Hollenbach (1985) find for the total heating rate, including helium ionization

$$\Gamma_{\text{CR}} = 1.5 \times 10^{-11} \zeta n(\text{H}_2) \text{ erg cm}^{-3} \text{ s}^{-1}, \quad (5.24)$$

where ζ is the cosmic ray ionization rate per H_2 molecule.

5.2.2 Cooling processes

Cooling

The radiative cooling rate due to the transition from level i to level j of species x is given by

$$\Lambda_x(\nu_{ij}) = n_i A_{ij} h\nu_{ij} \beta_{\text{esc}}(\tau_{ij}) \frac{S_x(\nu_{ij}) - P(\nu_{ij})}{S_x(\nu_{ij})}, \quad (5.25)$$

where n_i is the population density of species x in level i , A_{ij} the spontaneous transition probability, $h\nu_{ij}$ is the energy difference between levels i and j , τ_{ij} is the optical depth averaged over the line, and $\beta_{\text{esc}}(\tau_{ij})$ is the escape probability at the optical depth τ_{ij} of the line. The source function is given by

$$S_x(\nu_{ij}) = \frac{2h\nu_{ij}^3}{c^2} \left(\frac{g_i n_j}{g_j n_i} - 1 \right)^{-1}, \quad (5.26)$$

where g_i and g_j are the statistical weights of the upper and lower level, respectively. The background radiation field is given by (Hollenbach et al. 1991)

$$P(\nu_{ij}) = B(\nu_{ij}, T = 2.7 \text{ K}) + (0.42 - \tau_d) \tau_d B(\nu_{ij}, T_0), \quad (5.27)$$

where a dust opacity $\tau_d \ll 1$ is assumed. It consist of the 2.7 K microwave radiation and the dust mean continuum background radiation characterized by a temperature T_0 and a total emission optical depth τ_d . T_0 and τ_{100} are given by

$$T_0 = 12.2 G_0^{0.2} \text{ K} \quad (5.28)$$

$$\tau_{100} = 2.7 \times 10^2 G_0 / T_0. \quad (5.29)$$

and the dust opacity at the appropriate wavelength λ follows:

$$\tau_{d,\lambda} = \tau_{100} \left(\frac{100 \mu\text{m}}{\lambda} \right). \quad (5.30)$$

The level populations are calculated by solving the equations of statistical equilibrium (de Jong et al. 1980)

$$n_i \sum_{j \neq i}^l R_{ij} = \sum_{j \neq i}^l n_j R_{ji}, \quad (5.31)$$

where l is the total number of levels included and

$$R_{ij} = A_{ij} \beta_{\text{esc}}(\tau_{ij})(1 + Q_{ij}) + C_{ij}, \quad i > j \quad (5.32)$$

$$R_{ij} = (g_j/g_i) A_{ji} \beta_{\text{esc}}(\tau_{ji}) Q_{ji} + C_{ij}, \quad i < j. \quad (5.33)$$

In these equations the collisional rate from level i to j is represented by C_{ij} . The background radiation is contained in Q_{ij}

$$Q_{ij} = \frac{c^2}{2h\nu_{ij}^3} P(\nu_{ij}). \quad (5.34)$$

Since the set of l statistical equilibrium equations is not independent, one of the equations has to be replaced by the conservation equation

$$n_x = \sum_{j=0}^l n_j, \quad (5.35)$$

where n_x is the total volume density of species x . The optical depth averaged over the line is given by

$$\tau_{ij}(z) = \frac{A_{ij} c^3}{8\pi\nu_{ij}} \int_0^z n_i(z') \left[\frac{n_j(z') g_i}{n_i(z') g_j} - 1 \right] \frac{dz'}{\delta v_d}. \quad (5.36)$$

The integration has to be done from the edge of the plane parallel cloud to depth z . The probability that a photon escapes through the nearest boundary is approximately given by (de Jong et al. 1980)

$$\begin{aligned} \beta_{\text{esc}}(\tau) &= \frac{1 - \exp(-2.34\tau)}{4.68\tau}, \quad \tau < 7 \\ &= \left\{ 4\tau \left[\ln \left(\frac{\tau}{\sqrt{\pi}} \right) \right]^{0.5} \right\}^{-1}, \quad \tau \geq 7. \end{aligned} \quad (5.37)$$

In equation (5.37) it is assumed that only half of the photons can escape, the other half is emitted in the semi-infinite slab.

Fine-structure line cooling

Since most of the gas is atomic in the radical region, the dominant coolants are the atomic fine-structure lines. The most prominent cooling lines are the [CII] 158 μm and [OI] 63 μm and 146 μm lines. For the calculation of the thermal balance we also take into account Si^+ , C, Si, S, Fe and Fe^+ . All atomic data used are listed in Table 5.1. We take into account collisions with electrons, H^+ , H and H_2 (ortho and para) for the excitation of the species to different levels. In the PDRs, collisions with H^+ are not the dominant excitation source but in XDRs the ionized fraction of hydrogen can be as large as ten percent and become important for the excitation of some levels.

Metastable-line cooling

We included the metastable cooling lines of C, C^+ , Si, Si^+ , O, O^+ , S, S^+ , Fe and Fe^+ . All the data is taken from Hollenbach & McKee (1989) except for Si^+ (Dufton & Kingston 1994), C^+ (Sampson et al. 1994) and O^+ (McLaughlin & Bell 1993).

Recombination cooling

At temperatures higher than ~ 5000 K, cooling due to recombination of electrons with grains (PAHs) is important. The cooling depends on the recombination rate which is proportional to the product $n_e n_{\text{H}}$. The cooling rate increases when $G_0 T_{\text{k}}^{0.5}/n_e$ goes up, due to an increase in charge and hence Coulomb interaction. Bakes & Tielens (1994) calculated numerically the recombination cooling for a variety of physical conditions. An analytical fit to the data is given by

$$\Lambda = 3.49 \cdot 10^{-30} T_{\text{k}}^{\alpha} (G_0 T_{\text{k}}^{1/2}/n_e)^{\beta} n_e n_{\text{H}} \text{ erg s}^{-1} \text{ cm}^{-3}, \quad (5.38)$$

where $\alpha = 0.944$ and $\beta = 0.735/T_{\text{k}}^{0.068}$.

Molecular cooling by H_2 , CO and H_2O

For the rotational and vibrational cooling of H_2 , CO and H_2O , we use the fitted rate coefficients of Neufeld & Kaufman (1993) and Neufeld et al. (1995). They present a cooling rate for species i through:

$$\Lambda = L n(x_i) n(\text{H}_2) \text{ erg cm}^{-3} \text{ s}^{-1}, \quad (5.39)$$

where $n(\text{H}_2)$ and $n(x_i)$ are the densities of H_2 and species x_i , respectively. L is given by

$$\frac{1}{L} = \frac{1}{L_0} + \frac{n(\text{H}_2)}{L_{\text{LTE}}} + \frac{1}{L_0} \left[\frac{n(\text{H}_2)}{n_{1/2}} \right]^{\alpha} \left(1 - \frac{n_{1/2}}{L_{\text{LTE}}} \right). \quad (5.40)$$

We interpolate in the tables given by Neufeld & Kaufman (1993) and Neufeld et al. (1995), to find the values L_0 , $n_{1/2}$ and L_{LTE} and α . L_0 is the cooling rate coefficient

in the low density limit and $n_{1/2}$ is the H_2 density, where L falls a factor 2 below L_0 . α is chosen to minimize the maximal fractional error in the fit at other densities. L_0 is a function of temperature, and L_{LTE} , $n_{1/2}$, and α are functions of temperature and the optical depth parameter $\tilde{N}(x_i)$, which is given by the gradient $N(x_i)/\delta v_d$. $N(x_i)$ is the column density of the species x_i . To take into account collisional excitation by electrons and atomic hydrogen, we follow Yan (1997) and replace $n(\text{H}_2)$ by n_{rot} and n_{vib} . For H_2 rotational and vibrational cooling, n_{rot} and n_{vib} are given by

$$n_{\text{rot}}(\text{H}_2) = n_{\text{vib}}(\text{H}_2) = n(\text{H}_2) + 7n(\text{H}) + 16n(\text{e}). \quad (5.41)$$

For rotational cooling by CO, n_{rot} is given by

$$n_{\text{rot}}(\text{CO}) = n(\text{H}_2) + 1.414n(\text{H})\sigma_{\text{H}}/\sigma_{\text{H}_2} + 1.3 \times 10^{-8}n(\text{e})/\sigma_{\text{H}_2}v, \quad (5.42)$$

where $\sigma_{\text{H}} = 2.3 \times 10^{-15} \text{ cm}^{-2}$, $\sigma_{\text{H}_2} = 3.3 \times 10^{-16}(T_{\text{k}}/10^3)^{-1/4} \text{ cm}^{-2}$ and $v = 1.03 \times 10^4 T_{\text{k}}^{0.5} \text{ cm s}^{-1}$. For H_2O rotational cooling, n_{rot} is given by

$$n_{\text{rot}}(\text{H}_2\text{O}) = n(\text{H}_2) + 10n(\text{H}) + n(\text{e})k_e(1, 20, 1.9, T_{\text{k}})/k_{\text{H}_2}, \quad (5.43)$$

where $k_{\text{H}_2} = 7.4 \times 10^{-12} T_{\text{k}}^{0.5} \text{ cm}^3 \text{ s}^{-1}$ and $k_e(i, b, d, T_{\text{k}})$ are the H_2 and electron impact excitation rate coefficients, respectively. $k_e(i, b, d, T_{\text{k}})$ for the excitation from level $i \rightarrow i + 1$ in units of $\text{cm}^3 \text{ s}^{-1}$ is given by

$$k_e(i, b, d, T_{\text{k}}) = \frac{3.56 \times 10^{-6} d^2}{T_{\text{k}}^{0.5} [2 - 1/(i + 1)]} \exp(\beta \Delta E) \times \ln \left[C \Delta E + \frac{C}{\beta} \exp \left(\frac{-0.577}{1 + 2\beta \Delta E} \right) \right], \quad (5.44)$$

where b is the rotational constant in cm^{-1} , d the dipole moment in Debye, $\beta = 11600/T_{\text{k}}$, $\Delta E = 2.48 \times 10^{-4} b(i + 1)$ and C is given by

$$C = \frac{9.08 \times 10^3}{b(i + 1)} \quad d \leq 1.53 \quad (5.45)$$

$$C = \frac{1.93 \times 10^4}{db(i + 1)} \exp(-1.18/d^3) \quad d > 1.53.$$

For CO vibrational cooling, n_{vib} is given by

$$n_{\text{vib}}(\text{CO}) = n(\text{H}_2) + 50n(\text{H}) + n(\text{e})L_{\text{CO,e}}/L_{\text{CO},0}, \quad (5.46)$$

where

$$\begin{aligned}
L_{\text{CO},e} &= 1.03 \times 10^{-10} (T_k/300)^{0.938} \exp(-3080/T_k) \\
L_{\text{CO},0} &= 1.14 \times 10^{-14} \exp(-68.0/T_k^{1/3}) \exp(-3080/T_k).
\end{aligned} \tag{5.47}$$

For H₂O vibrational cooling, n_{vib} is given by

$$n_{\text{vib}}(\text{H}_2\text{O}) = n(\text{H}_2) + 10n(\text{H}) + n(e)L_{\text{H}_2\text{O},e}/L_{\text{H}_2\text{O},0}, \tag{5.48}$$

where

$$\begin{aligned}
L_{\text{H}_2\text{O},e} &= 2.6 \times 10^{-6} T_k^{-0.5} \exp(-2325/T_k) \\
L_{\text{H}_2\text{O},0} &= 0.64 \times 10^{-14} \exp(-47.5/T_k^{1/3}) \exp(-2325/T_k).
\end{aligned} \tag{5.49}$$

5.2.3 Chemistry

For most of the chemical reaction rates, we make use of the UMIST database for astrochemistry by Le Teuff et al. (2000). In the PDR model we use a network containing all species with 6 atoms or less.

H₂ formation on dust grains

The formation of H₂ is very efficient over a wide range of temperatures. It was already shown by Gould & Salpeter (1963) that H₂ is not formed efficiently in the gas phase. Most of the formation, which is still not very well understood, takes place on grain surfaces (Hollenbach & Salpeter 1971). Recently, Cazaux & Tielens (2002, 2004) developed a model for the formation of hydrogen under astrophysically relevant conditions. They compared their results with the laboratory experiments by Pirronello et al. (1999) and Katz et al. (1999). They find a recombination rate of

$$\begin{aligned}
R_{\text{H}_2} &= 0.5 n_{\text{H}} v_{\text{H}} n_{\text{d}} \sigma_{\text{d}} \epsilon_{\text{H}_2} S_{\text{H}}(T_k) \\
&\approx 6 \times 10^{-17} (T_k/300)^{0.5} n_{\text{H}} n \epsilon_{\text{H}_2} S(T_k) \text{ cm}^{-3} \text{ s}^{-1},
\end{aligned} \tag{5.50}$$

where n_{d} and σ_{d} are the volume density and cross section of dust grains and n_{H} , v_{H} and $S(T_k)$ are the volume density, thermal velocity and thermally averaged sticking coefficient of hydrogen atoms. We use the sticking coefficient given by Hollenbach & McKee (1979)

$$S(T_k) = [1 + 0.4(T_k + T_d)^{0.5} + 2 \times 10^{-3} T_k + 8 \times 10^{-6} T_k^2]^{-1}, \tag{5.51}$$

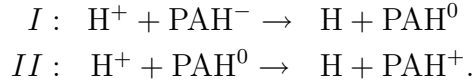
where T_d is the dust temperature. Eq. (5.51) is the same as eq. (4) in Tielens & Hollenbach (1985), except for the term ϵ_{H_2} , the recombination efficiency, which is given by

$$\epsilon_{\text{H}_2} = \left(\frac{\mu F}{2\beta_{\text{H}_2}} + 1 + \frac{\beta_{\text{H}_p}}{\alpha_{pc}} \right)^{-1} \xi, \quad (5.52)$$

where μ is the H_2 fraction that stays on the surface after formation, β_{H_2} and β_{H_p} are the desorption rates of molecular hydrogen and physisorbed hydrogen atoms, respectively, F is the flux of hydrogen atoms and α_{pc} is the evaporation rate from physisorbed to chemisorbed sites. These three terms dominate in different temperature regimes. See Cazaux & Tielens (2002, 2004) for a more detailed discussion.

Recombination on PAHs

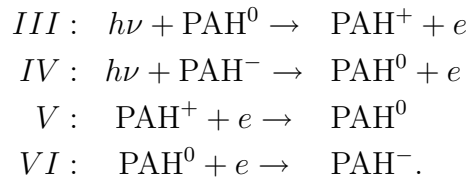
Collisions of electrons and ions with grains can become an important recombination process in dense clouds of low ionization.



We use only one PAH size, since our main interest is to obtain an estimate of the electron abundance for the energy balance. We adopt disk-like/planar PAHs of $N_C = 35$ carbon atoms and disk radius of $a = (N_C/1.222)^{0.5}$ as used by Wolfire et al. (2003), who calculated the rate coefficient with the results of Draine & Sutin (1987):

$$\begin{aligned} R_I &= 8.3 \times 10^{-7} \phi_{\text{PAH}} (T_k/100)^{-0.5} \text{ cm}^3 \text{ s}^{-1} \\ R_{II} &= 3.1 \times 10^{-8} \phi_{\text{PAH}} \text{ cm}^3 \text{ s}^{-1}, \end{aligned}$$

where ϕ_{PAH} is a scaling factor for the collision rates of ions and electrons with PAHs. Following Sect. 5 of Wolfire et al. (2003), we adopt a value $\phi_{\text{PAH}} = 0.5$. Rates for the recombinations with other atoms scale with $(m_{\text{H}}/m_i)^{0.5}$. PAH^+ and PAH^- are formed and destroyed by the following reactions:



Wolfire et al. (2003) calculated the following rate coefficient from Bakes & Tielens (1994) using $N_C = 35$ carbon atoms and assuming a disk geometry:

$$\begin{aligned} R_{III} &= 7.85 \times 10^{-9} G_0 \exp(-2.0 A_V) \text{ s}^{-1} \\ R_{IV} &= 2.00 \times 10^{-8} G_0 \exp(-2.0 A_V) \text{ s}^{-1} \\ R_V &= 3.50 \times 10^{-5} \phi_{\text{PAH}} (T_k/100)^{-0.5} \text{ cm}^3 \text{ s}^{-1} \\ R_{VI} &= 1.34 \times 10^{-6} \phi_{\text{PAH}} \text{ cm}^3 \text{ s}^{-1}. \end{aligned}$$

To illustrate the effect of PAHs on the chemistry, we show the $C^+/C/CO$ transitions for model 4 (see 6.2) in Fig. 5.1. When PAHs are absent, C^+ extends deeper into the cloud by two magnitudes of extinction (i.e. $N_H \approx 3.8 \times 10^{21} \text{ cm}^{-2}$) and CO is formed closer to the surface.

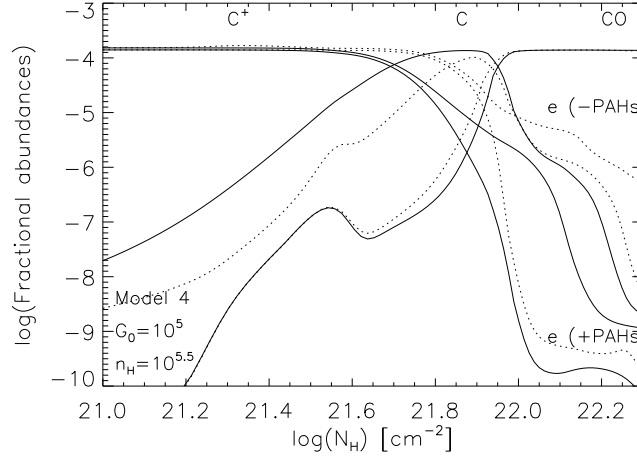


Figure 5.1: The $C^+/C/CO$ transition and the electron abundance with (solid) and without (dotted) the inclusion of PAHs.

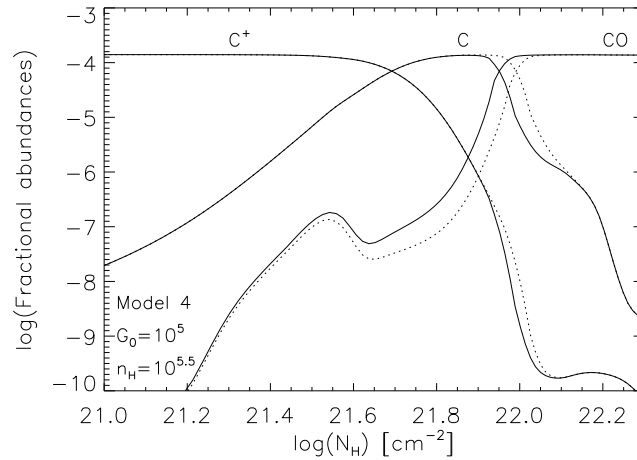


Figure 5.2: The $C^+/C/CO$ transition with (solid) and without (dotted) H_2 mutual shielding.

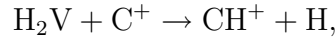
Vibrational excitation of H_2

In PDRs, molecular hydrogen can be excited by absorption of FUV photons in the Lyman-Werner bands. Fluorescence leads to dissociation in about 10% of the cases (see Field et al. 1966; Stecher & Williams 1967), and in the remaining 90% of the cases to a vibrationally excited state in the ground electronic state (Black & Dalgarno 1976). To simplify matters, we treat the electronic ground state as having a vibrational ground state and a single excited vibrational state. London (1978) found that the effective quantum number

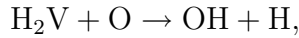
for this pseudo-level is $v = 6$, and the effective energy is $E_*/k = 2.6 \text{ eV}/k = 30163 \text{ K}$. We treat excited molecular hydrogen, H_2V , as a separate species in our chemistry. H_2V can be destroyed by direct FUV dissociation, radiative decay or collisional de-excitation, and chemical reactions with other species. Since vibrational decay is a forbidden process, a large abundance of H_2V can be maintained. H_2V can react with other species with no activation barrier or a reduced one. That is, in the UMIST database, the rates for a reaction between two species are parameterized as

$$R = \alpha (T_k/300)^\beta \exp(-\gamma/T_k) \text{ cm}^3 \text{ s}^{-1}. \quad (5.53)$$

For reactions with H_2V , γ is replaced by $\gamma^* = \max(0.0, \gamma - 30163)$. When reactions have an activation barrier lower than 2.6 eV, the barrier is set to zero. When the barrier is larger than 2.6 eV, the barrier is reduced by 2.6 eV. Tielens & Hollenbach (1985) state that for important reactions such as



and



this is a good approximation since the activation barrier of $\sim 0.5 \text{ eV}$ is a lot smaller than the vibrational excitation energy of 2.6 eV. For reactions with barriers of the same order or larger one can overestimate the reaction rates.

Shielding of H_2 and CO

The photo-dissociation rate of both H_2 and CO is influenced by line as well as continuum absorption. The dissociation rate of H_2 is decreased by self-shielding. For an H_2 line optical depth $\tau \leq 10$, we adopt the self-shielding factor given by (Shull 1978)

$$\beta(\tau) = \sum_{n=0}^{\infty} \frac{(-1)^n \tau^n}{n!(n+1)^{1/2} \pi^{n/2}}. \quad (5.54)$$

When the line absorption is dominated by the Doppler cores or the Lorentz wings (i.e., $\tau > 10$), we use the self-shielding factor as given by de Jong et al. (1980)

$$\beta(\tau) = \{\tau^{-1} [\ln(\tau/\sqrt{\pi})]^{-0.5}\} \text{erfc}(\tau b \pi^{-1} v_1^{-2})^{0.5}, \quad (5.55)$$

where τ , b , and v_1 are given in eqn. 5.9, 5.10 and 5.11.

The CO photo-dissociation rate is decreased by both CO self-shielding and H_2 mutual shielding. We use Table 5 of van Dishoeck & Black (1988), to determine the shielding

factor as a function of column densities $N(\text{H}_2)$ and $N(\text{CO})$. To illustrate the importance of H_2 mutual shielding, we show the $\text{C}^+/\text{C}/\text{CO}$ transition for model 4 (see 6.2), with and without H_2 mutual shielding in Fig. 5.2. Without H_2 shielding, CO is formed a magnitude of extinction (i.e. $N_{\text{H}} \approx 1.9 \times 10^{21} \text{ cm}^{-2}$) deeper into the cloud, and as a consequence $N(\text{CO})$ is lower.

5.3 The X-ray dominated region model

Unlike PDRs, XDRs are mostly heated by direct photo-ionization of the gas, which produces fast electrons that lose energy through collisions with other electrons, as well as H and H_2 . These fast electrons collisionally excite H and H_2 , which subsequently emit Lyman α and Lyman-Werner band photons, respectively. These photons in turn are capable of ionizing atoms such as C and Si or ionize and dissociate molecules such as H_2 and CO.

Compared to PDRs, the following processes play a role in XDRs (c.f. Maloney et al. 1996), in part because of the production of UV photons as described above:

- Photo-ionization heating (i.e., Coulomb heating with thermal electrons) dominates by a large factor over the heating through photo-electric emission by dust grains and PAHs (c.f. Maloney et al. 1996; Bakes & Tielens 1994).
- Emission from meta-stable lines of [CI] 9823, 9850 Å and [OI] 6300 Å; fine-structure line cooling of [CII] 158 and [OI] 63 and 146 μm as well as Lyman α emission (c.f. Maloney et al. 1996; Tielens & Hollenbach 1985; Spaans et al. 1994).
- Molecular line cooling by warm molecular gas containing CO, H_2 , H_2O and OH as well as gas-grain cooling where warm gas is cooled at the surfaces of lower temperature dust grains (c.f. Neufeld et al. 1995; Spaans & Silk 2000).
- Ion-molecule reactions driven by the ionization degree of $\sim 10^{-4}$ maintained by the ionization of carbon in the FUV (c.f. Black & Dalgarno 1977; van Dishoeck & Black 1986).
- The ionization balance of atomic gas under the influence of photo-ionization reactions driven by X-ray photons and charge transfer. Recombination of ions on grain surfaces is a major ionic loss route at electron fractions less than 10^{-3} (c.f. Lepp & Dalgarno 1988; Bakes & Tielens 1994; Maloney et al. 1996).

The global structure of any XDR is defined by a few key parameters, the density n_{H} and the energy deposition rate H_X per hydrogen atom. Because the heating in XDRs is driven by photo-ionization, the heating efficiency is close to unity as opposed to that in PDRs where the photo-electric heating efficiency is of the order of 0.3 – 1.0% (Maloney et al. 1996; Bakes & Tielens 1994). Unlike PDRs, XDRs are exposed to X-rays as well as FUV photons.

As one moves into the XDR, X-ray photons get attenuated due to atomic electronic absorptions. The lowest energy photons are attenuated strongest, which leads to a dependence of the X-ray heating and ionization rates at a given point on the slope of the X-ray

spectrum. We assume, for energies between 0.1 and 10 keV, that the primary ionization rate of hydrogen is negligible compared to the secondary ionization rate and that Auger electrons contribute an energy that is equal to the photo-ionization threshold energy (Voit 1991).

The treatment below follows, in part, the unpublished and little known work by Yan (1997). Also, we extend the work of Maloney et al. (1996) in terms of depth dependence, H₂ excitation and extent of the chemical network.

5.3.1 Energy deposition rate per hydrogen nucleus

The photon energy absorbed per hydrogen nucleus, H_X , is given by

$$H_X = \int_{E_{\min}}^{E_{\max}} \sigma_{\text{pa}}(E) F(E, z) dE. \quad (5.56)$$

The interval $[E_{\min}, E_{\max}]$ is the spectral range where the energy is emitted. The photo-electric absorption cross section per hydrogen nucleus, σ_{pa} , is given by

$$\sigma_{\text{pa}}(E) = \sum_i \mathcal{A}_i(\text{total}) \sigma_i(E). \quad (5.57)$$

Morrison & McCammon (1983) state that the X-ray opacity is independent of the degree of depletion onto grains. Therefore, we take the total (gas and dust) elemental abundances, $\mathcal{A}_i(\text{total})$, as given in Table 6.2 to calculate σ_{pa} . The X-ray absorption cross sections, σ_i , are taken from Verner & Yakovlev (1995) and the total cross section σ_{pa} is shown in Fig. 5.3. The flux $F(E, z)$ at depth z into the cloud is given by

$$F(E, z) = F(E, z = 0) \exp(-\sigma_{\text{pa}}(E) N_{\text{H}}), \quad (5.58)$$

where N_{H} is the total column of hydrogen nuclei and $F(E, z = 0)$ the flux at the surface of the cloud.

5.3.2 Heating processes

Heating due to Coulomb interactions

When X-rays are absorbed, fast electrons are produced. These fast electrons lose part of their energy through Coulomb interactions with thermal electrons, so the X-ray heating is given by

$$\Gamma_X = \eta n H_X, \quad (5.59)$$

where η is the heating efficiency, depending on the H₂/H ratio and the electron abundance x . We use the results of Dalgarno et al. (1999). Their calculated heating efficiency η in an ionized gas mixture is given by

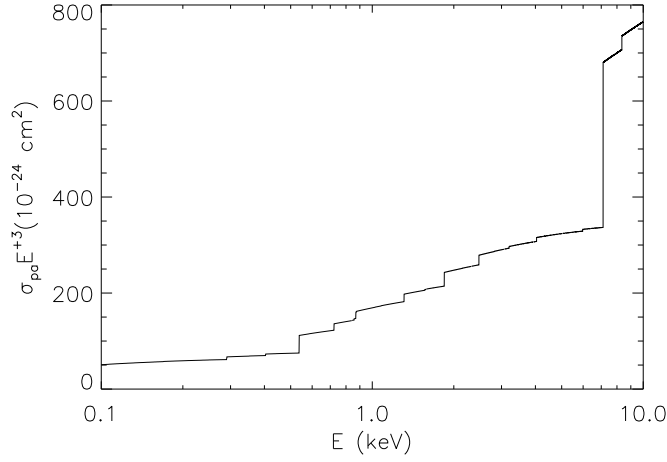


Figure 5.3: Photo-electric cross section times E^3 , with E in keV, based on Verner & Yakovlev (1995).

$$\eta = \frac{10r\eta_{\text{H}_2\text{He}} + \eta_{\text{HeH}}}{10r + 1}, \quad (5.60)$$

where $r = n(\text{H}_2)/n(\text{H})$. $\eta_{\text{H}_2\text{H}}$ and η_{HeH} are the heating efficiencies for the ionized pure He and H_2 mixture and the He and H mixture, respectively. Both are parameterized through

$$\eta' = 1 + (\eta_0 - 1)/(1 + cx^\alpha). \quad (5.61)$$

The values of η_0 , c and α are given in Table 7 of Dalgarno et al. (1999), and x is the electron fractional abundance. It has to be modified when the H_2 -He mixture is considered:

$$x' = \frac{1.83x}{1 + 0.83x}. \quad (5.62)$$

Heating due to H_2 ionization

H_2 ionization can lead to gas heating (Glassgold & Langer 1973). When H_2 is ionized by a fast electron and subsequently recombines dissociatively, about 10.9 eV (1.75×10^{-11} erg) of the ionization energy can go into kinetic energy. H_2^+ can also charge transfer with H. This is an exoergic reaction, with an energy yield of 1.88 eV, of which we assume half, 0.94 eV (1.51×10^{-12} erg), to go into heating. H_2^+ can also react to H_3^+ , and subsequently recombine dissociatively or react with other species. Glassgold & Langer (1973) argued that for every H_3^+ ion formed, 8.6 eV (1.37×10^{-11} erg) goes into gas heating. The H_2 ionization rate cooling is then given by

$$\Gamma_{\text{H}_2 \text{ ion}} = \frac{17.5k_e x_e + 1.51k_H x_H + 13.7k_{\text{H}_2} x_{\text{H}_2}}{k_e x_e + k_H x_H + k_{\text{H}_2} x_{\text{H}_2}} \times 10^{-12} \zeta_{\text{H}_2} x_{\text{H}_2} n \text{ erg cm}^{-3} \text{ s}^{-1}, \quad (5.63)$$

where k_e , k_H and k_{H_2} are the rates of dissociative recombination, charge transfer with hydrogen and the reaction to H_3^+ , respectively.

Gas-grain collisional heating

We use the results of Sect. 5.2.1. The dust temperature was found by Yan (1997):

$$T_d = 1.5 \times 10^4 (H_X/x_d)^{0.2} \text{ K}, \quad (5.64)$$

where $x_d = 1.9 \times 10^{-8}$ is the grain abundance and H_X is in erg s^{-1} . We assume that the grain temperature is determined by the local production of FUV photons. Therefore, the dust temperature is proportional to H_X , the locally absorbed X-ray energy per hydrogen atom. When the dust abundance is larger, there is less (locally produced FUV) energy per dust particle, and the average T_d drops.

H₂ vibrational heating/cooling

When the vibrational levels of H₂ are populated by non-thermal processes, thermal collisional quenching and excitation can result in a net heating despite downward radiations. When non-thermal reactions are not important, H₂ can be an important coolant. The resulting collisional vibrational heating or cooling is given by

$$\Gamma_{H_2\text{vib,col}} = \sum_{vj} n_{vj} \times \sum_{v'j'} C(vj \rightarrow v'j') \times (E_{vj} - E_{v'j'}) \text{ erg cm}^{-3} \text{ s}^{-1}, \quad (5.65)$$

where $C(vj \rightarrow v'j')$ is the total collision rate from level vj to $v'j'$ in units of s^{-1} . Radiative cooling due to downward decay of the vibrational levels is given by

$$\Lambda_{H_2\text{vib,rad}} = \sum_{vj} A(vj \rightarrow v'j') n_{vj} \text{ erg cm}^{-3} \text{ s}^{-1}. \quad (5.66)$$

The population of the vibrational levels is discussed in Sect. 5.3.4.

5.3.3 Cooling processes

Cooling by electron impact with H

The cooling due to the excitation of hydrogen is important at temperatures $T > 5000$ K. The cooling rate is given by Spitzer (1978):

$$\Lambda_{e-H} = 7.3 \times 10^{-19} n_e n(\text{H}) \times \exp(-118400/T_k) \text{ erg cm}^{-3} \text{ s}^{-1}. \quad (5.67)$$

Fine-structure, metastable and molecular cooling

For the calculation of the fine-structure and metastable cooling we use the same method and data as given in Sect. 5.2.2 and 5.2.2. We treat the molecular cooling of H₂, CO and H₂O in the same way as in the PDR. Only H₂ vibrational cooling is treated differently, since non-thermal processes play an important role, which is discussed in Sect. 5.3.2.

5.3.4 Chemistry

We use all species with sizes up to 3 atoms, and some up to 4 atoms, from the UMIST database. These species are taken from Yan (1997). The additional reactions included in the XDR model are discussed below.

Primary ionizations

X-rays are absorbed in K-shell levels releasing an electron. An electron from a higher level may fill the empty spot and with the energy surplus another so called Auger electron is ejected. This process leads to multiply ionized species (X^{m+}). Due to charge transfer with H, H_2 and He, they are quickly reduced to the doubly ionized state (X^{2+}). We therefore assume that the ionization by an X-ray photon leads to a doubly ionized species, as does absorption of an X-ray photon by a singly ionized species. When rates for charge transfer with H and He are very fast, elements are quickly reduced to singly ionized atoms, which is the case for O^{2+} , Si^{2+} and Cl^{2+} . Therefore, we add only O^{2+} to the chemical network to represent them. We assume that Si and Cl get singly ionized after absorbing an X-ray photon. We also include C^{2+} , N^{2+} , S^{2+} and Fe^{2+} . The direct (or primary) ionization rate of species i at a certain depth z into the cloud is given by

$$\zeta_{i,\text{prim}} = \int_{E_{\text{min}}}^{E_{\text{max}}} \sigma_i(E) \frac{F(E, z)}{E} dE, \quad (5.68)$$

where the ionization cross sections σ_i are taken from Verner & Yakovlev (1995).

Secondary ionizations

Part of the kinetic energy of fast photo-electrons is lost by ionizations. These secondary ionizations are far more important for H, H_2 and He than direct ionization. Dalgarno et al. (1999) calculate the number of ions N_{ion} produced for a given species i . For a given electron energy E , N_{ion} is given by

$$N_{\text{ion}} = E/W, \quad (5.69)$$

where W is the mean energy per ion pair. Dalgarno et al. (1999) calculated W for pure ionized H-He and H_2 -He mixtures and parameterized W as:

$$W = W_0(1 + cx^\alpha), \quad (5.70)$$

where W_0 , c and α are given in Table 4 of their paper. The corrected mean energies for ionization in the H- H_2 -He mixture are given by

$$W(H^+) = W_{\text{H,He}}(H^+) \left[1 + 1.89 \frac{n(H_2)}{n(H)} \right], \quad (5.71)$$

$$W(H_2^+) = W_{\text{H}_2,\text{He}}(H_2^+) \left[1 + 0.53 \frac{n(H)}{n(H_2)} \right]. \quad (5.72)$$

The ionization rate at depth z into the cloud for species i is then given by

$$\zeta_{i,\text{sec}} = \int_{E_{\text{min}}}^{E_{\text{max}}} \sigma_{\text{pa}}(E) F(E, z) \frac{E}{W} dE \text{ s}^{-1} \text{ per H nucleus.} \quad (5.73)$$

We rewrite this to a rate dependent on the fractional abundance of the species x_i :

$$\zeta_{i,\text{sec}} = \int_{E_{\text{min}}}^{E_{\text{max}}} \sigma_{\text{pa}}(E) F(E, z) \frac{E}{W x_i} dE \text{ s}^{-1} \text{ per species } i, \quad (5.74)$$

where x_i is the fraction of species i . Since we integrate over the range 1-10 keV and W goes to a limiting value, we use the parameters applicable to the 1 keV electron. The ionization rate then simplifies to:

$$\begin{aligned} \zeta_{i,\text{sec}} &= \frac{1 \text{ keV}}{W(1 \text{ keV})x_i} \int_{E_{\text{min}}}^{E_{\text{max}}} \sigma_{\text{pa}}(E) F(E, z) dE \\ &= \frac{1 \text{ keV}}{W(1 \text{ keV})x_i} H_X \text{ s}^{-1} \text{ per species } i. \end{aligned} \quad (5.75)$$

We also include secondary ionizations for C, N, O, Si, S, Cl, Fe, C⁺, N⁺, O⁺, S⁺ and Fe⁺. We scale the ionization rate of these species to that of atomic hydrogen by

$$\zeta_i = \zeta_{\text{H}} \frac{\sigma_{\text{ei},i}}{\sigma_{\text{ei,H}}} \text{ s}^{-1}. \quad (5.76)$$

We integrate over the range 0.1-1.0 keV to get an average value of the electron impact ionization cross section σ_{ei} . Using the experimental data fits of Lennon et al. (1988). The scaling factors $\sigma_{\text{ei},i}/\sigma_{\text{ei,H}}$ for C, N, O, Si, S, Cl, Fe, C⁺, N⁺, O⁺, S⁺, and Fe⁺ are 3.92, 3.22, 2.97, 6.67, 6.11, 6.51, 4.18, 1.06, 1.24, 1.32, 1.97, and 2.38, respectively.

FUV photons from secondary electrons

When energetic electrons created in X-ray ionizations collide with atomic and molecular hydrogen, H₂ Lyman-Werner and H Lyman α photons are produced, which can significantly affect the chemistry. The photo-reaction rate R_i per atom or molecule of species i is given by

$$R_i = \frac{x_{\text{H}_2} \zeta_{\text{H}_2} p_m + x_{\text{H}} \zeta_{\text{H}} p_a}{1 - \omega} \text{ s}^{-1}. \quad (5.77)$$

The values of p_a are taken from table 4.7 of Yan (1997) and values of p_m are the rates for cosmic-ray induced reactions from Le Teuff et al. (2000). There is an exception for CO, however, where we take the rate, corrected for self-shielding, given by Maloney et al. (1996):

$$R_{\text{CO}} = 2.7 x_{\text{CO}}^{-1/2} (T_{\text{k}}/1000)^{0.5} \zeta_{\text{H}_2} x_{\text{H}_2} \text{ s}^{-1}. \quad (5.78)$$

Vibrationally excited H₂

Vibrationally excited H₂ can enhance reactions with an activation barrier and can be an important heating or cooling source as well. To calculate the populations of the vibrational levels of H₂, we take into account:

- Collisions with fast electrons produced by X-ray photo-ionization.
- Collisions with thermal electrons, H, H₂ and He.
- Chemical destruction and production in chemical reactions.
- Radiative decay.

We use the results of Dalgarno et al. (1999) to calculate the X-ray induced excitation to the vibrational levels $v = 1$ and $v = 2$. The ratio of the yields $Y(v = 2)/Y(v = 1)$ is about 0.070. Excitation to higher levels is not taken into account, since the yield to higher levels decreases very rapidly. First we calculate the mean energy for excitation, W , in the H₂-He mixture. The parameters are listed in Table 5 of Dalgarno et al. (1999). The function W has the same form as equation (5.70). The mean energy for excitation also depends on the abundances of H and H₂. The yield has to be corrected with a factor $C(\text{H}, \text{H}_2)$, which is given by

$$C(\text{H}, \text{H}_2) = \frac{2n(\text{H}_2)}{n(\text{H}) + 2n(\text{H}_2)}, \quad x \geq 10^{-4} \quad (5.79)$$

$$C(\text{H}, \text{H}_2) = \frac{n(\text{H}_2)/n(\text{H})}{n(\text{H}_2)/n(\text{H}) + a(x)}, \quad 10^{-7} < x < 10^{-4},$$

where $a(x) = 0.5(x/10^{-4})^{0.15}$. The rates for excitation by thermal electrons are taken from Yan (1997), who finds that the transitions rates for H₂($v = 0$) to H₂($v = 1, 2$) are given by

$$R(0 \rightarrow 1) = 9.7 \times 10^{-11} (T_k/300)^{0.87} \exp(-6140/T_k) \quad (5.80)$$

$$R(0 \rightarrow 2) = 7.5 \times 10^{-12} (T_k/300)^{0.91} \exp(-11900/T_k). \quad (5.81)$$

The excitation rate for the transition $v \rightarrow v + 1$ is taken to be v times the $0 \rightarrow 1$ rate. Excitations with $\Delta v > 1$ are not taken into account. The quenching rates are calculated through detailed balance. The quenching rates from $v \rightarrow v'$ by atomic hydrogen are given in table 4.2 of Yan (1997) and are of the form:

$$R(v \rightarrow v') = \alpha (T_k/300)^\beta \exp(-\gamma/T_k) \text{ cm}^3 \text{ s}^{-1}. \quad (5.82)$$

The excitation rates are obtained by detailed balance. For the molecular excitation and quenching rates we use the results of Tine et al. (1997). Only collisions where, either

initially or finally, one of the H_2 molecules is in the $v = 0$ state are considered. The rate coefficients are of the form:

$$\log_{10} R(v_1, v'_1; v_2, v'_2) = A + B/T_k + C \log_{10} T_k, \quad (5.83)$$

and are given in table 1 of Tine et al. (1997), who also considered collisions with He. They give a rate coefficient for the $v = 1 \rightarrow 0$ transition:

$$\begin{aligned} \log_{10} R(1 \rightarrow 0) &= -8.8T_k^{-1/3} - 16.5 & T_k \leq 90\text{K} \\ &= -18.9T_k^{-1/3} - 14.2 & 90 < T_k \leq 230\text{K} \\ &= -47.4T_k^{-1/3} - 9.4 & T_k > 230\text{K}. \end{aligned} \quad (5.84)$$

For the other transitions with $\Delta v = 1$, the same rates are used. The upward transitions can be obtained by detailed balance. Yan (1997) also calculated the dissociation and ionization rates by thermal electrons and since the ionization threshold is much higher than the vibrational energies one rate is used for all vibrational energies:

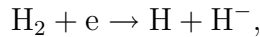
$$R_{e,\text{diss}} = 7.03 \times 10^{-9} (T_k/300)^{0.41} \exp(-118600/T_k) \quad (5.85)$$

$$R_{e,\text{ion}} = 8.9 \times 10^{-10} (T_k/300)^{0.57} \exp(-179400/T_k). \quad (5.86)$$

The dissociation rates by atomic hydrogen are given in table 4.3 of Yan (1997), which are of the same form as equation (5.82). For the dissociation rates by H_2 we use the results of Lepp & Shull (1983), which are given by

$$\begin{aligned} R_{\text{H}_2,\text{diss}} &= 6.29 \times 10^{-15} \times \\ &A \exp(1.44v - 0.037v^2) f(T_k)/f(4500\text{K}), \end{aligned} \quad (5.87)$$

where $A = 1.38$, $f(T_k) = T_k^{0.5} \alpha \exp(-\alpha)$, $\alpha = [1 + (E_{\text{th}} + 1)/kT_k]$ and $E_{\text{th}} = 4.48\text{eV} - E(v)$. For the dissociative attachment reaction:



we use the results of Wadehra & Bardsley (1978) and the reaction rates have the same form as equation (5.82). Vibrationally excited H_2 can be destroyed in chemical reactions. Endoergic reactions with vibrationally excited H_2 can lower the activation barrier, by using the energy of the vibrational level. The barrier is reduced, but cannot become negative: $E' = \min(0, E - E(v))$. When H_2 is formed in chemical reactions which are exoergic, part of the formation energy goes into the excitation of the vibrational levels. Formation of H_2 on grains can play a very significant role. H_2 has a binding energy of 4.48 eV. Following Sternberg & Dalgarno (1989), we assume one third of this energy to be distributed statistically over all the vibrational levels:

$$x(\text{H}_2(v)) = \frac{\exp(-E(v)/1.493)}{\sum_v \exp(-E(v)/1.493)}, \quad (5.88)$$

where $x(\text{H}_2(v))$ is the fraction of H_2 formed in vibrational state v . When H_2 formation reactions are endoergic, all the H_2 is in the ground vibrational state. When they are exoergic part of the energy is distributed statistically following equation (5.88). The Einstein A coefficients for radiative decay are taken from Turner et al. (1977). We take a weighted average over the rotational levels of each vibrational level, which we assume to be thermalized, to get an Einstein A coefficient for the decay from $v \rightarrow v'$.

Acknowledgements

We are indebted to Frank Israel, for initiating this project, and for his helpful suggestions and remarks. We also thank Ewine van Dishoeck for useful discussions on PDR and XDR physics. We thank the anonymous referee for a careful reading of the manuscript and constructive comments.

Table 5.1: Atomic Fine-structure data

Species	j	i	$E(\text{K})$	$\lambda(\mu\text{m})$	$A(\text{s}^{-1})$	$q(\text{cm}^3\text{s}^{-1})$	$T(\text{K})$	Partner	Ref.
C ⁺	$^2P_{1/2}$	$^2P_{3/2}$	92	157.7	2.4(-8)	$1.4 \times 10^{-6} T^{-0.37}$		e	3
						$5.8 \times 10^{-10} T^{0.02}$		H	1
						$3.1 \times 10^{-10} T^{0.02}$		H ₂	1
Si ⁺	$^2P_{1/2}$	$^2P_{3/2}$	414	34.8	2.1(-4)	$1.2 \times 10^{-5} T^{-0.5}$		e	4
						6.5×10^{-10}		H, H ₂	1
C	3P_0	3P_1	24	609.2	7.9(-8)	q_e^a		e	5
						$1.2 \times 10^{-9} (T/300)^{0.24}$		H ⁺	6
						$1.3 \times 10^{-10} T^{-0.045}$		H	1
						$1.61 \times 10^{-10} T^{-0.19}$	$< 10^2$	o-H ₂	7
						$3.50 \times 10^{-11} T^{0.13}$	$10^2 - 10^3$	o-H ₂	7
						8.10×10^{-11}	$> 10^3$	o-H ₂	7
						$1.05 \times 10^{-10} T^{-0.08}$	$< 10^2$	p-H ₂	7
	3P_1	3P_2	39	369.0	2.7(-7)	$3.72 \times 10^{-11} T^{0.12}$	$10^2 - 10^3$	p-H ₂	7
						8.50×10^{-11}	$> 10^3$	p-H ₂	7
						q_e^b		e	5
						$5.4 \times 10^{-9} (T/300)^{0.35}$		H ⁺	6
						$7.8 \times 10^{-11} T^{0.035}$		H	1
						$2.09 \times 10^{-10} T^{-0.04}$	$< 10^2$	o-H ₂	7
						$6.71 \times 10^{-11} T^{0.20}$	$10^2 - 10^3$	o-H ₂	7
						2.61×10^{-10}	$> 10^3$	o-H ₂	7
3P_0	3P_2	63	229.9	2.0(-14)	$4.50 \times 10^{-11} T^{0.27}$		p-H ₂	7	
					q_e^c		e	5	
					$8 \times 10^{-10} (T/300)^{0.57}$		H ⁺	6	
					$2 \times 10^{-10} T^{0.084}$		H	1	
					$1.18 \times 10^{-10} T^{-0.07}$	$< 10^2$	o-H ₂	7	
					$4.22 \times 10^{-11} T^{0.13}$	$10^2 - 10^3$	o-H ₂	7	
					1.03×10^{-10}	$> 10^3$	o-H ₂	7	
O	3P_2	3P_1	228	63.2	9.0(-5)	3.10×10^{-11}		p-H ₂	7
						$5.8 \times 10^{-12} T^{0.67}$		e	8
						$4.2 \times 10^{-11} T^{0.5} e^{-693/T}$		H ⁺	9
						$4.2 \times 10^{-12} T^{0.67}$		H	1
						$3.40 \times 10^{-11} T^{0.32}$		o-H ₂	10
						$2.45 \times 10^{-11} T^{0.38}$		p-H ₂	10
	3P_1	3P_0	98	145.6	1.7(-5)	$4.1 \times 10^{-12} T^{0.69}$		e	8
						$7.5 \times 10^{-12} T^{0.5} e^{-450/T}$		H ⁺	9
						$1.5 \times 10^{-11} T^{0.4}$		H	1
						$3.34 \times 10^{-15} T^{1.36}$		o-H ₂	10
						$2.74 \times 10^{-14} T^{1.06}$		p-H ₂	10
						$3.3 \times 10^{-12} T^{0.71}$		e	8
3P_2	3P_0	326	44.2	1.0(-10)	$7.5 \times 10^{-12} T^{0.5} e^{-1000/T}$		H ⁺	9	
					$1.1 \times 10^{-12} T^{0.44}$		H	1	
					$5.77 \times 10^{-11} T^{0.30}$		o-H ₂	10	
					$4.09 \times 10^{-11} T^{0.37}$		p-H ₂	10	
					3.3×10^{-8}		H ⁺	2	
					7.5×10^{-10}		H, H ₂	1	
S	3P_2	3P_1	571	25.2	1.4(-3)	1.2×10^{-8}		H ⁺	2
						4.2×10^{-10}		H, H ₂	1
						3.3×10^{-8}		H ⁺	2
Fe ⁺	$^6D_{9/2}$	$^6D_{7/2}$	554	26.0	2.5(-3)	7.1×10^{-10}		H, H ₂	1
						$1.8 \times 10^{-6} (T/100)^{-0.5}$		e	2
						9.5×10^{-10}		H, H ₂	1
Si	3P_0	3P_1	110	129.6	8.4(-6)	$8.7 \times 10^{-7} (T/100)^{-0.5}$		e	2
						4.7×10^{-10}		H, H ₂	1
						$1.8 \times 10^{-6} (T/100)^{-0.5}$		e	2
Si	3P_1	3P_2	210	68.4	4.2(-5)	5.7×10^{-10}		H, H ₂	1
						7.2×10^{-9}		H ⁺	2
						$3.5 \times 10^{-10} (T/100)^{-0.03}$		H, H ₂	2
Si	3P_0	3P_2	320	44.8	2.4(-10)	2.2×10^{-8}		H ⁺	2
						$5.0 \times 10^{-10} (T/100)^{0.17}$		H, H ₂	2
						7.2×10^{-9}		H ⁺	2
						$1.7 \times 10^{-10} (T/100)^{0.17}$		H, H ₂	2

Notes to Table 5.1: (1) Sternberg & Dalgarno (1995); (2) Hollenbach & McKee (1989); (3) Sampson et al. (1994); (4) Dufton & Kingston (1994); (5) Johnson et al. (1987); (6) Roueff & Le Bourlot (1990); (7) Schröder et al. (1991); (8) Mendoza (1983); (9) Chambaud et al. (1980); (10) Jaquet et al. (1992)

$T < 1000$ K:

$$\ln(q_e^a) = -0.925141e1 - 0.773782(\ln(T)) + 0.361184(\ln(T))^2 - 0.150892e-1(\ln(T))^3 - 0.656325(\ln(T))^4$$

$$\ln(q_e^b) = -0.743870e1 - 0.574430(\ln(T)) + 0.358264(\ln(T))^2 - 0.418166e-1(\ln(T))^3 + 0.234272e-2(\ln(T))^4$$

$$\ln(q_e^c) = -0.769735e1 - 0.130743e1(\ln(T)) + 0.697638(\ln(T))^2 - 0.111338(\ln(T))^3 + 0.705277e-2(\ln(T))^4$$

$T > 1000$ K:

$$\ln(q_e^a) = 0.444600e3 - 0.227913e3(\ln(T)) + 0.425952e2(\ln(T))^2 - 0.347620e1(\ln(T))^3 + 0.105085(\ln(T))^4$$

$$\ln(q_e^b) = 0.386186e3 - 0.202192e3(\ln(T)) + 0.385049e2(\ln(T))^2 - 0.319268e1(\ln(T))^3 + 0.978573e-1(\ln(T))^4$$

$$\ln(q_e^c) = 0.350609e3 - 0.187474e3(\ln(T)) + 0.361803e2(\ln(T))^2 - 0.303283e1(\ln(T))^3 + 0.938138e-1(\ln(T))^4$$

CHAPTER 6

PDR and XDR comparison

For both the PDR and XDR code, we calculate four depth-dependent models for different densities and radiation fields, relevant to conditions in star-burst galaxies and active galactic nuclei. A detailed comparison between PDR and XDR physics is made for total gas column densities between $\sim 10^{20}$ and $\sim 10^{25}$ cm^{-2} . We show cumulative line intensities for a number of fine-structure lines (e.g., [CII], [OI], [CI], [SiII], [FeII]), as well as cumulative column densities and column density ratios for a number of species (e.g., CO/H₂, CO/C, HCO⁺/HCN, HNC/HCN). The comparison between the results for the PDRs and XDRs shows that column density ratios are almost constant up to $N_{\text{H}} = 10^{22}$ cm^{-2} for XDRs, unlike those in PDRs. For example, CO/C in PDRs changes over four orders of magnitude from the edge to $N_{\text{H}} = 10^{22}$ cm^{-2} . The CO/C and CO/H₂ ratios are lower in XDRs at low column densities and rise at $N_{\text{H}} > 10^{23}$ cm^{-2} . The HNC/HCN column density ratio is typically larger than unity in XDRs for moderate H_X/n , i.e., at high column densities, and is ≤ 1 in PDRs.

This chapter contains modified parts from:
R. Meijerink & M. Spaans, 2005
Astronomy & Astrophysics, Volume 436, pp. 397–409

6.1 Introduction

Here we show the results for four PDR and XDR models with different radiation fields and densities, for a semi-infinite slab geometry and irradiation from one side without geometrical dilution. We make a comparison between the column densities, integrated line fluxes and abundance ratios. In the subsequent chapters, we will present a large set of models from which we derive line intensities, line intensity ratios and column density ratios, and use these results to interpret observations of the centers of nearby active galaxies, such as NGC 1068 and NGC 253.

6.2 PDR test models

In this section, we show the results for four PDR models in which we have varied the radiation field G_0 and the density n_{H} . The models are for a semi-infinite slab geometry, but the code also allows for two-sided slab geometries. The adopted model parameters are listed in Table 6.1. Models 2 and 4 will also be shown in a paper by Röllig et al. (in preparation), where they are used to compare 12 different PDR codes that are commonly used. The parameters are listed in Table 6.1. These values are typical for the high density, strong radiation field conditions we want to investigate in, e.g., a star-burst.

Table 6.1: Adopted model parameters

Model	G_0	F_{FUV} [erg cm ⁻² s ⁻¹]	n_{H} [cm ⁻³]
1	10 ³	1.6	10 ³
2	10 ⁵	160	10 ³
3	10 ³	1.6	10 ^{5.5}
4	10 ⁵	160	10 ^{5.5}
δv_{d} (km s ⁻¹)	2.7		
δ_{d}	1.0		

The fixed gas-phase and total abundances we use are given in Table 6.2. The total abundances are the average values of Asplund et al. (2005) and Jenkins (2004). To calculate the gas-phase abundances, we use the depletion factors calculated by Jenkins (2004).

6.2.1 Heating

In Fig. 6.1, we show heating as a function of column density. For both radiation fields and densities, the dominant heating source to a column density $N_{\text{H}} \approx 10^{22}$ cm⁻² is photoelectric emission from grains. Other processes such as carbon ionization, H₂ pumping and dissociation, and viscous heating also contribute in these regions, but not more than a few percent and only in specific regions in the cloud. H₂ pumping and dissociation heating become more important at higher densities, in Models 3 and 4, since H₂ is more abundant

Table 6.2: Abundances

Species	$\mathcal{A}_i(\text{gas})$	δ_i	$\mathcal{A}_i(\text{total})$
He ^{a,c}	8.5×10^{-2}	1.0	8.5×10^{-2}
C	1.4×10^{-4}	0.6	2.5×10^{-4}
N	5.2×10^{-5}	0.7	7.2×10^{-5}
O	3.4×10^{-4}	0.7	4.7×10^{-4}
Si	1.7×10^{-6}	0.05	3.4×10^{-5}
S	6.9×10^{-6}	0.5	1.4×10^{-5}
Cl	5.4×10^{-8}	0.2	2.4×10^{-7}
Fe	2.0×10^{-7}	0.007	2.8×10^{-5}
P ^{b,c}	3.9×10^{-8}	0.1	2.9×10^{-7}
Na	5.9×10^{-7}	0.4	1.5×10^{-6}
Mg	2.7×10^{-7}	0.08	3.4×10^{-6}
Ne ^c			6.9×10^{-5}
Al			2.3×10^{-6}
Ar			1.5×10^{-6}
Ca			2.0×10^{-6}
Cr			4.4×10^{-7}
Ni			1.7×10^{-6}

Notes to Table 6.2:

^a: Present in both PDR and XDR chemical network

^b: Present in PDR chemical network

^c: Used to calculate σ_{pa} for XDR

due to a higher H_2 formation rate, which scales with n^2 . Carbon ionization heating is highest at the C^+ to C transition. Viscous heating never contributes significantly to the heating. At high column densities ($N_{\text{H}} > 10^{22.5} \text{ cm}^{-2}$), [OI] 63 μm absorption and gas-grain heating are important. For the low density PDR Models 1 and 2, only [OI] 63 μm dominates. When the density is increased in Models 3 and 4, gas-grain heating is equally important if not dominant. Other heating processes contribute less than 10 percent, but are sometimes important in determining the thermal balance.

6.2.2 Cooling

In Fig. 6.1, we show cooling as a function of column density. In all models [OI] 63 μm cooling dominates to $N_{\text{H}} = 10^{21.5} \text{ cm}^{-2}$. In the low density PDRs, [CII] 158 μm cooling contributes more than ten percent to the cooling in this range, where at high densities, gas-grain cooling is the second most important coolant. In the high density, high radiation-field Model 4, this contribution can be almost forty percent. Deeper into the cloud, [CI] 610 μm and CO line cooling become important. H_2 line cooling can contribute up to ten

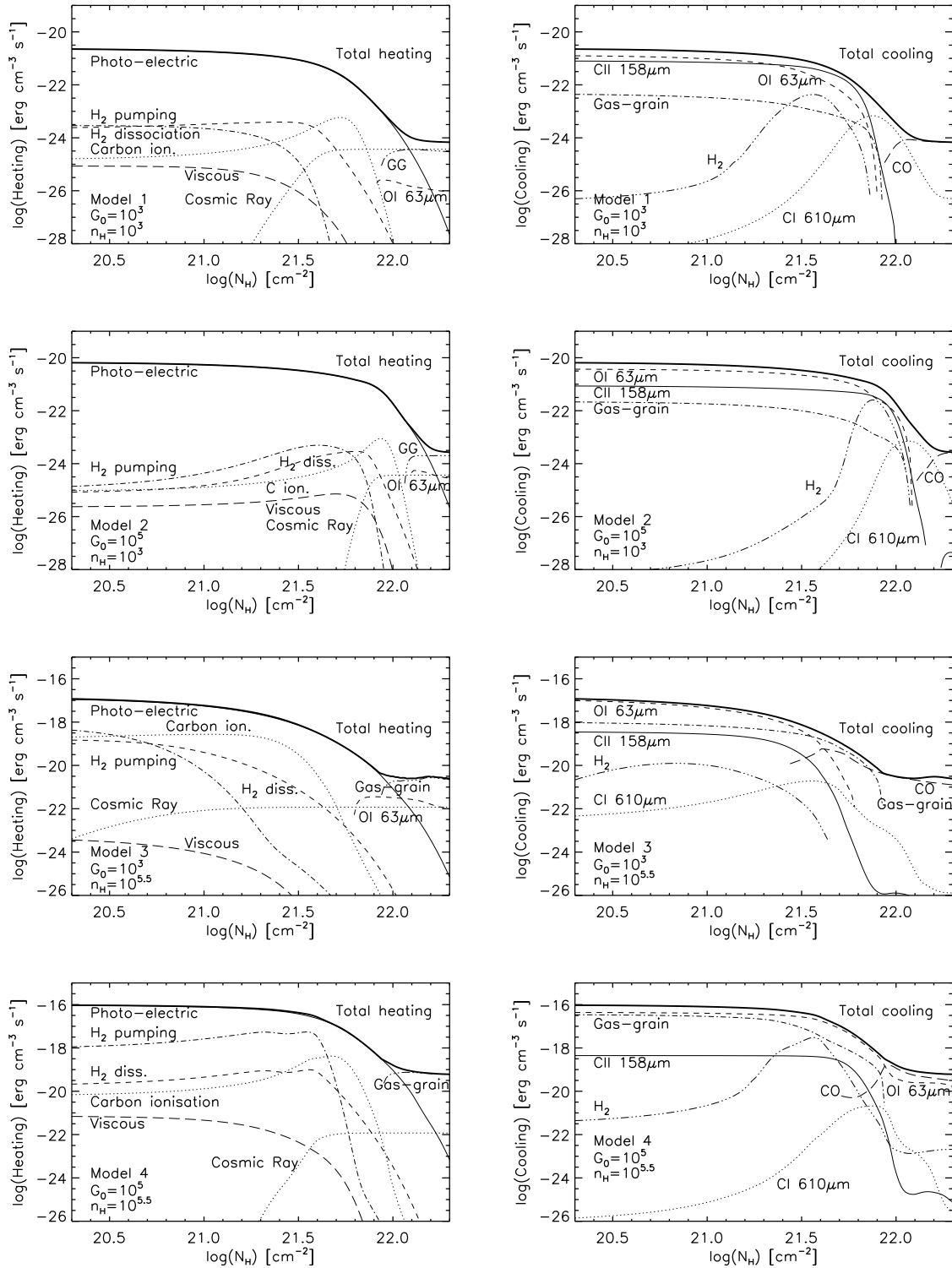


Figure 6.1: Important heating (left) and cooling (right) processes for PDR Models 1, 2, 3 and 4.

percent to the total cooling rate at some point, but is always a minor coolant.

6.2.3 Temperature structure

Gas temperatures as a function of column density are shown in Fig. 6.2. The edge temperatures are affected most by the strength of the radiation field when the density is largest. At a density of $n_{\text{H}} = 10^{5.5} \text{ cm}^{-3}$, the difference is a factor of thirty for an increase from $G_0 = 10^3$ to $G_0 = 10^5$. In the low density case this is only a factor of two. Because of optical depth effects, CO cooling is less effective at high column densities. For this reason, temperatures rise again at $N_{\text{H}} \approx 10^{22} \text{ cm}^{-2}$ in the low density models.

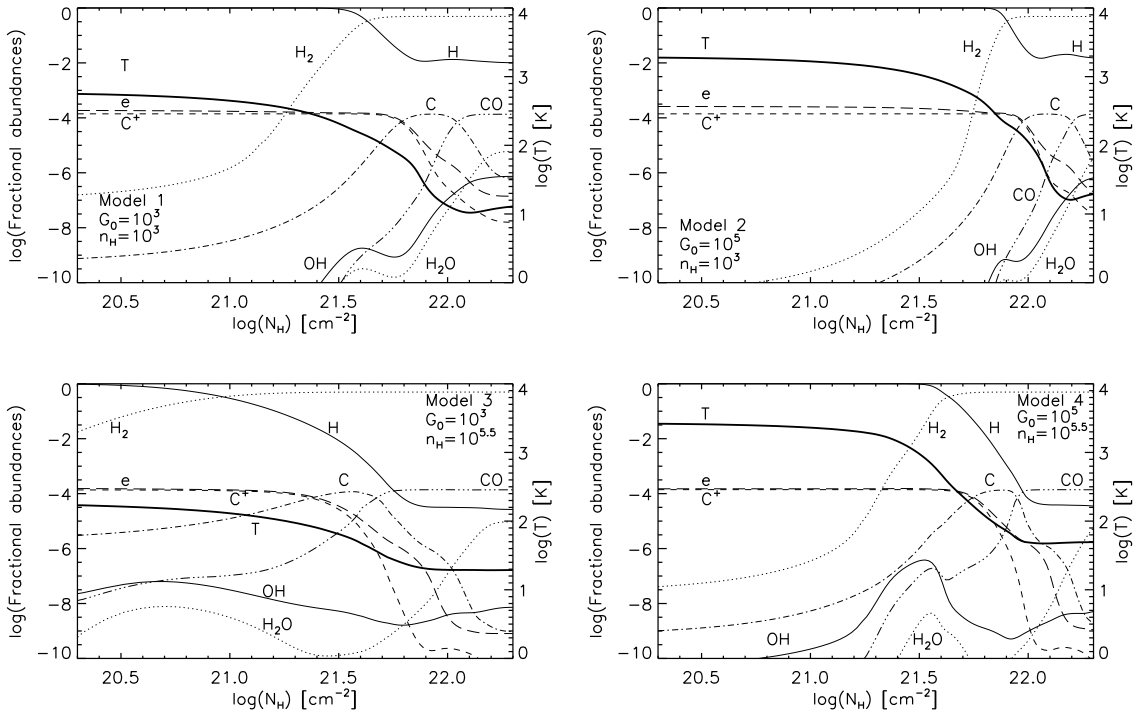


Figure 6.2: $\text{H} \rightarrow \text{H}_2$ and $\text{C}^+ \rightarrow \text{C} \rightarrow \text{CO}$ transitions and electron, OH and H_2O abundances for Models 1 (top left), 2 (top right), 3 (bottom left) and 4 (bottom right).

6.2.4 Chemistry

In Figs. 6.2 and 6.3, we show the depth-dependent abundances of selected important species. The $\text{H} \rightarrow \text{H}_2$ and $\text{C}^+ \rightarrow \text{C} \rightarrow \text{CO}$ transitions are quite sharp. Their actual location greatly varies, since this is strongly dependent on density and radiation field. Exposed to stronger radiation fields, the transitions occur deeper into the cloud, since the photo-dissociation rates are larger. At higher densities, the transitions occur closer to the surface of the cloud, since the recombination rates scale as n^2 . For the same reason, the H^+ and O^+ (Fig 6.3) fractional abundances are systematically higher in the low density

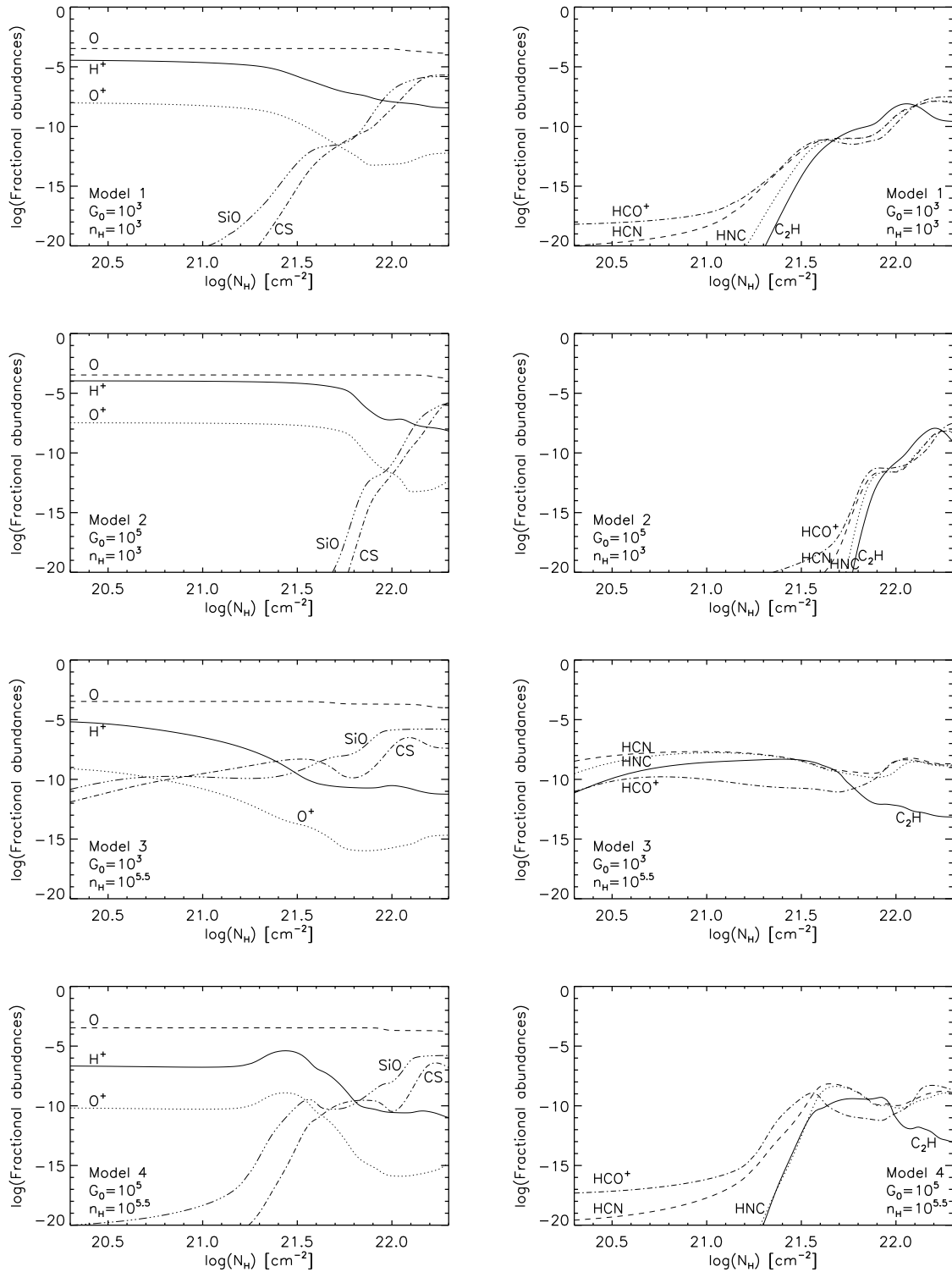


Figure 6.3: H^+ , O , O^+ , CS , and SiO (left), and C_2H , HNC , HCN , and HCO^+ abundances for PDR Models 1, 2, 3, and 4.

models. SiO and CS are more abundant and formed closer to the surface in the high density models, which is also the case for HCO⁺, HCN, HNC and C₂H (Fig. 6.3).

6.3 XDR test models

In this section, we consider four models with the same energy inputs and densities as the PDRs in Table 6.1. The spectral energy distribution is of the form $\exp(-E/10 \text{ keV})$. The energy is emitted between 1 and 10 keV and F_{FUV} should be replaced by F_X in Table 6.1. This spectral shape and spectral range can be changed depending on the application. We take the parameters of the 1 keV electron of Dalgarno et al. (1999) to determine the heating efficiency of Coulomb heating (Sect. 5.3.2) and ionization rates (Sect. 5.3.4), since the initial energies of the electrons are 1 keV or higher, and these parameters remain the same for these energies. When the spectral energy distribution is shifted towards higher energies, the X-rays will dominate a larger volume, since the absorption cross sections are smaller for higher energies. H_X/n is the most important parameter for the chemical and thermal balance, where H_X is the energy deposition rate per hydrogen nucleus. The abundances used are given in Table 6.2. The elements H, He, C, N, O, Si, S, Cl and Fe are included in the chemical network. The other elements listed are only used to calculate the photoelectric absorption cross section, σ_{pa} .

6.3.1 Heating

In Fig. 6.4, the different heating sources are shown as a function of the total hydrogen column density, N_{H} . All heating is done by X-rays, but the way it is transferred to gas depends on the ionization fraction. When the gas is highly ionized, $x_e \sim 0.1$, most ($\sim 70\%$) of the kinetic energy of the non-thermal electrons goes into Coulomb heating, which is the case in Models 1, 2 and 4 where H_X/n is high to $N_{\text{H}} > 10^{23} \text{ cm}^{-2}$. For smaller ionization fractions, $x_e \sim 10^{-4}$, ionization heating as discussed in Sect. 5.3.2 is important or even dominant. In Model 3, ionization heating and Coulomb heating are equally important at $N_{\text{H}} < 10^{21.8} \text{ cm}^{-2}$. In all models ionization heating dominates at the largest column densities. When the excitation of H₂ is dominated by non-thermal processes, collisional quenching of H₂ can heat the gas. Naively, one would expect this dominance to occur where most of the X-rays are absorbed, but for high energy deposition rates H_X/n , the temperature is high and thermal collisions dominate the population of the vibrational levels. Non-thermal excitation is dominant at low temperature, i.e., low H_X/n .

6.3.2 Cooling

In Fig. 6.4, the important cooling processes are shown as a function of total hydrogen column density, N_{H} . At high temperatures (see Fig. 6.5), cooling by [CI] 9823, 9850 Å and [OI] 6300 Å metastable lines dominates, as is the case in the models with high radiation fields, Models 2 and 4. At lower temperatures, most of the cooling is provided by the fine-structure line [OI] 63 μm (90%), e.g., at the edge in the low-radiation field Models

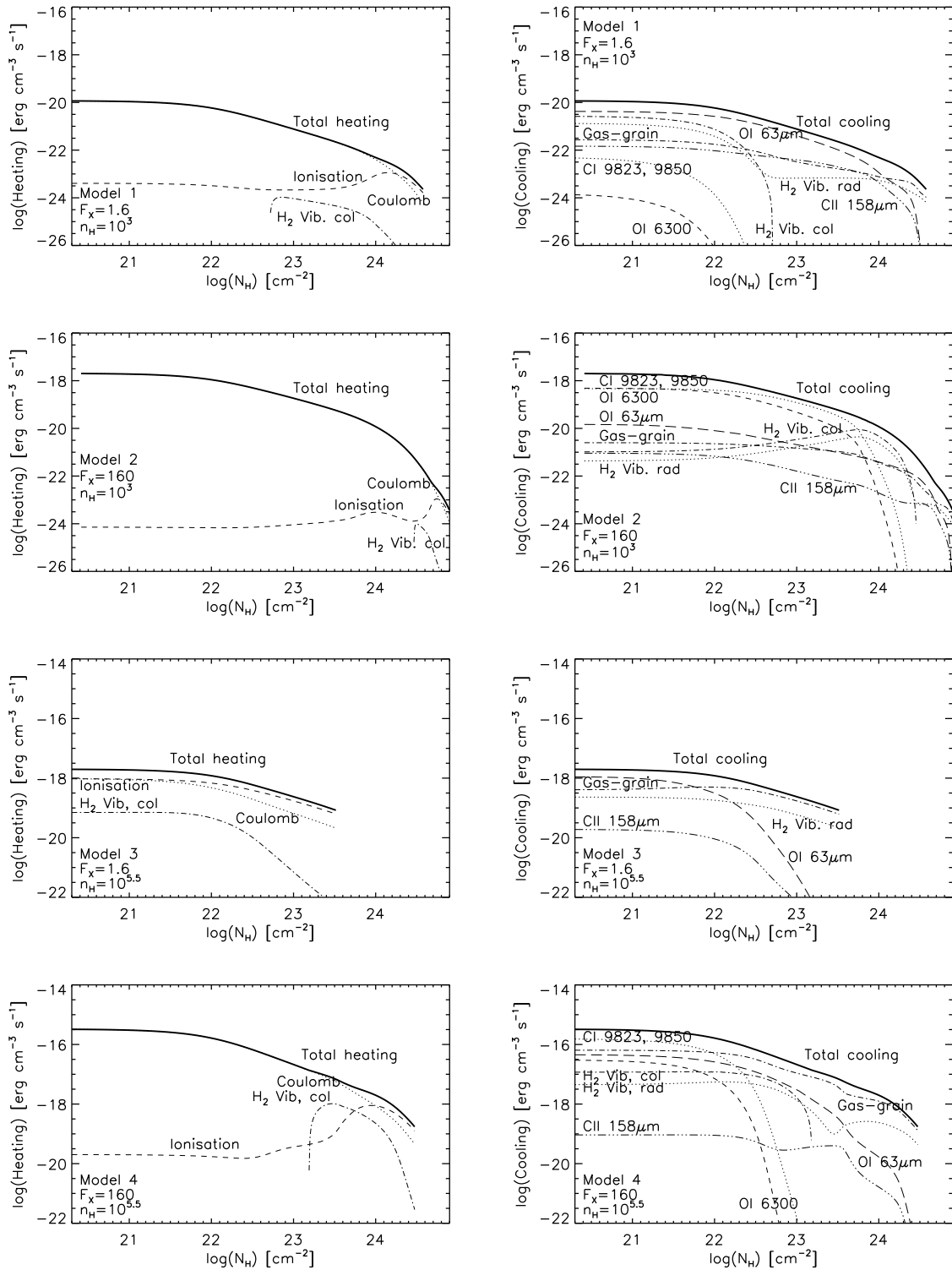


Figure 6.4: Important heating (left) and cooling (right) processes for XDR Models 1, 2, 3 and 4.

1 and 3. In each model, gas-grain cooling dominates for low H_X/n . In addition, specific cooling processes can be important in special cases. H_2 vibrational cooling dominates at large depths in Model 2, but in Models 1, 3 and 4 it contributes no more than 10%. H_2 vibrational cooling is split into a radiative and a collisional part. When the excitation of H_2 is dominated by non-thermal electrons, the gas is heated by collisional de-excitation of H_2 .

6.3.3 Temperature structure

In Fig. 6.5, we show the temperature as a function of total hydrogen column density, N_H . Variations in radiation field strength most strongly affect the high-density models. The temperature at the edge differs a factor of 30 in the high-density case. Since X-rays penetrate much deeper into a cloud than FUV photons, high temperatures are maintained to much greater depths into the clouds. H_X/n is very important in determining the thermal balance. When H_X/n is larger, this results in a higher temperature. Therefore, Model 2 has the largest temperature throughout the cloud. Density turns out to be important as well. Note that models 1 and 4 have similar incident H_X/n and therefore have about the same temperature throughout the cloud.

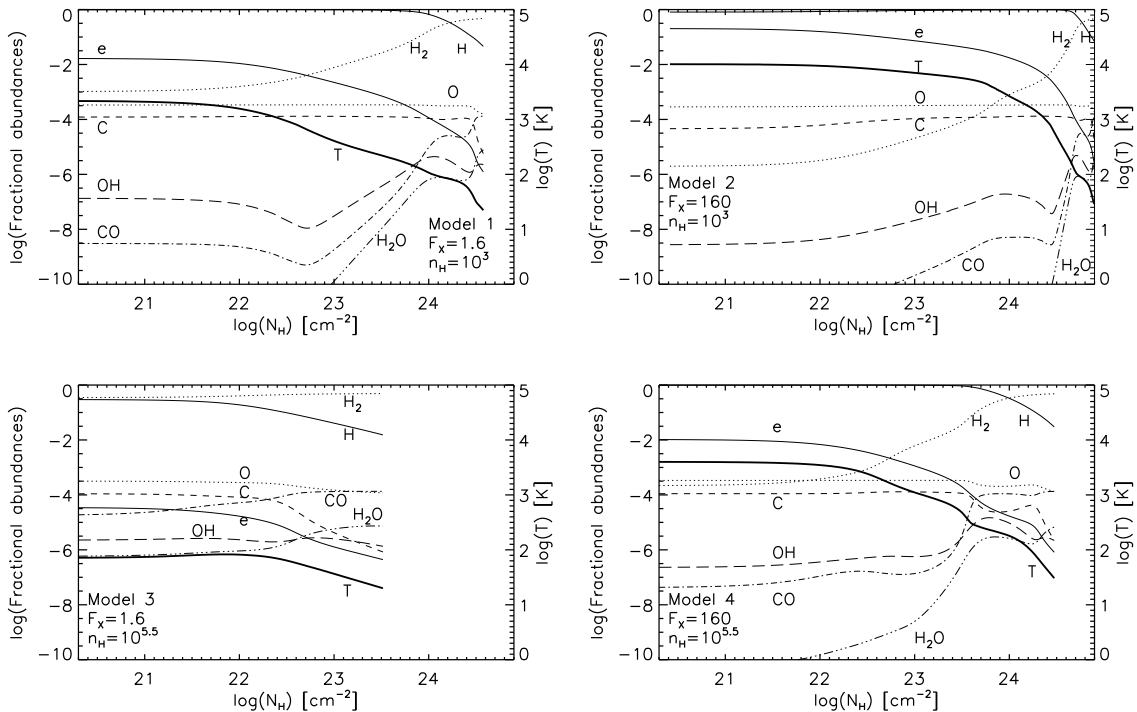


Figure 6.5: Fractional abundances and temperature for Model 1 (top left), 2 (top right), 3 (bottom left) and 4 (bottom right).

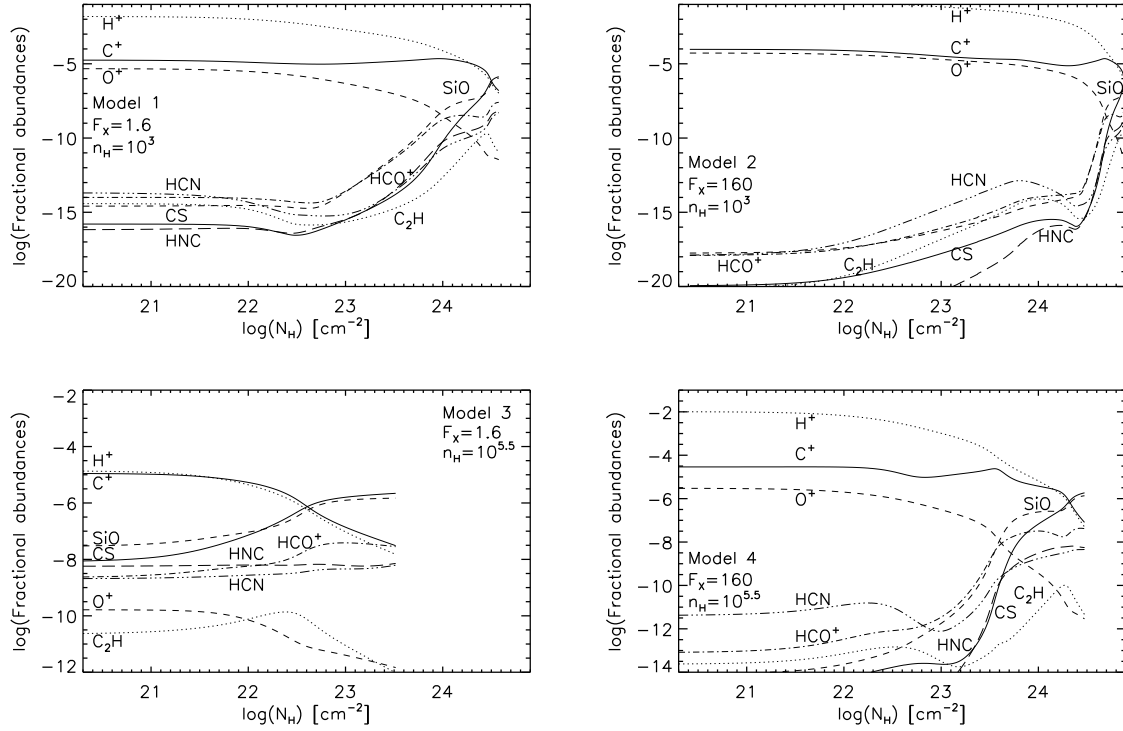


Figure 6.6: Fractional abundances for Models 1 (top left), 2 (top right), 3 (bottom left) and 4 (bottom right).

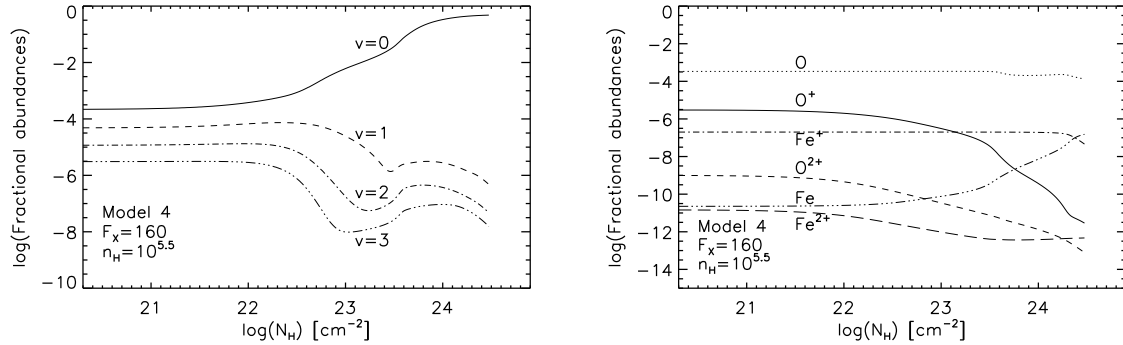


Figure 6.7: Left: The abundances of H_2 vibrational levels $v = 0, 1, 2$ and 3 . Right: The abundance of O, O^+, O^{2+}, Fe, Fe^+ and Fe^{2+}

6.3.4 Chemistry

In Figs. 6.5 and 6.6, we show the fractional abundances of selected species. H_X/n is not only important in the thermal balance, but also in the chemistry. Therefore Models 1 and 4 with about the same incident H_X/n , show similar abundances. The most striking difference with the PDR models is that there is no longer a well-defined transition layer $C^+ \rightarrow C \rightarrow CO$ present. On the contrary, both C and C^+ are present throughout most of

the cloud having fractional abundances of $\sim 10^{-5} - 10^{-4}$. Only at very low H_X/n , which results in a low temperature, there is a partial transition to CO. The transition from atomic to molecular hydrogen is much more gradual than in the PDR models. A considerable amount of OH is present in all models at all column densities. The temperature determined by H_X/n is important. In Model 3, OH has the largest abundance ($> 10^{-6}$) at all column densities. In other models such large fractions are seen only at very high depths into the cloud. The formation of CO and H₂O is most efficient at high densities and low H_X/n . Therefore, these species have large abundances throughout the high-density, low-radiation field Model 3. In Model 4, where the radiation field is somewhat higher, CO and H₂O reach large abundances only at high N_H . At low densities, they are only formed at large depths into the cloud (Models 1 and 2). Secondary ionizations are most important for the production of H⁺. Recombination is slower at lower densities. Therefore, the H⁺ fractional abundance is highest in Model 4. HCN, HCO⁺, HNC, C₂H, CS and SiO have much larger abundances at high temperatures than in the PDR models.

In Fig. 6.7, the abundances of H₂ vibrational levels $v = 0, 1, 2$ and 3 are shown in order to illustrate that also at low temperatures considerable amounts of vibrationally excited H₂ are present due to non-thermal excitation. The abundances are constant to a column density of $N_H \sim 5 \times 10^{22} \text{ cm}^{-2}$. Then the temperature goes down while the transition from atomic to molecular hydrogen starts. First, the abundances of the excited levels decrease. The rise of H₂ abundance counteracts this and around $N_H \sim 5 \times 10^{23} \text{ cm}^{-2}$, somewhat before the H/H₂ transition, another maximum is reached. In the same figure the abundances of O, O⁺, O²⁺, Fe, Fe⁺ and Fe⁺⁺ are shown. This illustrates that oxygen is easily neutralized, while almost all iron is singly ionized throughout the cloud.

6.4 Conclusion

We conclude this chapter by a direct comparison between the PDR and XDR models. To emphasize that XDRs penetrate much deeper into cloud volumes than PDRs, we use the same scale for all models. Then, it is also possible to distinguish between gradients in abundance, cumulative intensity, column density and column density ratios. XDR Model 3 is only plotted to $N_H \approx 10^{23.5} \text{ cm}^{-2}$, since H_X/n becomes too small and no reliable results are obtained at higher column densities.

In Fig. 6.8, we show for Model 4 the abundances of selected species. At the edge, both neutral and ionized species are more abundant in the XDR models, and the relative abundances also differ with respect to one another. In the XDR for example, the neutral species CH and CH₂ are more abundant than CH⁺ and CH₂⁺, respectively. In the PDR, this is the other way around. CN and CN⁺ are almost equally abundant at the edge in the PDR, while CN exceeds CN⁺ by three orders of magnitude in the XDR. Although the amounts of CS⁺ and HCS⁺ are larger than those for CS and HCS, respectively, at the edge of the cloud in the XDR, the abundance difference is less than in the PDR. The abundance of He⁺ is five orders of magnitude larger in the XDR, due to secondary ionizations. H⁻ is enhanced by three orders of magnitude, due to the higher ionization degree. It is also easily seen that in PDRs the fractional abundances vary over many orders of magnitude, while the abundances in XDR Model 4 stay almost constant to a column

density of $N_{\text{H}} \approx 10^{22} \text{ cm}^{-2}$, where the transition from H to H_2 starts.

In Figs. 6.9 and 6.10, we show cumulative line intensities for fine-structure lines at every column density, i.e., the emergent intensity arising from the edge of the cloud to column density $N_{\text{H}} = n_{\text{H}}z$:

$$I(z) = \frac{1}{2\pi} \int_0^z \Lambda(z') dz'. \quad (6.1)$$

Although the total [CII] 158 μm line intensity is higher in the XDR, the flux originating from the edge to $N_{\text{H}} \approx 10^{22} \text{ cm}^{-2}$ is higher in the PDR except when the XDR is characterized by very high H_X/n values which is the case in Model 2. In all PDR models, all carbon is in C^+ at the edge, while a large part of the carbon is neutral in XDR Models 1,3 and 4. In all models, oxygen is mostly in atomic form. The [OI] 63 μm line intensity to $N_{\text{H}} \approx 10^{22} \text{ cm}^{-2}$ is larger in the low-density XDR models, which is due to the higher heating rate. The intensity is lower in the low radiation, high density XDR Model 3, since the temperature is higher in the PDR. For Model 4 they are about the same, since the density where the line gets thermalized is almost reached. In the XDR, all line intensities increase more or less steadily with increasing column density. PDRs, however, primarily affect cloud surfaces causing more sudden changes. The PDR line intensities of [CI] 609 μm and 369 μm arise from a more or less well defined part of the cloud and start to increase at column densities $N_{\text{H}} \geq 10^{21.5} \text{ cm}^{-2}$. The line intensities of [CII] 158 μm are larger than those of [SiII] 35 μm in the PDRs except in Model 4. This is in contrast to the XDR models, where the [SiII] 35 μm line intensity is always stronger. The fact that [SiII] 35 μm lines are quite strong in XDRs was already noted by Maloney et al. (1996). The line intensities for [FeII] 26 μm and 35 μm are larger for the XDR models except again for Model 3.

In Figs. 6.11 and 6.12, we show cumulative column densities for selected species. They illustrate again that XDRs affect whole cloud volumes and PDRs create layered structures. In PDRs, the increase in column densities are very sudden for all species. For example, C and CO show this due to the very distinct $\text{C}^+/\text{C}/\text{CO}$ transition. In the XDRs, however, the increases in column density are much more gradual. The only sudden change in XDRs is where the H/H_2 transition occurs.

In Fig. 6.13, the cumulative column density ratios for CO/H_2 , CO/C , HNC/HCN , and HCO^+/HCN are shown as a function of total hydrogen column density. The ratios for the XDRs are almost constant up to $N_{\text{H}} \approx 10^{22} \text{ cm}^{-2}$, unlike those in PDR models. In PDRs, CO/C ratios increase by approximately four orders of magnitude from the edge ($\leq 10^{-4}$) to $N_{\text{H}} = 10^{22.3} \text{ cm}^{-2}$ (≥ 1). In XDRs, this ratio is constant to $N_{\text{H}} \approx 10^{22} \text{ cm}^{-2}$ and then increases slowly. For each cloud size, while keeping the energy input the same, CO/C ratios increase at higher densities. The ratios go down for higher radiation fields. For the same density and energy input, CO/C is lower when the cloud is irradiated by X-ray photons, with the exception of Model 3 where this is only valid at $N_{\text{H}} > 10^{21.7} \text{ cm}^{-2}$. CO/H_2 is somewhat more complex. When only the energy input is increased in PDRs, this ratio is higher when $N_{\text{H}} < 10^{21} \text{ cm}^{-2}$. For $N_{\text{H}} = 10^{22.3} \text{ cm}^{-2}$, the ratios are about the same. There is also a minimum where the H/H_2 transition occurs. This minimum is more prominent for higher radiation fields. In XDRs, the CO/H_2 ratio is lower when

the radiation field is higher. In PDRs and XDRs, the CO/H₂ ratios are higher when the density is increased. When the cloud is irradiated by X-ray photons, CO/H₂ ratios are lower, with the exception of Model 3 again at $N_{\text{H}} < 10^{21.5} \text{ cm}^{-2}$. In PDR Models 1, 2 and 3, significant column densities for HCN, HNC and HCO⁺ are reached between $N_{\text{H}} = 10^{21.5}$ and 10^{22} cm^{-2} . Therefore, the HNC/HCN and HCO⁺/HCN ratios discussed are for column densities $N_{\text{H}} > 10^{22} \text{ cm}^{-2}$. In PDRs, HNC/HCN is lower when the density is higher. No significant changes are seen for different radiation fields at these columns. HNC/HCN is generally lower for high H_X/n in XDRs. At high column densities, where H_X/n is low, HNC/HCN ratios are larger than unity and higher than those for the PDR. HCO⁺/HCN and HNC/HCN are of the same order in PDRs, but in XDRs HCO⁺/HCN is higher in most cases.

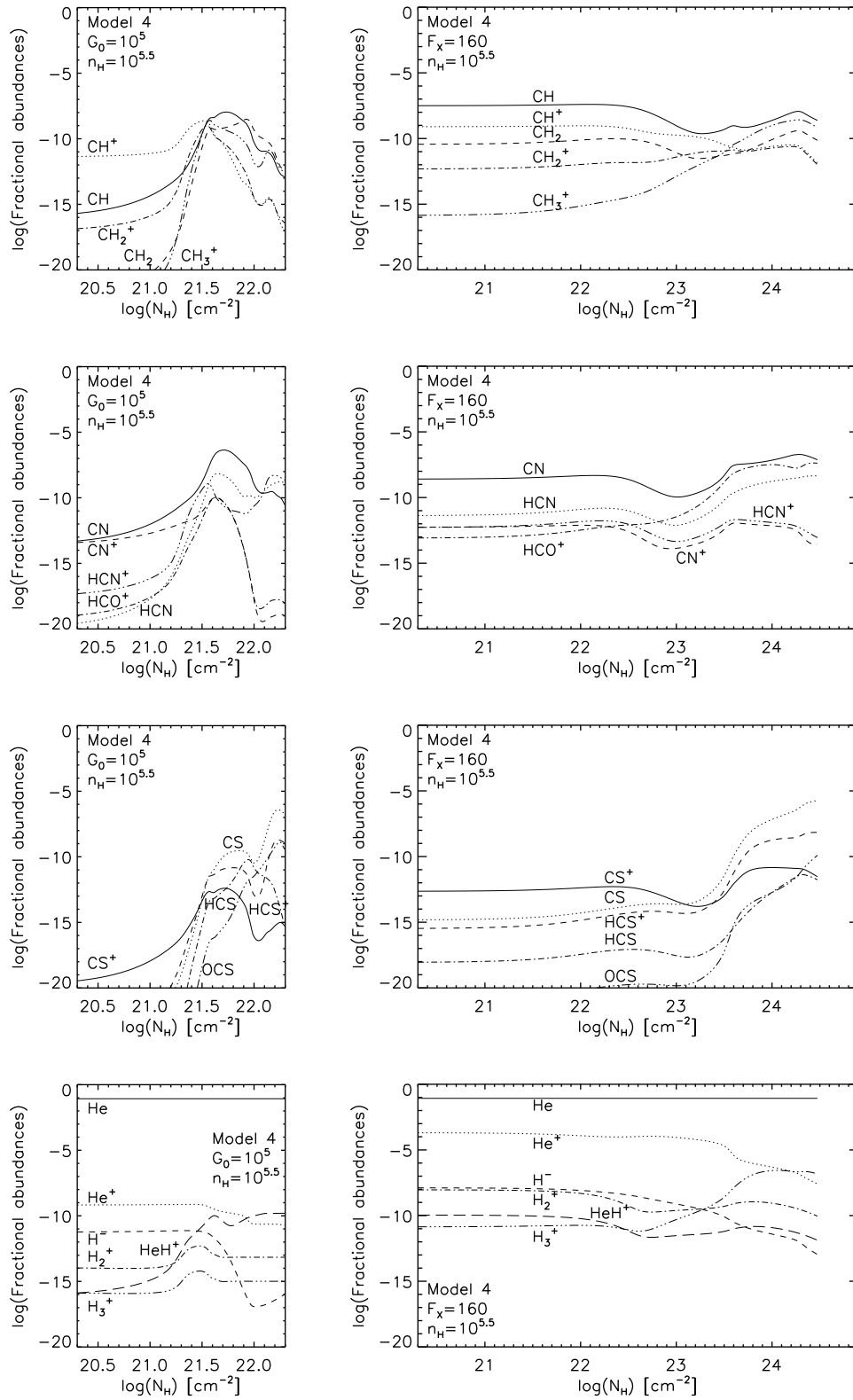


Figure 6.8: Comparison between the fractional abundances in the PDR (left) and XDR (right) for Model 4.

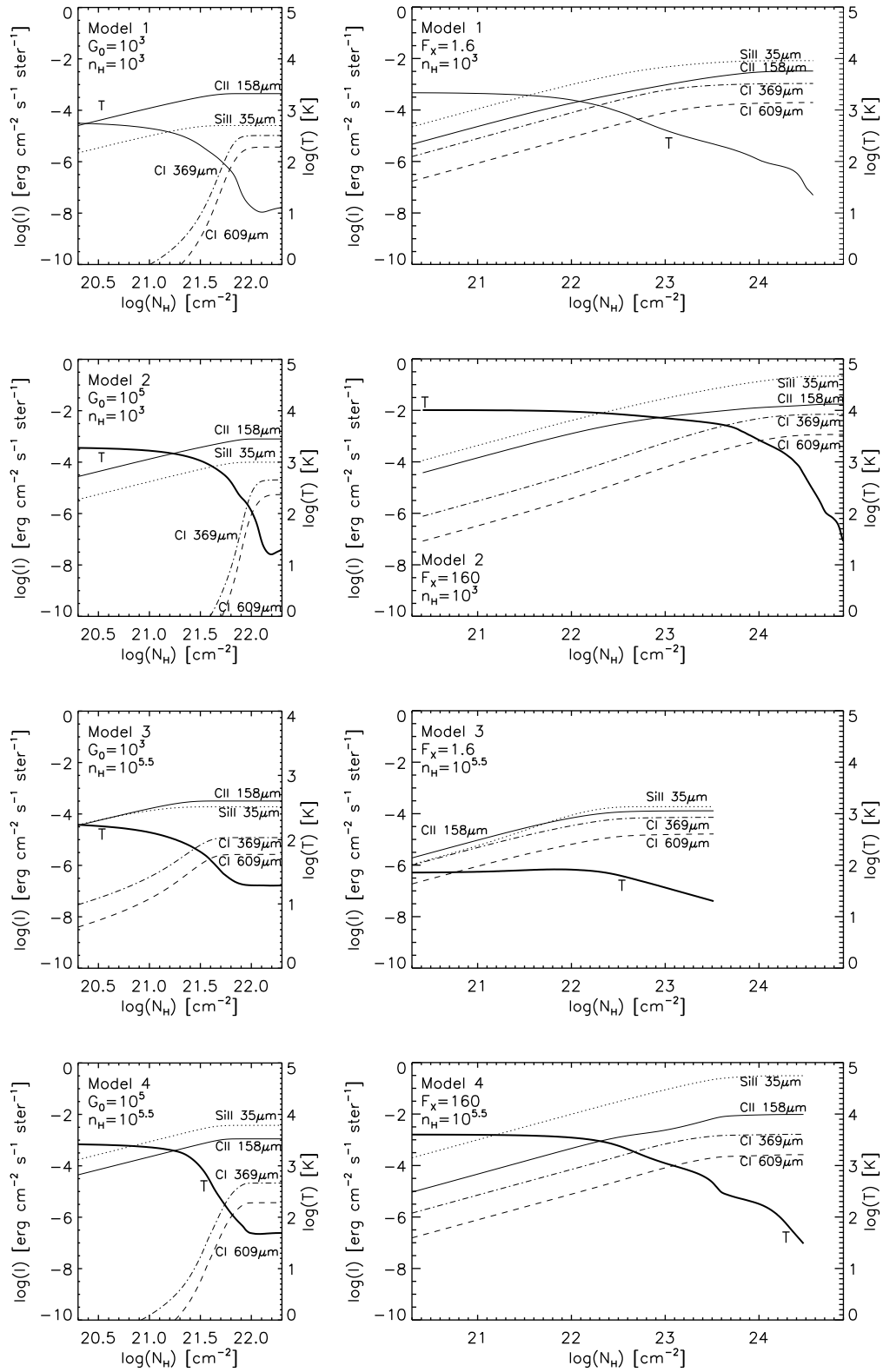


Figure 6.9: Cumulative line intensities of [CII] 158 (solid), [SiII] 34.8 (dotted), [CI] 609 (dashed) and 369 μm (dash-dotted), for PDR (left) and XDR (right) models.

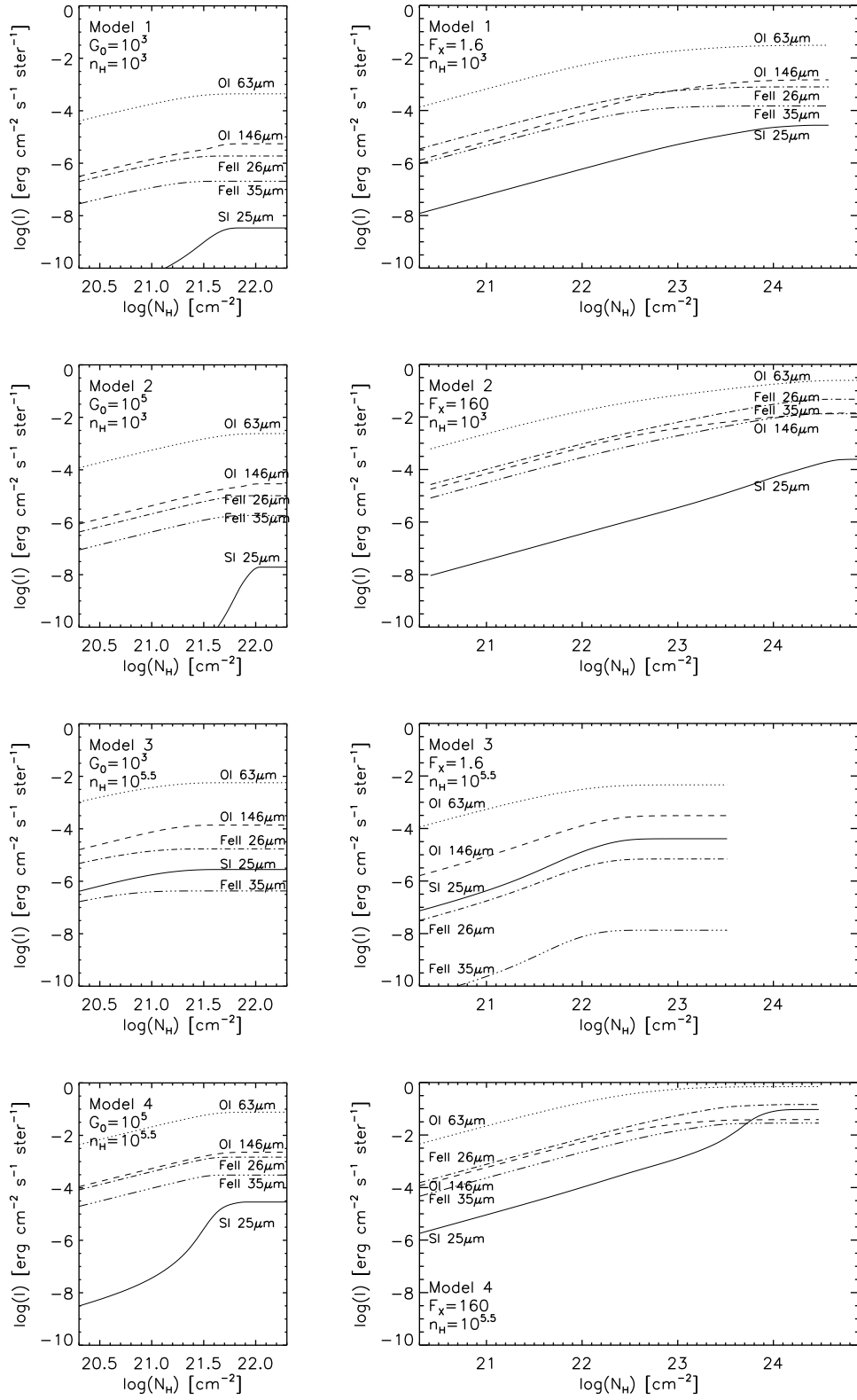


Figure 6.10: Cumulative line intensities of [SI] 25.2 (solid), [OI] 63.2 (dotted), 145.6 (dashed), [FeII] 26.0 (dot-dashed) and 35.4 μm (dotted-dashed), for PDR (left) and XDR (right) models.

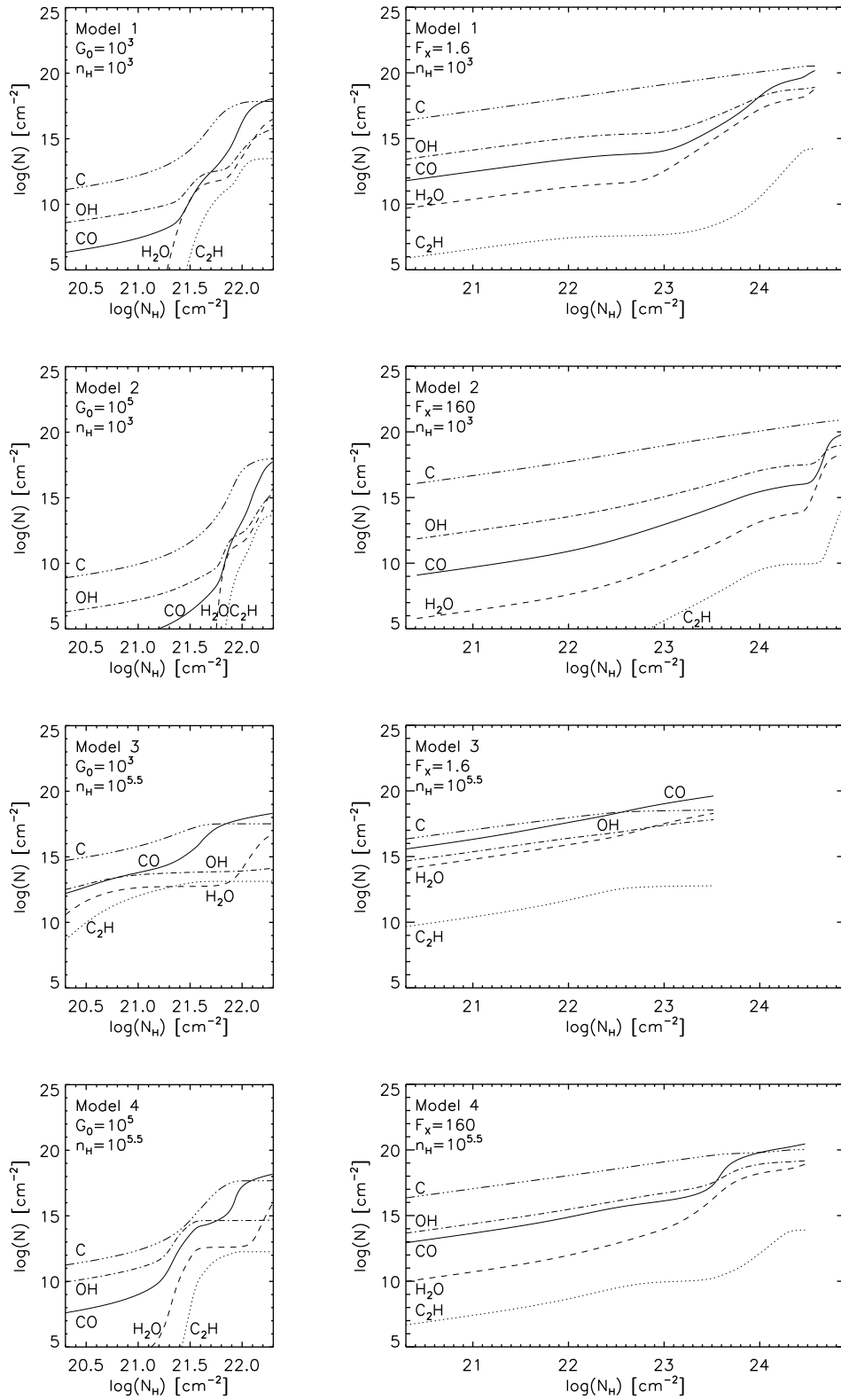


Figure 6.11: Cumulative column densities of C (dotted-dashed), CO (solid), C₂H (dotted), H₂O (dashed) and OH (dot-dashed), for PDR (left) and XDR (right) models.

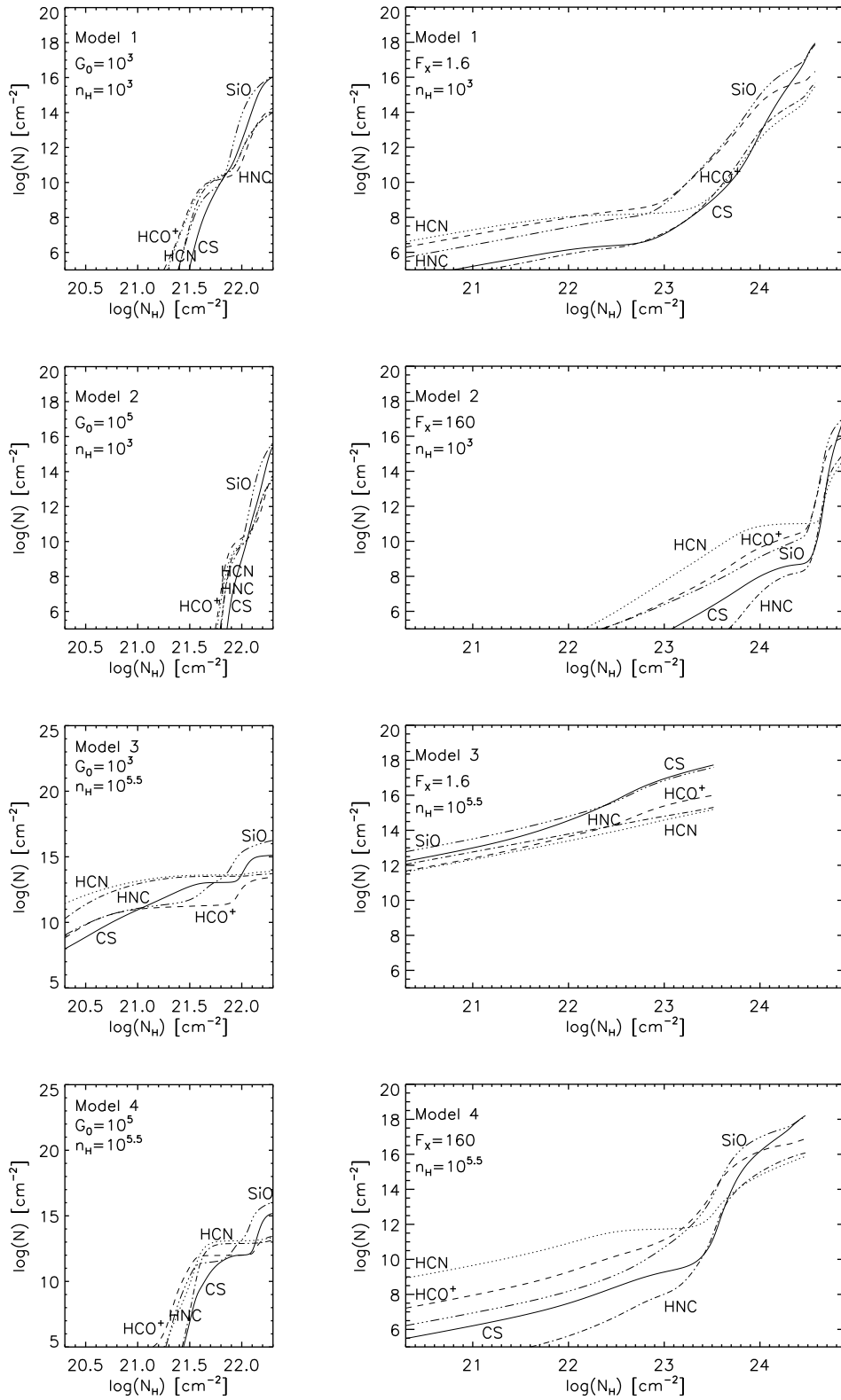


Figure 6.12: Cumulative column densities of CS (solid), HCN (dotted), HCO⁺ (dashed), HNC (dot-dashed) and SiO (dotted-dashed), for PDR (left) and XDR (right) models.

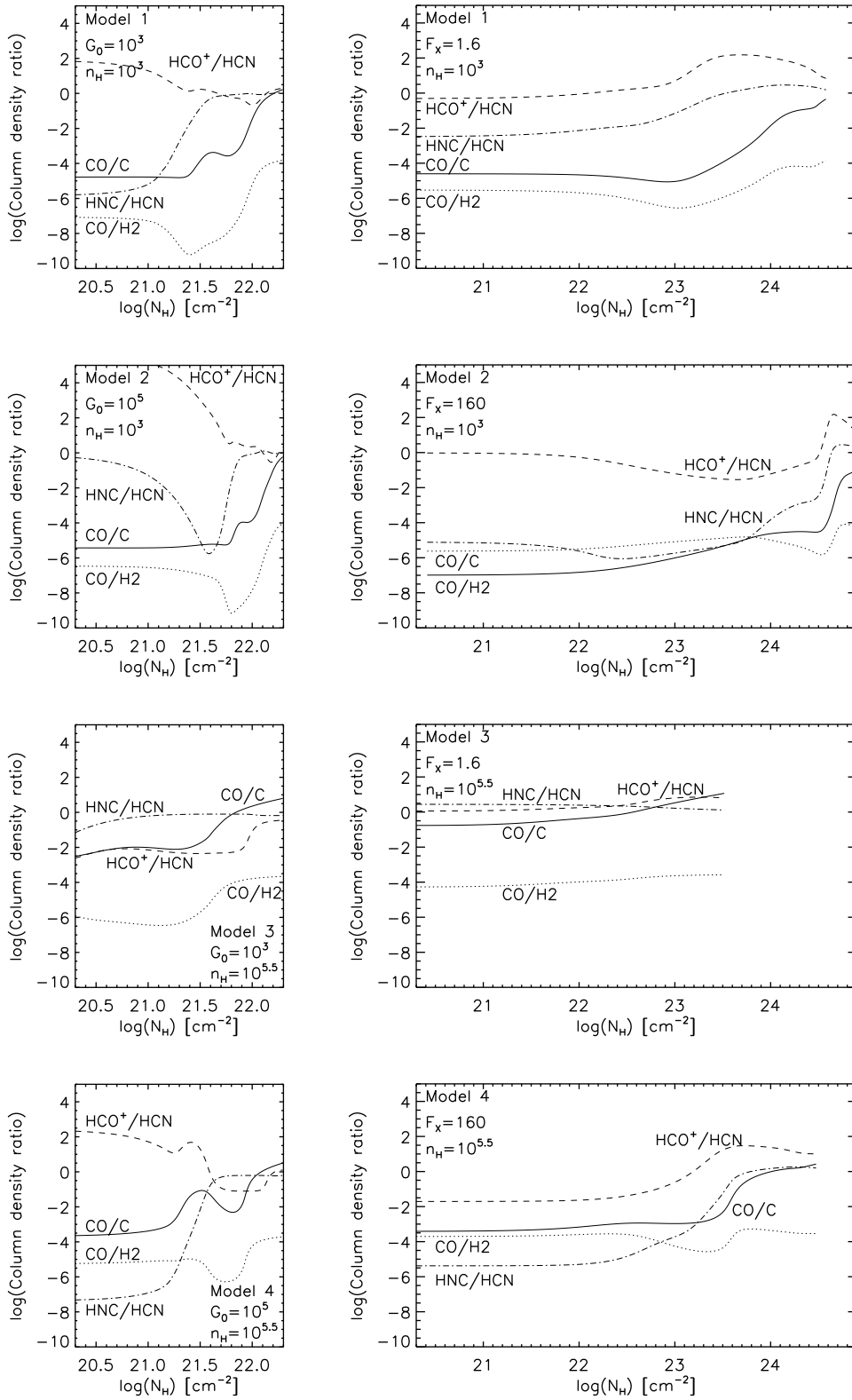


Figure 6.13: Column density ratios CO/C (solid), CO/H₂ (dotted), HCO⁺/HCN (dashed) and HNC/HCN (dot-dashed), for PDR (left) and XDR (right) models.

CHAPTER 7

Comparison to other PDR codes

We present a comparison between independent computer codes that model the physics and chemistry of photon dominated regions (PDRs). A number of benchmark models are calculated, covering low and high gas densities n and far ultraviolet intensities χ (FUV: $6 < h\nu < 13.6$ eV). χ is in units of the Draine (1978) field, where $\chi = G_0/1.71$. The benchmark models are computed in two ways: one set assuming constant temperatures, thus testing the consistency of the chemical network and photo-reactions, and a second set determining the temperature self-consistently by solving the thermal balance, thus testing the modeling of the heating and cooling mechanisms accounting for the detailed energy balance throughout the clouds. Our goal is to understand the mutual differences in the PDR codes and their effects on the physical and chemical structure of the model clouds, and to converge the output of different codes to a common solution. We identify a number of key processes that govern the chemical network and which are treated differently in the various codes, such as the contribution of PAHs to the electron density or the temperature dependence of the dissociation of CO by cosmic ray induced secondary photons, and formulate and define a proper common treatment. By understanding the impact of the PDR geometry we agree on how to compare the results from spherical and plane-parallel PDR models. As a result from the benchmark calculations we establish a comprehensive set of reference models for ongoing and future PDR modeling. We conclude that the benchmark results from the PDR code, which is described in Chapters 5 and 6, compare very well with the results obtained by other participating codes.

This chapter contains selected parts from:

M. Röllig, N. P. Abel, T. Bell, F. Bensch, J. Black, G. J. Ferland, B. Jonkheid, I. Kamp, M.J. Kaufman, J. Le Bourlot, F. Le Petit, R. Meijerink, O. Morata Chirivella, V. Ossenkopf, E. Roueff, G. Shaw, M. Spaans, A. Sternberg, J. Stutzki, W.-F. Thi, E. F. van Dishoeck, P. A. M. van Hoof, S. Viti, M.G. Wolfire
Astronomy & Astrophysics, submitted

7.1 Introduction

Theoretical models that address the structure of PDRs have been available for approximately 30 years and have evolved into advanced computer codes that account for a growing number of physical effects with increasing accuracy. The model setups vary greatly among different model codes. This includes the assumed model geometry, their physical and chemical structure, the choice of free parameters, and other details. Consequently it is not always straightforward to directly compare the results from different PDR codes. Taking into account that there are multiple ways of implementing physical effects in numerical codes, it is obvious that the model output of different PDR codes can differ from each other. As a result, significant variations in the physical and chemical PDR structure predicted by the various PDR codes can occur. The goals of our PDR-benchmarking are:

- to understand the differences in the different code results
- to obtain (as much as possible) the same model output with every PDR code when using the same input
- to agree on the correct handling of important processes
- to identify the specific limits of applicability of the available codes

To this end, a PDR-benchmarking workshop was held at the Lorentz Center in Leiden (URL: <http://www.lorentzcenter.nl/>), Netherlands in 2004 to work jointly on these topics. Here we present the results from this workshop and the results originating from the follow-up activities.

Sect. 7.2 describes the setup of the benchmark calculations. In Sect. 7.3, the results are presented. For the detailed results of the benchmark calculations, however, we refer to the following URL: <http://www.ph1.uni-koeln.de/pdr-comparison>, where all pre- and post-benchmark results are posted, and Röllig et al. (2006). In Sect. 7.4 we discuss the results and summarize the lessons learned from the benchmark effort. For an overview of the individual code characteristics, we again refer to Röllig et al. (2006).

7.2 Description of the Benchmark Models

7.2.1 PDR Code Characteristics

A total number of 11 model codes participated in the PDR model comparison study during and after the workshop in Leiden. Table 7.1 gives an overview of these codes. The codes are different in many aspects:

- finite and semi-infinite plane-parallel and spherical geometry, disk geometry
- chemistry: steady state vs. time-dependent, different chemical reaction rates, chemical network

- IR and FUV radiative transfer (effective or explicitly wavelength dependent), shielding, atomic and molecular rate coefficients
- treatment of dust and PAHs
- treatment of gas heating and cooling
- range of input parameters
- model output
- numerical treatment, gridding, etc.

This manifold in physical, chemical and technical differences makes it difficult to compare directly results from the different codes. Thus we try to standardize the computation

Table 7.1: List of participating codes. See the appendix in Röllig et al. (2006) for a short description of the individual models.

Model Name	Authors
Aikawa	H.-H. Lee, E. Herbst, G. Pineau des Forêts, J. Le Bourlot, Y. Aikawa, N. Kuboi (Lee et al. 1996)
Cloudy	G. J. Ferland, P. van Hoof, N. P. Abel, G. Shaw (Ferland et al. 1998; Abel et al. 2005)
COSTAR	I. Kamp, F. Bertoldi, G.-J. van Zadelhoff (Kamp & Bertoldi 2000; Kamp & van Zadelhoff 2001)
HTBKW	D. Hollenbach, A.G.G.M. Tielens, M.G. Burton, M.J. Kaufman, M.G. Wolfire (Tielens & Hollenbach 1985; Kaufman et al. 1999; Wolfire et al. 2003)
KOSMA- τ	H. Störzer, J. Stutzki, A. Sternberg (Stoerzer et al. 1996), B. Köster, M. Zielinsky, U. Leuenhagen (Bensch et al. 2003; Röllig et al. 2006)
Lee96mod	H.-H. Lee, E. Herbst, G. Pineau des Forêts, E. Roueff, J. Le Bourlot, O. Morata (Lee et al. 1996)
Leiden	J. Black, E. van Dishoeck, D. Jansen and B. Jonkheid (Black & van Dishoeck 1987; van Dishoeck & Black 1988; Jansen et al. 1995)
Meijerink	R. Meijerink, M. Spaans (Meijerink & Spaans 2005)
Meudon	J. Le Bourlot, E. Roueff, F. Le Petit (Le Petit et al. 2006, 2002; Le Bourlot et al. 1993)
Sternberg	A. Sternberg, A. Dalgarno (Sternberg & Dalgarno 1995; Sternberg & Neufeld 1999)
UCL_PDR	S. Viti, W.-F. Thi, T. Bell (Taylor et al. 1993; Papadopoulos et al. 2002)

of the benchmark model clouds as much as possible. This requires all codes to reduce their complexity and sophistication, often beyond what their authors consider to be acceptable, considering detailed knowledge of some of the physical processes. However, as the main goal of this study is to understand why and how these codes differ these simplifications are acceptable. Our aim is not to provide the most realistic model of real astronomical objects. The individual strengths (and weaknesses) of each PDR code are briefly summarized in the appendix given in Röllig et al. (2006) and on the website: <http://www.ph1.uni-koeln.de/pdr-comparison>.

7.2.2 Benchmark Frame and Input Values

A total of 8 different model clouds are agreed upon for the benchmark comparison. The density and FUV parameter space is covered exemplarily by accounting for low and high densities and FUV fields under isothermal conditions, giving 4 different model clouds. The complexity of the model calculations is reduced by setting the gas and dust temperatures to a given constant value (models F1-F4, 'F' denoting a fixed temperature), making the results independent of the solution of the local energy balance. In a second benchmark set, the thermal balance is solved explicitly thus determining the temperature profile of the cloud (models V1-V4, 'V' denoting variable temperatures). Table 7.2 gives an overview of the cloud parameter of all eight benchmark clouds.

Table 7.2: Specification of the model clouds computed during the benchmark. The models F1-F4 have constant gas and dust temperatures, while V1-V4 have their temperatures calculated self-consistently.

F1 T=const=50 K $n = 10^3 \text{ cm}^{-3}, \chi = 10$	F2 T=const=50 K $n = 10^3 \text{ cm}^{-3}, \chi = 10^5$
F3 T=const=50 K $n = 10^{5.5} \text{ cm}^{-3}, \chi = 10$	F4 T=const=50 K $n = 10^{5.5} \text{ cm}^{-3}, \chi = 10^5$
V1 T=variable $n = 10^3 \text{ cm}^{-3}, \chi = 10$	V2 T=variable $n = 10^3 \text{ cm}^{-3}, \chi = 10^5$
V3 T=variable $n = 10^{5.5} \text{ cm}^{-3}, \chi = 10$	V4 T=variable $n = 10^{5.5} \text{ cm}^{-3}, \chi = 10^5$

Benchmark Chemistry

One of the crucial steps in arriving at a useful code comparison is to agree on the use of a standardized set of chemical species and reactions to be accounted for in the benchmark calculations. For the benchmark models we include only the four most abundant

elements H, He, O and C. Additionally, only the species given in Table 7.3 are included in the chemical network calculations.

Table 7.3: Chemical content of the benchmark calculations.

Chemical species in the models
H, H ⁺ , H ₂ , H ₂ ⁺ , H ₃ ⁺
O, O ⁺ , OH ⁺ , OH, O ₂ , O ₂ ⁺ , H ₂ O, H ₂ O ⁺ , H ₃ O ⁺
C, C ⁺ , CH, CH ⁺ , CH ₂ , CH ₂ ⁺ , CH ₃ ,
CH ₃ ⁺ , CH ₄ , CH ₄ ⁺ , CH ₅ ⁺ , CO, CO ⁺ , HCO ⁺
He, He ⁺ , e ⁻

The chemical reaction rates are taken from the UMIST99 database (Le Teuff et al. 2000) together with some corrections suggested by A. Sternberg. The complete reaction rate file is available on-line (<http://www.ph1.uni-koeln.de/pdr-comparison>). To reduce the overall modeling complexity PAHs are neglected in the chemical network and are only considered for the photoelectric heating (photoelectric heating efficiency as given by Bakes & Tielens 1994) in models V1-V4. Codes which calculate time-dependent chemistry use a suitably long time-scale in order to reach steady state.

Benchmark Geometry

All model clouds are plane-parallel, semi-infinite clouds of constant total hydrogen density $n = n(\text{H}) + 2n(\text{H}_2)$. Spherical codes approximate this by assuming a very large radius for the cloud. All groups deliver stationary solutions, thus integrating up to $t = 10^8$ yrs for time-dependent codes.

Physical Specifications

As many model parameters as possible are agreed upon at the start of the benchmark calculations, to avoid initial confusion in comparing model results. To this end we set most crucial model parameters to the following values: the value for the standard UV field is taken as $\chi = 10$ and 10^5 times the Draine (1978) field. For a semi-infinite plane parallel cloud the CO dissociation rate at the cloud surface for $\chi = 10$ should equal 10^{-9} s^{-1} , using this for optically thin conditions (for which a point is exposed to the full 4π steradians as opposed to just 2π at the cloud surface) the CO dissociation rate is $2 \times 10^{-10} \text{ s}^{-1}$ for a unit Draine field. The cosmic ray H ionization rate is assumed to be $\zeta = 5 \times 10^{-17} \text{ s}^{-1}$ and the visual extinction $A_V = 6.289 \times 10^{-22} N_{\text{H,tot}}$. If the codes do not explicitly calculate the unattenuated H₂ photo-dissociation rates (by summing over oscillator strengths etc.) we assume that the unattenuated H₂ photo-dissociation rate in a unit Draine field is equal to $5.18 \times 10^{-11} \text{ s}^{-1}$, so that at the surface of a semi-infinite cloud for 10 times the Draine field the H₂ dissociation rate is $2.59 \times 10^{-10} \text{ s}^{-1}$. For the dust attenuation factor in the H₂ dissociation rate we assume $\exp(-k A_V)$ if not treated

explicitly wavelength dependent. The value $k = 3.02$ is representative for the effective opacity in the 912-1110 Å range. We use a very simple H₂ formation rate coefficient $R = 3 \times 10^{-18} T^{1/2} = 2.121 \times 10^{-17} \text{ cm}^3 \text{ s}^{-1}$ at $T = 50 \text{ K}$, assuming that every hitting atom sticks to the grain and reacts to form H₂. A summary of the most important model parameters is given in Table 7.4.

Table 7.4: Overview of the most important model parameter. All abundances are given w.r.t. total H abundance.

Model Parameters		
A_{He}	0.1	elemental He abundance
A_{O}	3×10^{-4}	elemental O abundance
A_{C}	1×10^{-4}	elemental C abundance
ζ_{CR}	$5 \times 10^{-17} \text{ s}^{-1}$	CR ionization rate
A_{V}	$6.289 \times 10^{-22} N_{\text{H}_{\text{total}}}$	visual extinction
τ_{UV}	$3.02 A_{\text{v}}$	FUV dust attenuation
v_b	1 km s^{-1}	Doppler width
D_{H_2}	$5 \times 10^{-18} \text{ s}^{-1}$	H ₂ dissociation rate
R	$3 \times 10^{-18} T^{1/2} \text{ cm}^3 \text{ s}^{-1}$	H ₂ formation rate
$T_{\text{gas,fix}}$	50 K	gas temperature (for F1-F4)
$T_{\text{dust,fix}}$	20 K	dust temperature (for F1-F4)
n	$10^3, 10^{5.5} \text{ cm}^{-3}$	total density
χ	$10, 10^5$	FUV intensity w.r.t. Draine (1978) field

7.3 Results

There are two stages for the benchmarking results, the pre- and post-benchmark, which are all posted at <http://www.ph1.uni-koeln.de/pdr-comparison>. The impact of the benchmark effort is illustrated by considering the well known C⁺/C/CO transition. Before the benchmark a significant scatter is seen in the C⁺, C and CO abundances. This scatter is mostly gone at the end of the workshop. Most of the deviations can be attributed to bugs in the pre-benchmark codes, misunderstandings, or to incorrect geometrical factors (e.g. 2π vs. 4π). In Fig. 7.1 it is shown how well the different PDR codes compare by showing the Post-Benchmark results for the C⁺/C/CO transition of model V2.

The restrictions artificially posed by the benchmark standards limit the capacity of the participating model codes. For example, some models encounter major numerical difficulties in reaching a stable temperature solution for the benchmark models V4, mainly caused by the diverging H₂ formation rate at high temperatures that results in a diverging H₂ formation heating. Other codes also show similar numerical problems especially for

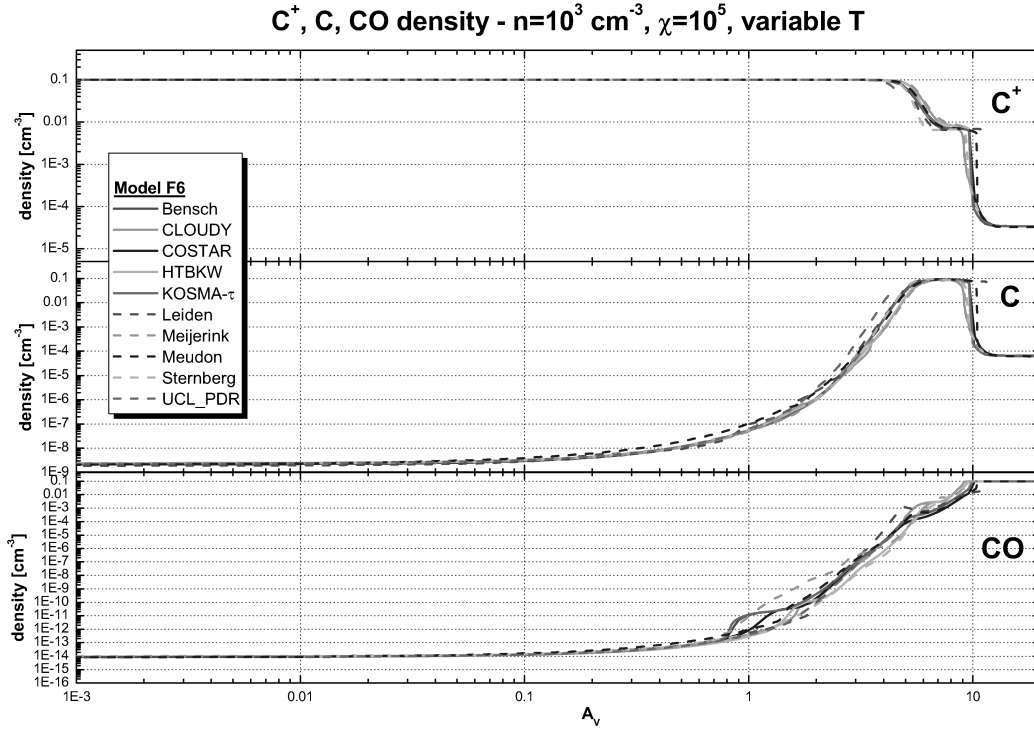
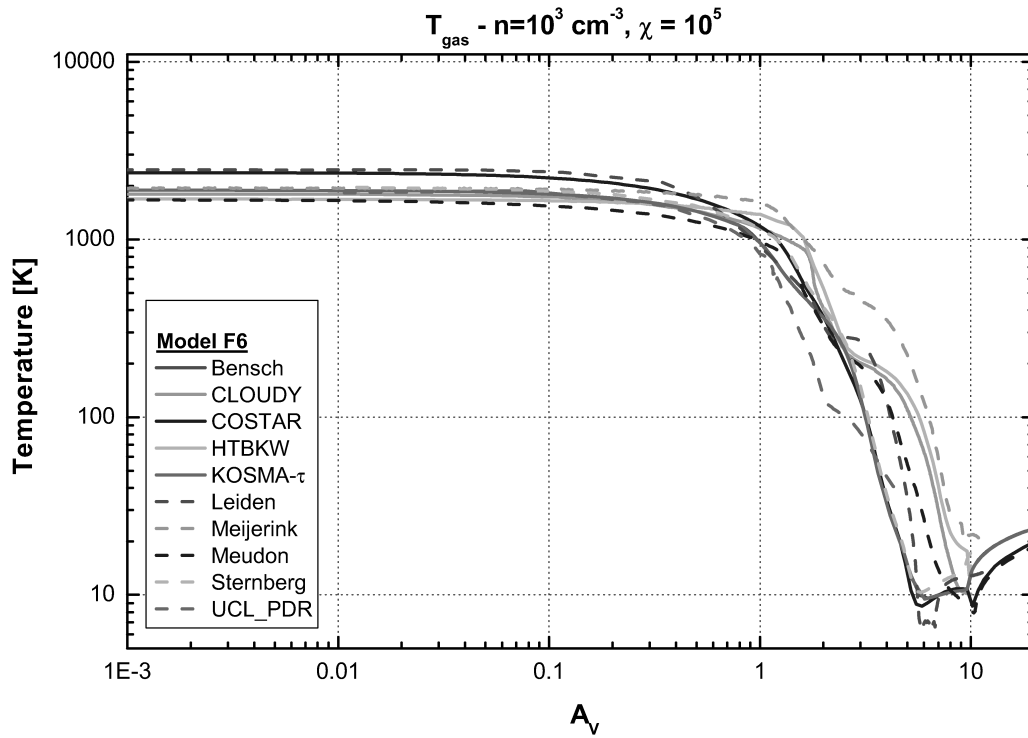


Figure 7.1: Temperature structure and $\text{C}^+/\text{C}/\text{CO}$ transition for model V2.

the model V4. This numerical noise vanishes when we apply more physical conditions. Nevertheless, it is very instructive to study the codes under these extreme conditions. In Fig. 7.1, we show the Post-Benchmark temperature structure for model V2. Here, we find that still significant differences between the PDR codes.

For a detailed discussion of the PDR model comparison, we refer to Sect. 5 of Röllig et al. (2006).

7.4 Concluding remarks

7.4.1 Meijerink & Spaans code

The PDR code as described in Chapters 5 and 6 (Meijerink & Spaans 2005) also participated in the PDR comparison test. We (Meijerink & Spaans) experienced the workshop as very instructive, and learned much about the influences of the various involved processes on the thermal and chemical balance. We found that the results before the benchmark test were already quite promising. This was very encouraging, especially since the development of the code started only one year earlier. During the benchmark test, we discovered some minor bugs, which were subsequently removed. After the benchmark test, the code results compare quite well to those obtained with other participating codes.

The complexity of our code is much less than that of some other codes (e.g., Cloudy). For example, H₂ and CO shielding are treated in a one line approximation, while some codes use multiple lines. An advantage is that we are able to calculate models for a rather large parameter space in a very short time. A drawback is that we cannot determine the precise H/H₂ transition of the cloud. However, we are interested in the *integrated* atomic and molecular line ratios and these are not very sensitive to the details of the H/H₂ transition in the cloud.

7.4.2 All codes

The major general results of this study are:

- The collected results from all participating models represent an excellent reference for all present PDR codes and for those to be developed in the future. For the first time such a reference is easily available not only in graphical form but also as raw data: URL: <http://www.ph1.uni-koeln.de/pdr-comparison>.
- We present an overview of the common PDR model codes and summarize their properties and field of application.
- As a natural result all participating PDR codes are now better debugged, much better understood, and many differences between the results from different groups are now much clearer resulting in good guidance for further improvements.
- Many critical parameters, model properties and physical processes have been identified or understood better in the course of this study.

- We have been able to increase the agreement in model predictions for all benchmark models. Uncertainties still remain, visible, e.g., in the deviating temperature profiles of model V2 or the large differences for the H₂ photo-rates and density profiles in model V4 (cf. on-line data archive).
- All PDR models are heavily dependent on the chemistry and micro-physics involved in PDRs. Consequently, the results from PDR models are only as reliable as the description of the microphysics (rate coefficients, etc.) that they are based on.

One of the lessons from this study is that observers should not take the PDR results too literally to constrain, for example, physical parameters like density and radiation field in the region they observe. The current benchmarking shows that the relative trends are consistent between codes but that there remain differences in absolute values of observables. Moreover, it is not possible to simply infer how detailed differences in density or temperature translate into differences in observables. They are the result of a complex, nonlinear interplay between density, temperature, and radiative transfer. We want to emphasize again that all participating PDR codes are much 'smarter' than required during the benchmark. Many sophisticated model features have been switched off in order to provide comparable results. Our motivation is technical not strictly physical. The presented results are not meant to model any real astronomical object and should not be applied as such in any analysis. The current benchmarking results are not meant as our recommended or best values, but simply as a comparison test. During this study we demonstrate that an increasing level of standardization results in a significant reduction of the model dependent scatter in PDR predictions. It is encouraging to note the overall agreement in model results. On the other hand, it is important to understand that small changes may make a big difference. We are able to identify a number of these key points, e.g., the influence of excited molecular hydrogen, or the importance of secondary photons induced by cosmic rays.

Future work should focus on the energy balance problem, clearly evident from the sometimes significant scatter in the results for the non-isothermal models V1-V4. The heating by photoelectric emission is closely related to the electron density and to the detailed description of grain charges, grain surface recombinations and photoelectric yield. The high temperature regime also requires an enlarged set of cooling processes. As a consequence we plan to continue our benchmark effort in the future. This should include a calibration on real observational findings as well.

Part III

Model applications

CHAPTER 8

A grid of PDR and XDR models

The nuclei of active galaxies harbor massive young stars, an accreting central black hole, or both. In order to determine the physical conditions that pertain to molecular gas close to the sources of radiation, numerical models are constructed. These models iteratively determine the thermal and chemical balance of molecular gas that is exposed to X-rays (1-100 keV) and far-ultraviolet radiation (6-13.6 eV), as a function of depth. We present a grid of XDR and PDR models that span ranges in density ($10^2 - 10^{6.5} \text{ cm}^{-3}$), irradiation ($10^{0.5} - 10^5 G_0$ and $F_X = 1.6 \times 10^{-2} - 160 \text{ erg cm}^{-2} \text{ s}^{-1}$) and column density ($3 \times 10^{21} - 1 \times 10^{25} \text{ cm}^{-2}$). Predictions are made for the most important atomic fine-structure lines, e.g., [CII], [OI], [CI], [SiII], and for molecular species like HCO^+ , HCN, HNC, CS and SiO up to $J = 4$, CO and ^{13}CO up to $J = 16$, and column densities for CN, CH, CH^+ , HCO, HOC^+ , NO and N_2H^+ . We find that surface temperatures are higher (lower) in PDRs compared to XDRs for densities $> 10^4$ ($< 10^4$) cm^{-3} . For the atomic lines, we find that, largely due to the different XDR ionization balance, the fine-structure line ratios of [SiII] 35 μm /[CII] 158 μm , [OI] 63 μm /[CII] 158 μm , [FeII] 26 μm /[CII] 158 μm and [CI] 369 μm /[CI] 609 μm are larger in XDRs than in PDRs, for a given density, column and irradiation strength. Similarly, for the molecular lines, we find that the line ratios HCN/HCO^+ and HNC/HCN , as well as the column density ratio CN/HCN , discriminate between PDRs and XDRs. In particular, the HCN/HCO^+ 1-0 ratio is < 1 (> 1) for XDRs (PDRs) if the density exceeds 10^5 cm^{-3} and if the column density is larger than 10^{23} cm^{-2} . For columns less than $10^{22.5} \text{ cm}^{-2}$ the XDR HCN/HCO^+ 1-0 ratio becomes larger than one, although the individual HCN 1-0 and HCO^+ 1-0 line intensities are weaker. For modest densities, $n = 10^4 - 10^5 \text{ cm}^{-3}$, and strong radiation fields ($> 100 \text{ erg s}^{-1} \text{ cm}^{-2}$), HCN/HCO^+ ratios can become larger in XDRs than PDRs as well. Also, the HCN/CO 1-0 ratio is typically smaller in XDRs, and the HCN emission in XDRs is boosted with respect to CO only for high (column) density gas, with columns in excess of 10^{23} cm^{-2} and densities larger than 10^4 cm^{-3} . Furthermore, CO is typically warmer in XDRs than in PDRs, for the same total energy input. This leads to higher CO $J=N+1-N/\text{CO}$ 1-0, $N \geq 1$, line ratios in XDRs. In particular, lines with $N \geq 10$, like CO(16-15) and CO(10-9) observable with HIFI/Herschel, discriminate very well between XDRs and PDRs. This is crucial since the XDR/AGN contribution will typically be of a much smaller (possibly beam diluted) angular scale and a 10-25% PDR contribution can already suppress XDR distinguishing features involving HCN/HCO^+ and HNC/HCN . For possible future observations, column density ratios indicate that CH, CH^+ , NO, HOC^+ and HCO are good PDR/XDR discriminators.

8.1 Introduction

The radiation that emanates from galaxy nuclei, such as those of NGC 253 and NGC 1068 or even more extreme (ultra-)luminous infrared galaxies, is believed to originate from regions with active star formation, an accretion disk around a central super-massive black hole or both (e.g. Silk 2005; Maloney 1999; Sanders & Mirabel 1996). The unambiguous identification of the central energy source, or the relative contributions from stars and an active galaxy nucleus (AGN), remains a major challenge in the study of active galaxy centers. The general aim of this paper is to determine how the properties of the irradiated interstellar medium (ISM) may further our understanding.

Unlike emission at optical wavelengths, atomic, molecular and dust emission in the far-infrared and (sub-)mm range allow one to probe deeply into the large column densities of gas and dust that occupy the centers of active galaxies. Observational studies of the ISM in galaxy centers have been presented by various authors (c.f. Aalto 2005; Baan 2005; Ott et al. 2005; Israel 2005; Spoon et al. 2001; 2003; 2005; Klöckner et al. 2003; Israel and Baas 2002; Garrett et al. 2001; Hüttemeister and Aalto 2001; Curran et al. 2000). Theoretical models show that the spectral energy distribution of the radiation representing star formation (peaking in the ultraviolet) and AGN (peaking in the X-ray regime) activity respectively influences the thermal and chemical balance of the ambient ISM in fundamentally different ways (Meijerink & Spaans 2005; Maloney, Hollenbach & Tielens 1996; Lepp & Dalgarno 1996). The specific aim of this paper is thus to study the extent to which emission from commonly observed molecular and atomic line transitions may be used as a diagnostic tool in the study of external galaxy centers to determine the ambient conditions in general, and the type of irradiation in particular.

To this effect, we have extended the chemical calculations described by Meijerink & Spaans (2005; hereafter Paper I) for ultraviolet and X-ray irradiated gas to a much larger parameter space of ambient conditions and we have performed detailed radiative transfer calculations to compute the line intensities of many atomic and molecular transitions. We refer the interested reader to Paper I for a detailed description of the combined photon-dominated region (PDR)/X-ray dominated region (XDR) code that we have used to compute the impact of ultraviolet (PDR) and X-ray (XDR) photons on nearby ISM. The results described here will be applied to observations of external galaxy centers in a subsequent paper (Meijerink et al., in preparation). Stäuber et al. (2005) also developed PDR and XDR codes, for applications to Young Stellar Objects. The main difference is that this code has a time dependent chemistry and that it includes ice evaporation at $t = 0$. This affects the chemistry compared with traditional steady-state models of pure gas-phase PDRs (e.g., CN/HCN is affected). This is not relevant for our cloud models. However, freeze-out and evaporation start to become important for clouds with density $n_{\text{H}} \geq 10^5 \text{ cm}^{-3}$.

8.2 'Standard' clouds

The current spatial resolution of sub-millimeter telescopes, such as the James Clerk Maxwell Telescope (JCMT), the Institut de Radio Astronomie Millimétrique (IRAM) telescope

Table 8.1: 'Standard' clouds

Type	$r(\text{pc})$	$n(\text{cm}^{-3})$	$N(\text{cm}^{-2})$	G_0	$F_X [\text{erg s}^{-1} \text{cm}^{-2}]$
A	1	$10^4 - 10^{6.5}$	$3 \times 10^{22} - 1 \times 10^{25}$	$10^2 - 10^5$	1.6 - 160
B	10	$10^3 - 10^4$	$3 \times 10^{22} - 3 \times 10^{23}$	$10^1 - 10^4$	$1.6 \times 10^{-1} - 16$
C	10	$10^2 - 10^3$	$3 \times 10^{21} - 3 \times 10^{22}$	$10^{0.5} - 10^3$	$1.6 \times 10^{-2} - 1.6$

and even the Combined Array for Research in Submillimeter Astronomy (CARMA) or the Submillimeter Array (SMA), is insufficient to resolve individual clouds in extragalactic sources. By using these telescopes, each resolution element thus measures the combined emission from a large ensemble of molecular clouds. As a consequence, it is frequently impossible to use a single model cloud solution to describe the observed molecular lines. Instead, more complicated solutions involving two or more model clouds, with differing densities and incident radiation fields, are needed. This contrasts with the study of Galactic objects, where usually a single model cloud solution is sufficient to fit the measurements of single resolution elements.

In this paper, we calculate a grid of 'standard' clouds sampling the different physical conditions believed to be relevant for the centers of active galaxy nuclei. In order to sample both the hierarchical size and (column) density properties of the ISM, we have chosen to construct models for a number of fixed sizes as well as densities. Note that the column densities are not the same for each model, since we use fixed cloud sizes. In these clouds, we investigate the detailed column density dependence for the line ratios HCN/CO, HNC/HCN, HCO⁺/HCN, SiO/CO and CS/HCN, which include line ratios observed in several galaxies. From our computational grid, one or more, properly weighted, models can be chosen to reproduce observed atomic and molecular lines.

We distinguish three different 'standard' clouds, each with their own characteristic combinations of size and volume density range, hence also column density (cf. Table 8.1), for which we calculate a set of models for different incident radiation fields, and where a distinction between irradiation by far-ultraviolet (FUV) and X-ray photons is made. The X-ray radiation field is a power-law distribution $F(E) = F(0)(E/1\text{keV})^{-\alpha}$ integrated between 1 and 100 keV, where $\alpha = -0.9$. This power law spectrum is generally believed to be representative for accreting black holes. Please note that this differs from Paper I, where we used a thermal distribution at 10^6 K instead. The ultraviolet radiation field (6-13.6 eV) is expressed in multiples of the Habing flux, $1.6 \times 10^{-3} \text{ erg cm}^{-2} \text{ s}^{-1}$. We use a line width $\delta_v = 2.7 \text{ km s}^{-1}$. Cloud type A represents compact, high-density environments such as molecular cloud cores, and clouds very close to active nuclei; cloud type B corresponds to more traditional molecular cloud environments, and cloud type C is representative of the more diffuse extended (molecular) medium in which clouds of type B are usually embedded.

Late-type galaxies frequently have radial metallicity gradients, with the highest metallicity in the center (Vila-Costas & Edmunds 1992; Zaritsky et al. 1994). For this reason, we have adjusted the metallicity used in Table 2 of Paper I. The published metallicity gradients and suggestions of a gradient flattening in the very center have led us to adopt a twice Solar metallicity as a reasonable value. Since [C]/[O] abundance ratios decrease

at higher metallicities, we have taken the carbon abundance equal to the oxygen abundance (see, for instance, Garnett et al. 1999; Kobulnicky & Skillman 1998). Note that the [C]/[O] ratio affects the abundances of O₂ and H₂O. See for example Spaans & van Dishoeck (2001) and especially Fig. 2 in Bergin et al. (2000).

From the models, we have calculated the intensities of the molecular rotational lines of HCN, HNC, HCO⁺, CS and SiO (upto $J = 4$), [CI], [CII], [OI], [SiIII] and other fine-structure lines. For CO and ¹³CO we calculated the intensities of the rotational lines up to $J = 16$, in order to make predictions for future observing facilities such as the ESO Herschel/HIFI space mission. We use the Leiden Atomic and Molecular Database (LAMDA) as described in Schöier et al. (2005) to retrieve the collisional data needed for the calculations. Where no collisional data are available for commonly observed molecules such as CN, CH, CH⁺, HCO, HOC⁺, NO and N₂H⁺, we only give column densities..

8.3 Surface temperatures

To illustrate the coupling differences of FUV and X-ray photons to the gas, we first discuss the surface temperatures of the low, mid, and high density models respectively over the parameter space given for the PDR and XDR models in Table 8.1. We calculated a larger range of radiation fields for the PDR models than for the XDR models, for reasons related to the heating efficiency which are discussed below. The resulting surface temperatures as a function of gas density and incident radiation intensity for both PDR and XDR models are shown in Fig. 8.1.

The most important heating mechanism at the edge of a PDR is photo-electric heating. FUV photons are absorbed by dust grains, which release electrons that lose their surplus kinetic energy to the gas by Coulomb interactions. The efficiency of this process increases, when the grains are more negatively charged, which is determined by a complex interplay of the impinging radiation field G_0 , electron density n_e and gas temperature T . The absolute efficiency is very low, since about 0.5-3 percent of the photon energy goes into gas heating. This sharply contrasts with direct X-ray heating, important at the edge of XDRs. Direct ionization of an atom yields a kinetic electron with an energy higher than 1 keV. This electron heats, ionizes and excites the gas. Depending on the H, H₂, He and electron abundances, the heating efficiency can be up to 70 percent, much higher than for photo-electric heating. However, there is an opposing effect, namely the much lower absorption cross section for X-rays. Since the cross sections scale roughly as E^{-3} , there are many fewer X-ray photons absorbed than FUV photons.

We find that at high densities ($n > 10^4 \text{ cm}^{-3}$) PDR models produce higher surface temperatures than the XDR models. At low densities, however, we find the opposite, especially in the case of high radiation fields. This is explained by the drop in the efficiency of photo-electric heating at densities $n < 10^5 \text{ cm}^{-3}$ when the same impinging radiation field is considered. This is nicely illustrated in Fig. 6 of Kaufman et al. (1999), where the ratios of the intensity of the [CII] 158 μm and [OI] 63 μm lines to the total far-infrared intensity emitted from the surface of the clouds are plotted as a function of density and radiation field. This ratio is a measure of the heating efficiency, since [CII] 158 μm and [OI] 63 μm are the most important coolants in PDRs.

In the regime discussed here, the surface temperatures of the XDR models are quite well correlated with H_X/n , where H_X is the energy deposition per particle and n the total hydrogen density. This means that the highest surface temperatures are found at the lowest densities and highest impinging radiation fields. Consequently, the contours of equal surface temperature are almost straight lines in the XDR plot of Fig. 8.1. In the PDR models their behavior is more complicated, as already discussed by Kaufman et al. (1999), since grains are involved in heating the gas. At the edge of the cloud, the cooling is dominated by [CII] $158 \mu\text{m}$ and [OI] $63 \mu\text{m}$, which have critical densities of $n_{cr}(\text{CII}) \approx 3 \times 10^3 \text{ cm}^{-3}$ and $n_{cr}(\text{OI}) \approx 5 \times 10^5 \text{ cm}^{-3}$. The cooling rate in this regime is more or less proportional to n^2 . The heating rate is at least proportional to n ,

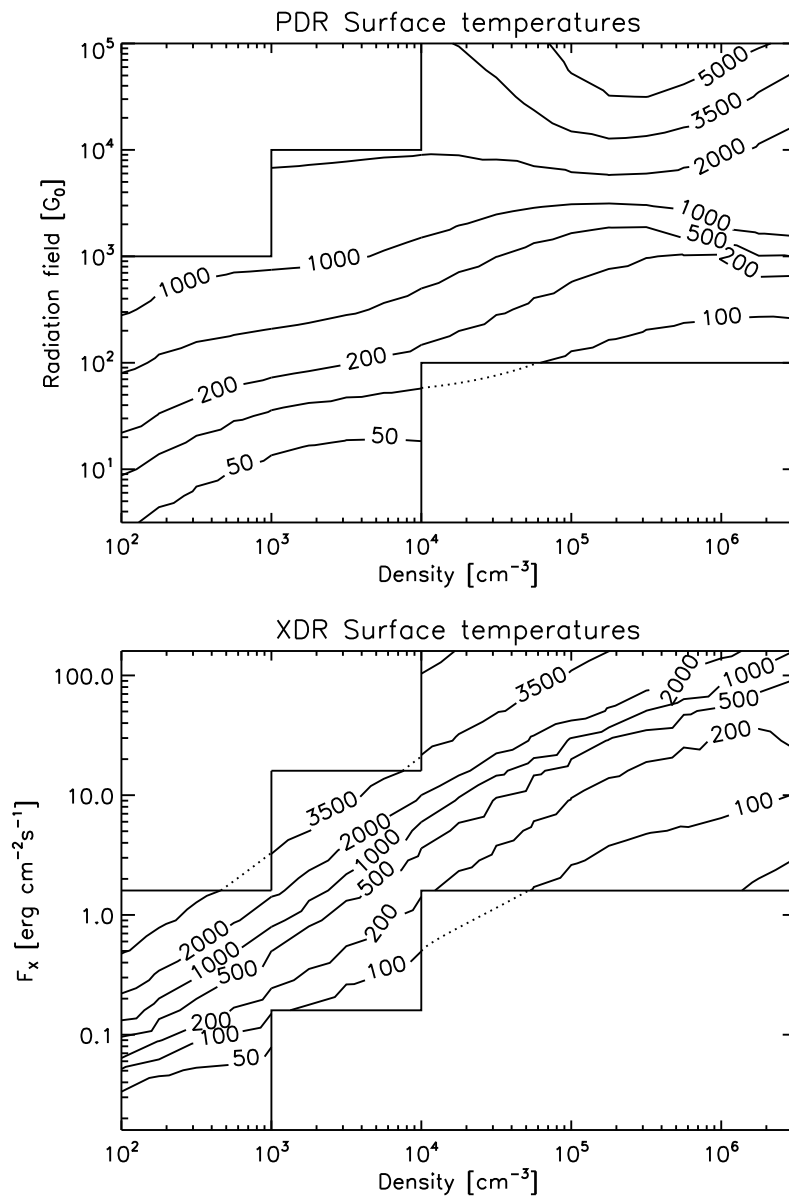


Figure 8.1: Surface temperatures for PDR (top) and XDR (bottom) models.

because the grain density is proportional to n . It can be larger, because grains become less positively charged at increasing electron densities making it easier for electrons to escape the grains, so that the heating efficiency increases. Nevertheless, the density dependence of heating remains less steep than n^2 , i.e., less than that of cooling, which causes a drop in the temperature at $n < 10^4 \text{ cm}^{-3}$ and for fixed G_0 with increasing density. Between $n \approx 1 - 3 \times 10^3 \text{ cm}^{-3}$ where the [CII] 158 μm line thermalizes, the drop in temperature stagnates. For densities between $n = 10^4 - 10^5 \text{ cm}^{-3}$ and $G_0 < 10^4$, we also find that the surface temperature drops with increasing n . The [OI] 63 μm line thermalizes at higher densities $n = 10^5 - 10^6 \text{ cm}^{-3}$ and, therefore, cooling will be proportional to n . Heating increases faster with density, which results in a higher surface temperature. For $G_0 > 10^4$, we find that the surface temperature rises up to $n \approx 5 \times 10^5 \text{ cm}^{-3}$ due to the increase in the heating efficiency with density at fixed G_0 . Above this density and at these high temperatures, coolants with high critical densities and excitation energies such as the [OI] 6300 \AA line become important, causing the surface temperature to drop again.

When we compare the surface temperatures with those derived by Kaufman et al. (1999), we find that our model surface temperatures are higher. A possible explanation for this has been discussed recently by Röllig et al. (2006), who present scaling relations for heating and cooling as a function of metallicity Z . They state that the photo-electric heating rate is $\propto Z$ for $n < 10^3 \text{ cm}^{-3}$ increasing to Z^2 when $n > 10^6 \text{ cm}^{-3}$. The cooling rate is always proportional to Z , and, therefore, higher metallicities result in higher surface temperatures. Note however that the temperature differences found are very likely not only because of a change in metallicity. In the PDR comparison test (Röllig et al. 2006), we found significant scatter between different PDR codes in the thermal balance. Therefore, one should not take the absolute values of line intensities too literally in the interpretation of data.

8.4 Fine-structure lines

In principle, we can use combinations of fine-structure line intensities to constrain densities and incident radiation fields. Here we discuss how such line ratios depend on gas density, ambient radiation field strength, and cloud column density, and compare the results for the PDR and XDR models.

8.4.1 [SiII] 35 μm /[CII] 158 μm intensity ratio

In Fig. 8.2, we show the [SiII] 34.8 μm / [CII] 158 μm fine-structure line ratio for both the PDR and the XDR models. The [SiII] 34.8 μm line has an energy of $E/k = 414 \text{ K}$ and a critical density of $n_{cr} = 3.4 \times 10^5 \text{ cm}^{-3}$, while this is $E/k = 92 \text{ K}$ and $n_{cr} = 2.8 \times 10^3 \text{ cm}^{-3}$ for the [CII] 158 μm . Very high radiation fields produce ambient temperatures in the PDR models that are sufficiently high to excite their upper states and the ratio depends mostly on density. With lower radiation fields, the surface temperature drops. The upper level energy of [SiII] 34.8 μm is reached first and the [SiII]/[CII] line ratio drops. As the density increases at a given FUV radiation field, the ratios limit to roughly constant values that are set by the corresponding surface temperatures.

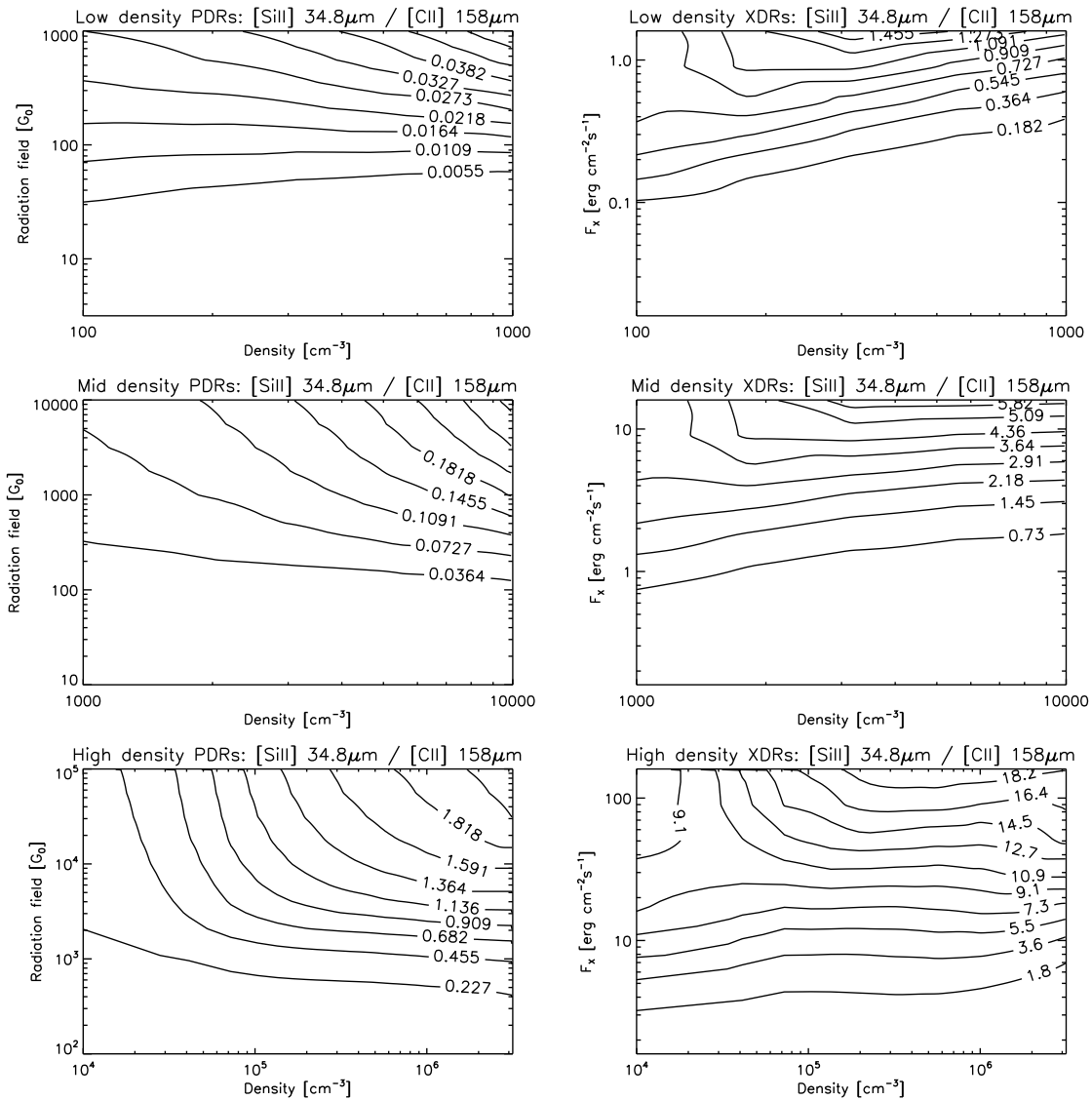


Figure 8.2: [SiII] 34.8 μm / [CII] 158 μm ratio for PDR (left) and XDR (right) models.

In the XDR models, the ratio is not only determined by the temperature and density, but also by the fractional abundances and column densities. In PDRs clearly defined layers occur, in which carbon and silicon are both almost fully ionized, but throughout XDRs neutral and ionized species co-exist. Despite the fact that surface temperatures in the XDR models are lower, we find much higher [SiII]/[CII] ratios, since silicon is much easier to ionize than carbon. The dominant source for ionization is not the direct absorption of an X-ray photon (primary ionization), but the produced kinetic electron. This electron can ionize a species either directly by collisions (secondary ionizations) or indirectly by first exciting H and H₂ and producing Lyman α and Lyman-Werner photons, which then may ionize species in turn. The cross section of Si for secondary ionization is about twice that of C. This does not, however, fully explain the order of magnitude difference between the calculated PDR and XDR ratios. This difference also reflects the fact that ionization of C

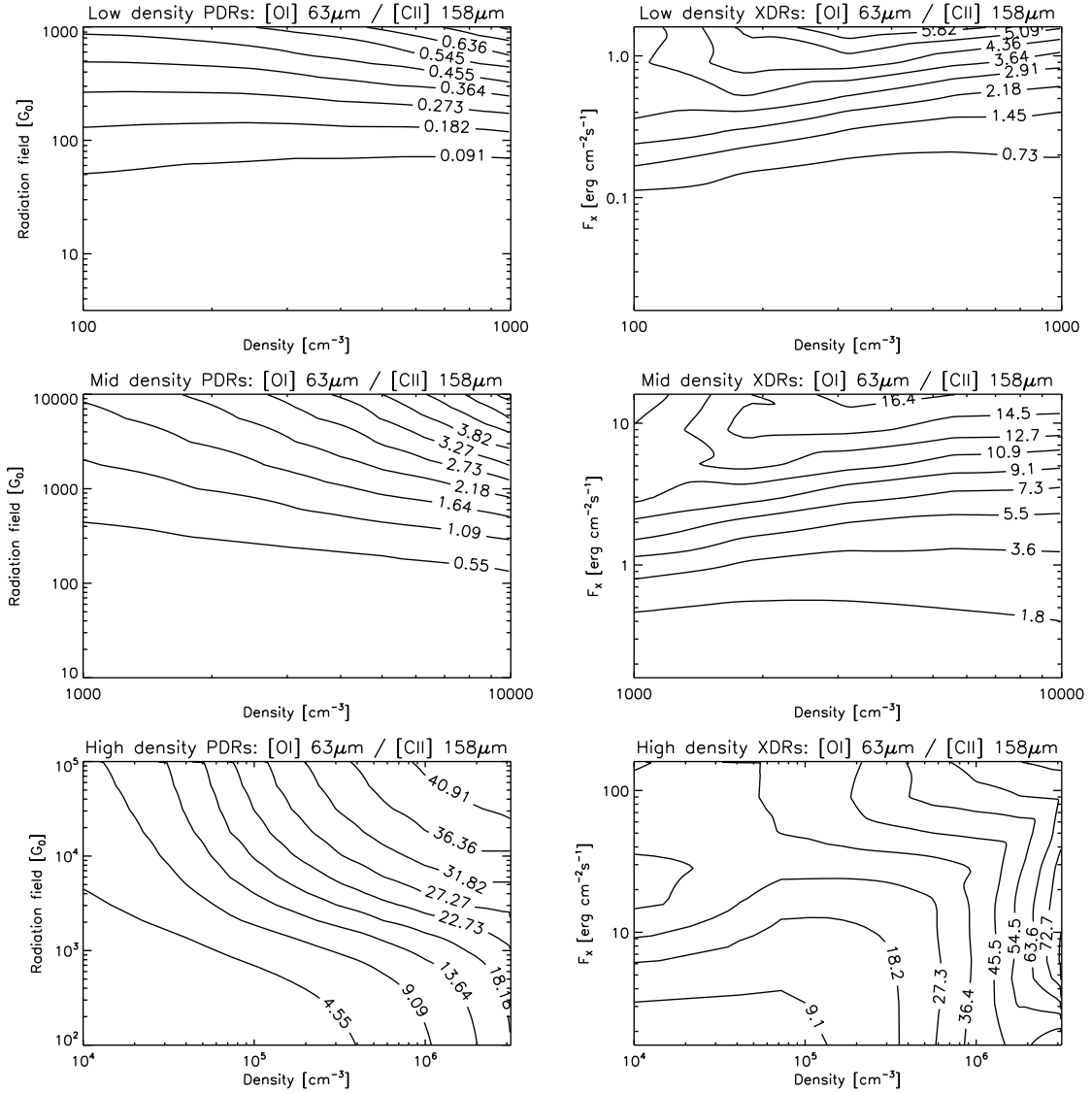


Figure 8.3: [OI] 63 μm / [CII] 158 μm ratio for PDR (left) and XDR (right) models.

can only be done by Lyman-Werner photons, whereas both Lyman α and Lyman-Werner photons are capable of ionizing Si. It is thus harder to ionize C than Si in regions where the gas is mostly atomic, which results in a large increase of the ratio for all densities at a given irradiation strength.

This also explains the fairly constant ratio below $F_X \approx 10 \text{ erg s}^{-1} \text{ cm}^{-2}$ for $n \sim 2 \times 10^3 - 3 \times 10^6 \text{ cm}^{-3}$, which results from an interplay between various effects. With ambient radiation fields constant, we find that the surface temperatures drop with increasing density in the XDR. At lower temperatures and higher densities, H_2 is more easily formed. Both the temperature drop itself and the enhanced H_2 (leading to more carbon ionizations) thus suppresses the [SiIII]/[CII] ratio, but this is compensated by the relatively high critical density of the [SiIII] 34.8 μm line.

For the highest, $> 16 \text{ erg s}^{-1} \text{ cm}^{-2}$, radiation fields, where carbon is highly ionized,

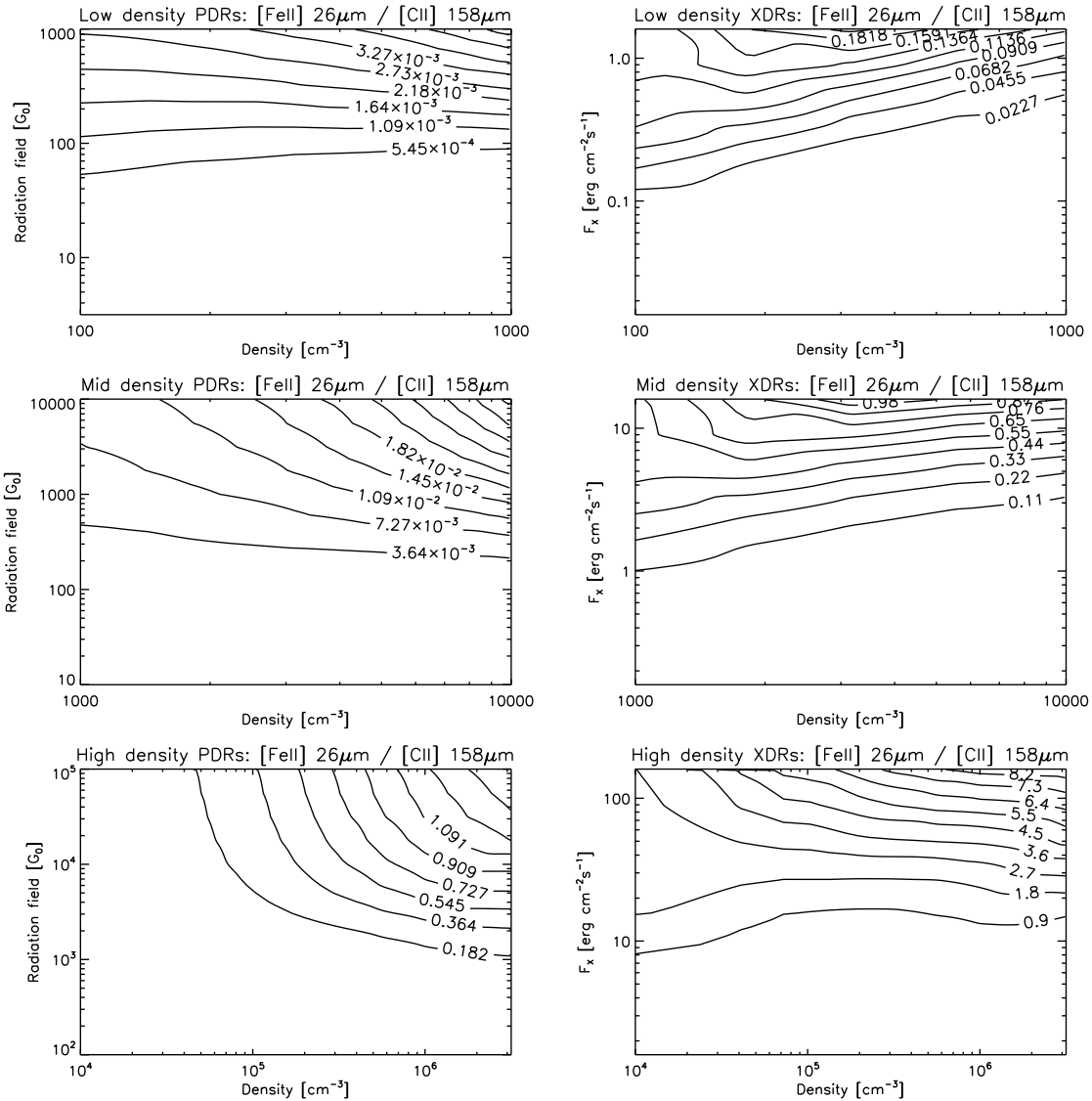


Figure 8.4: [FeII] 26 μm / [CII] 158 μm ratio for PDR (left) and XDR (right) models.

we find the same trend as seen for the PDR, i.e., the ratio is mostly dependent on density for the highest radiation fields, and then there is a decrease in the ratio when the temperature drops toward the upper-state energy of [SiII].

At the lowest densities and highest X-ray radiation fields, we find that the effect of column density become important as well. Since we fixed cloud sizes, in each cloud type the lowest density models imply also the lowest column densities. In the high irradiation models, carbon is almost fully ionized at the XDR edge. The fractional abundance of ionized carbon drops toward the H/H₂ transition and then increases again for the reasons discussed earlier. In the lowest (column) density models, we only produce the highly ionized part, suppressing the ratio even more. This is best seen in the diagram for the high density XDR models, at densities $n = 10^4 \text{ cm}^{-3}$. The ratio increases from $F_X = 1.6$ to $30 \text{ erg s}^{-1} \text{ cm}^{-2}$ and then drops again. Hence, if we increase the column densities of these

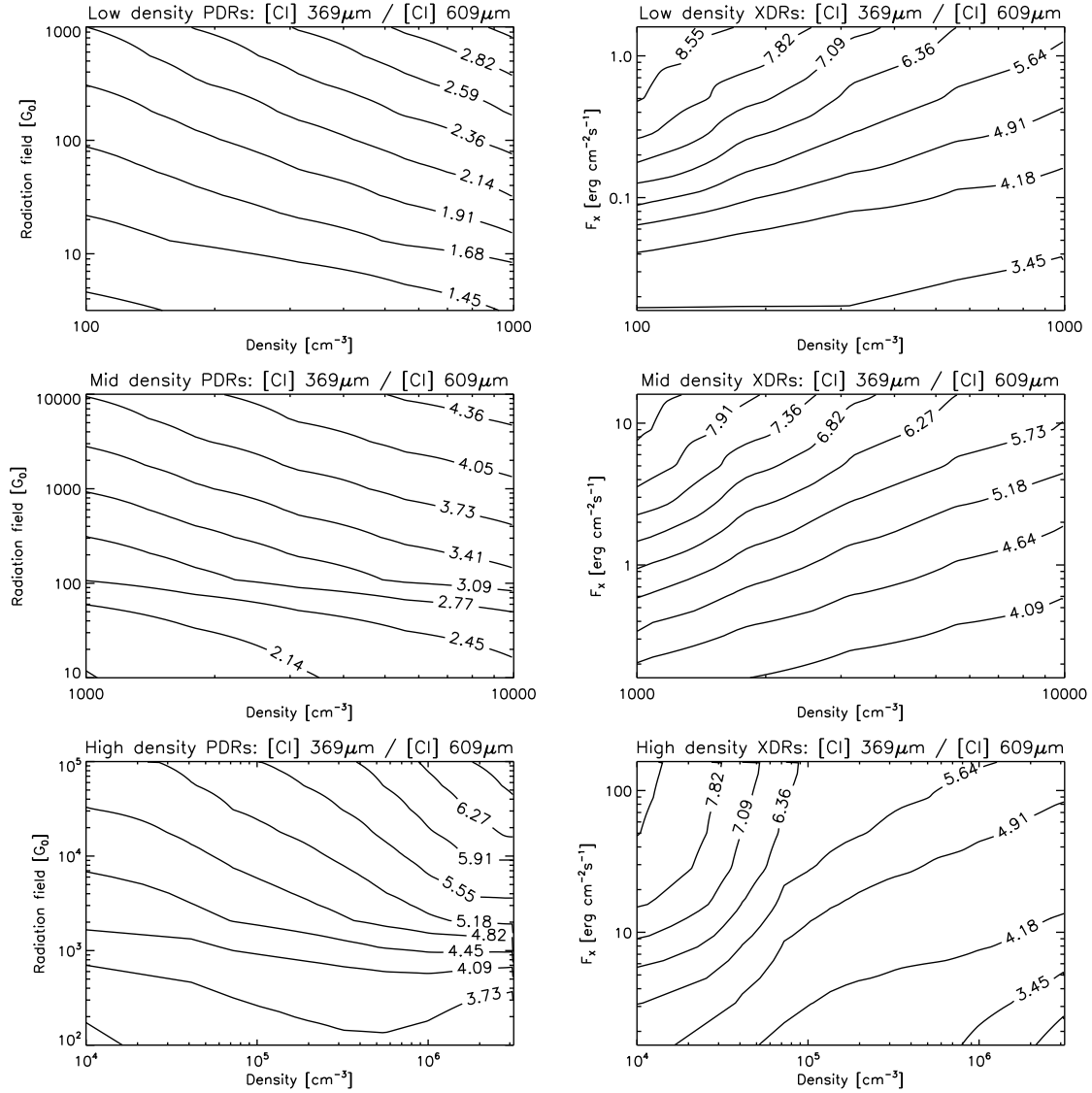


Figure 8.5: $[\text{CI}] 369 \mu\text{m} / [\text{CI}] 609 \mu\text{m}$ ratio for PDR (left) and XDR (right) models.

models by a factor of ~ 30 , the ratios only depend on radiation field strength and not on density.

8.4.2 $[\text{OI}] 63 \mu\text{m} / [\text{CII}] 158 \mu\text{m}$ intensity ratio

In Fig. 8.3, we show the $[\text{OI}] 63 \mu\text{m} / [\text{CII}] 158 \mu\text{m}$ ratio. The critical density is $n_{cr} = 5 \times 10^5 \text{ cm}^{-3}$ and the upper-state energy is $E/k = 228 \text{ K}$ for $[\text{OI}] 63 \mu\text{m}$. In the PDR models and at very high incident radiation fields, this ratio depends mostly on density as in the case for the $[\text{SiII}]/[\text{CII}]$ ratio, since once again temperatures are sufficiently high to excite both upper-state levels. When the surface temperature drops for lower radiation fields, the upper-state energy of $[\text{OI}]$ is reached first. The $[\text{OI}]/[\text{CII}]$ ratio then drops, with a flat density dependence for $n < 10^4 \text{ cm}^{-3}$ and $G_0 < 10^3$. The decrease in this line

ratio is, however, less pronounced than that in the [SiII]/[CII] ratio, because the upper-state energy of [OI] is lower than that of [SiII]. When $G_0 < 10^3$ and $n > 10^{5.5} \text{ cm}^{-3}$, the ratio is roughly constant at the same density for all values of G_0 . Here, the more difficult excitation of [OI] at lower temperatures is counteracted by the C^+ layer becoming thinner at lower radiation fields.

In the XDR, the [OI]/[CII] ratio is again more complex due to its dependence on density, radiation field, ionized carbon fraction and total column density. The ratios are overall much higher than in the PDR models, since carbon does not become fully ionized. At the largest H_X/n , temperatures are high enough to create a dependence on density only. At lower radiation fields, the [OI]/[CII] ratio drops as temperatures approach the upper-state energy of the [OI] 63 μm line. When we decrease the radiation field even more, we find that the C^+ fraction is rapidly reduced at high ($> 10^5 \text{ cm}^{-3}$) densities and the ratio increases again. At high ($> 16 \text{ erg s}^{-1} \text{ cm}^{-2}$) radiation field strength and low densities, a large H_X/n is maintained throughout the whole cloud, since the relevant type A cloud size is only one parsec. For that reason, we find here the same effect as already seen in the [SiII]/[CII] ratio, since column densities increase toward higher densities. At the highest radiation fields and lowest densities, the ratio is suppressed since carbon remains partially ionized over the full extent of the clouds considered here. We do not find the highest ratio at the highest radiation field in the lower density models.

8.4.3 [FeII] 26 μm /[CII] 158 μm intensity ratio

In Fig. 8.4, we show the [FeII] 26 μm / [CII] 158 μm intensity ratio. [FeII] 26 μm is very difficult to excite due to its high critical density $n_{cr} = 2.2 \times 10^6 \text{ cm}^{-3}$ and upper-state energy $E/k = 554 \text{ K}$. Thus, the change in ratio with increasing density at high incident radiation fields is much larger than that seen for the [SiII] 34.8 μm / [CII] 158 μm ratio. In the PDR models and at high incident radiation fields, the ratio mostly depends on the density. At lower radiation field strengths, approaching the upper-state energy of [FeII], the ratio drops.

The same trends are seen at high radiation fields in the XDR models, but again, we find much higher ratios than in the PDR models. It is possible to ionize iron with Lyman α photons, but not carbon. At moderate radiation fields, we again find ratios to be more or less independent of density, for the reason that we have already discussed in the [SiII]/[CII] case. At the lowest densities and highest radiation fields in each cloud type, we find that the ratios are similarly suppressed as was the case for [SiII] 35 μm /[CII] 158 μm and [OI] 63 μm /[CII] 158 μm .

8.4.4 [CI] 369 μm /[CI] 609 μm intensity ratio

In Fig. 8.5, we show the [CI] 369 μm / [CI] 609 μm intensity ratio. The critical densities of these lines are $n_{cr} = 3 \times 10^2 \text{ cm}^{-2}$ for [CI] 609 μm and $n_{cr} = 2 \times 10^3 \text{ cm}^{-2}$ for [CI] 369 μm , typically lower than the densities we are considering here. The upper-state energies are $E/k = 24$ and 63 K for [CI] 609 μm and [CI] 369 μm , respectively. In the PDR models, the [CI] lines originate from the $\text{C}^+/\text{C}/\text{CO}$ transition layer. The

temperatures in this layer slightly rise with increasing incident radiation field strengths and range between $T = 20 - 100$ K (comparable to the upper-state energies). This explains the small increase in the ratio for larger G_0 at the same density. The ratio does not change much as a function of density, since we are above the critical density. The change we do see, however, has a temperature dependence. When densities are lowered, recombination rates are lower as well. By consequence, at higher densities, the transition layer is closer to the edge of the cloud and at higher temperatures, which raises the ratio.

In the XDR, neutral carbon occurs throughout the cloud, and is also abundant at relatively high temperatures. The spread in temperatures is large, which was already seen in Sect. 3, and this determines for a large part differences in the ratios. The temperature of a cloud is determined by H_X/n , resulting in the highest ratios for low n and high F_X , opposite to the situation in the PDR models. The three cloud types, with their different low, mid and high density ranges nevertheless show very similar spreads in ratios. This is caused by the difference in column densities, which also has a very important effect. The low, mid, and high density models have their own fixed cloud size, and in each standard cloud type, column densities increase toward higher densities in the same density range. The higher density models contain larger regions of low temperature, which suppresses the ratio at these densities even more. This can also be understood by considering the ratio at $n = 10^4 \text{ cm}^{-3}$ in the mid (type B) and high (type C) density range. The high density model at $n = 10^4 \text{ cm}^{-3}$ has a smaller cloud size and therefore a higher line ratio.

8.5 Rotational lines

Molecular rotational lines are also characteristic for the physical condition of ISM gas and may also be used to constrain gas densities and incident radiation fields. In the following, we discuss a number of ratios, involving the molecular species ^{12}CO , ^{13}CO , HCN, HNC, HCO^+ , SiO and CS. Although we reproduce in this Paper only a limited number of the diagrams showing the calculated line intensity ratios, all model data are available on-line¹. Hence, the reader can determine all line ratios and integrate over all possible lines of sight as interest dictates. Here we concentrate on molecular lines that we consider particularly useful to distinguish between PDRs and XDRs. We have calculated the line intensities by using a one-dimensional version of the radiation transfer code described in Poelman & Spaans (2005, 2006).

8.5.1 CO rotational lines

In Fig. 8.6, we show the CO(1-0) line intensity for cloud types A (high-density), B (mid-density) and C (low-density) for both the PDR and XDR model cases (cf. Table 8.1). All three cloud types are relevant for CO (and ^{13}CO) since these molecules are present ubiquitously on all galactic scales. The CO(1-0) line has an upper state energy $E/k = 5.53$ K and a critical density $n_{cr} \sim 3 \times 10^3 \text{ cm}^{-3}$. In the low density PDR models ($n = 10^2 - 10^3 \text{ cm}^{-3}$), we find that the intensity increases with density only. In

¹<http://www.strw.leidenuniv.nl/~meijerin/grid/>

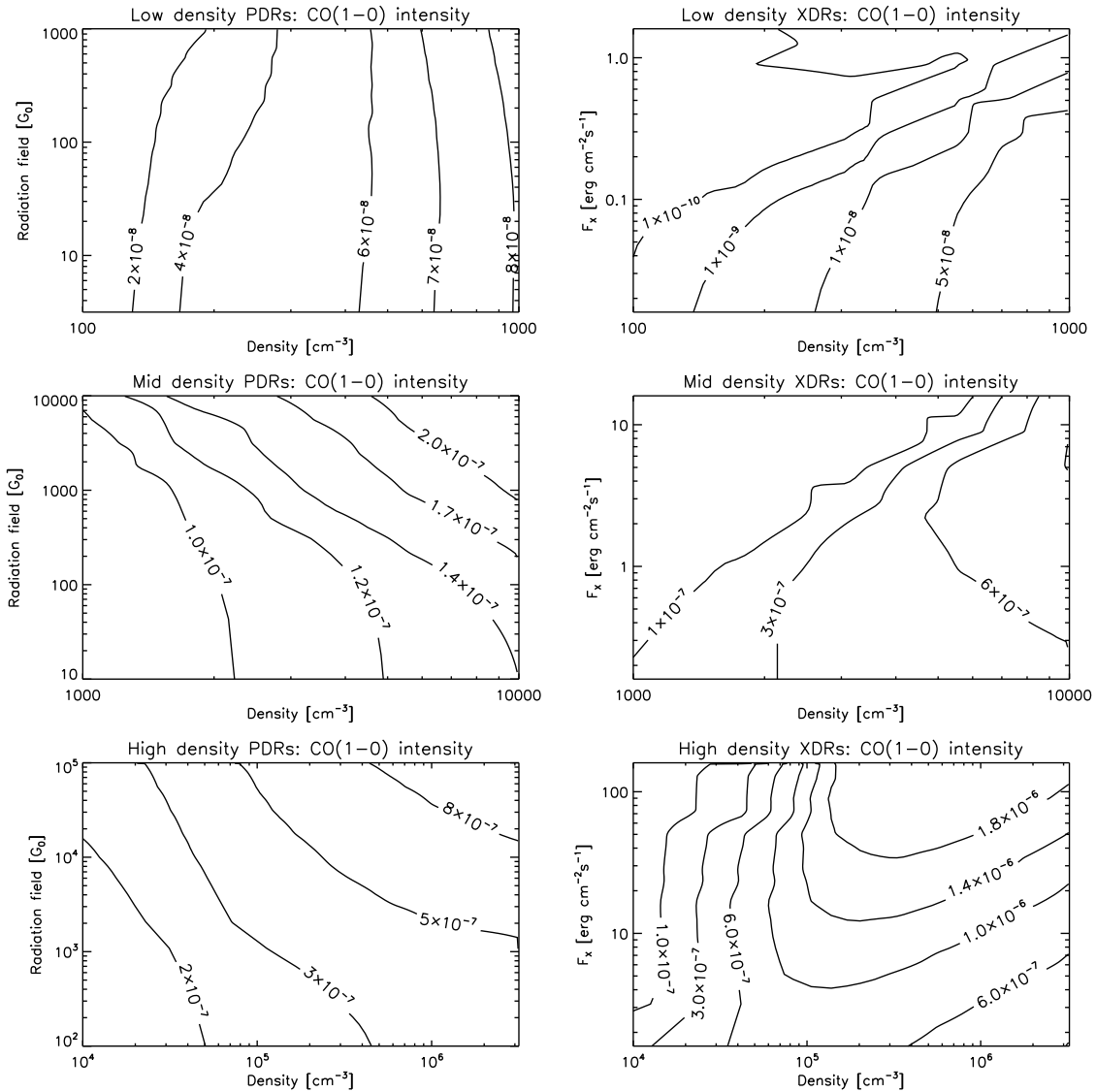


Figure 8.6: CO(1-0) intensity in $\text{erg cm}^{-2} \text{s}^{-1} \text{sr}^{-1}$ for PDR (left) and XDR (right) models.

the mid ($n = 10^3 - 10^4 \text{ cm}^{-3}$) and high ($n = 10^4 - 10^{6.5} \text{ cm}^{-3}$) density range, we also find a small line intensity increase at higher incident radiation fields. At higher densities, gas-grain interactions may significantly increase gas temperatures in the highly attenuated part of the cloud. Although the upper-state energy is below the gas temperature, we find a significant increase in the line intensity. In general, the line intensities do not vary much in the PDR models, as opposed to what is seen in the XDR models. In all PDR models, the CO(1-0) lines are optically thick. In the XDR models for type C clouds ($n = 10^2 - 10^3 \text{ cm}^{-3}$), the line intensities vary over two orders of magnitude. Because of the fixed cloud size, models at higher densities have larger column densities. Even at the point farthest from the cloud edge, the low density gas in type C clouds causes relatively little radiation attenuation, and with high incident radiation it is at very high temperature and in a highly ionized state throughout. Under these conditions warm CO

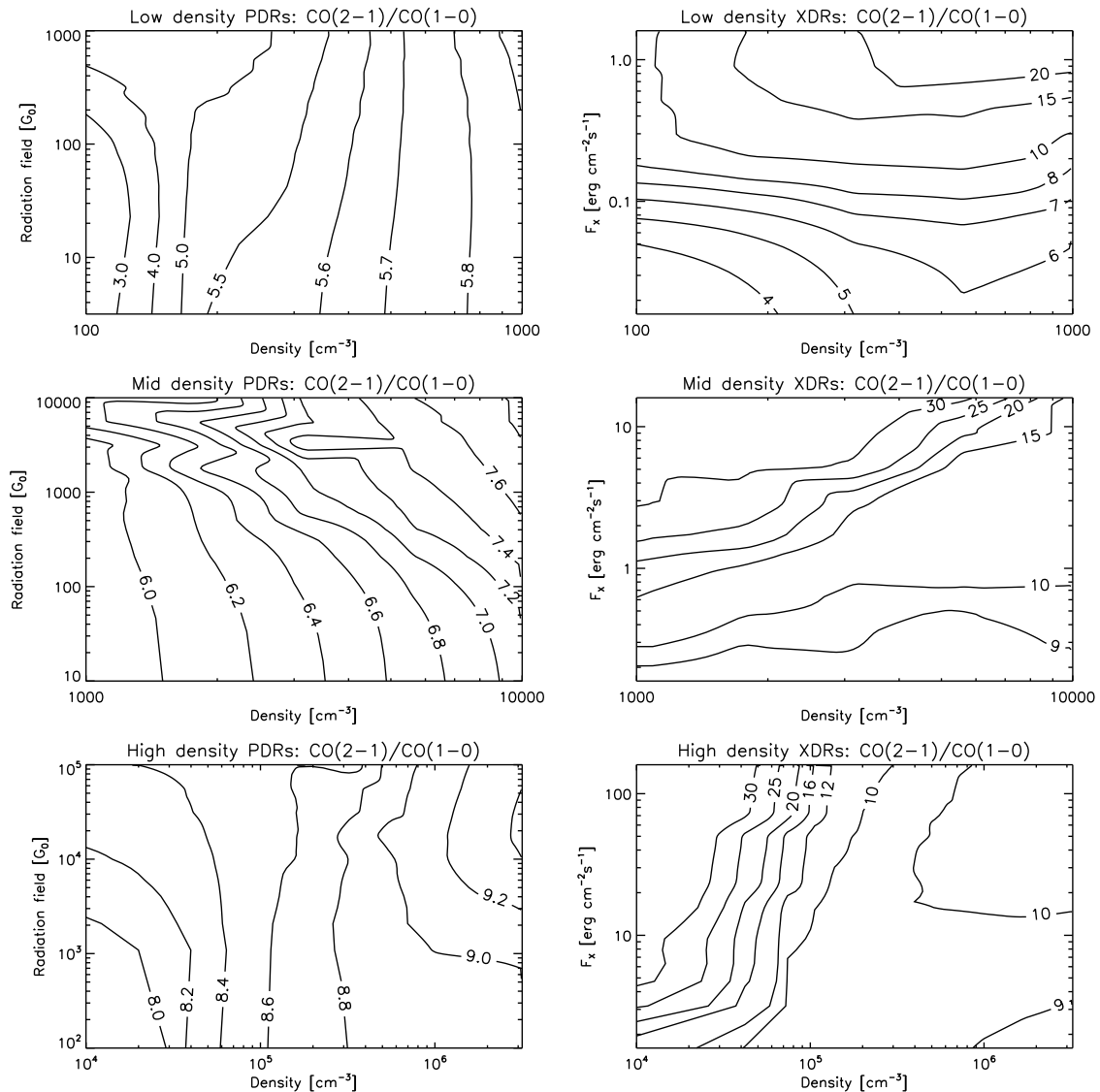


Figure 8.7: CO(2-1)/CO(1-0) ratio for PDR (left) and XDR (right) models.

gas present, but only in very small amounts. Therefore, at such points in parameter only very weak line emission is produced and the lines are optically thin. In the high density range ($n = 10^4 - 10^{6.5} \text{ cm}^{-3}$) of type A clouds, on the other hand, the spread in intensity is much reduced. Although at densities of $n = 10^4 \text{ cm}^{-3}$ most of the cloud is still at a high temperature and in a highly ionized state, there is sufficient column density to have CO abundances large enough to produce significant line emission. At even higher densities ($n = 10^6 \text{ cm}^{-3}$), the column densities are high enough to attenuate the radiation field in such a way that a large CO fraction is produced ($\sim 10^{-4}$), but still at a temperature of $T \sim 100 \text{ K}$. Here, the CO(1-0) line emission produced in XDRs can be two to four times stronger than that in PDRs.

For the CO(2-1) line, the upper state energy is $E/k = 16.60 \text{ K}$ and the critical density is $n_{cr} \sim 1 \times 10^4 \text{ cm}^{-3}$. Although not shown, the line intensities exhibit a behaviour as a

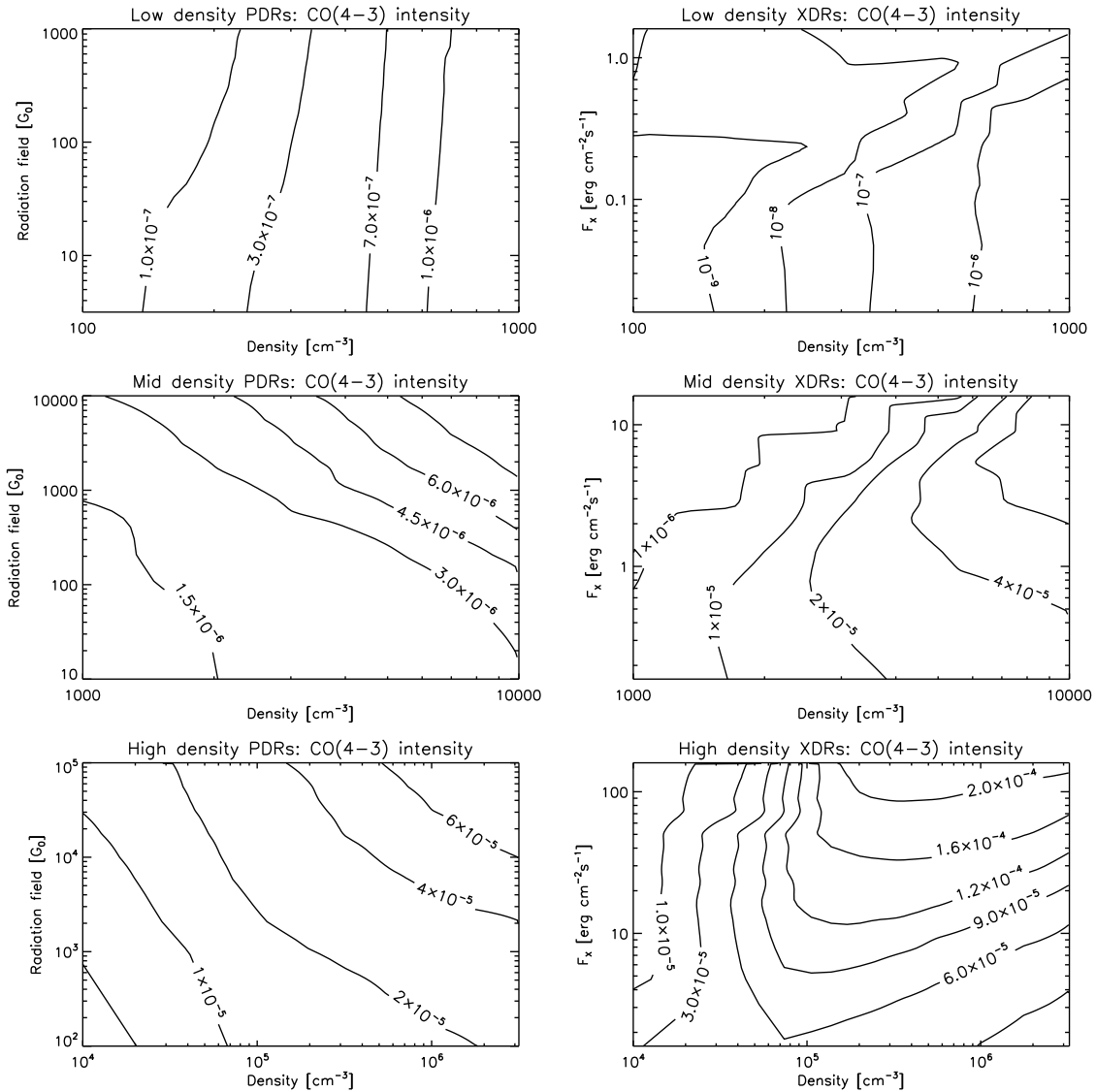


Figure 8.8: CO(4-3) intensity in $\text{erg cm}^{-2} \text{s}^{-1} \text{sr}^{-1}$ for PDR (left) and XDR (right) models.

function of density and radiation field very similar that that of the CO(1-0) line. Because of the higher upper state energy, we find a somewhat stronger dependence on radiation field in the PDR models. The effect of the larger critical density is hard to see, due to the large optical depths, but do show up when we consider the CO(2-1)/CO(1-0) ratio. This ratio is shown in Fig. 8.7. In the PDR models, the ratio does not differ more than a factor of two over the full density range considered here. In the XDR models, very large line intensity ratios of 30 or more are found, especially at high incident radiation fields. It is, however, very questionable whether we will actually observe these high ratios, since the intensity of the emitted emission is low. The CO(2-1)/CO(1-0) ratio dependence on density and radiation field is in general weak, especially in PDRs, since the upper state energies are not very high and the difference in critical density is small.

The CO(4-3) line (see Fig. 8.8) has an upper state energy $E/k = 55.32 \text{ K}$ and critical

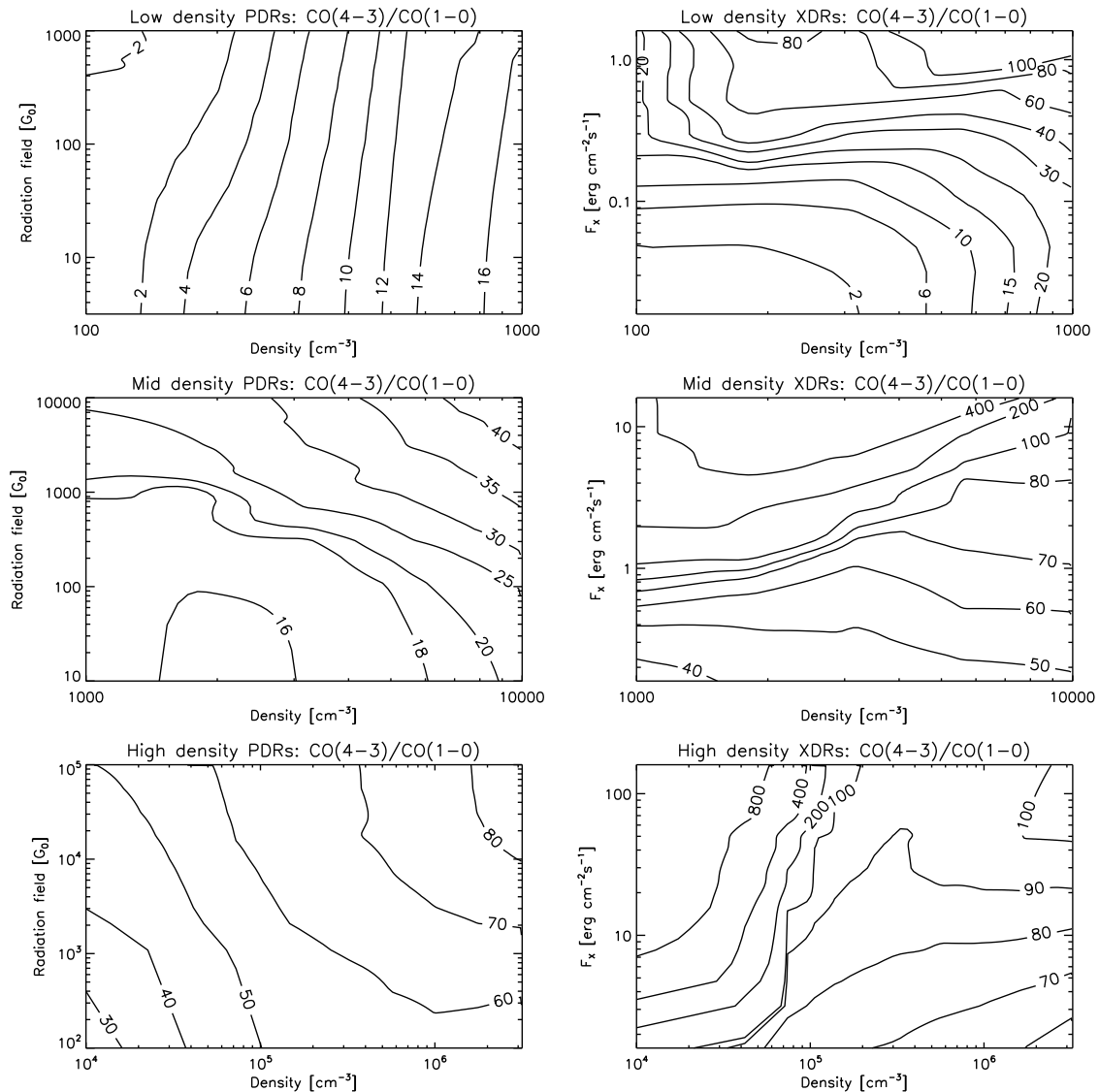


Figure 8.9: CO(4-3)/CO(1-0) ratio for PDR (left) and XDR (right) models.

density $n_{cr} \sim 4 \times 10^4 \text{ cm}^{-3}$. As expected, the emitted intensity shows more variation with density and radiation field. In Fig. 8.9, we show the CO(4-3)/CO(1-0) line intensity ratio. In the low density range (cloud type C), PDR models still produce a line ratio increase only as function of density, but the variation in the ratio has grown to more than a factor of two, as opposed to only 20 percent in the corresponding CO(2-1)/CO(1-0) ratio. The XDRs for this cloud type show a complex behavior with density and radiation field and the ratios cover a much larger range from about 2 to 40. At low radiation fields, only a density dependence is seen. At high radiation field strengths, the effect of the column density comes into play. In the mid density (type B) PDRs, the highest line ratios are seen for the highest densities and radiation fields. The XDRs in this range show only a dependence on radiation field. The effect of the higher density is compensated by the fact that at lower densities relatively more gas is at high temperatures. The gas temperature

plays a large role in the density range applicable to this cloud type. CO is present at much higher temperatures in the XDRs. Therefore, the XDR line ratios for the same density and incident radiation field can be more than ten times larger than in the PDR. This difference slowly disappears when the critical density of the CO(4-3) line is reached and the CO(4-3) line also thermalizes, which is seen in the high density range (cloud type A) at densities $n > 10^5 \text{ cm}^{-3}$.

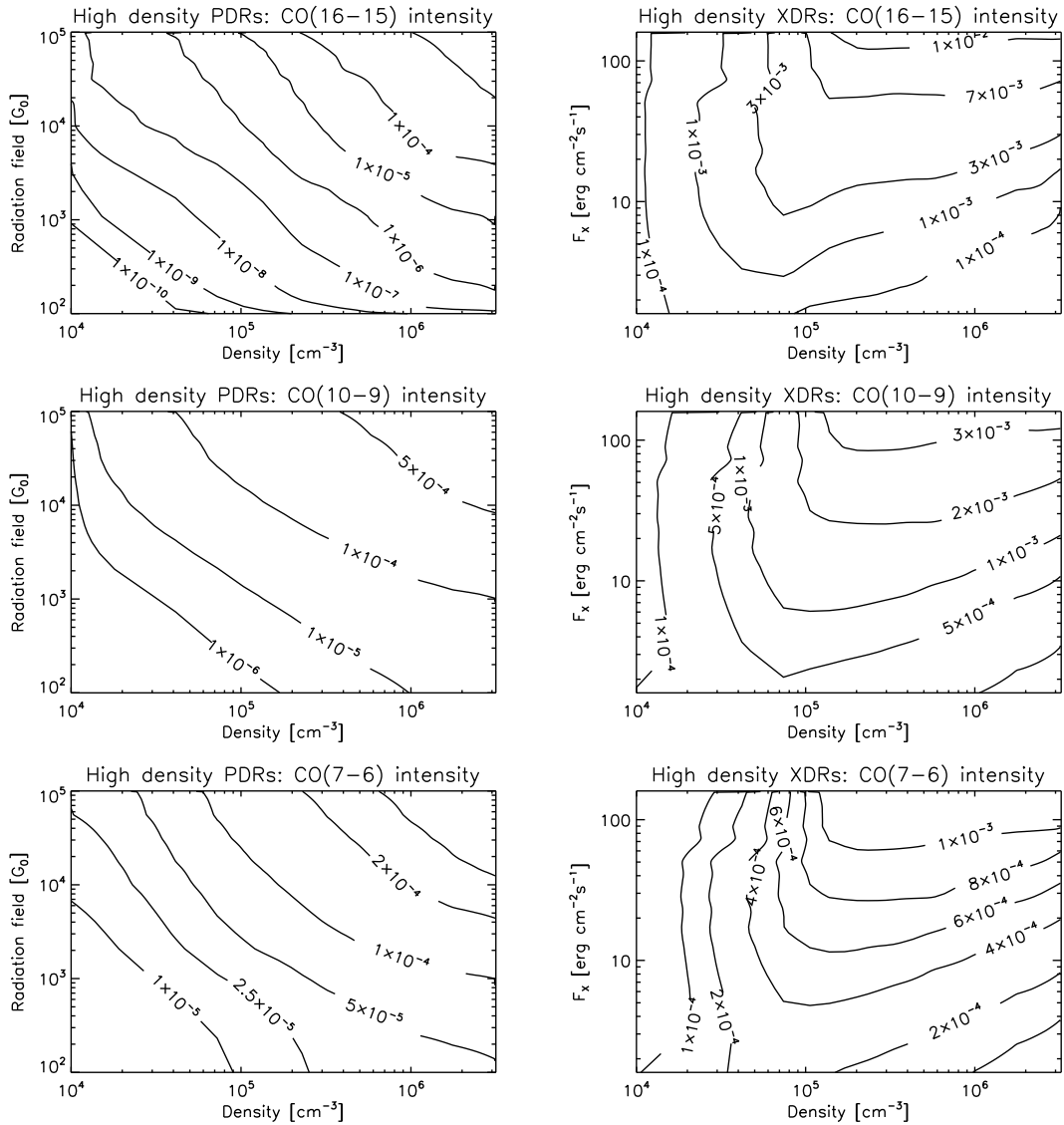


Figure 8.10: CO(16-15), CO(10-9), and CO(7-6) intensity in $\text{erg cm}^{-2} \text{ s}^{-1} \text{ sr}^{-1}$ for PDR (left) and XDR (right) models.

8.5.2 High J -CO rotational transitions

In cloud type A XDRs ($n = 10^4 - 10^{6.5} \text{ cm}^{-3}$), CO is present throughout the cloud, even when energy deposition rates H_X/n are large and temperatures are high ($T \sim 200 \text{ K}$).

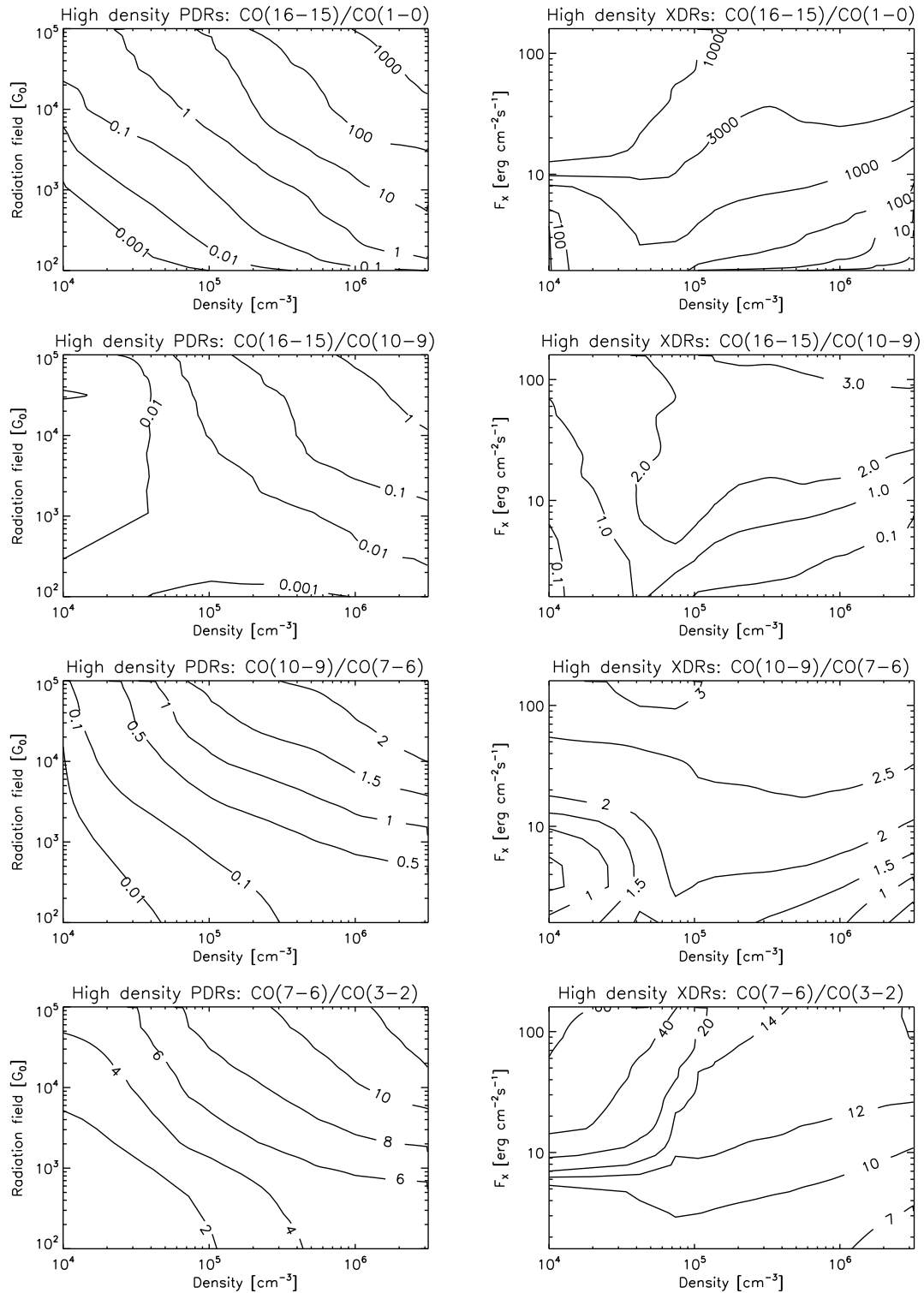


Figure 8.11: CO(16-15)/CO(1-0), CO(16-15)/CO(10-9), CO(10-9)/CO(7-6) and CO(7-6)/CO(3-2) ratio for PDR (left) and XDR (right) models.

This warm CO gas produces emission originating from high rotational transitions even when densities are not high (e.g., $n = 10^4 \text{ cm}^{-3}$). Contrary to the situation in XDRs, most CO in PDRs is produced beyond the H/H₂ transition and it has on average much lower temperatures ($T \sim 20 - 50 \text{ K}$), causing lower intensities and line ratios. Therefore, it is very likely, that future missions such as Herschel/HIFI will be able to distinguish between PDRs and XDRs, by observing high rotational transitions such as CO(16-15), CO(10-9), and CO(7-6).

In Fig. 8.10, we show the PDR and XDR intensities of the CO(7-6), CO(10-9) and CO(16-15) lines for the high density range (cloud type A). We find that for both PDRs and XDRs, the spread in intensities increases for higher rotational lines, since the critical densities of these transitions are higher. However, this spread is much larger for PDRs than for XDRs. The CO(16-15) line intensity ranges from $\sim 10^{-10}$ ($n = 10^4 \text{ cm}^{-3}$ and $G_0 = 10^2$) to $\sim 10^{-3} \text{ erg s}^{-1} \text{ cm}^{-2} \text{ sr}^{-1}$ ($n = 10^{6.5} \text{ cm}^{-3}$ and $G_0 = 10^5$) for the PDR models, while this is $\sim 10^{-4}$ ($n = 10^4 \text{ cm}^{-3}$) to $\sim 10^{-2} \text{ erg s}^{-1} \text{ cm}^{-2} \text{ sr}^{-1}$ ($n = 10^{6.5} \text{ cm}^{-3}$) for the XDR models. PDRs show only significant CO(16-15) emission at very high densities and radiation fields ($n \sim 10^6 \text{ cm}^{-3}$ and $G_0 \sim 10^4$). This very dense and strongly irradiated gas, however, has a very small filling factor on large (galaxy) scales, and, the probability of observing a PDR with a very high CO(16-15) intensity is low.

The difference between the PDR and XDR models is seen even better by considering the intensity ratios of these high rotational transitions (see Fig. 8.11). A good example is the CO(16-15)/CO(1-0) ratio, which ranges from 10^{-3} to 10^3 for PDRs, and from 10 to $> 10^4$ for XDRs. Especially for densities between $10^4 - 10^5 \text{ cm}^{-3}$, it is very easy to distinguish PDRs from XDRs.

8.5.3 ¹³CO rotational lines

The ¹³CO lines have critical densities and upper state energies for the rotational transitions almost identical to those of ¹²CO. As we have adopted an abundance ratio ¹²C/¹³C = 40 in our models, ¹³CO abundances are relatively low and the lines are much less optically thick.

The ¹³CO(1-0) line intensities (Fig.8.12), show the same trends with density and radiation field as the CO(1-0) line, but there is a larger spread in intensity. For example, the difference in the CO(1-0) line emission in the low density PDRs (cloud type C) is a factor of two and more than a factor of 3 for the ¹³CO line. This effect is even larger for the XDRs. We find similar results for both the ¹³CO(2-1) (not shown) and ¹³CO(3-2) line intensities as is evident from the corresponding ¹³CO line ratios (see Fig. 8.13 and 8.15). A nice illustration of the CO and ¹³CO behavior is supplied by the the CO(4-3)/CO(1-0) versus the ¹³CO(3-2)/¹³CO(1-0) intensity ratio for the low density PDRs (cloud type C). The CO(4-3) line is pumped due to the fact that the lower rotational lines become optically thick. The CO(4-3)/CO(1-0) ratio changes only a factor of two, which is a factor two and a half for the ¹³CO(3-2)/¹³CO(1-0) ratio, despite the lower critical density of ¹³CO(3-2).

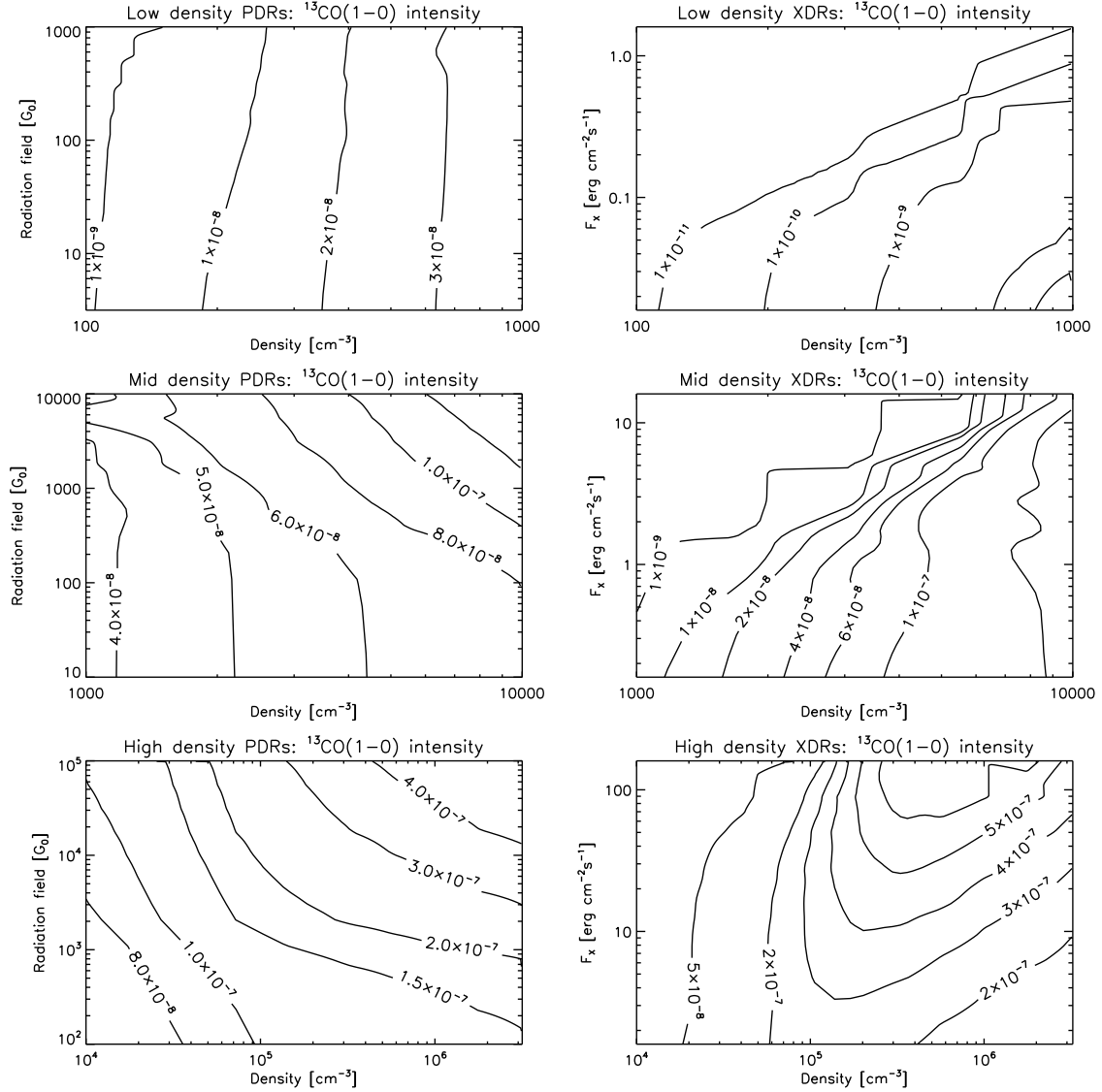


Figure 8.12: $^{13}\text{CO}(1-0)$ intensity in $\text{erg cm}^{-2} \text{s}^{-1} \text{sr}^{-1}$ for PDR (left) and XDR (right) models.

8.5.4 $^{13}\text{CO}/\text{CO}$ ratios

In Fig. 8.16 and 8.17, the important isotopical intensity ratios of $^{13}\text{CO}(1-0)/\text{CO}(1-0)$ and $^{13}\text{CO}(3-2)/\text{CO}(3-2)$ are shown. Although for all cloud types (density regimes) the line intensities are larger in the XDR, the PDR isotopical ratios exceed those of XDRs, which means that the opacities of the XDR lines are larger as well.

8.5.5 $[\text{CI}] 609 \mu\text{m}/^{13}\text{CO}(2-1)$ ratio

Fig. 8.18 shows the $[\text{CI}] 609 \mu\text{m}/^{13}\text{CO}(2-1)$ ratios. For the same gas density and incident radiation field, PDRs have much lower ratios than XDRs. In the PDRs, the spread in

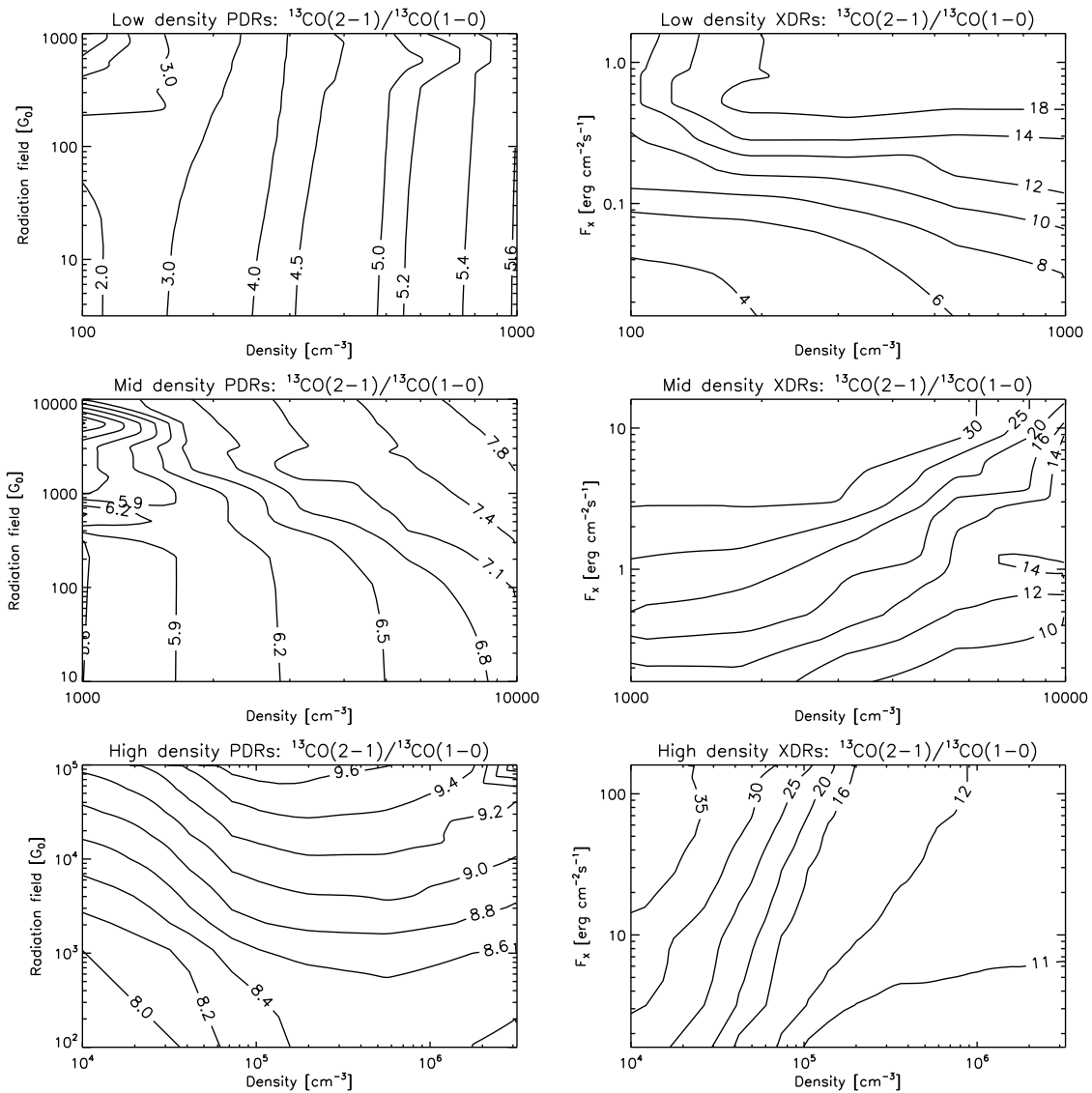


Figure 8.13: $^{13}\text{CO}(2-1)/^{13}\text{CO}(1-0)$ ratio for PDR (left) and XDR (right) models.

the ratio is generally not very large. At low densities, ratios rapidly decrease from 72 ($n = 10^2 \text{ cm}^{-3}$) to 18 ($n = 10^3$) and then slowly fall off from 14.5 ($n = 10^4 \text{ cm}^{-3}$) to 2 ($n = 10^6 \text{ cm}^{-3}$). While the PDR ratios show a more or less steady decrease with density, a rather different picture is seen in XDRs. In each density range (cloud type), the ratio changes by several orders of magnitude. For the lowest density in each cloud type, the column density is too low to attenuate the incident radiation field sufficiently to allow large amounts of CO to be present. On the other hand, neutral carbon occurs throughout the cloud, and, therefore, a large increase in the ratios are seen toward high H_X/n .

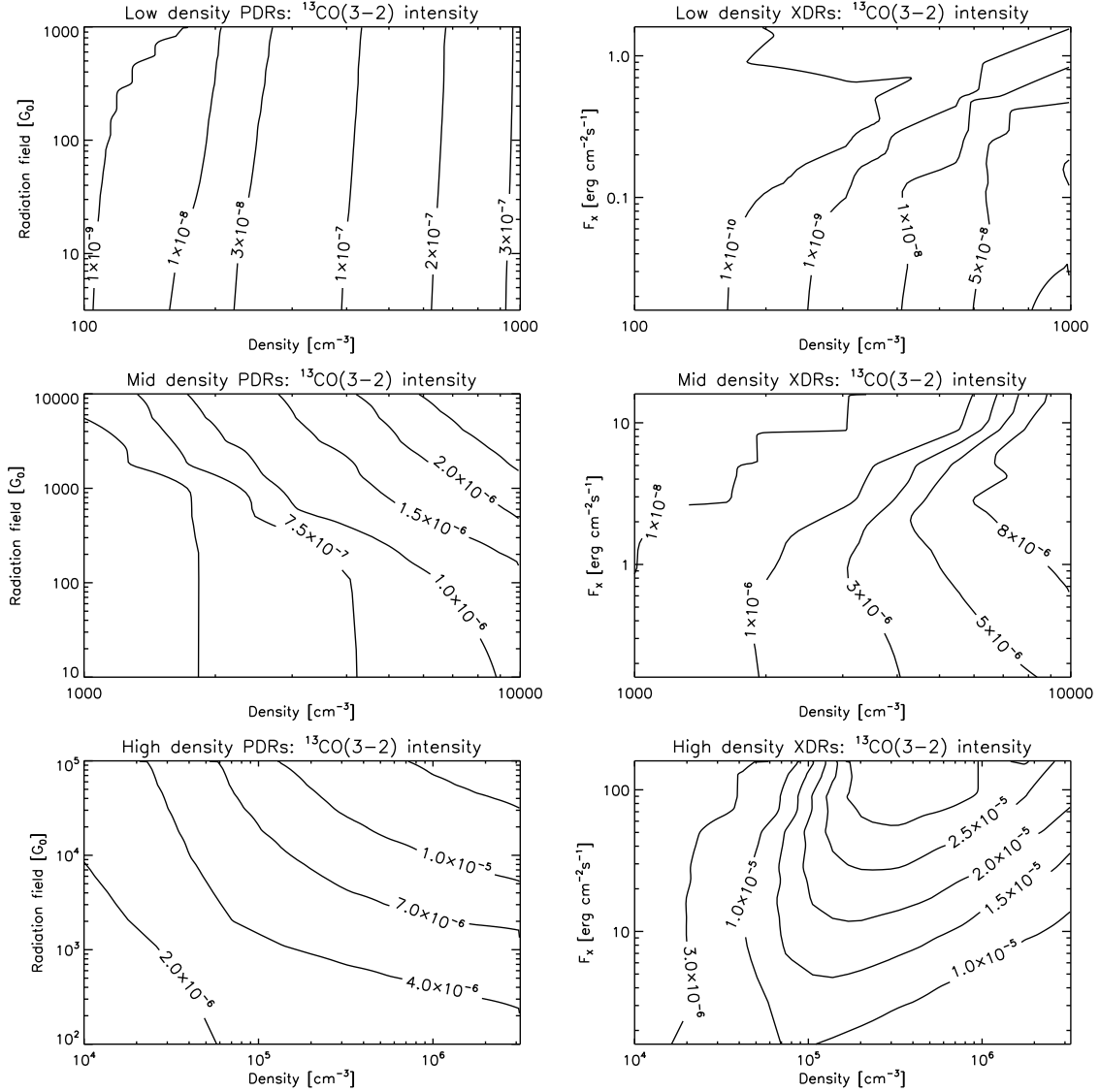


Figure 8.14: $^{13}\text{CO}(3-2)$ intensity in $\text{erg cm}^{-2} \text{s}^{-1} \text{sr}^{-1}$ for PDR (left) and XDR (right) models.

8.5.6 HCN rotational lines

In Fig. 8.19, we show the HCN(1-0) and HCN(4-3) line intensities for high density (cloud A type) PDR and XDR models only. Where the CO(4-3) line has a critical density of $n_{cr} \sim 4 \times 10^4 \text{ cm}^{-3}$, the HCN(1-0) line has a critical density of $n_{cr} \sim 3 \times 10^6 \text{ cm}^{-3}$. Higher rotational transitions such as HCN(2-1), $n_{cr} \sim 4 \times 10^6 \text{ cm}^{-3}$, and HCN(4-3), $n_{cr} \sim 2 \times 10^7 \text{ cm}^{-3}$, have even higher critical densities. The HCN rotational lines specifically trace the dense gas component in galaxies, and the line intensities from low and medium density gas are low. The HCN(1-0) line intensities range from 3×10^{-11} to $2 \times 10^{-8} \text{ erg s}^{-1} \text{ cm}^{-2} \text{ sr}^{-1}$ for the low and mid density (type C en B) PDR models, and even less for the corresponding XDR models. Because of their poor observational

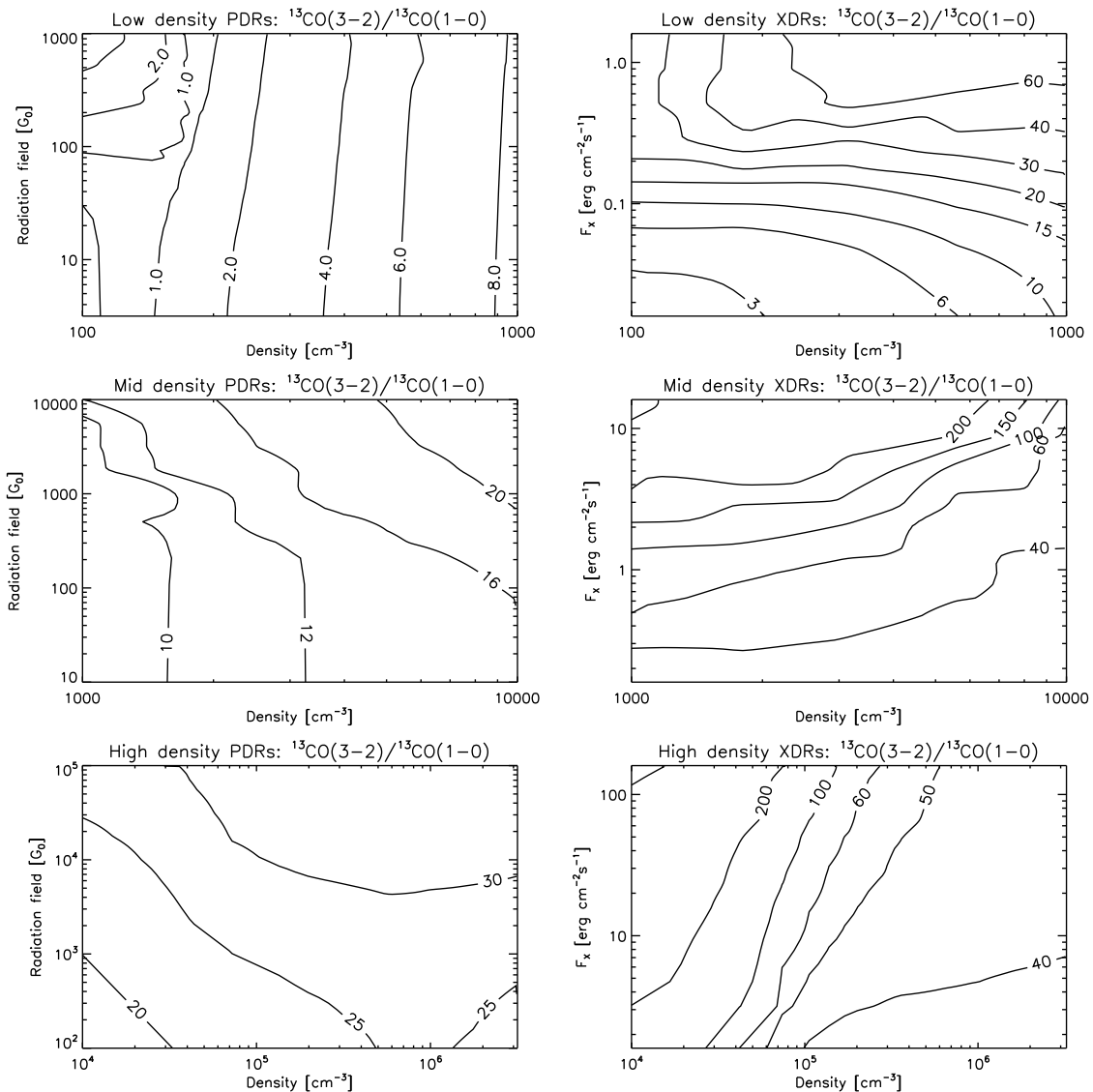


Figure 8.15: $^{13}\text{CO}(3-2)/^{13}\text{CO}(1-0)$ ratio for PDR (left) and XDR (right) models.

prospects, we have limited ourselves to only showing the model results in the high density range (cloud type A). Typically, the HCN(1-0) emission is stronger in PDRs by a factor of about two for densities larger than 10^5 cm^{-3} . The HCN(4-3) diagrams show behaviour very similar to that of HCN(1-0), but the PDR and XDR line strengths are now somewhat closer.

Typically, the HCN(1-0) emission is stronger in PDRs by a factor of about two for densities larger than 10^5 cm^{-3} . Our results are consistent with the chemical calculations of Lepp & Dalgarno (1996) for different ionization rates, as follows. Our depth dependent models cause the HCN line emissivities to be the result of a line-of-sight integral over the HCN abundance pattern that results from a varying (attenuated) X-ray flux. Lepp & Dalgarno (1996, their Fig. 3) find a rather narrow range of ionization rates for which the HCN abundance is high and consequently the XDR HCN line emissivities have difficulty

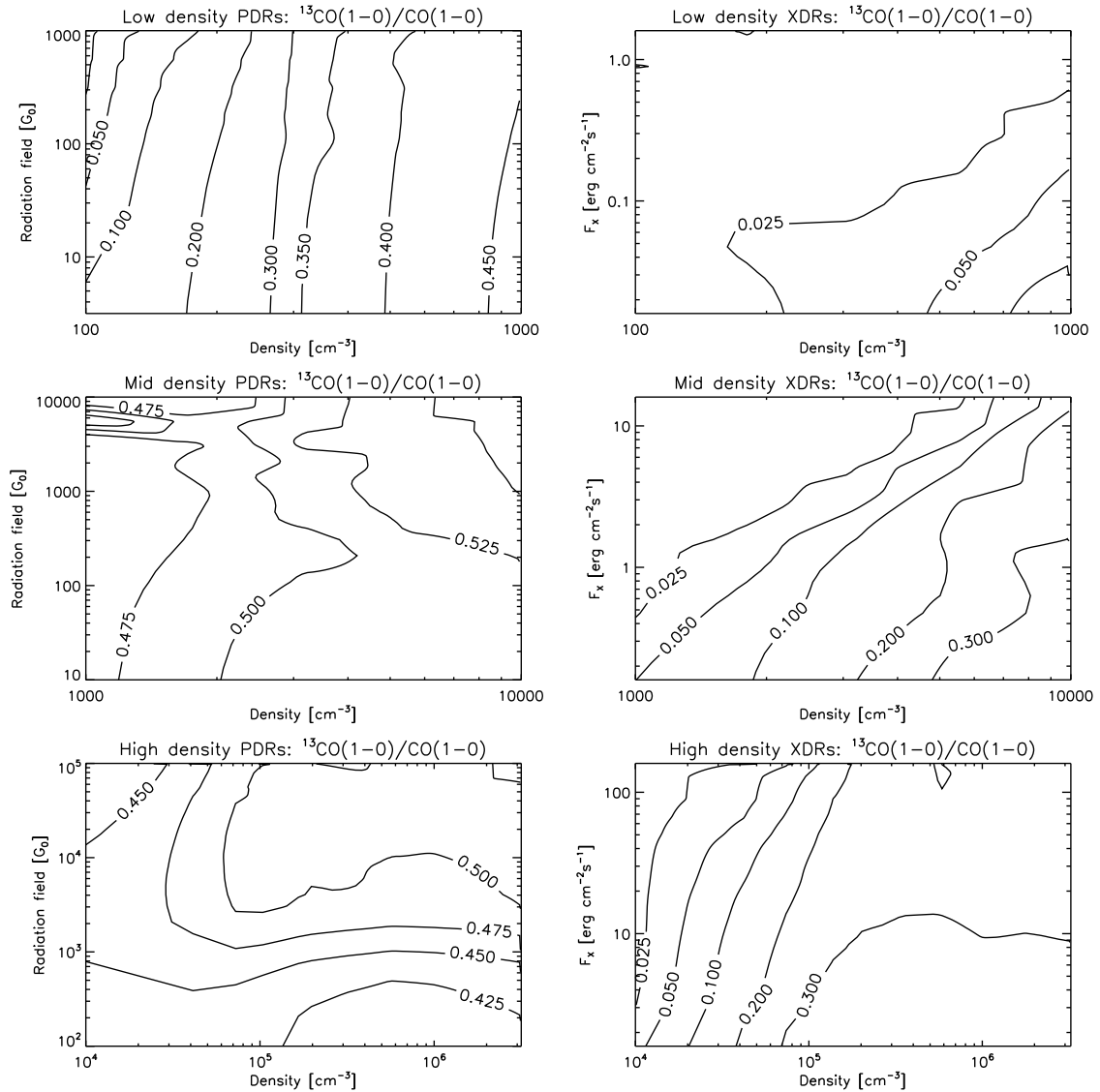


Figure 8.16: $^{13}\text{CO}(1-0)/\text{CO}(1-0)$ ratio for PDR (left) and XDR (right) models.

to compete with the PDR ones. The HCN(4-3) contour plots show about the same features as seen for the HCN(1-0). However, the PDR and XDR line strengths are now somewhat closer.

8.5.7 HCN/CO line intensity ratios

Intensity ratios of lines from the same species, such as the CO(4-3)/CO(1-0) ratio, vary with column density, due to the temperature gradient throughout the cloud, optical depth effects, varying abundance etc. Intensity ratios of lines from different species, in addition vary because of abundance ratio differences, complicating the interpretation of such line intensity ratios. In this section we turn our attention to the HCN/CO ratio, and start by showing in Figs. 8.20 and 8.21 the cumulative line intensity ratios for a set of PDRs

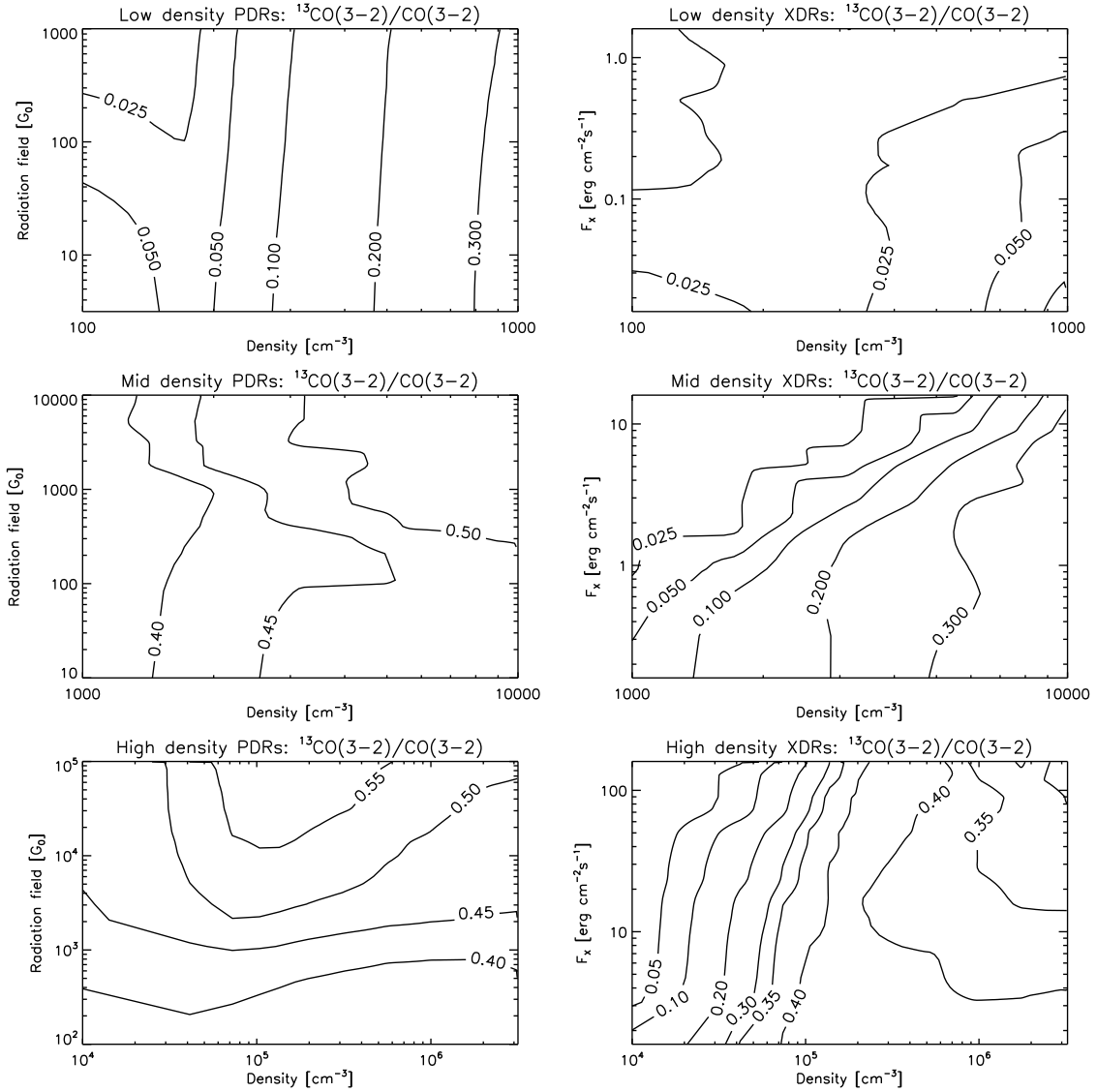


Figure 8.17: $^{13}\text{CO}(3-2)/\text{CO}(3-2)$ ratio for PDR (left) and XDR (right) models.

and XDRs at densities ranging from $n = 10^4 - 10^6 \text{ cm}^{-3}$ and incident fluxes between $G_0 = 10^3 - 10^5$ ($F_X = 1.6 - 160 \text{ erg s}^{-1} \text{ cm}^{-2}$). The cumulative line intensity is the emergent intensity arising from the edge of the cloud to column density $N_{\text{H}} = n_{\text{H}}z$:

$$I(z) = \frac{1}{2\pi} \int_0^z \Lambda(z') dz'. \quad (8.1)$$

In the PDR, both the $\text{HCN}(1-0)/\text{CO}(1-0)$ and the $\text{HCN}(4-3)/\text{CO}(4-3)$ ratio show a minimum. The HCN abundance shows a drop around the H/H_2 transition, while CO has its maximum abundance beyond the CO transition. Deeper in the cloud, the HCN/CO abundance ratio is more or less constant, but the CO line becomes optically thick and therefore the ratio increases.

When H_X/n is low in the XDR model, the gas is molecular, and the HCN/CO abun-

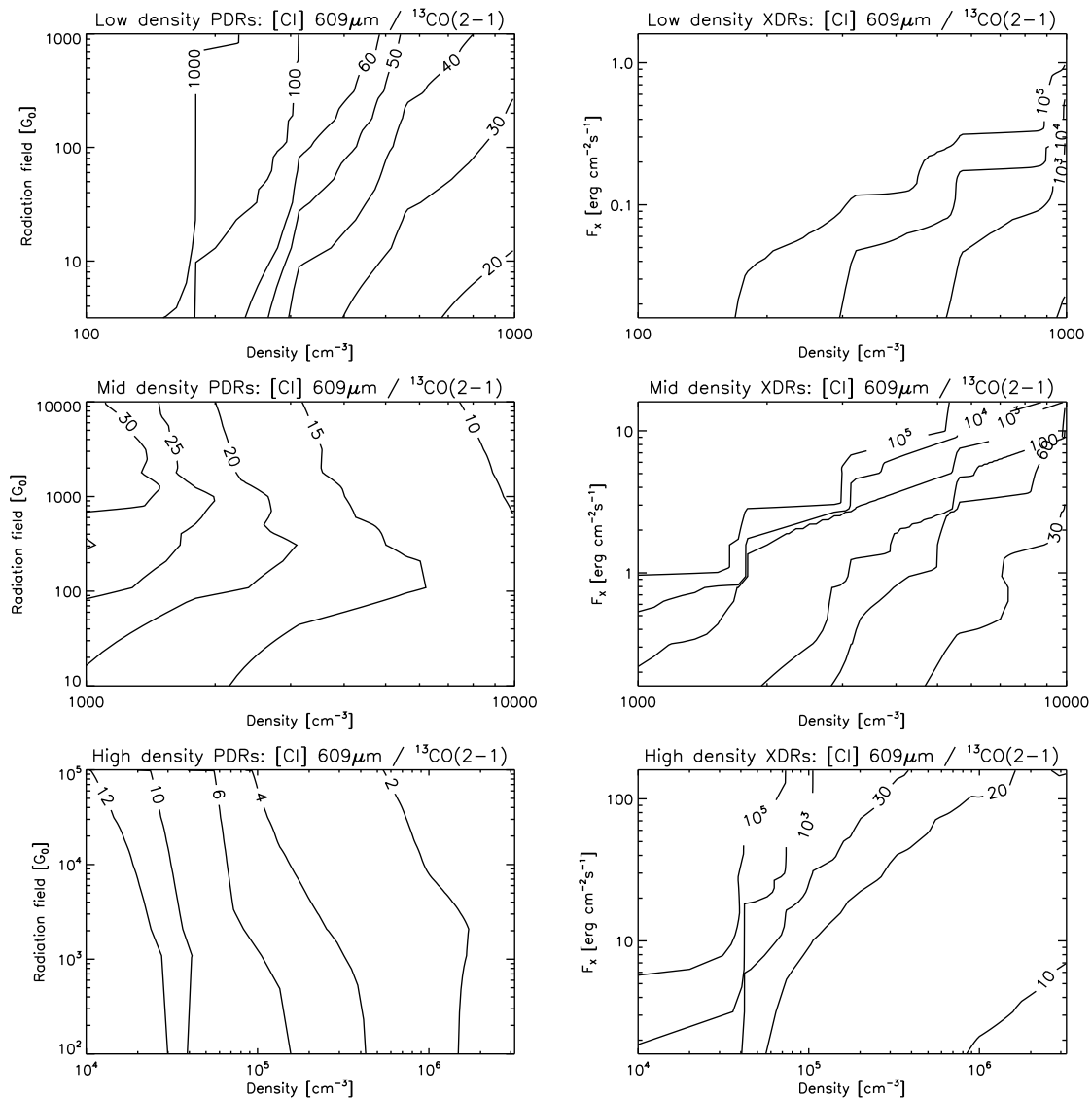


Figure 8.18: CI $609 \mu\text{m}/^{13}\text{CO}(2-1)$ ratio for PDR (left) and XDR (right) models.

dance ratio is more or less constant. A slow rise in the ratio is seen, as the CO line becomes optically thick. When the outer part of the cloud is atomic (for high H_X/n), HCN shows a maximum, before the H/H_2 transition. This also produces a maximum in the $\text{HCN}(1-0)/\text{CO}(1-0)$ ratio. In the PDR, the variation is not that large for column densities $N_H > 10^{22} \text{ cm}^{-2}$. In the XDRs, however, the variation between $N_H = 10^{22}$ and 10^{23} cm^{-2} can be rather large.

In Fig. 8.22, we show the $\text{HCN}(1-0)/\text{CO}(1-0)$ and $\text{HCN}(4-3)/\text{CO}(4-3)$ line ratios for a fixed cloud size of one parsec (cloud type A). The variation in the ratios is relatively large, due to the high critical densities of the HCN transitions. The PDR models produce the highest $\text{HCN}(1-0)/\text{CO}(1-0)$ ratios, which are attained at large densities ($n > 10^6 \text{ cm}^{-3}$) and may exceed unity. The corresponding XDRs have ratios are only 0.1-0.2. The interpretation of the low J transitions is very difficult due to high opacities, especially in the

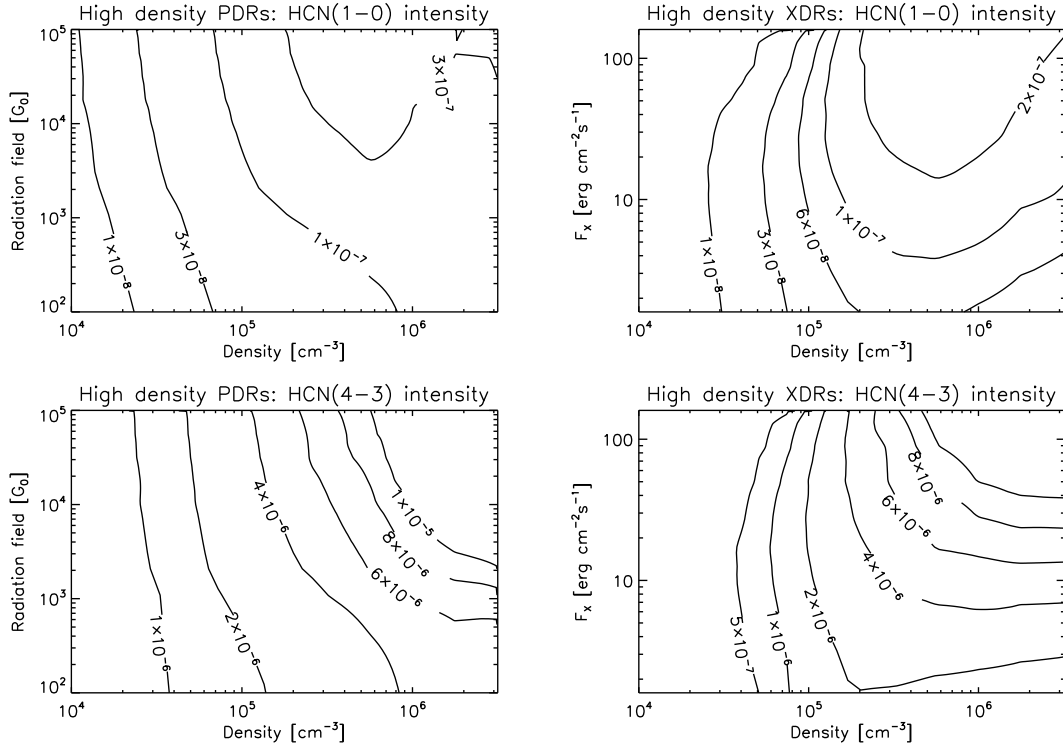


Figure 8.19: HCN(1-0) and HCN(4-3) intensity in $\text{erg cm}^{-2} \text{ s}^{-1} \text{ sr}^{-1}$ for PDR (left) and XDR (right) models.

PDRs. For this reason, we also show the HCN(4-3)/CO(4-3) ratio, which shows similar trends with density and radiation field, but with somewhat lower absolute ratios.

8.5.8 HCO⁺ rotational lines and HCN/HCO⁺ line intensity ratios

In Fig. 8.23, we show the HCO⁺(1-0) and HCO⁺(4-3) line intensities, with critical densities $n_{cr} \sim 2 \times 10^5$ and $4 \times 10^6 \text{ cm}^{-3}$, respectively. These critical densities are significantly lower than for HCN, causing a smaller spread in line intensities. Typically, the HCO⁺ lines are stronger in XDRs than in PDRs by a factor of at least three. This is a direct consequence of the higher ionization degree in XDRs (Meijerink & Spaans 2005), leading to an enhanced HCO⁺ formation rate.

Note in this that Lepp & Dalgarno (1996, their Fig. 2) find a rather wide range of ionization rates for which the HCO⁺ abundance is large. As for the HCN discussed above, this is consistent with our results since we integrate the depth dependent HCO⁺ abundance profile that results from the attenuation of the impinging X-ray flux. The HCO⁺ line-of-sight integral thus picks up a large contribution and competes favorably with the PDR line emissivities.

In Figs. 8.24 and 8.25, we show the cumulative HCN(1-0)/HCO⁺(1-0) and HCN(4-3)/HCO⁺(4-3) line intensity ratios, for the same PDR and XDR models as in Section 5.5. Depending on the incident radiation field, HCN or HCO⁺ is more abundant at the PDR edge of the cloud. Around the H/H₂ transition a minimum in the HCO⁺ abundance is

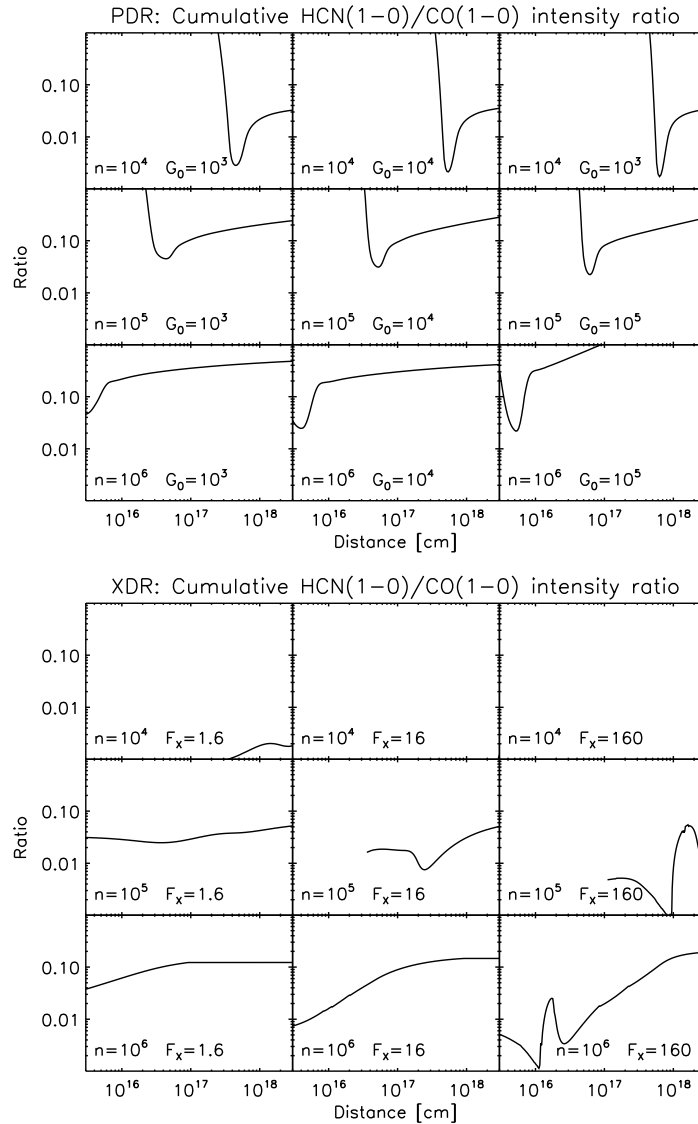


Figure 8.20: Cumulative HCN(1-0)/CO(1-0) line intensity ratios for PDR (top) and XDR (bottom).

seen in the PDR. Deeper into the cloud, the HCO^+ abundance increases again, and is then constant. This is also the case for HCN, and the HCN/HCO^+ abundance ratio is larger than unity. Therefore, at sufficiently large columns and densities, the $\text{HCN}(1-0)/\text{HCO}^+(1-0)$ line intensity ratio becomes larger than one.

In the XDR models, HCO^+ is chemically less abundant than HCN for very large H_X/n (Meijerink & Spaans 2005). For larger columns HCO^+ becomes more abundant, however, and eventually the cumulative column density of HCO^+ becomes larger than HCN (see specifically Fig. 10 in Paper I). This follows directly from the fact that the HCO^+ abundance is high over a much wider range of ionization rates than HCN (Lepp & Dalgarno 1996, their Figs. 2 and 3).

Fig. 8.26 clearly shows that the HCN/HCO^+ ratio discriminates between PDRs and

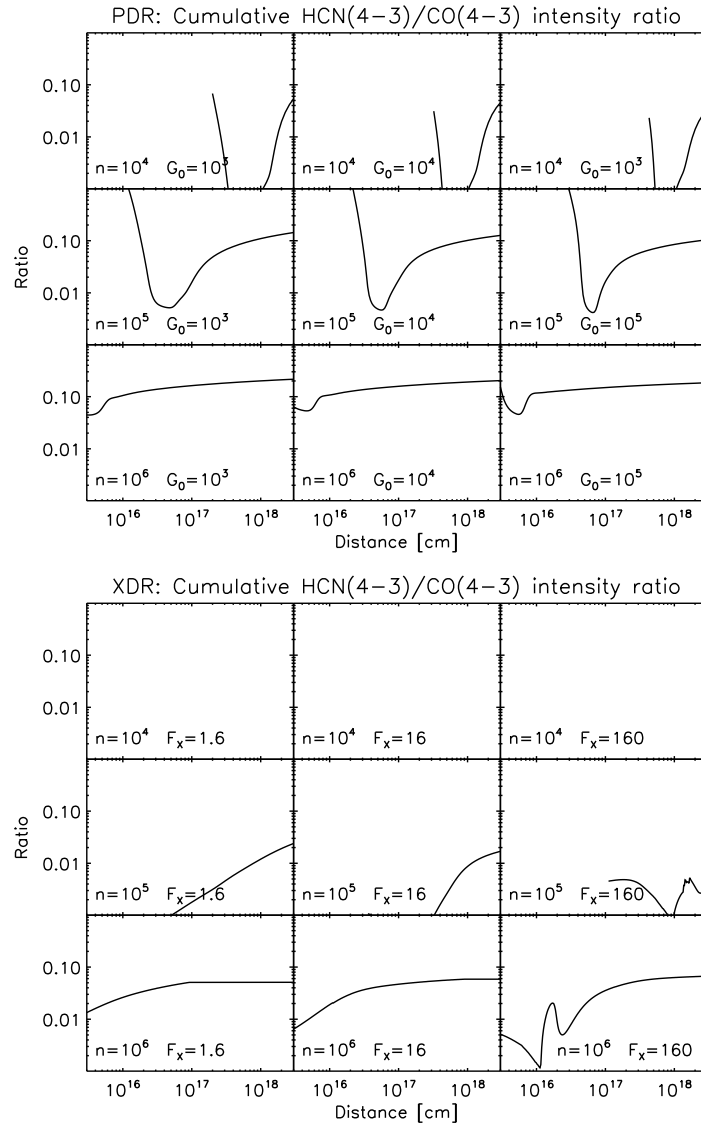


Figure 8.21: Cumulative HCN(4-3)/CO(4-3) line intensity ratios for PDR (top) and XDR (bottom).

XDRs in the density range between $n = 10^5$ and $10^{6.5} \text{ cm}^{-3}$ (cloud type A). The HCN(1-0)/HCO⁺(1-0) and HCN(4-3)/HCO⁺(4-3) line ratios are both much larger in the PDR models than XDR models, for columns of 10^{23} cm^{-2} and larger (Paper I). The difference ranges between a factor of 4-10, depending on the density. The XDR HCN(1-0)/HCO⁺(1-0) ratio becomes larger than unity for more modest columns of $10^{22.5} \text{ cm}^{-2}$ and less.

8.5.9 HNC/HCN ratios

The critical densities of HCN and HNC are almost identical, so that the only differences in line ratio should be due to differences in the abundances. In PDRs, HCN is more abundant in the radical region, but deeper in the cloud the abundance ratio approaches unity. In

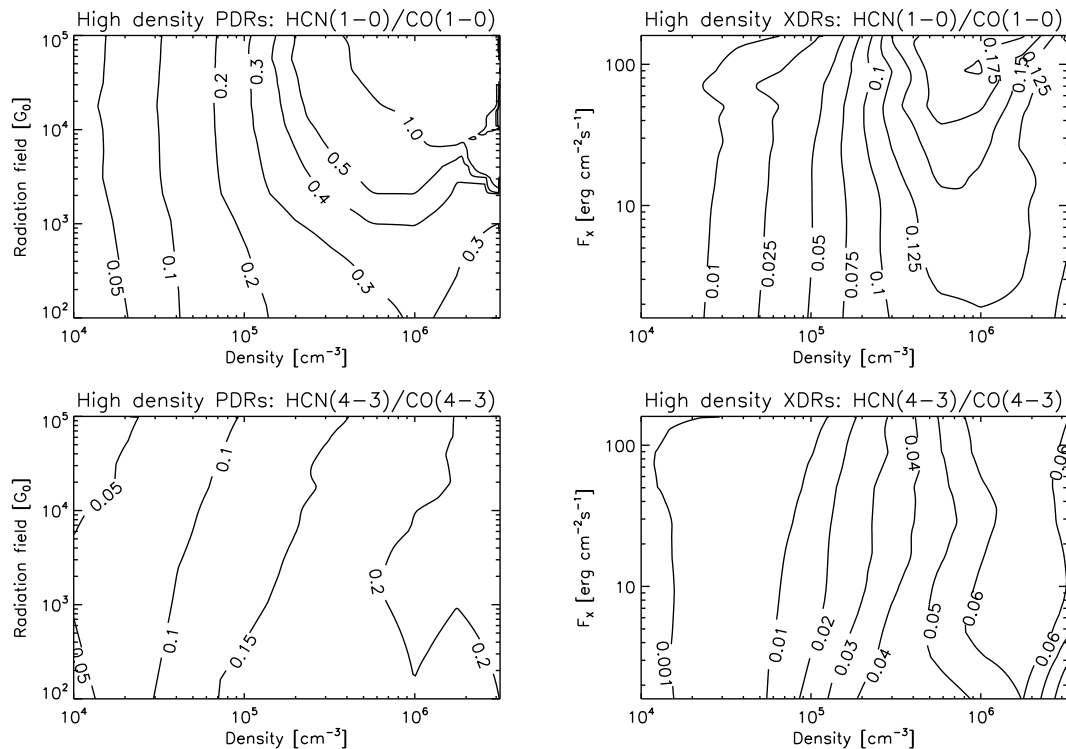


Figure 8.22: HCN(1-0)/CO(1-0) and HCN(4-3)/CO(4-3) ratios for PDR (left) and XDR (right) models.

XDRs, HCN is more abundant in the highly ionized part of the cloud. However, HNC is equally or even more abundant than HCN deep into the cloud. As a result, the HNC(1-0)/HCN(1-0) line intensity ratio is around one for the PDRs if the column density is larger than 10^{22} cm^{-2} , while the HNC(1-0)/HCN(1-0) ratio is less than unity for $N_H < 10^{22} \text{ cm}^{-2}$. The XDR models, however, show low ratios for the low, $\sim 10^4 \text{ cm}^{-3}$, densities and strong, $> 10 \text{ erg s}^{-1} \text{ cm}^{-2}$, radiation fields. The ratios increase for lower incident radiation fields, and at highest densities ($n = 10^{6.5} \text{ cm}^{-3}$) the line ratios are always larger than one, irrespective of irradiation.

In the PDRs, the HNC(4-3)/HCN(4-3) ratio quickly drops below unity at densities below $n = 10^5 \text{ cm}^{-3}$. This density is far below the critical densities of the lines, and therefore high temperatures are needed to excite them. Such high temperatures are indeed found in the radical regions of the PDRs, but there the HNC abundance is much lower than the HCN abundance, which explains the drop in the ratio. In the XDRs, the HNC(4-3)/HCN(4-3) ratios are quite similar to the HNC(1-0)/HCN(1-0) ratios, except for densities $n > 10^6 \text{ cm}^{-3}$, where they are even high than these.

8.5.10 SiO and CS

Although SiO is usually considered to be a good tracer of shocks, we do find that the SiO(1-0)/CO(1-0) ratio is typically larger in XDRs than in PDRs by a factor of 2-3, for densities around $10^{5.5} \text{ cm}^{-3}$. For the higher excitation J=4-3 lines, the effect disappears

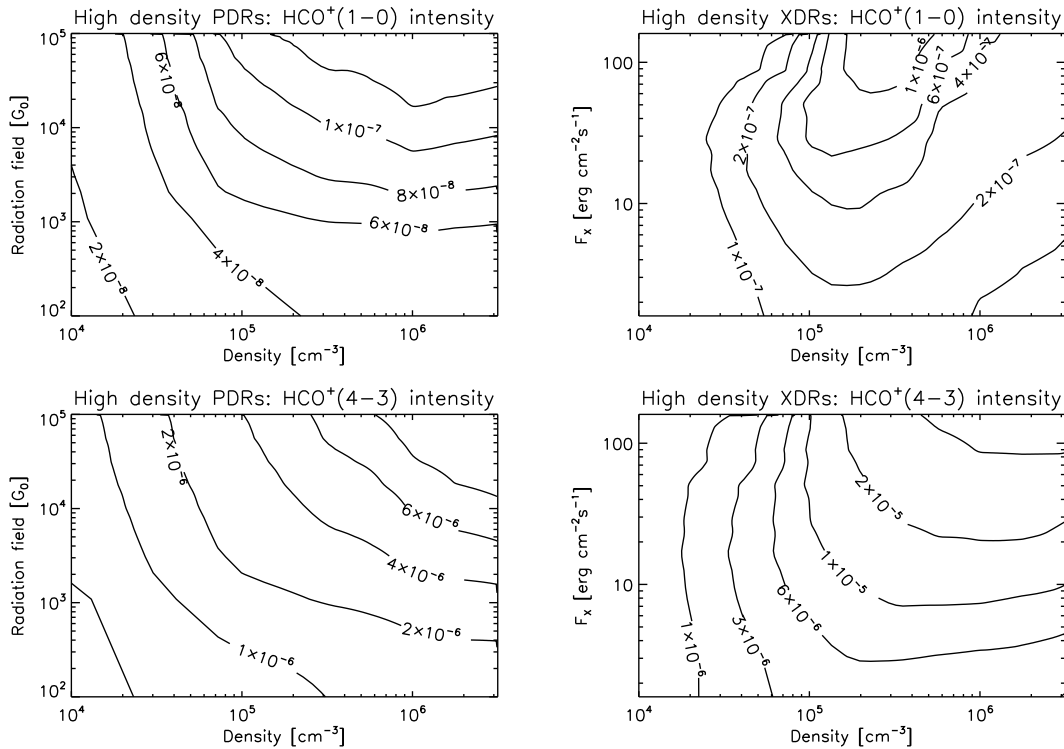


Figure 8.23: HCO⁺(1-0) and HCO⁺(4-3) intensity in erg cm⁻² s⁻¹ sr⁻¹ for PDR (left) and XDR (right) models.

because CO is generally warmer in XDRs compared to PDRs.

The CS(1-0)/HCN(1-0) ratio is a factor of two larger (smaller) in XDRs for densities above (below) 10⁵ cm⁻³. Interestingly, the corresponding 4-3 ratio continues this trend but changes in the ratio from 10⁴ to 10⁶ cm⁻³ are now as large as a factor of 10.

8.6 Column density ratios

Unfortunately, for many molecular species of interest no reliable collisional cross sections are available. For these species we are unable to accurately predict line intensities, but we can still calculate the column density ratios. In this section, we discuss column density ratios for a number of species that are of potential interest in attempts to discriminate between PDRs and XDRs.

8.6.1 CN/HCN column density ratio

In Fig. 8.34, we show the CN/HCN column density ratios. There is an enormous difference between the ratios for PDRs and XDRs. In the PDRs, the cloud type A ratios range from 0.5 ($n \sim 10^6$ cm⁻³) to 2.0 ($n \sim 10^4$ cm⁻³), while in the XDR models the same ratio varies from 40 ($n \sim 10^6$ cm⁻³) to over a 1000 ($n \sim 10^4$ cm⁻³). We find higher CN/HCN ratios at lower densities, where the chemical rates are lower, making it

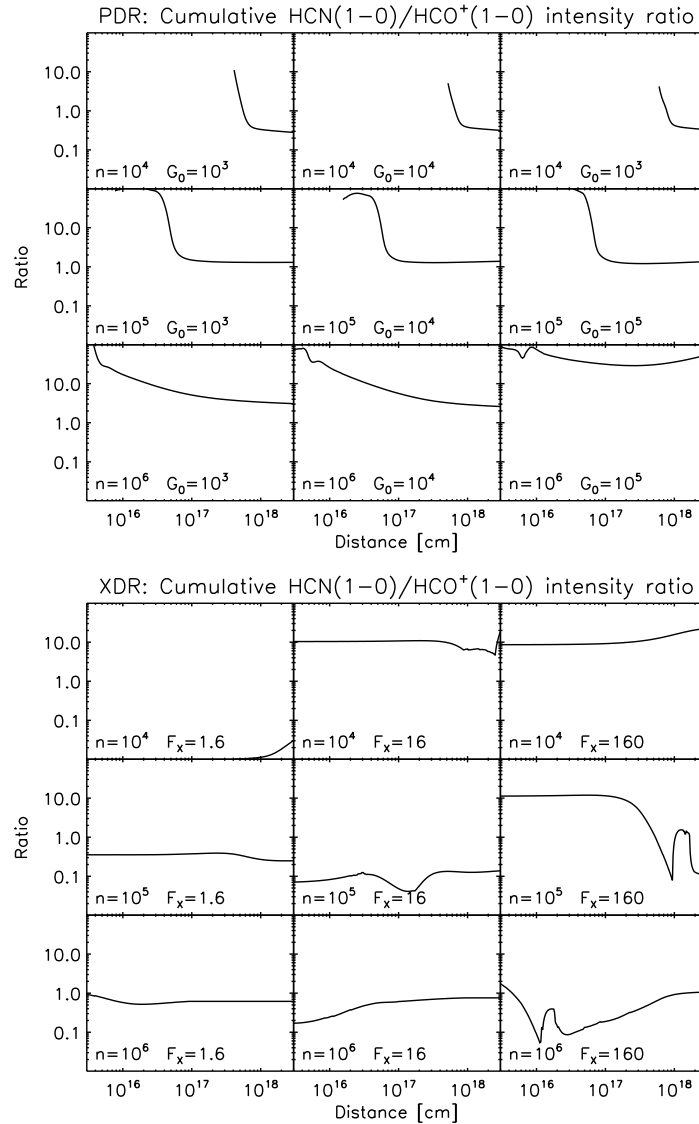


Figure 8.24: Cumulative HCN(1-0)/HCO⁺(1-0) line intensity ratios for PDR (top) and XDR (bottom).

more difficult to form large molecules. The PDR ratios are only dependent on density, which is explained by the fact that most CN and HCN molecules are formed beyond the H/H₂ transition. This part of the cloud is shielded from FUV photons and the chemistry is dominated by the cosmic ray ionization rate, which is the same in every model. In the XDR models, there is much less variation in the CN and HCN abundance throughout the cloud. The variations do not exceed more than two to three orders of magnitude, while this is over ten orders of magnitude in the PDR models. All parts of the cloud contribute almost equally to the column density ratio, including the region with very high H_X/n . H_X/n is a major factor in the resulting ratio, and therefore the XDRs also show a large dependence on incident radiation field.

In Fig. 8.35, we show the PDR and XDR cumulative CN/HCN ratios for a few specific

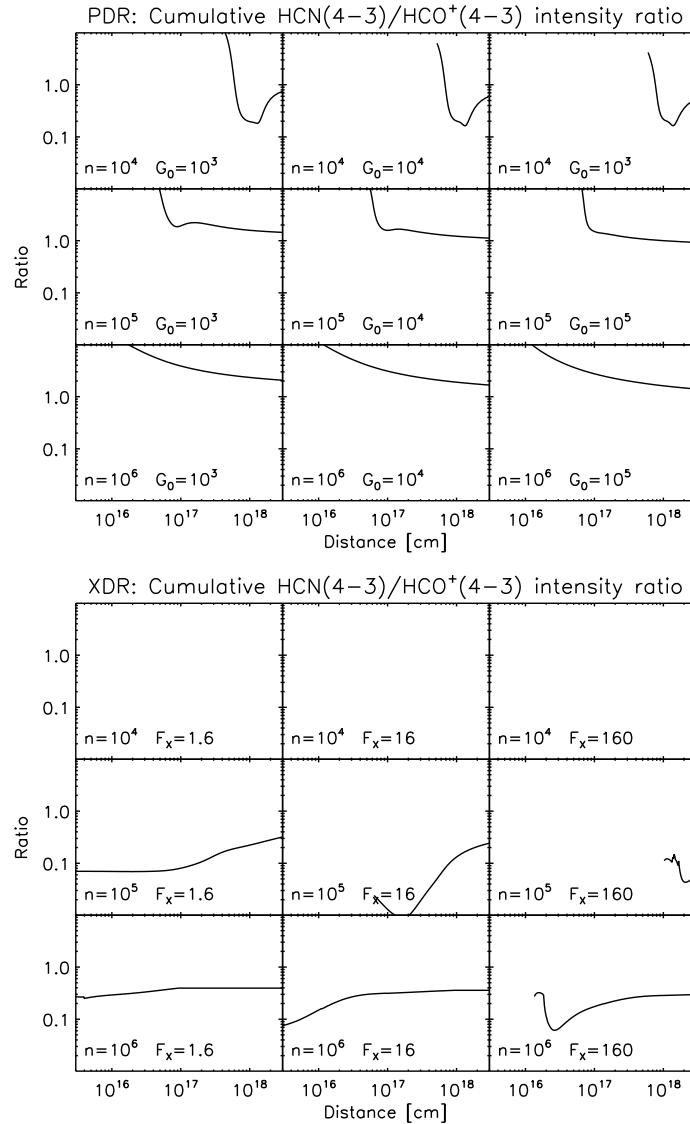


Figure 8.25: Cumulative HCN(4-3)/HCO⁺(4-3) line intensity ratios for PDR (top) and XDR (bottom).

densities and radiation fields. The variation in the cumulative column density ratio is much less in the XDR models than in the PDR models. At PDR edges, the gas is highly ionized (as in the XDRs), and here we find ratios resembling those of XDRs. Abundances, however, are very low here because of the high photo-dissociation rate.

8.6.2 CH/HCN column density ratios

In Fig. 8.36, we show the CH/HCN column density ratio. The differences between the ratios in PDRs and XDRs are even larger than in the case of CN/HCN. While the PDR ratios increase from 0.2 ($n \sim 10^6 \text{ cm}^{-3}$) to 0.9 ($n \sim 10^4 \text{ cm}^{-3}$), the XDR ratios range from 20 to more than 10000. The PDR ratio does not depend on density only. At relatively

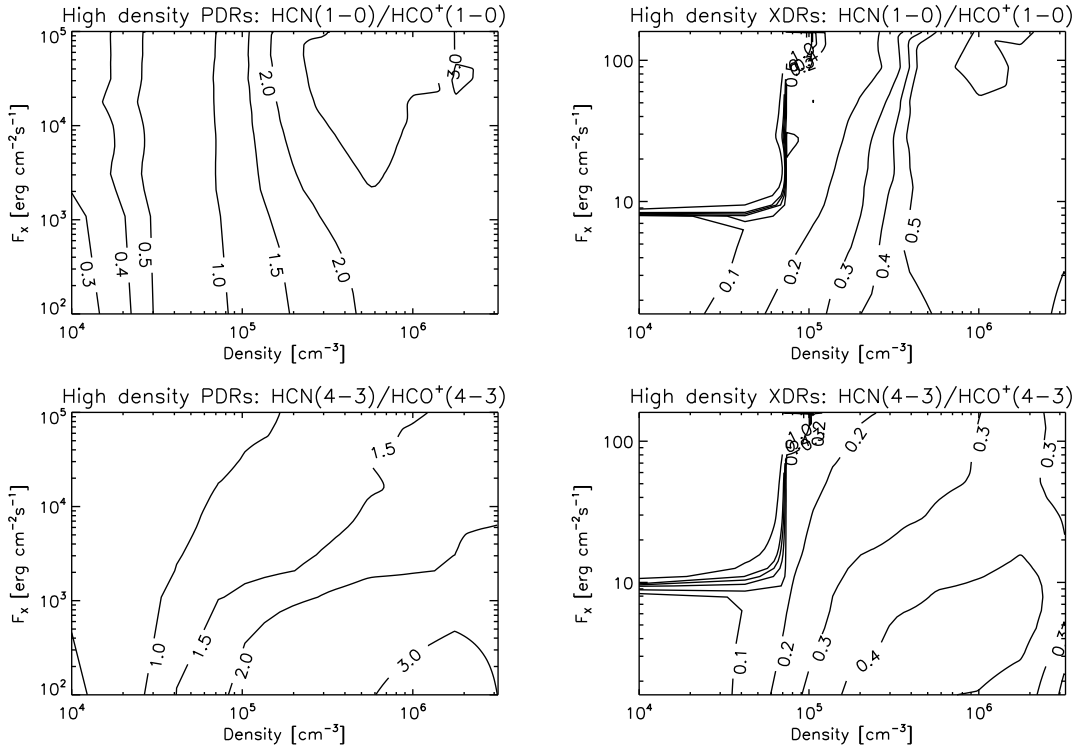


Figure 8.26: HCN(1-0)/HCO⁺(1-0) and HCN(4-3)/HCO⁺(4-3) ratios for PDR (left) and XDR (right) models.

low densities ($n = 1 - 3 \times 10^4 \text{ cm}^{-3}$), we find a dependency on incident radiation field as well. CH reaches its maximum abundance at greater depths than HCN, which means that the cumulative ratio is still increasing at large column densities. Our model cloud sizes are not large enough to allow the ratio to converge to a constant ratio (see Fig. 8.37). For the XDR models, we can roughly state that the ratio increases toward higher H_X/n . However, at $n \sim 10^5 \text{ cm}^{-3}$ the lowest ratio is not found at the lowest incident radiation field strength. At such densities, the limited cloud sizes are comparable to the depth of the H/H₂ transition. This transition is included in models with the lowest radiation field strengths, but not in those with the highest radiation field strengths.

8.6.3 CH⁺/HCN column density ratios

In Fig. 8.38, we show the CH⁺/HCN ratios for both PDR and XDR models. They range from 10^{-6} ($n \sim 10^6 \text{ cm}^{-3}$) to 6×10^{-4} ($n \sim 10^4 \text{ cm}^{-3}$) in the PDRs, and from 10^{-3} ($n \sim 10^6 \text{ cm}^{-3}$) to over 1000 ($n \sim 10^4 \text{ cm}^{-3}$) in the XDRs. In the PDR models, the highest CH⁺ abundance is seen close to the edge of the cloud but it decreases very quickly beyond the H/H₂ transition. HCN, on the contrary, reaches its highest abundance beyond this transition. This explains the decrease of the PDR cumulative column density ratios with increasing depth (Fig. 8.39). The PDR models show a dependence on both density and incident radiation field for this ratio. The decrease in the ratio with increasing density is caused by the fact that on the one hand CH⁺ is more easily destroyed (due to higher

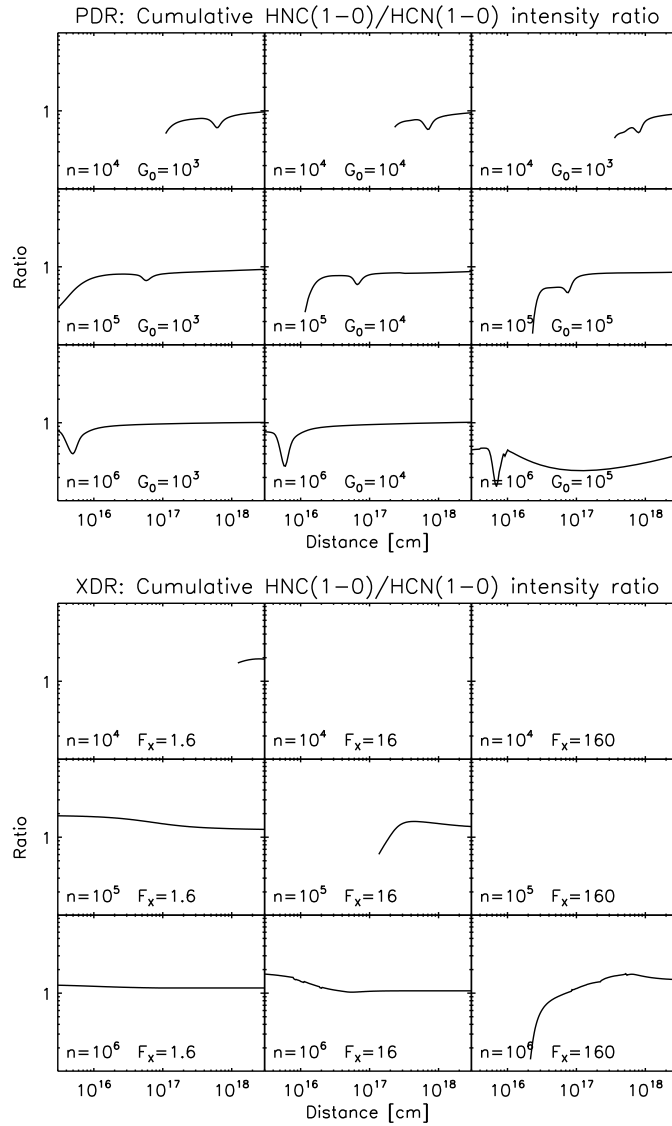


Figure 8.27: Cumulative HNC(1-0)/HCN(1-0) line intensity ratios for PDR (top) and XDR (bottom).

recombination rates) and on the other hand HCN more easily formed when densities are higher. The ratios do not converge to a constant value deep into the cloud. At identical densities, the ratio increases with increasing radiation field, since the HCN column densities become smaller while the CH^+ column densities become larger for the cloud-size considered here. In the XDR models, the largest ratios are seen for the highest H_X/n (low density and high incident radiation field). The fluctuations in the CH^+ and HCN abundances are more gradual. The HCN abundance increases and the CH^+ abundance decreases when the X-ray photons are gradually absorbed. Therefore, the XDR cumulative column densities ratios show less variation than the PDR ratios (see Fig. 8.39).

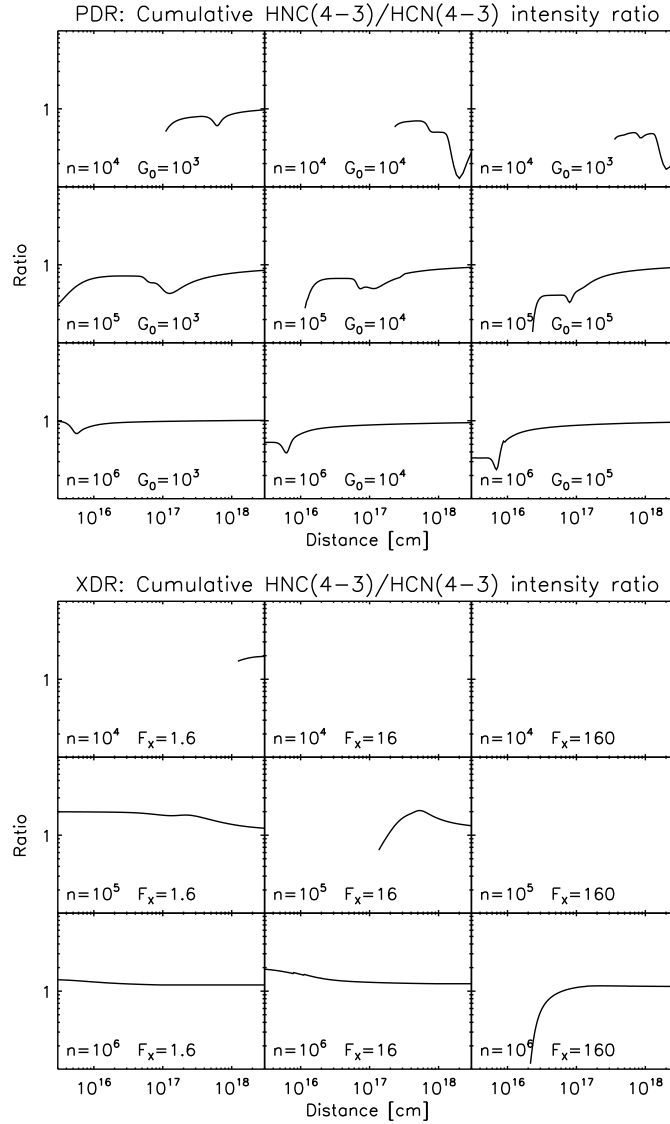


Figure 8.28: Cumulative HNC(4-3)/HCN(4-3) line intensity ratios for PDR (top) and XDR (bottom).

8.6.4 HCO/HCO⁺ column density ratios

Fig. 8.40 shows the HCO/HCO⁺ column density ratios. For the PDRs, we find much larger ratios than for the XDRs. The PDRs show ratios between 0.1 ($n \sim 10^4$ cm $^{-3}$) and 10.0 ($n \sim 10^6$ cm $^{-3}$), while the ratios in the XDR range from 10^{-5} ($n \sim 10^4$ cm $^{-3}$) to 10^{-3} ($n \sim 10^6$ cm $^{-3}$). In the PDRs, the ratios depend only on density for radiation fields $G_0 < 10^4$. With larger incident radiation fields, the ratio becomes dependent on the radiation field strength as well. The HCO abundance reaches its maximum and more or less constant abundance somewhat deeper into the cloud than HCO⁺. As column density increases, the HCO/HCO⁺ ratio slowly converges to a constant value (see Fig.8.41). For large radiation fields ($G_0 > 10^4$), the cloud size considered here is too small to allow

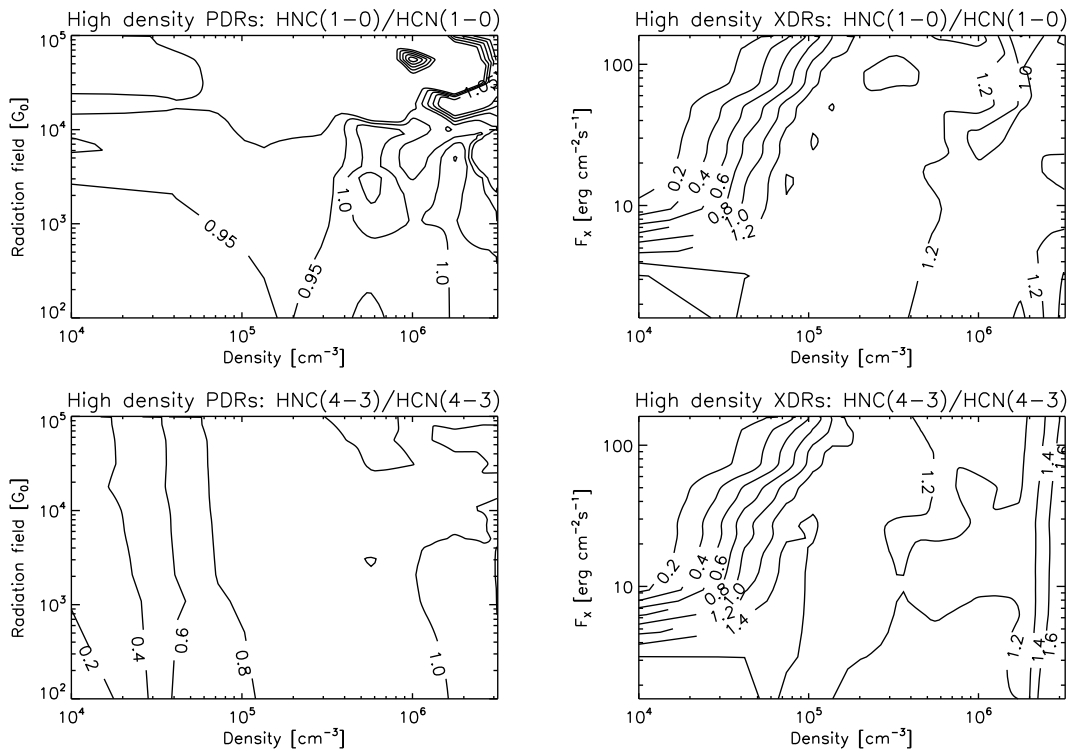


Figure 8.29: HNC(1-0)/HCN and HNC(4-3)/HCN(4-3) ratios for PDR (left) and XDR (right) models.

column densities to converge to a constant ratio. In the XDR models, the ratio depends on both density and radiation field in all regimes. The lowest ratios are seen for high H_X/n ($n = 10^4 \text{ cm}^{-3}$ and $F_X = 160$).

8.6.5 $\text{HOC}^+/\text{HCO}^+$ column density ratios

In Fig. 8.42, we show the $\text{HOC}^+/\text{HCO}^+$ column density ratios. The XDRs show larger ratios, ranging from 10^{-4} ($n \sim 10^6 \text{ cm}^{-3}$) to 0.6 ($n \sim 10^4 \text{ cm}^{-3}$), than PDRs, where the ratios range from 10^{-7} to 10^{-5} . The XDR ratios increase for larger H_X/n (with maximum at $n \sim 10^4 \text{ cm}^{-3}$ and $F_X = 160$). The behavior is more complex for the PDR models. The ratios depend on density only for $G_0 > 10^4$, but below this value there is also a dependency on radiation field strength. This is explained by the fact that ratios drop very fast, when the gas becomes molecular (Fig. 8.43), but abundances are still significant. A large fraction of the gas at the edge of the cloud is molecular for densities $n > 10^{5.5} \text{ cm}^{-3}$ and radiation fields $G_0 < 10^4$. Here we find a fast decrease in the ratio for lower radiation fields.

8.6.6 NO/CO column density ratios

In Fig 8.44, we show the NO/CO column density ratios. The ratios in XDRs are much larger, 10^{-4} ($n \sim 10^6 \text{ cm}^{-3}$) to 10^{-3} ($n \sim 10^4 \text{ cm}^{-3}$), than for PDRs ($10^{-6} - 10^{-5}$). In

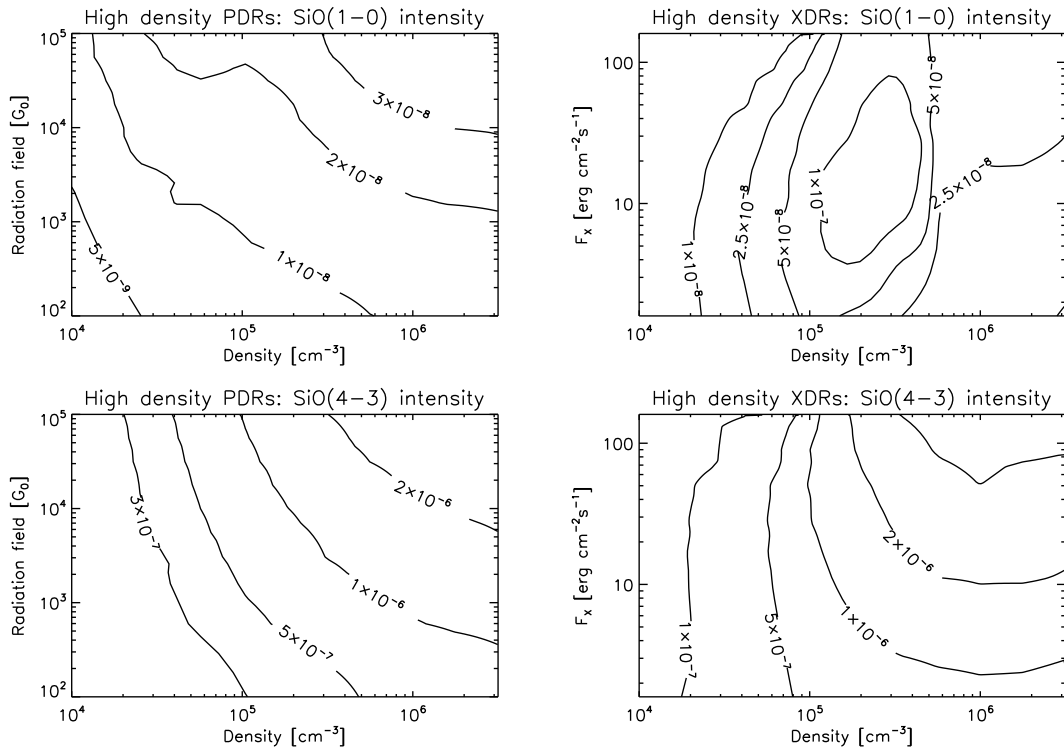


Figure 8.30: SiO(1-0) and SiO(4-3) intensity in $\text{erg cm}^{-2} \text{s}^{-1} \text{sr}^{-1}$ for PDR (left) and XDR (right) models.

the PDR the ratios are largely determined in the molecular part of the cloud and depend more or less on density only. The ratios in the XDR depend mostly on H_X/n . The largest ratios are seen for the largest H_X/n ($n \sim 10^4 \text{ cm}^{-3}$ and $F_X = 160$).

CO(1-0) lines have optical depths of $\tau(\text{CO}(1-0)) \sim 100$. Therefore, it could be possible to observe NO(1-0)/CO(1-0) line intensity ratios as large as 0.1, while the maximum column density ratios are only 10^{-3} .

8.6.7 $\text{N}_2\text{H}^+/\text{CO}$ column density ratios

In Fig. 8.46, we show the $\text{N}_2\text{H}^+/\text{CO}$ column density ratio. In both PDRs and XDRs the model ratios are rather low. They decrease with density in the PDR ($10^{-7} - 10^{-9}$), which is opposite to the behavior in XDRs. In the XDRs, we find a decrease with increasing H_X/n . There are collisional data available for N_2H^+ , but since the abundances are so low, the line intensities are too small to be observable.

8.7 Summary and outlook

We have presented a large set of PDR and XDR models that can be used to determine the physical conditions that pertain to irradiated gas clouds. This grid spans a large range in densities ($n_{\text{H}} = 10^2 - 10^{6.5} \text{ cm}^{-3}$), irradiation ($G_0 = 10^{0.5} - 10^5$ and $F_X = 1.6 \times$

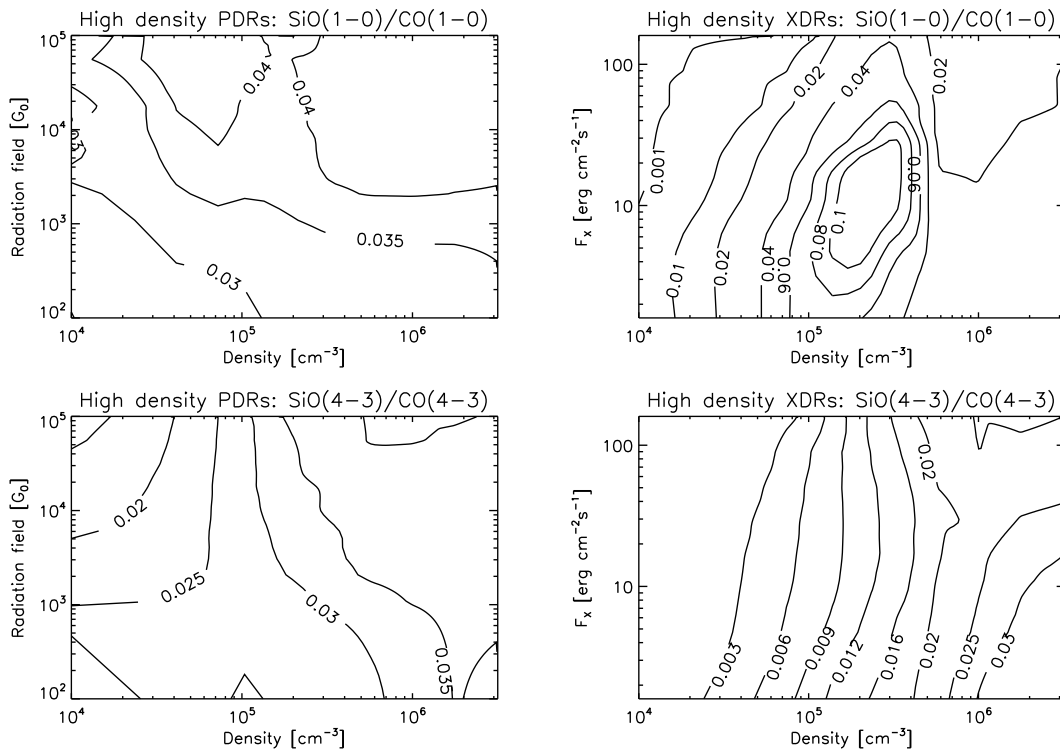


Figure 8.31: SiO(1-0)/CO and SiO(4-3)/CO(4-3) ratios for PDR (left) and XDR (right) models.

$10^{-2} - 160 \text{ erg cm}^{-2} \text{ s}^{-1}$) and column densities ($N_{\text{H}} = 1.5 \times 10^{22} - 1 \times 10^{25} \text{ cm}^{-2}$). We have used the results to make predictions for the intensities and ratios of the most important atomic fine-structure lines, e.g., [CII], [OI], [CI], [SiII], and [FeII], rotational lines for molecular species such as HCO^+ , HCN, HNC, CS and SiO (up to $J = 4$), CO and ^{13}CO up to $J = 16$, and for column densities for CN, CH, CH^+ , HCO, HOC^+ , NO, and N_2H^+ . It is not possible to present all the results, but they are available on-line at the following URL: <http://www.strw.leidenuniv.nl/~meijerin/grid/>. Here we summarize the most important conclusions:

1. The surface temperatures are higher (lower) in PDRs compared to XDRs for densities $n > 10^4 \text{ cm}^{-3}$ ($n < 10^4 \text{ cm}^{-3}$). Two opposing effects play a major role in determining the resulting surface temperature: (1) The heating efficiency, which is much higher in XDRs (up to 70 percent) than in PDRs (0.5-3.0 percent); (2) The absorption cross sections which are much smaller for X-rays than for FUV photons.
2. For the atomic lines, we find that the fine-structure line ratios of [SiII] $35 \mu\text{m}$ /[CII] $158 \mu\text{m}$, [OI] $63 \mu\text{m}$ /[CII] $158 \mu\text{m}$, [FeII] $26 \mu\text{m}$ /[CII] $158 \mu\text{m}$, and [CI] $369 \mu\text{m}$ /[CI] $609 \mu\text{m}$ are higher in XDRs than in PDRs, for a given density, column, and irradiation strength. Whereas PDR ratios depend on density and irradiation strength only, XDR depend on column density as well. In PDRs, fine-structure line emission is only produced at the edge of the cloud, while in XDRs almost all parts of the cloud contribute.

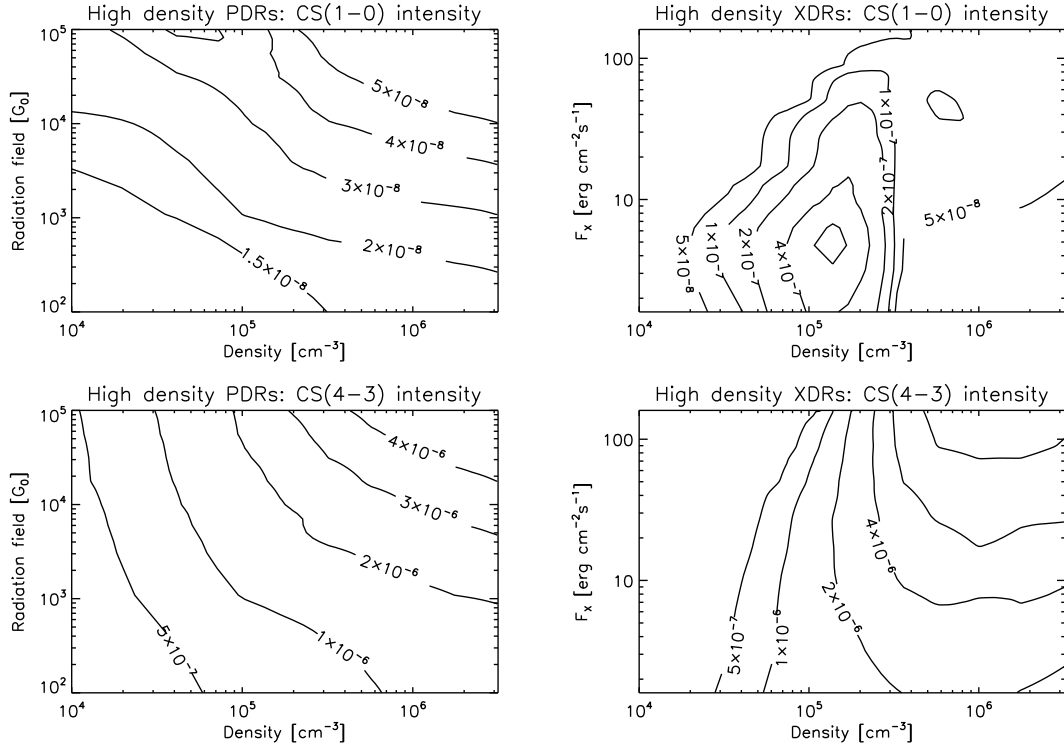


Figure 8.32: SiO(1-0) and SiO(4-3) intensity in $\text{erg cm}^{-2} \text{s}^{-1} \text{sr}^{-1}$ for PDR (left) and XDR (right) models.

3. We find higher CO line ratios for XDRs. In PDRs, CO is formed beyond the H/H_2 transition and typically has temperatures in the range $T \sim 20 - 50$ K. In XDRs, CO is present throughout the cloud in significant abundances, even in the highly ionized part. When using CO line ratios, the best way to distinguish between PDRs and XDRs is to consider ratios such as $\text{CO}(16-15)/\text{CO}(1-0)$, where the differences are largest (Fig. 8.11).
4. HCN/HCO^+ ratios discriminate well between PDRs and XDRs, even in the lower rotational lines, and especially when densities are as high as $n > 10^5 \text{ cm}^{-3}$. At such densities, the $\text{HCN}(1-0)/\text{HCO}^+(1-0)$ line intensity ratios are < 1 in XDRs, while PDRs have ratios > 1 for column densities $N_{\text{H}} > 10^{23} \text{ cm}^{-2}$. Although the HCN/HCO^+ line ratio in an XDR may become even larger in clouds of relatively modest density (10^4 cm^{-3}) subjected to high radiation field strengths ($> 100 \text{ erg s}^{-1} \text{ cm}^{-2}$), we find that the line intensities in this part of parameter space are too low to be detectable (see also Meijerink et al. 2006a).
5. For densities between 10^4 and $10^{6.5} \text{ cm}^{-3}$, $\text{HNC}(1-0)/\text{HCN}(1-0)$ ratios in PDRs are of order 1 (< 1) for columns larger (smaller) than 10^{22} cm^{-2} , while the ratios range between 0.2-1.2 for XDRs. For densities $n > 10^6 \text{ cm}^{-3}$, PDR $\text{HNC}(4-3)/\text{HCN}(4-3)$ ratios remain of order 1, while we find XDR ratios up to 1.6.
6. HCN/CO ratios are typically smaller for in XDRs than in PDRs, for two reasons: (1)

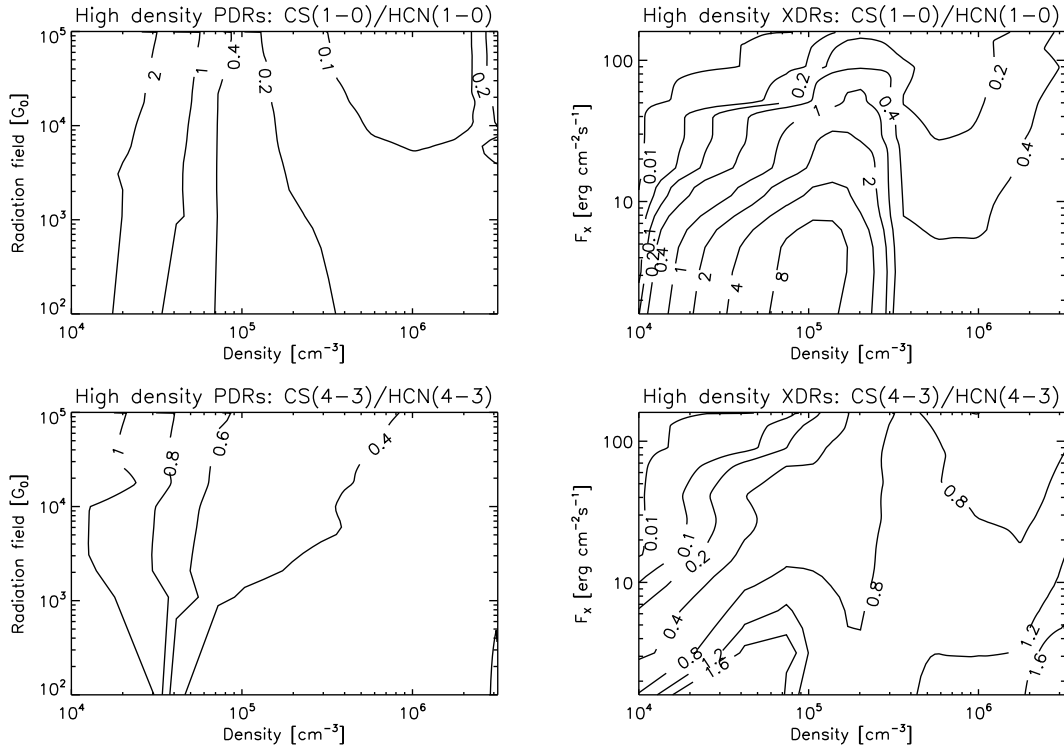


Figure 8.33: CS(1-0)/HCN and CS(4-3)/HCN(4-3) ratios for PDR (left) and XDR (right) models.

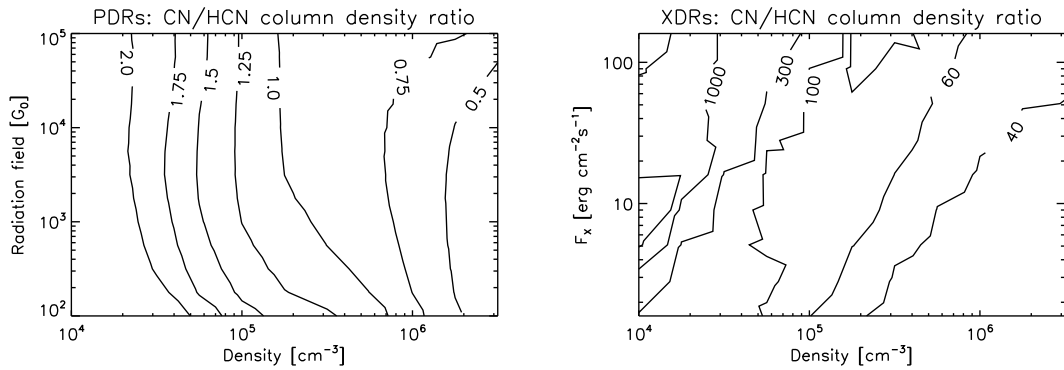


Figure 8.34: CN/HCN column density ratios for PDR (left) and XDR (right) models.

The HCN abundance is boosted only in high (column) density gas, with columns in excess of 10^{23} cm^{-2} and densities larger than 10^4 cm^{-2} ; (2) CO is warmer in XDRs, which leads to stronger emission, and this suppresses the HCN/CO ratios as well. In PDRs, the very high HCN(1-0)/CO(1-0) ratios of order > 1 are only obtained at very high column densities ($N_{\text{H}} > 10^{23} \text{ cm}^{-2}$).

7. We find that CN/HCN, NO/CO, and $\text{HOC}^+/\text{HCO}^+$ column density ratios are discriminant between PDRs and XDRs. Molecules such as CH and CH^+ also look very promising. However, we urgently need reliable collisional cross section data

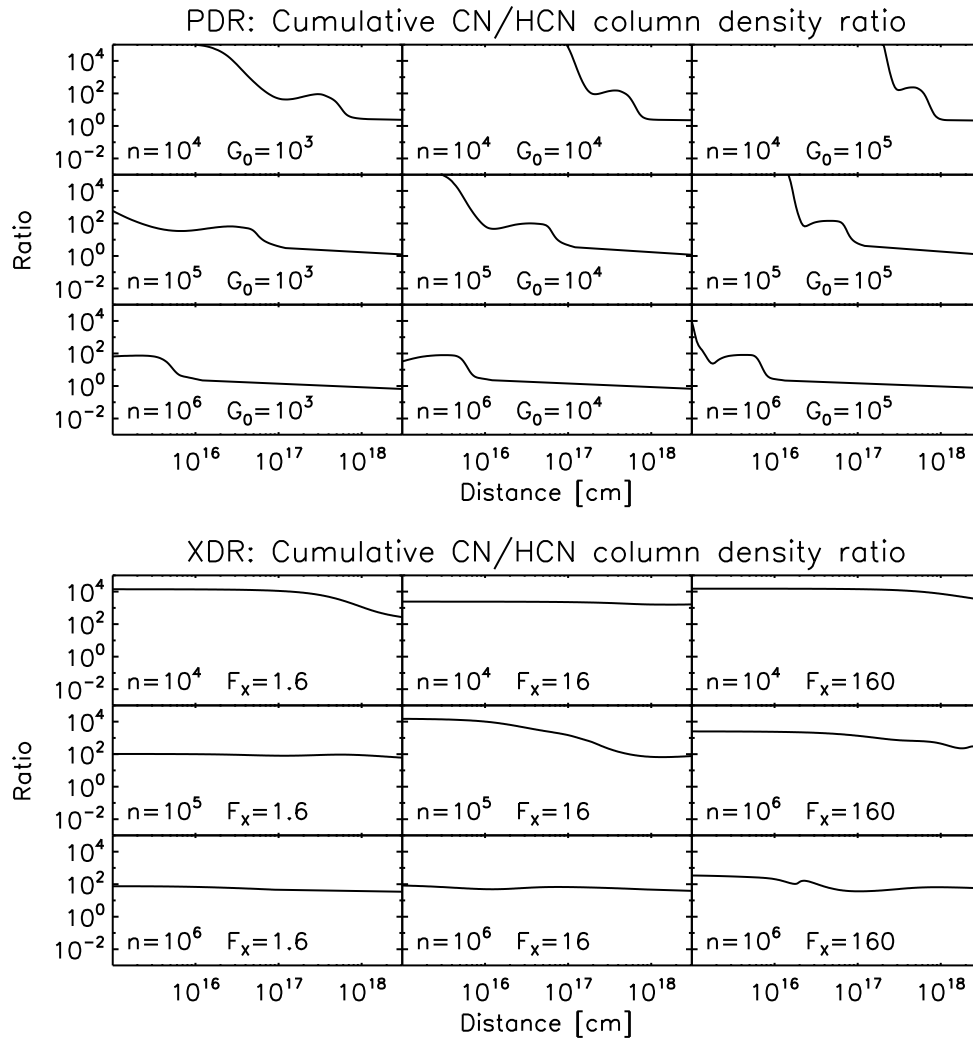


Figure 8.35: Cumulative CN/HCN column density ratios for PDR (top) and XDR (bottom) models.

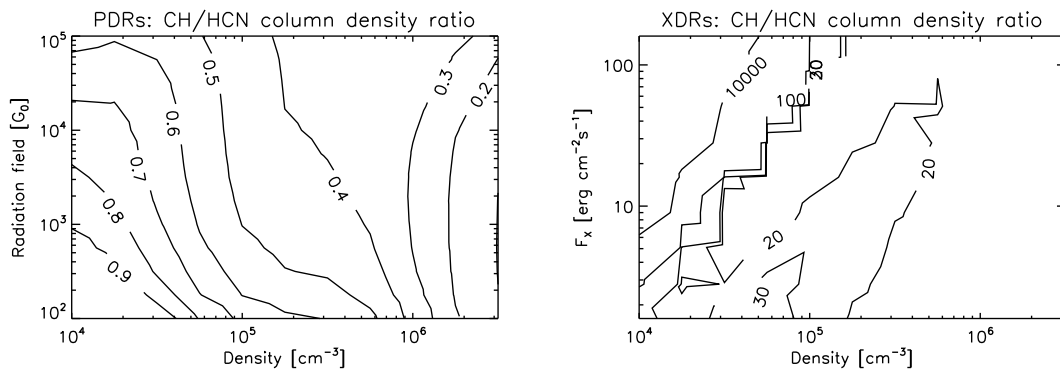


Figure 8.36: CH/HCN column density ratios for PDR (left) and XDR (right) models.

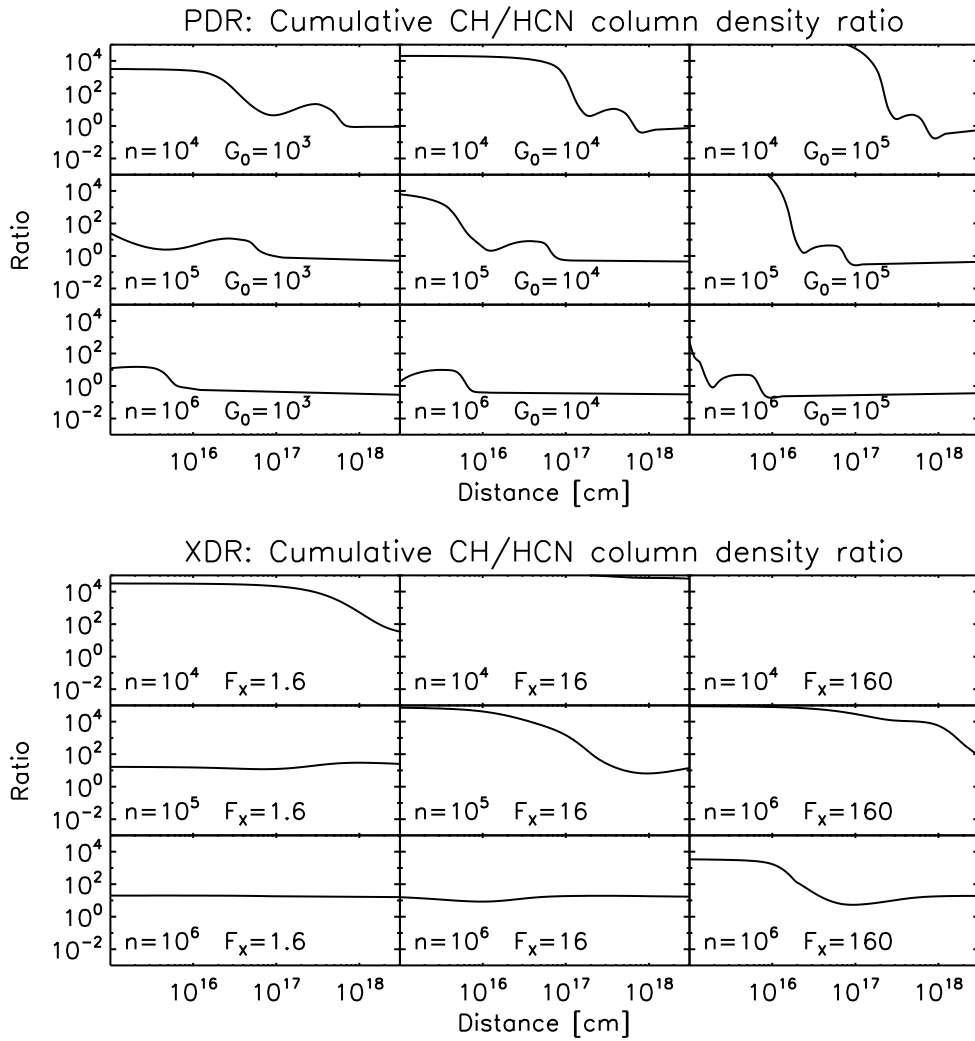


Figure 8.37: Cumulative CH/HCN column density ratios for PDR (top) and XDR (bottom) models.

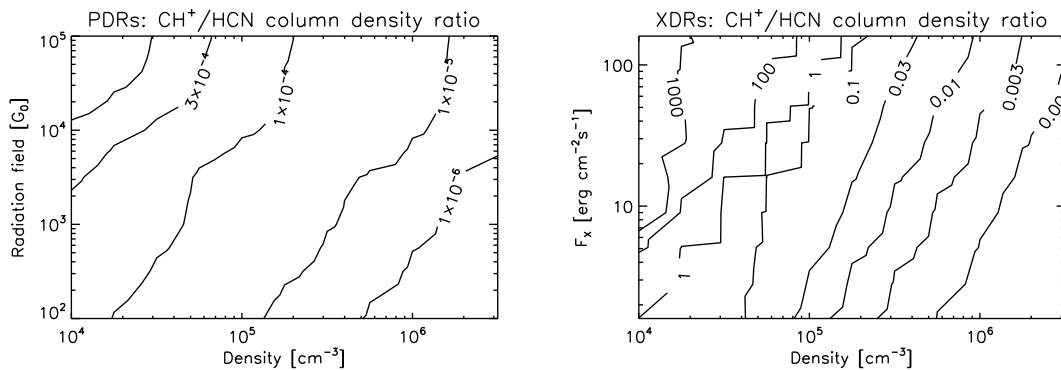


Figure 8.38: CH⁺/HCN column density ratios for PDR (left) and XDR (right) models.

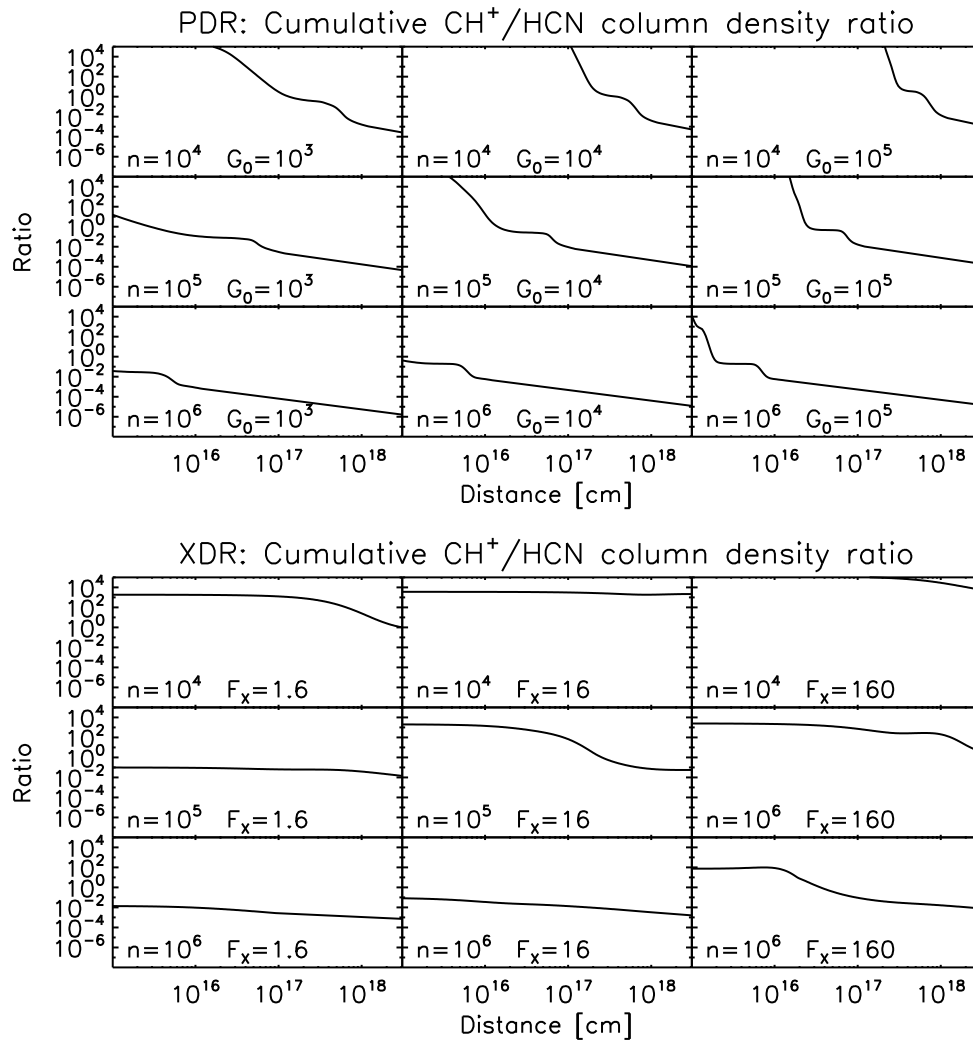


Figure 8.39: Cumulative CH^+/HCN column density ratios for PDR (top) and XDR (bottom) models.

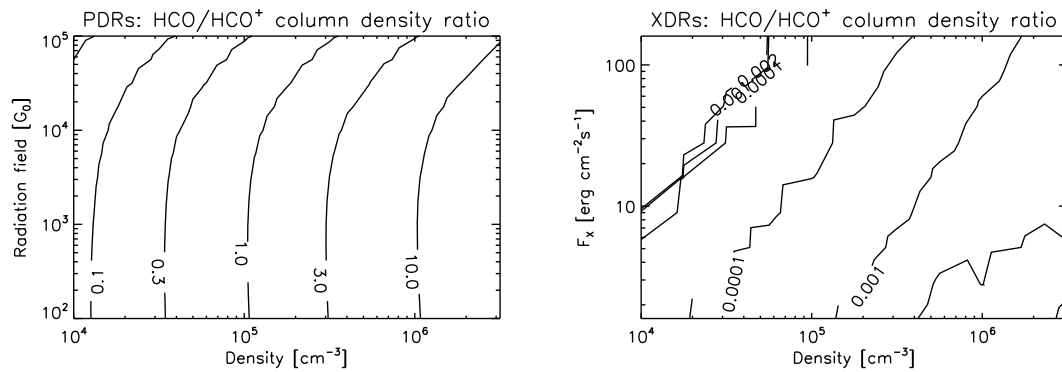


Figure 8.40: HCO/HCO^+ column density ratios for PDR (left) and XDR (right) models.

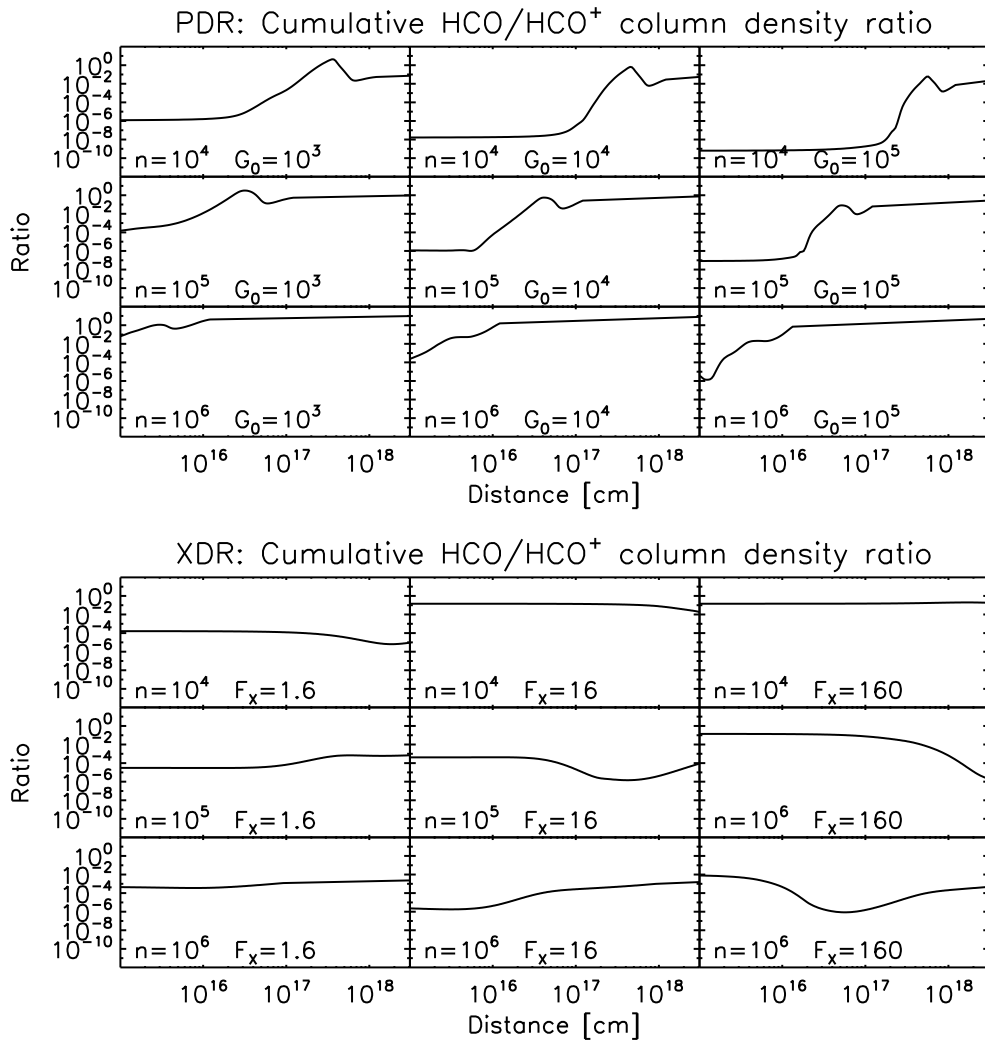


Figure 8.41: Cumulative HCO/HCO⁺ column density ratios for PDR (top) and XDR (bottom) models.

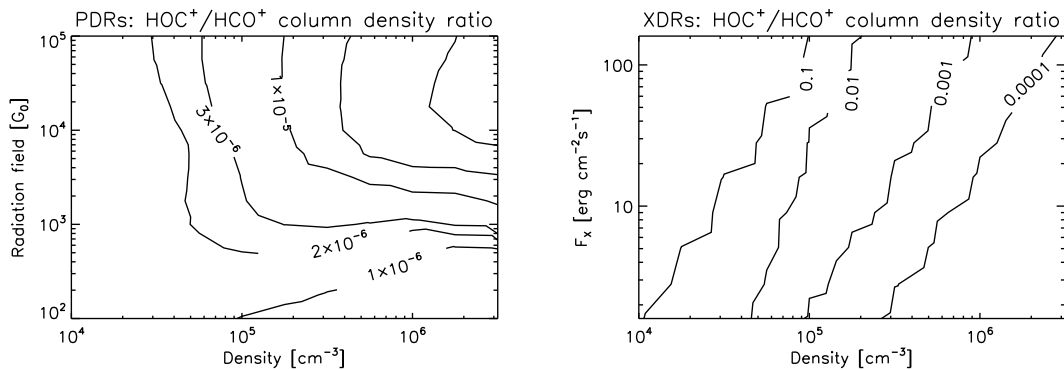


Figure 8.42: HOC⁺/HCO⁺ column density ratios for PDR (left) and XDR (right) models.

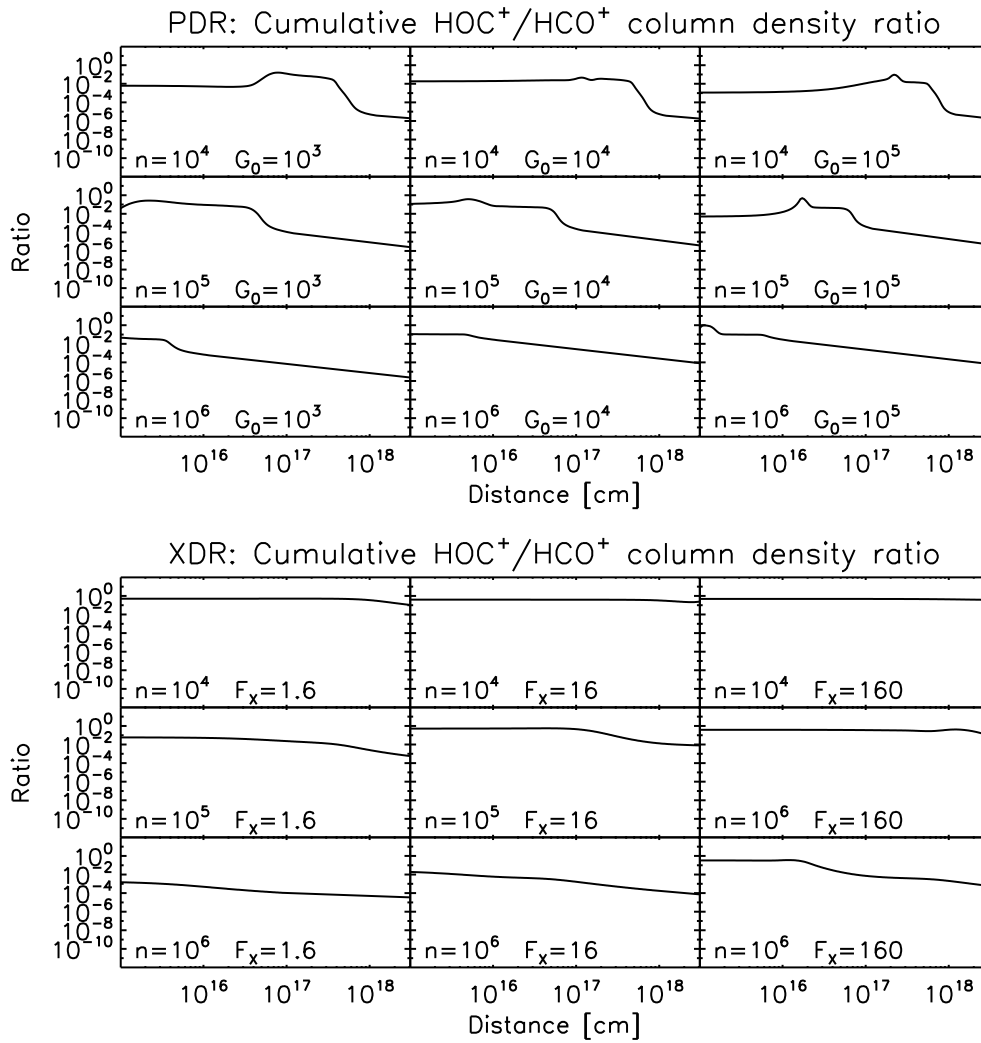


Figure 8.43: Cumulative $\text{HOC}^+/\text{HCO}^+$ column density ratios for PDR (top) and XDR (bottom) models.

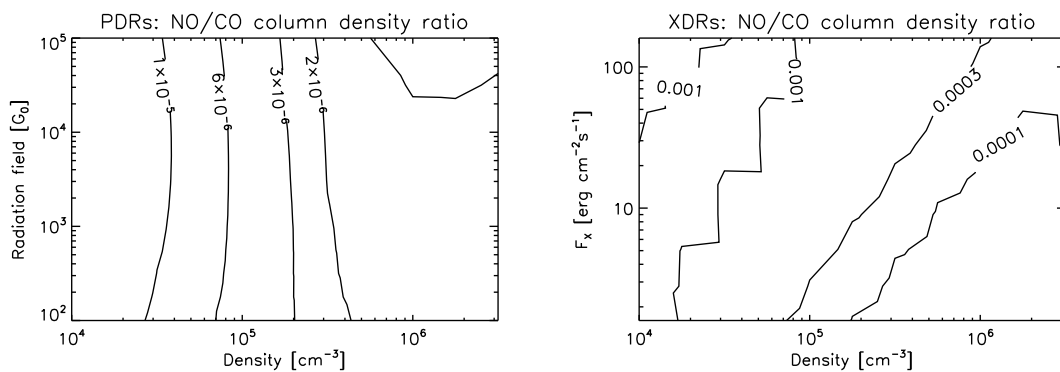


Figure 8.44: NO/CO column density ratios for PDR (left) and XDR (right) models.

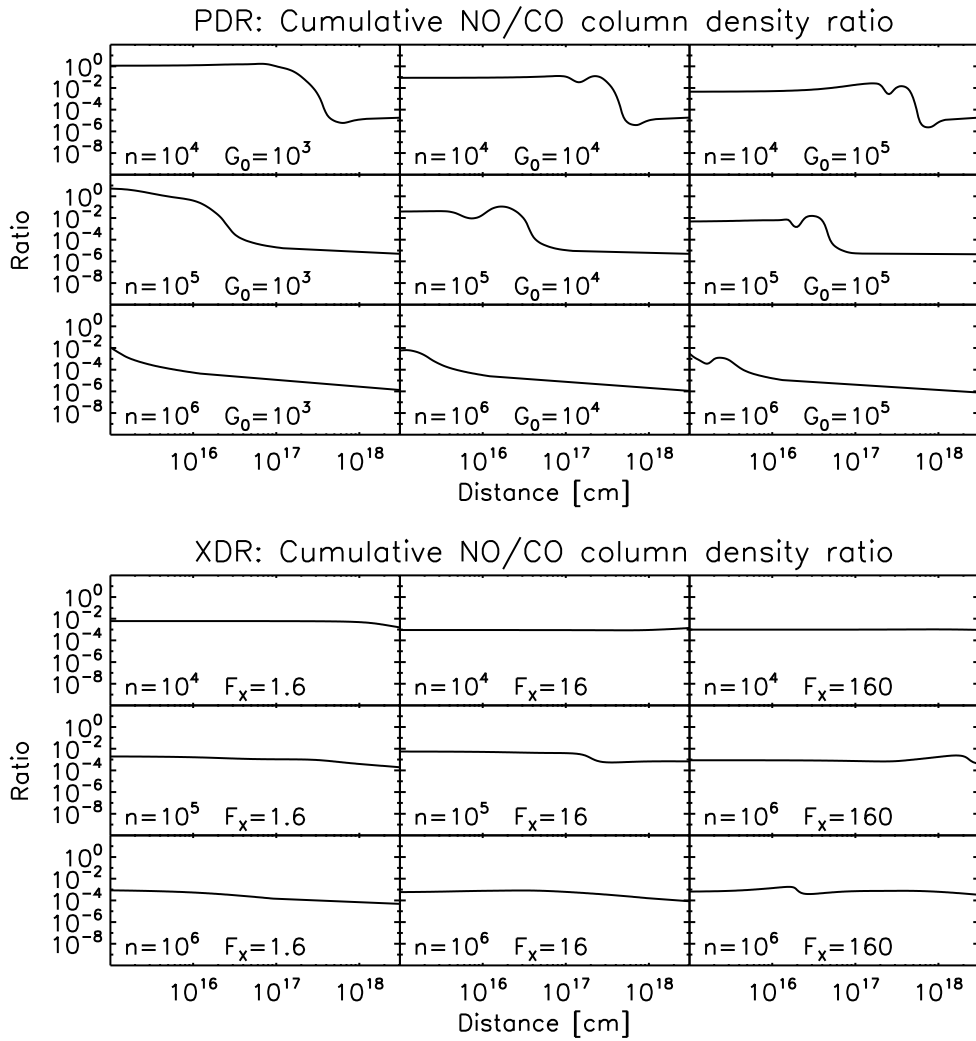


Figure 8.45: Cumulative NO/CO column density ratios for PDR (top) and XDR (bottom) models.

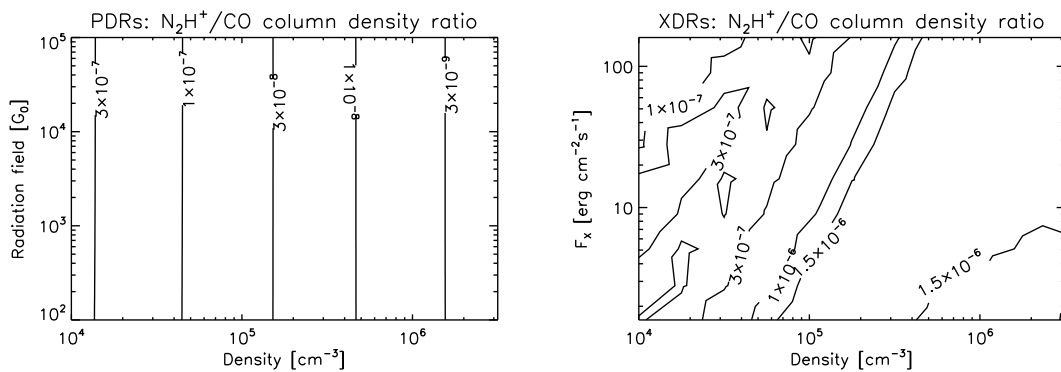


Figure 8.46: N_2H^+/CO column density ratios for PDR (left) and XDR (right) models.

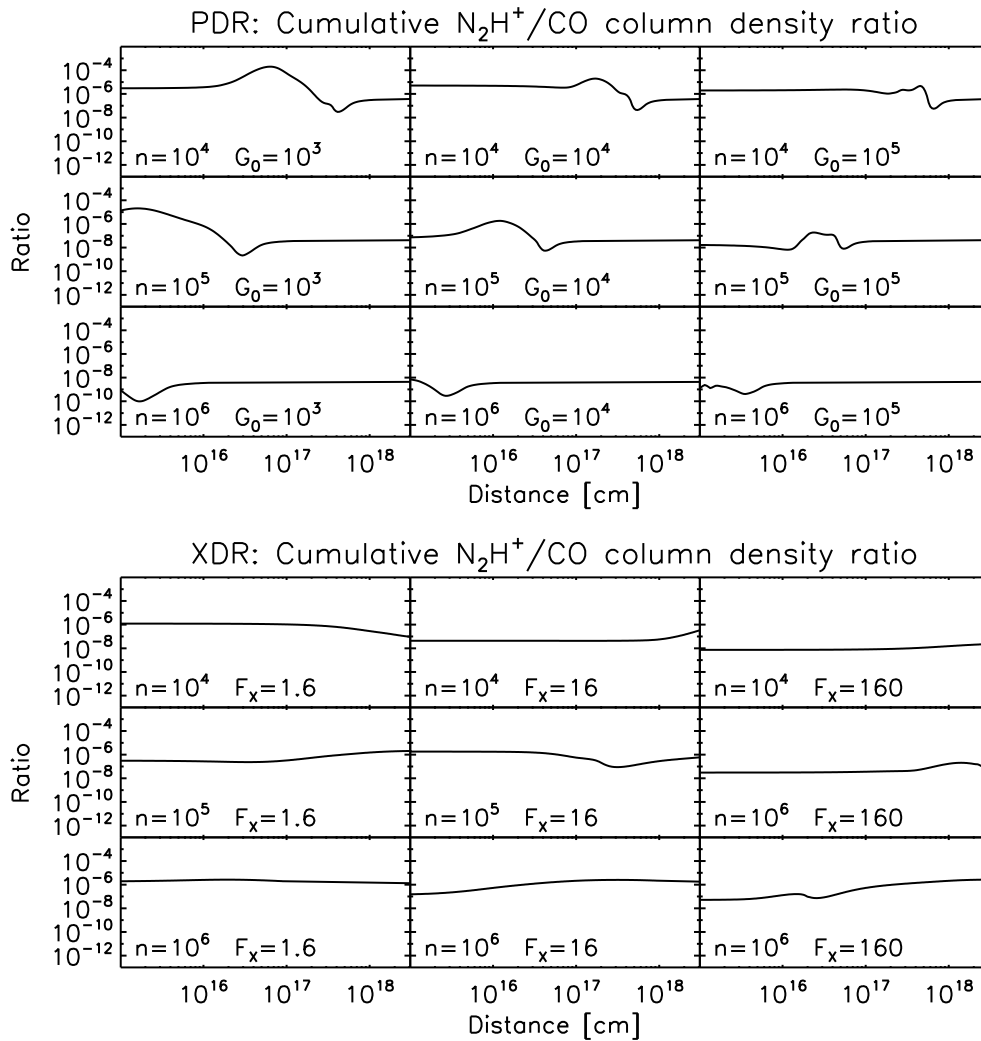


Figure 8.47: Cumulative N_2H^+ /CO column density ratios for PDR (top) and XDR (bottom) models.

in order to make predictions for observed line ratios.

We conclude that both atomic fine-structure and molecular rotational lines have significant diagnostic value to allow us to distinguish between clouds irradiated by star-bursts (FUV) and by active galactic nuclei (X-ray) in the centers of galaxies. Note, however, that the line intensities (and ratios) presented in this work do not take the, likely complex, kinematics of nuclear gas into account. For example, gas rotating in an accretion disk around an AGN will cause the line widths of, say, HCN, HNC and HCO^+ transitions to differ, depending on where their chemical abundances peak with depth.

The XDR/AGN contribution will typically be of a much smaller (possibly beam diluted) angular scale than that of a PDR/Starburst. A 10-25% PDR contribution may already suppress our ability to recognize XDR excitation from HCN/ HCO^+ and HNC/HCN line ratios. A solution to this can be found in the very high J CO lines (e.g., CO(16-15)),

that are excellent indicators of an XDR contribution. These very high rotational lines will be observable with the ESA Herschel (HIFI) space observatory scheduled for launch in the near future; they can be seen in absorption in the near-infrared with Subaru. Currently available (sub)millimeter facilities lack the spatial resolution to separate the PDR/stellar and XDR/AGN contributions in distant active galaxies. Up to now, these components can only be spatially resolved in the Milky Way. However, the resolving power of ALMA will bring this possibility within reach for external galaxy centers as well.

Acknowledgements

We thank Dieter Poelman for making his radiation transfer code *beta3D* available to us.

CHAPTER 9

Irradiated ISM: Discriminating between Cosmic Rays and X-rays

The ISM of active galaxy centers is exposed to a combination of cosmic ray, FUV and X-ray radiation. We apply PDR models to this ISM with both ‘normal’ and highly elevated ($5 \times 10^{-15} \text{ s}^{-1}$) cosmic-ray rates and compare the results to those obtained for XDRs. Our existing PDR-XDR code is used to construct models over a $10^3 - 10^5 \text{ cm}^{-3}$ density range and for $0.16\text{-}160 \text{ erg s}^{-1} \text{ cm}^{-2}$ impinging fluxes. We obtain larger high J ($J > 10$) CO ratios in PDRs when we use the highly elevated cosmic ray rate, but these are always exceeded by the corresponding XDR ratios. The [CI] $609 \mu\text{m}/^{13}\text{CO}(2-1)$ line ratio is boosted by a factor of a few in PDRs with $n \sim 10^3 \text{ cm}^{-3}$ exposed to a high cosmic ray rate. At higher densities ratios become identical irrespective of cosmic ray flux, while XDRs always show elevated [CI] emission per CO column. The HCN/CO and HCN/HCO⁺ line ratios, combined with high J CO emission lines, are good diagnostics to distinguish between PDRs under either low or high cosmic ray irradiation conditions, and XDRs. Hence, the HIFI instrument on Herschel, which can detect these CO lines, will be crucial in the study of active galaxies.

R. Meijerink, M. Spaans, and F.P. Israel
Astrophysical Journal Letters, accepted

9.1 Introduction

In centers of late-type galaxies, such as M 82, NGC 253, and Maffei 2, molecular line intensity ratios¹ are frequently found to be high, e.g. $\text{CO}(4-3)/\text{CO}(1-0) \sim 60$ (Israel et al. 1995; White et al. 1994; Israel & Baas 2003) requiring high gas densities $n > 10^{5.5} \text{ cm}^{-3}$, and high temperatures of $T \geq 50 \text{ K}$. However, FUV photons are easily attenuated by dust and do not penetrate very deep into clouds and the galaxies are observed with beams covering regions typically hundreds of parsecs in size. At such large spatial scales, excited dense gas is not expected to have very large filling factors. UV radiation seems incapable of maintaining very large gas fractions at temperatures of $T \sim 50 - 150 \text{ K}$, and regular PDR models do not explain the observed high ratios. In addition, Israel & Baas (2002) have observed the [CI] 609 μm line in the centers of late-type galaxies, and measured [CI] 609 $\mu\text{m}/^{13}\text{CO}(2-1)$ line intensity ratios in the range 20 – 60, which are hard to explain by (low-CR) PDR models. The $\text{C}^+/\text{C}/\text{CO}$ transition zones in these PDRs contain only a thin layer in which neutral carbon has a high abundance. At the cloud edge, carbon is ionized, and deep in the cloud all carbon is locked up in CO.

In our Milky Way, cloud clumping is the favorite explanation for high [CI] 609 $\mu\text{m}/^{13}\text{CO}(2-1)$ line intensity ratios (Spaans & van Dishoeck 1997). Various authors have invoked elevated cosmic ray fluxes caused by greatly enhanced supernova rates in galaxy centers in order to explain large molecular gas masses at high temperatures (Suchkov et al. 1993; Bradford et al. 2003), and to explain high [CI] intensities and column densities relative to ^{12}CO and ^{13}CO (Pineau des Fôrets et al. 1992; Schilke et al. 1993; Flower et al. 1994). As most cosmic rays are produced in supernovae, their flux is proportional to the star formation rate, which is about $1 \text{ M}_{\odot} \text{ yr}^{-1}$ for the Milky Way. In circumnuclear starbursts, star formation rates may be two orders of magnitude higher or more. Such galaxy centers may also contain an embedded accreting black hole producing X-rays. Like cosmic rays, but unlike UV photons, these X-rays can also penetrate through large column densities ($N_H > 10^{24} \text{ cm}^{-2}$), and can cause the observed high line ratios over areas as large as 500 pc, when the emitted flux is high enough (Meijerink & Spaans 2005; Meijerink et al. 2006b).

In this paper, we investigate whether in galaxy central regions PDRs with and without enhanced cosmic ray fluxes can be distinguished from XDRs on the basis of observable atomic and molecular line ratios. To this end, we calculate line intensities for PDRs with very different cosmic ray rates and compare the results to those obtained for XDRs with the same radiation fields and column densities.

9.2 PDR and XDR models

We have constructed a set of PDR and XDR models from the codes described by Meijerink & Spaans (2005) and Meijerink et al. (2006b), in which we varied both the incident radiation field and the density. The thermal balance (with line transfer) is calculated self-consistently with the chemical balance through iteration. Absorption cross sections for

¹Intensity ratios of lines a to lines b are related to brightness temperature ratios by the cube of the line frequencies: $(\nu_a/\nu_b)^3$

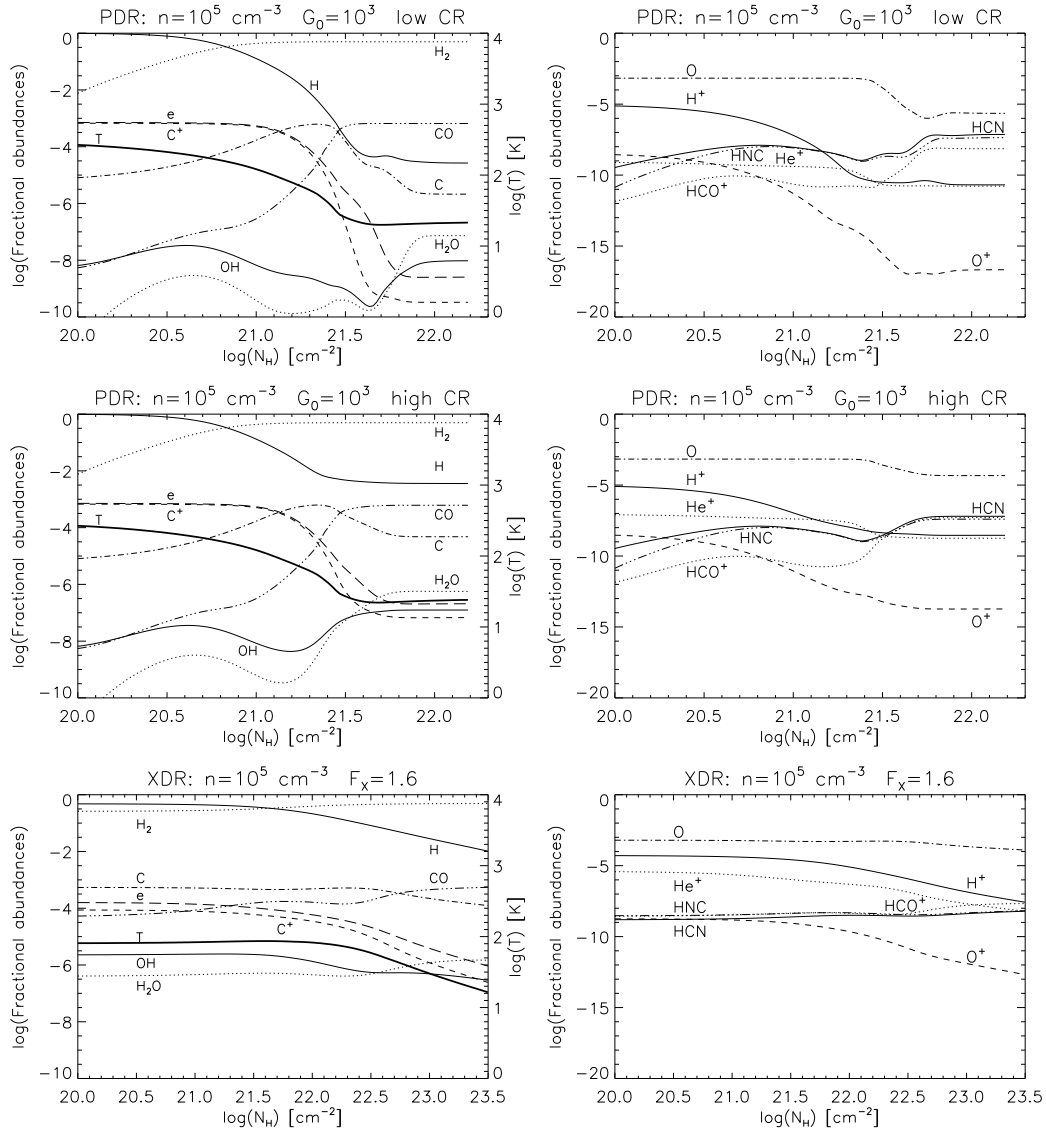


Figure 9.1: Chemical and thermal structure of PDR and XDR models at density $n = 10^5 \text{ cm}^{-3}$ and $G_0 = 10^3$ ($F_X = 1.6 \text{ ergs s}^{-1} \text{ cm}^{-2}$)

X-rays (1-100 keV) are smaller, $\sim 1/E^3$, than for FUV photons. Therefore, PDRs show a stratified structure while the changes in the chemical and thermal structure in XDRs are very gradual. Species like C^+ , C and CO co-exist in XDRs, and large columns of neutral carbon (unlike in PDRs) are produced. In the XDRs, additional reactions for fast electrons that ionize, excite and heat the gas are included. The heating efficiency in XDRs is much higher. Since we focus on galaxy centers, we have assumed the metallicity to be twice Solar. We take the abundance of carbon to be equal to that of oxygen, since the carbon abundance increases faster than oxygen for larger metallicity. The precise C:O ratio does not affect our general results. We have calculated PDR models for both a ‘normal’ (low: $\zeta = 5 \times 10^{-17} \text{ s}^{-1}$ – cf. van der Tak & van Dishoeck 2000) and a high

Table 9.1: PDR and XDR models

Density	PDR (G_0)	XDR (F_x)	Size (pc)
10^3	$10^2, 10^3, 10^4$	0.16, 1.6, 16	10
10^4	$10^3, 10^4, 10^5$	1.6, 16, 160	1
10^5	$10^3, 10^4, 10^5$	1.6, 16, 160	1

($\zeta = 5 \times 10^{-15} \text{ s}^{-1}$) cosmic ray flux corresponding to a star formation rate of $\sim 100 M_\odot \text{ yr}^{-1}$. The model input parameters are summarized in Table 6.1. The range of free parameters ($n = 10^3 - 10^5 \text{ cm}^{-3}$, $G_0 = 10^2 - 10^5/F_X = 0.16 - 160 \text{ erg s}^{-1} \text{ cm}^{-2}$) is representative for the conditions in galaxy centers. That is, from low- J CO (critical density $10^3 - 10^4 \text{ cm}^{-3}$) and HCN 1-0 (critical density $\sim 10^5 \text{ cm}^{-3}$) observations it is apparent that gas in galaxy centers must exhibit the density range that we model. The irradiation conditions are typical for Milky Way PDRs like the Orion Bar (a high mass star-forming region) as well as a generic $10^{44} \text{ erg s}^{-1}$ Seyfert nucleus X-ray luminosity for distances of about 100 pc and up.

9.3 Chemical and thermal structure

Higher cosmic ray (CR) ionization rates do not much affect the chemistry at the cloud edge, but large effects occur beyond the H/H₂ transition (see e.g. Fig. 9.1). As the CR flux in the PDRs is enhanced, electron, carbon and hydrogen abundances decrease much less beyond the H/H₂ transition, due to larger ionization/dissociation rates. Ion abundances also remain higher, causing H₂O and OH to have higher abundances as well. As cosmic ray ionization contributes to the gas heating, higher incident CR fluxes raise gas temperatures deep in the cloud, with roughly $T \sim \zeta^{1/3}$ at low densities ($n \sim 10^3 \text{ cm}^{-3}$). At high densities, $n = 10^5 \text{ cm}^{-3}$, dust acts as an effective coolant if $T > T_d$, and the rise in the kinetic temperature is less pronounced. Both temperatures and abundances in a PDR become higher when CR rates are increased and ratios of emergent line emissions are also modified.

9.4 CO line intensities and ratios

a. Density $n = 10^3 \text{ cm}^{-3}$ (Table 9.2). In high-CR PDR clouds, a large fraction of all CO is dissociated, and CO is a factor ~ 100 less abundant than in low-CR PDRs. However, in the latter, the CO lines are optically thick and CO line intensities are comparable for the same incident flux. In high-CR PDRs, the low- J CO line ratios are somewhat larger than those in low-CR PDRs. The higher transitions show more of a difference and are diagnostically more valuable. In the XDRs, the CO gas temperature is on average much higher than in the PDRs, but marginally higher CO intensities occur only for the weak radiation field $F_X = 1.6 \text{ ergs s}^{-1} \text{ cm}^{-2}$. *In XDRs with stronger radiation fields, CO*

line intensities are much lower than in PDRs, because column densities are too small to attenuate the X-rays significantly, and CO abundances are very low throughout the cloud. The very high CO(2-1)/CO(1-0) and CO(4-3)/CO(1-0) ratios in XDRs, which can be much higher than in the corresponding PDR cases, merely reflect the weakness of the lower J lines.

b. Density $n = 10^4 \text{ cm}^{-3}$ (Table 9.3). High-CR PDRs have more intense CO lines than low-CR PDRs, but *their high- J /low- J CO line ratios* are only marginally higher than those of the corresponding low-CR PDRs. Again we find that XDR CO line intensities exceed those in PDRs in relatively weak radiation fields ($G_0 = 10^3$ or $F_X = 1.6 \text{ ergs s}^{-1} \text{ cm}^{-2}$). In XDRs with stronger radiation fields, the lower J CO lines (up to CO(4-3)) are much weaker than in PDRs, but the higher rotational lines are stronger. All XDR CO ratios are (much) larger than even the high-CR PDR CO ratios, and ratios at the intermediate and high J levels above CO(6-5) are diagnostically particularly meaningful.

c. Density $n = 10^5 \text{ cm}^{-3}$ (Table 9.4). There are no longer significant differences between low-CR and high-CR PDRs. However, the XDR CO lines are strong in the lower transitions, and even more so at the intermediate and higher rotational transitions above CO(4-3). Their ratios are always larger than the corresponding ratios in any PDR model (see Meijerink et al. 2006b for a more detailed discussion). Some high- J CO intensities and ratios are left blank, since no significant emission was found for these lines due to the low fractional abundances of CO and the high critical densities of the transitions.

9.5 [CI] 609 $\mu\text{m}/^{13}\text{CO}(2-1)$ ratios

XDRs, quite unlike PDRs, have significant neutral carbon abundances; their [CI] intensities behave as volume tracers. At the same time, XDRs generally have weaker low J CO and ^{13}CO lines than PDRs, for $n \leq 10^4 \text{ cm}^{-3}$ and $F_X > 1 \text{ ergs s}^{-1} \text{ cm}^{-2}$. Thus, in XDRs [CI] 609 $\mu\text{m}/^{13}\text{CO}(2-1)$ line intensity ratios are much larger than in corresponding PDRs. Only at low densities, $n \leq 10^3 \text{ cm}^{-3}$, do high-CR PDRs behave in a fashion intermediate between XDRs and low-CR PDRs. In such low-density, high-CR PDRs, CO and ^{13}CO dissociation causes simultaneous ^{13}CO line weakening and [CI] line strengthening, resulting in [CI]/ ^{13}CO line intensity ratios four times higher than seen in low CR-PDRs, but still (much) lower than those seen in XDRs. Even at higher densities ($n \geq 10^4 \text{ cm}^{-3}$) and stronger radiation fields ($G_0 = 10^5$), the high-CR PDRs fail to produce [CI]/ ^{13}CO ratios more than 1.5 times those of low-CR PDRs. However, *in XDRs the [CI]/ ^{13}CO ratios remain very much larger* and thus provide an excellent tool to distinguish between PDRs and XDRs.

9.6 HCN/CO and HCN/HCO⁺ ratios

Meijerink et al. (2006b) found that HCN/CO and HCN/HCO⁺ line intensity ratios distinguish between ‘normal’ (low-CR) PDRs and XDRs. These ratios are slightly different in high-CR PDRs. At densities of $n = 10^4 \text{ cm}^{-3}$, the HCN/CO ratios are lower in high-CR PDRs than in low-CR PDRs, especially for the $J = 4 - 3$ transition, but they become

more or less identical at densities of $n = 10^5 \text{ cm}^{-3}$. In XDRs, the HCN/CO ratios are almost invariably significantly lower than in either PDR. High-CR PDRs with densities of $n = 10^4 \text{ cm}^{-3}$ have HCN/HCO⁺ ratios *higher* than low-CR PDRs in the $J = 1 - 0$ transition and *lower* than low-CR PDRs in the $J = 4 - 3$ transition. This opposite behaviour reflects a cosmic ray induced shift in the HCN and HCO⁺ abundances to larger (cooler) columns. However, at higher densities ($n = 10^5 \text{ cm}^{-3}$), high-CR PDRs have HCN/HCO⁺ ratios always lower than those in low-CR PDRs, mainly because of a boost in the HCO⁺ production. In all cases where XDRs produce HCN and HCO⁺ emission observable at all, the *HCN/HCO⁺ ratios are (much) lower in the XDR than in either PDR.*

9.7 Conclusions

1. CO line intensity ratios increase when cosmic ray ionization rates are enhanced, but they remain smaller than those in XDRs. In particular high- J ($J > 10$) CO lines (which will become observable with HIFI in ESA's Herschel space observatory) allow to distinguish between (high-CR) PDRs and XDRs. Using the HIFI time estimator and a beam filling factor of 0.05, we find that a line intensity of $9 \times 10^{-6} \text{ erg s}^{-1} \text{ cm}^{-2}$, the largest CO(16-15) intensity produced by our PDR models, will be detectable with HIFI in about 4 hours, while the very bright lines received from highly irradiated XDRs are detectable within minutes.
2. [CI] 609 $\mu\text{m}/^{13}\text{CO}(2-1)$ ratios are much higher in high-CR PDRs than in low-CR PDRs at modest densities of $n = 10^3 \text{ cm}^{-3}$. At higher densities of $n \geq 10^4 \text{ cm}^{-3}$, this difference vanishes. In XDRs, the ratios are always larger than in PDRs at the same density, independent of incident radiation field.
3. HCN/CO and HCN/HCO⁺ line ratios are good diagnostics to distinguish between PDRs and XDRs. As the ratios obtained for low-CR and high-CR PDRs are different, combination with high- J CO lines is both crucial and profitable in the study of the active galaxy centers.
4. Although our model results broadly distinguish between low and high CR PDRs and XDRs, there is some degeneracy when constraining the four parameters (density, CR rate, G_0 and F_X) through individual ratios. Therefore, a combination of various ratios should be considered

Acknowledgements

We thank J. le Bourlot and M. Elitzur for useful discussions on X-ray versus cosmic-ray irradiation, M. Hogerheijde and P. van der Werf for discussions on HIFI sensitivities, and an anonymous referee for his constructive comments.

Table 9.2: Line intensities ($\text{erg s}^{-1} \text{cm}^{-2} \text{sr}^{-1}$) and ratios at density $n = 10^3 \text{cm}^{-3}$

Model Radiation field	Low-CR PDR			High-CR PDR			XDR		
	$G_0 = 10^2$	$G_0 = 10^3$	$G_0 = 10^4$	$G_0 = 10^2$	$G_0 = 10^3$	$G_0 = 10^4$	$F_x = 0.16$	$F_x = 1.6$	$F_x = 16$
CO(1-0)	8.2(-8)	8.6(-8)	1.0(-7)	8.4(-8)	8.3(-8)	8.1(-8)	1.2(-7)	3.7(-10)	3.0(-10)
CO(2-1)	4.8(-7)	5.1(-7)	6.6(-7)	6.3(-7)	6.3(-7)	6.4(-7)	1.0(-6)	9.3(-9)	9.1(-9)
CO(3-2)	9.4(-7)	9.9(-7)	1.5(-6)	1.6(-6)	1.6(-6)	1.6(-6)	2.8(-6)	3.4(-8)	5.2(-8)
CO(4-3)	1.4(-6)	1.6(-6)	2.8(-6)	2.2(-6)	2.1(-6)	2.1(-6)	4.5(-6)	5.3(-8)	1.1(-7)
CO(7-6)	3.2(-9)	1.1(-7)	7.8(-6)	1.4(-7)	1.2(-7)	1.3(-7)	-	3.4(-8)	1.1(-7)
CO(10-9)	8.4(-11)	1.7(-11)	2.3(-10)	9.2(-9)	4.7(-9)	2.4(-9)	-	-	-
CO(16-15)	-	1.0(-12)	1.2(-10)	-	4.2(-9)	7.1(-11)	-	-	-
$^{13}\text{CO}(2-1)$	2.1(-7)	2.1(-7)	2.8(-7)	1.1(-7)	1.0(-7)	9.7(-8)	8.1(-8)	1.8(-10)	1.6(-10)
[CI] 609 μm	5.6(-6)	7.2(-6)	8.9(-6)	1.1(-5)	1.2(-5)	1.4(-5)	3.6(-5)	1.0(-4)	1.2(-4)
CO(2-1)/CO(1-0)	5.9	5.9	6.3	7.5	7.6	7.8	8.4	25.4	30.3
CO(4-3)/CO(1-0)	17.0	18.7	27.2	26.2	25.6	25.8	36.2	1.5(2)	3.6(2)
CO(7-6)/CO(3-2)	3.4(-3)	1.1(-1)	5.2	8.6(-2)	7.9(-2)	8.0(-2)	-	9.8(-1)	2.2
CO(10-9)/CO(7-6)	2.5(-2)	1.5(-4)	3.0(-5)	6.7(-2)	3.7(-2)	1.9(-2)	-	-	-
CO(16-15)/CO(1-0)	-	1.2(-5)	1.1(-3)	-	5.0(-2)	8.7(-4)	-	-	-
CO(16-15)/CO(10-9)	-	6.2(-2)	0.51	-	9.0(-1)	3.0(-2)	-	-	-
[CI] 609 $\mu\text{m}/^{13}\text{CO}(2-1)$	26.7	34.1	31.5	97.1	1.2(2)	1.4(2)	4.4(2)	5.6(5)	7.4(5)

Table 9.3: Line intensities ($\text{erg s}^{-1} \text{cm}^{-2} \text{sr}^{-1}$) and ratios at density $n = 10^4 \text{cm}^{-3}$

Model Radiation field	Low-CR PDR			High-CR PDR			XDR		
	$G_0 = 10^3$	$G_0 = 10^4$	$G_0 = 10^5$	$G_0 = 10^3$	$G_0 = 10^4$	$G_0 = 10^5$	$F_x = 1.6$	$F_x = 16$	$F_x = 160$
CO(1-0)	1.6(-7)	1.9(-7)	2.5(-7)	2.1(-7)	2.4(-7)	2.7(-7)	2.6(-7)	1.4(-10)	3.4(-11)
CO(2-1)	1.2(-6)	1.6(-6)	2.0(-6)	1.8(-6)	2.0(-6)	2.4(-6)	3.5(-6)	5.2(-9)	1.4(-9)
CO(3-2)	3.4(-6)	4.6(-6)	6.2(-6)	5.3(-6)	6.2(-6)	7.5(-6)	1.3(-5)	4.0(-8)	1.0(-8)
CO(4-3)	5.7(-6)	8.5(-6)	1.2(-5)	1.0(-5)	1.2(-5)	1.5(-5)	2.9(-5)	1.7(-7)	4.3(-8)
CO(7-6)	2.9(-6)	1.3(-5)	2.7(-5)	1.6(-5)	2.3(-5)	3.5(-5)	9.7(-5)	1.8(-6)	6.4(-7)
CO(10-9)	2.4(-9)	7.4(-8)	1.8(-6)	2.4(-7)	1.0(-6)	4.9(-6)	1.1(-4)	3.5(-6)	1.6(-6)
CO(16-15)	1.1(-10)	6.8(-9)	2.3(-8)	2.1(-10)	3.1(-9)	2.9(-8)	1.1(-7)	2.5(-6)	1.7(-6)
HCN(1-0)	5.2(-9)	6.8(-9)	3.8(-9)	3.9(-9)	3.8(-9)	3.8(-9)	4.9(-10)	2.2(-13)	3.1(-14)
HCN(4-3)	3.3(-7)	4.0(-7)	1.0(-8)	9.5(-9)	1.0(-8)	1.0(-8)	1.3(-9)	4.0(-11)	3.2(-11)
HCO ⁺ (1-0)	1.9(-8)	2.2(-8)	2.6(-8)	1.1(-8)	1.1(-8)	1.1(-8)	1.5(-8)	1.0(-14)	1.4(-15)
HCO ⁺ (4-3)	4.3(-7)	6.6(-7)	7.9(-7)	6.2(-8)	7.0(-8)	7.2(-8)	2.0(-7)	1.0(-11)	1.4(-12)
¹³ CO(2-1)	5.8(-7)	7.4(-7)	9.3(-7)	8.0(-7)	8.8(-7)	9.6(-7)	3.0(-7)	1.0(-10)	2.3(-11)
[CI] 609 μm	8.4(-6)	9.9(-6)	1.1(-5)	1.2(-5)	1.4(-5)	1.7(-5)	5.2(-5)	1.2(-4)	1.2(-4)
CO(2-1)/CO(1-0)	7.8	8.1	8.2	8.4	8.6	8.8	13.3	36.9	39.6
CO(4-3)/CO(1-0)	35.8	44.2	50.4	47.5	51.8	56.9	1.1(2)	1.2(3)	1.3(3)
CO(7-6)/CO(3-2)	8.4(-1)	2.8	4.3	3.1	3.7	4.7	7.5	46.1	61.9
CO(10-9)/CO(7-6)	8.3(-4)	5.6(-3)	6.5(-2)	1.5(-2)	4.4(-2)	1.4(-1)	1.1	1.9	2.6
CO(16-15)/CO(1-0)	7.0(-4)	3.5(-2)	9.2(-2)	1.0(-3)	1.3(-2)	1.1(-1)	4.1(-1)	1.8(4)	5.0(4)
CO(16-15)/CO(10-9)	4.6(-2)	9.2(-2)	1.2(-2)	8.8(-4)	3.1(-3)	6.0(-3)	1.0(-3)	7.0(-1)	1.0
HCN(1-0)/CO(1-0)	3.2(-2)	3.5(-2)	3.4(-2)	1.9(-2)	1.6(-2)	1.4(-2)	1.9(-3)	1.6(-3)	9.1(-4)
HCN(4-3)/CO(4-3)	5.7(-2)	4.7(-2)	3.4(-2)	9.5(-4)	8.4(-4)	6.8(-4)	4.4(-5)	2.4(-4)	7.3(-4)
HCN(1-0)/HCO ⁺ (1-0)	2.8(-1)	3.1(-1)	3.3(-1)	3.6(-1)	3.4(-1)	3.6(-1)	3.2(-2)	21.7	22.6
HCN(4-3)/HCO ⁺ (4-3)	7.6(-1)	6.1(-1)	5.4(-1)	1.5(-1)	1.5(-1)	1.4(-1)	6.3(-3)	4.0	22.6
[CI] 609 μm / ¹³ CO(2-1)	14.6	13.4	12.1	14.9	16.2	17.6	1.7(2)	1.2(6)	5.1(6)

Table 9.4: Line intensities ($\text{erg s}^{-1} \text{cm}^{-2} \text{sr}^{-1}$) and ratios at density $n = 10^5 \text{cm}^{-3}$

Model Radiation field	Low-CR PDR			High-CR PDR			XDR		
	$G_0 = 10^3$	$G_0 = 10^4$	$G_0 = 10^5$	$G_0 = 10^3$	$G_0 = 10^4$	$G_0 = 10^5$	$F_x = 1.6$	$F_x = 16$	$F_x = 160$
CO(1-0)	3.1(-7)	4.1(-7)	5.5(-7)	3.3(-7)	4.3(-7)	5.6(-7)	7.6(-7)	1.4(-6)	1.2(-6)
CO(2-1)	2.7(-6)	3.5(-6)	4.7(-6)	2.8(-6)	3.7(-6)	4.9(-6)	7.1(-6)	1.4(-5)	1.5(-5)
CO(3-2)	8.5(-6)	1.2(-5)	1.6(-5)	9.1(-6)	1.2(-5)	1.7(-5)	2.5(-5)	5.2(-5)	6.2(-5)
CO(4-3)	1.8(-5)	2.5(-5)	3.6(-5)	1.9(-5)	2.7(-5)	3.7(-5)	5.6(-5)	1.2(-4)	1.7(-4)
CO(7-6)	3.6(-5)	8.0(-5)	1.4(-4)	4.4(-5)	8.8(-5)	1.4(-4)	2.1(-4)	6.6(-4)	1.0(-3)
CO(10-9)	4.3(-6)	7.7(-5)	2.4(-4)	1.2(-5)	9.0(-5)	2.7(-4)	3.7(-4)	1.6(-3)	2.9(-3)
CO(16-15)	2.1(-8)	7.8(-7)	5.1(-6)	2.2(-8)	7.9(-7)	8.8(-6)	5.1(-6)	4.3(-3)	8.6(-3)
HCN(1-0)	7.6(-8)	1.2(-7)	1.5(-7)	8.2(-8)	1.2(-7)	1.5(-7)	4.0(-8)	7.2(-8)	1.7(-8)
HCN(4-3)	2.5(-6)	3.2(-6)	3.7(-6)	2.6(-6)	3.2(-6)	3.7(-6)	1.4(-6)	2.2(-6)	7.0(-7)
HCO ⁺ (1-0)	5.8(-8)	8.4(-8)	1.1(-7)	9.6(-8)	1.5(-7)	2.3(-7)	1.6(-7)	5.2(-7)	1.7(-7)
HCO ⁺ (4-3)	1.8(-6)	2.9(-6)	4.0(-6)	3.3(-6)	5.0(-6)	6.8(-6)	4.2(-6)	8.9(-6)	9.8(-6)
¹³ CO(2-1)	1.3(-6)	1.9(-6)	4.7(-6)	1.4(-6)	2.0(-6)	2.6(-6)	2.8(-6)	4.9(-6)	2.3(-6)
[CI] 609 μm	7.4(-6)	8.7(-6)	9.8(-6)	9.1(-6)	1.1(-5)	1.3(-5)	4.1(-5)	1.1(-4)	4.4(-4)
CO(2-1)/CO(1-0)	8.6	8.5	8.5	8.6	8.6	8.7	9.3	10.0	12.2
CO(4-3)/CO(1-0)	56.6	61.1	64.6	57.8	62.3	66.2	73.1	91.1	1.3(2)
CO(7-6)/CO(3-2)	4.2	6.9	9.1	4.8	7.14	8.8	8.9	12.9	16.5
CO(10-9)/CO(7-6)	1.2(-1)	1.0	1.7	2.6(-1)	1.0	1.8	1.7	2.4	2.8
CO(16-15)/CO(1-0)	6.6(-2)	1.9	9.2	6.7(-2)	1.8	15.6	6.7	3.1(3)	6.9(3)
CO(16-15)/CO(10-9)	4.8(-3)	1.0(-2)	2.1(-2)	1.9(-3)	8.7(-3)	3.3(-2)	1.4(-2)	2.7	3.0
HCN(1-0)/CO(1-0)	2.4(-1)	2.8(-1)	2.8(-1)	2.5(-1)	2.7(-1)	2.7(-1)	5.2(-2)	5.1(-2)	1.3(-2)
HCN(4-3)/CO(4-3)	1.4(-1)	1.2(-1)	1.0(-1)	1.3(-1)	1.1(-1)	1.0(-1)	2.5(-2)	1.7(-2)	4.2(-3)
HCN(1-0)/HCO ⁺ (1-0)	1.3	1.4	1.4	8.5(-1)	8.0(-1)	6.7(-1)	2.5(-1)	1.4(-1)	9.9(-2)
HCN(4-3)/HCO ⁺ (4-3)	1.4	1.1	9.3(-1)	7.8(-1)	6.3(-1)	5.4(-1)	3.2(-1)	2.5(-1)	7.1(-2)
[CI] 609 μm / ¹³ CO(2-1)	5.7	4.5	3.6	6.3	5.5	4.8	14.7	24.0	1.9(2)

CHAPTER 10

Interpretation of observed sub-mm emission of nearby galaxies

We assess the presence of star-forming regions, active galactic nuclei, and enhanced cosmic ray rates in the centers of nearby galaxies through molecular emission of HCN, HCO⁺, HNC, CO, ¹³CO, CS and [CI]. We use a grid of photon dominated region and X-ray dominated region models, where density, impinging FUV and X-ray flux, and column density are varied for homogeneous slabs. We derive the (high cosmic ray) PDR and XDR components for individual galaxies, and define a diagnostic table, which can be applied to other galaxies, e.g., (U)LIRGS, as well. In general, we find that XDRs or elevated cosmic ray PDRs are necessary to explain CO(2-1)/CO(1-0) and [CI]/¹³CO(2-1) ratios, which are tracing the diffuse part of the ISM. In particular, we find that NGC 1068, often viewed as a pure AGN, needs a dense PDR component.

R. Meijerink, M. Spaans, and F.P. Israel, A&A, in preparation

10.1 Introduction

Gas in the centers of (active) galaxies is often exposed to FUV and/or X-ray radiation. FUV photons originate mostly from the O and B stars produced in starbursts, while X-rays dominate the radiation from accreting black holes (AGN). The thermal and chemical structure of gas exposed to FUV radiation (Photon Dominated Regions: PDRs) is quite different compared to gas irradiated by X-rays (X-ray Dominated Regions: XDRs). The processes relevant in PDRs and XDRs, and how these cause a different chemical/thermal structure of gas clouds are extensively discussed in Meijerink & Spaans (2005). The differences in the cloud's thermal and chemical structure results in different atomic finestructure and molecular rotational line emission and line ratios. In Meijerink et al. (2006b), we show the line emission and the line ratios for a set of PDR and XDR models, where both density and impinging fluxes are varied. Models with density $n < 10^4 \text{ cm}^{-3}$ have a cloud size of 10 pc. For higher densities we adopt 1 pc for the cloudsize. The metallicity in galaxy centers is expected to be 2-4 times higher than in the Solar Neighbourhood (Zaritsky et al. 1994; Vila-Costas & Edmunds 1992). In the cloud models, we have adopted a twice Solar metallicity, and a carbon abundance equal to the oxygen abundance (see, for instance, Garnett et al. 1999; Kobulnicky & Skillman 1998). Note that the [C]/[O] ratio affects the abundances of O_2 and H_2O . See for example Spaans & van Dishoeck (2001) and especially Fig. 2 in Bergin et al. (2000). Here, we apply these models to the observed sub-mm emission of nearby galaxies.

10.2 Observations

We use observations of atomic finestructure and molecular rotational emission lines (CO, ^{13}CO , HCO^+ , HCN, HNC, CS, and [CI]) in the centers of a sample of nearby galaxies, obtained with the James Clerk Maxwell Telescope (JCMT), the Institut de Radio Astronomie Millimétrique (IRAM) 30m telescope, and Swedish-ESO Submillimetre Telescope (SEST), and supplemented these with observations from the literature (see Tables 10.2, 10.4 and 10.3). All observations have been reduced to a $21''$ beam to obtain proper line ratios. Where large velocity-integrated maps exist, we obtain the central ($0''$, $0''$) velocity-integrated line intensity, and convolve to $21''$ resolution, using the Specx-interpole function of the DAS data reduction software¹. Unfortunately, these large maps are only available for a limited number of lines. For the other lines we use a different method. For some lines we have either observations at several resolutions or we can obtain an intensity at the needed resolution using the Specx-interpole function. Then, it is possible to compute the ratio $I_{\text{init.res.}}/I_{21''}$, where I is the velocity-integrated intensity at a given resolution. When enough points are available, we can fit a powerlaw function:

$$Y = A \times X^B. \quad (10.1)$$

From this function, we can compute convolved values for data, for which we only have a single observation available assuming, in effect, similar spatial distributions of the species

¹See the JCMT website: <http://docs.jach.hawaii.edu/JCMT/>

involved. For a more detailed description of the fitting convolution method, we refer to Bayet et al. (2006).

10.3 Angular scales and their consequences

The list of observed galaxies is given in Table 10.1, together with their coordinates, estimated distance, angular scale, and properties such as inclination, X-ray flux, and galaxy type. For the smallest angular scale, which is $11''$ /kpc for NGC 3079 at an estimated distance of 18.0 Mpc, we observe a region as large as 2 kpc. For the largest angular scale ($113''$ /kpc for IC 342 at an estimated distance of 1.8 Mpc), this is still ~ 190 pc. Since we observe such large regions at once, the beam is not filled with just one homogeneous component, as is often the case in our Milky Way. The observed line emission originates in an ensemble of several different components, which can be traced by different species. While CO rotational lines better trace the more diffuse component ($n \sim 10^3 \text{ cm}^{-3}$) of gas in galaxies, species such as HNC, HCN and HCO^+ trace dense regions best ($n \sim 10^5 \text{ cm}^{-3}$). For all species, the actually observed emission, however, is contributed to all components. Previous investigations suggest that the diffuse gas contains about 50-80 percent of the mass seen in the beam, which leaves 20-50 percent for the dense part (Israel et al. 2006 and references therein).

10.4 Comparison to model ratios

In tables 10.7 through 10.21, we list the observed intensity ratios for CO, ^{13}CO , CI, HCN and HCO^+ . We fit every ratio with a single component, and never obtain a unique solution, but always a range of possible solutions. When a solution exists in our parameter space, we give the solutions for both PDR and XDR models. Below we discuss the ratios obtained for the galaxies for each species, followed by a brief discussion of each individual galaxy.

10.4.1 CO ratios

The CO(2-1)/CO(1-0) intensity ratios range from 5.7 (NGC 891) to 9.5 (IC 342), and are summarized in Table 10.4. Low ratios (5.7-6.0) can be reproduced with low density PDRs ($n = 0.5 - 1.5 \times 10^3 \text{ cm}^{-3}$), and moderate incident radiation fields ($G_0 = 10^{0.5} - 10^3$). Ratios as high as 9.5 require very high densities ($n > 10^{6.5} \text{ cm}^{-3}$) and high radiation fields ($G_0 > 10^4$). We find the same for some CO(4-3)/CO(1-0) ratios of which some are as large as 64, requiring more or less the same set of solutions as for the CO(2-1)/CO(1-0). However, it does not seem very plausible that a region as large as 500 pc is dominated by such a high density and strongly FUV irradiated gas (Israel et al. 1995; White et al. 1994; Israel & Baas 2003). Note that in the centers of galaxies, which are actively forming stars, global interstellar radiation fields ranging from $G_0 = 10^2 - 10^3$ are not uncommon.

Table 10.1: Observed galaxies

Galaxy	R.A. (2000)	Dec. (2000)	Type	Bar	AGN	cSB	$L_X/10^{39}$ (erg s^{-1})	$L_{FIR}/10^{42}$	Orientation	D (Mpc)	Scale ("/kpc)
NGC 253	00 ^h 47 ^m 36.0 ^s	-25° 17' 00"	Sbc	+	+	+	4.3 ¹	42	highly inclined	2.5	81
					(outflow)		3.9 ²				
NGC 4945	13 ^h 05 ^m 26.2 ^s	-49° 28' 15"	Scd	(+)	+	?	4.7 ¹	67	highly inclined	3.9	52
M 82	09 ^h 55 ^m 52.2 ^s	+69° 40' 49"	Ir	-	-	+	29 ²	76	edge-on ?	3.3	62
					(outflow)				interacting		
IC 342	03 ^h 46 ^m 49.1 ^s	+68° 05' 47"	Scd	?	(+)	+	1.9 ²	6.6	face-on	1.8	113
Maffei 2	02 ^h 41 ^m 54.9 ^s	+59° 36' 14"	Sbc	+	+	-	-	6.5	inclined	2.7	75
M 83	13 ^h 37 ^m 00.8 ^s	-29° 51' 59"	Sc	+	?	+	4.5 ¹	25	mostly face-on	3.5	58
							7.2 ²				
NGC 6946	20 ^h 34 ^m 51.4 ^s	+60° 09' 18"	Sd	-	-	+	12 ²	32	face-on	5.5	37
M 51	13 ^h 29 ^m 52.4 ^s	+47° 11' 41"	Sc	-	+	-	-	55	face-on	9.7	21
					(small outflow)				interacting		
NGC 891	02 ^h 22 ^m 32.9 ^s	+42° 20' 46"	Sb?	?	?	-	-	49	edge-on	9.5	21
NGC 1068	02 ^h 42 ^m 40.8 ^s	-00° 00' 48"	Sb	+	+	(+)	870 ¹	350	face-on	14.4	14
					(outflow)		521 ²				
							124 ³				
NGC 1365	03 ^h 33 ^m 36.3 ^s	-36° 08' 28"	Sb	+	+	-	38 ²	110	inclined	13.7	15
NGC 2146	06 ^h 18 ^m 37.5 ^s	+78° 21' 21"	Sab	?	(-)	(+)	11 ¹	232	edge-on	12.2	17
									recent merger		
NGC 3628	11 ^h 20 ^m 16.9 ^s	+13° 35' 14"	Sb	?	?	(+)	8.6 ²	17	edge-on	6.7	30
									interacting		
NGC 2903	09 ^h 32 ^m 09.7 ^s	+21° 30' 03"	Sc	+	(+)	-	1.4 ¹	34	inclined	8.9	23
							14 ²				
NGC 3079	10 ^h 01 ^m 58.5 ^s	+55° 40' 50"	Sc	(+)	+	+	264 ¹	112	almost edge-on	18.0	11
					(outflow)		23 ²				

¹Rosat satellite (0.1-2.4 keV); ²Einstein satellite (0.2-4.0 keV); ³EXOSAT satellite (2-10 keV)

Table 10.2: Transitions normalized to 21'' beam [K km/s]¹

Transition	N253	N4945	M82	IC342	Maffei2	M83	N6946	M51	N891	N1068	N1365	N2146	N3628	N2903	N3079
¹² CO(1-0)	910	1185	677	130	163	194	220	49	127	174	270	166	201	80	218
¹² CO(2-1)	1033	990	649	154	192	218	230	53	90	185	205	181	142	60	191
¹² CO(3-2)	947	700	639	136	166	154	107	54	36	122	188	154	142	62	144
¹² CO(4-3)	906	-	540	121	160	131	118	24	-	85	-	105	94	-	120
¹³ CO(1-0)	86	80	45	13	16	18	20	7	16	13	24	13	18	7.0	14
¹³ CO(2-1)	95	74	50	18	22	20	15	8	11	11	20	21	10	6.4	14
¹³ CO(3-2)	87	60	54	15	11	14	11	7	-	10	18	12	11	-	23
CS(1-0)	46	-	29	4.3	<5	-	12	<3	-	-	-	-	-	-	-
CS(2-1)	38	45	24	5.4	2.7	8	4	2.7	4	10	-	7	<1	2	-
CS(3-2)	24	22	12	2.4	4.7	1	3	-	-	-	7	<2	-	-	2.3
CS(4-3)	10	-	-	-	-	-	-	-	-	-	-	-	-	-	-
CS(5-4)	11	5.9	10	0.8	-	-	<1.1	-	-	-	-	-	-	-	-
HCO ⁺ (1-0)	76	111	63	12	12.5	26	13	5.1	2.4	33	-	5	5	3	<3
HCO ⁺ (3-2)	56	16	18	-	-	-	-	-	-	-	-	-	-	-	-
HCO ⁺ (4-3)	50	9	14	3.5	-	-	-	-	-	-	-	-	-	-	-
HCN(1-0)	95	87	35	17	17	37	11	6.0	4.0	35	25	6	8	7	12
HCN(3-2)	49	25	14	5	5	2.6	1.7	<1.6	-	5.4	-	3	-	<3	<8
HCN(4-3)	70	5.3	11	6	-	-	-	-	-	-	-	-	-	-	-
HNC(1-0)	63	58	17	8	4.7	5.3	5.2	1.7	1.2	16	-	2	4.5	1.8	8.7
[CI] 609 μ m	305	-	-	35	18	55	39	14	-	27	-	-	50	-	142

¹References for molecular line observations are given in Table 10.3

Table 10.3: References for molecular line observations

Line	References
^{12}CO	Bayet et al. (2004); Curran et al. (2000, 2001); Dumke et al. (2001); Eckart et al. (1990); Gao & Solomon (2004) Güsten et al. (1993); Harrison et al. (1999); Helfer & Blitz (1993); Henkel & Bally (1985); Henkel et al. (1993) Houghton et al. (1997); Hurt et al. (1993); Irwin & Avery (1992); Israel (1992); Israel et al. (1995, 2006) Israel & Baas (2001, 2003); Israel (unpublished); Kramer et al. (2005); Mao et al. (2000) Mauersberger et al. (1995, 1996a,b, 1999, 2003); Meier et al. (2000); Meier & Turner (2004); Olofsson & Rydbeck (1984) Sage et al. (1990, 1991); Sage & Isbell (1991); Sandqvist et al. (1988, 1995); Sorai et al. (2000, 2002) Steppe et al. (1990); Wall & Jaffe (1990); Wall et al. (1991); Wang et al. (2004); Wild et al. (1992)
^{13}CO	Curran et al. (2001); Eckart et al. (1990); Harrison et al. (1999); Henkel et al. (1993); Israel (1992); Israel et al. (2006) Israel & Baas (2001, 2003); Israel (unpublished); Kramer et al. (2005); Mao et al. (2000) Mauersberger et al. (1991, 1996a, 2003); Meier et al. (2000); Meier & Turner (2004); Sage et al. (1991) Sage & Isbell (1991); Sandqvist et al. (1988); Wall & Jaffe (1990); Wall et al. (1991); Wang et al. (2004)
[CI]	Bradford et al. (2003); Harrison et al. (1995); Israel (unpublished); Israel et al. (1995, 2006) Israel & Baas (2001, 2003); Kramer et al. (2005)
HCO^+	Curran et al. (2001); Henkel & Bally (1985); Henkel et al. (1993); Israel (1992); Jackson et al. (1995) Nguyen-Q-Rieu et al. (1989); Nguyen et al. (1992); Sorai et al. (2002); Wang et al. (2004); Wild et al. (1992)
HCN	Curran et al. (2000, 2001); Gao & Solomon (2004); Helfer & Blitz (1993); Henkel & Bally (1985) Hüttemeister et al. (1995); Israel (1992); Jackson et al. (1995); Nguyen-Q-Rieu et al. (1989); Nguyen et al. (1992) Sorai et al. (2002); Wang et al. (2004)
HNC	Israel (1992); Hüttemeister et al. (1995); Henkel et al. (1993); Wang et al. (2004)
CS	Baan et al. (1990); Curran et al. (2000, 2001); Helfer & Blitz (1993); Henkel & Bally (1985); Henkel et al. (1993) Martín et al. (2005); Mauersberger & Henkel (1989); Mauersberger et al. (1989, 1991, 2003) Paglione et al. (1995); Nguyen-Q-Rieu et al. (1989); Sage et al. (1990); Wang et al. (2004)

Table 10.4: Line intensity ratios

Ratio	N253	N4945	M82	IC342	Maffei2	M83	N6946	M51	N891	N1068	N1365	N2146	N3628	N2903	N3079
CO(2-1)/CO(1-0)	9.1	6.7	7.7	9.5	9.4	9.0	8.4	8.7	5.7	8.5	6.1	8.7	5.7	6.0	7.0
CO(3-2)/CO(2-1)	3.1	2.4	3.3	3.0	2.9	2.4	1.6	3.4	1.3	2.2	3.1	2.9	3.4	3.5	2.5
CO(4-3)/CO(3-2)	2.3	-	2.0	2.1	2.3	2.0	2.6	1.1	-	1.7	-	1.6	1.6	-	2.0
CO(4-3)/CO(1-0)	63.7	-	51.0	60.0	62.8	43.2	34.3	31.3	-	31.3	-	40.5	30.0	-	35.2
¹³ CO(2-1)/ ¹³ CO(1-0)	8.8	7.4	8.9	11.1	11.0	8.9	6.0	9.1	5.5	6.8	6.7	12.9	4.4	7.3	8.0
¹³ CO(3-2)/ ¹³ CO(2-1)	3.1	2.7	3.6	2.8	1.7	2.4	2.5	3.0	-	3.1	3.0	1.9	3.7	-	5.5
¹³ CO(3-2)/ ¹³ CO(1-0)	27.3	20.2	32.4	31.1	18.6	21.0	14.8	27.0	-	20.8	20.2	25.0	16.5	-	44.4
[CI]609 μ m/ ¹³ CO(2-1)	37	-	-	22	9	31	30	20	-	28	-	-	57	-	116
¹³ CO(1-0)/CO(1-0)	0.082	0.059	0.058	0.087	0.086	0.081	0.079	0.12	0.11	0.065	0.077	0.068	0.078	0.076	0.056
¹³ CO(2-1)/CO(2-1)	0.080	0.065	0.067	0.10	0.10	0.080	0.057	0.13	0.11	0.052	0.085	0.10	0.061	0.093	0.064
¹³ CO(3-2)/CO(3-2)	0.080	0.075	0.074	0.096	0.058	0.079	0.090	0.11	-	0.072	0.084	0.068	0.068	-	0.14
CS(2-1)/CS(1-0)	6.61	-	6.62	10.05	>4.32	-	2.67	>7.20	-	-	-	-	-	-	-
CS(3-2)/CS(2-1)	2.13	1.65	1.69	1.50	5.87	0.42	2.53	-	-	-	-	<0.96	-	-	-
CS(4-3)/CS(3-2)	0.99	-	-	-	-	-	-	-	-	-	-	-	-	-	-
CS(5-4)/CS(4-3)	2.15	-	-	-	-	-	-	-	-	-	-	-	-	-	-
CS(5-4)/CS(1-0)	29.9	-	43.1	23.3	-	-	<11.5	-	-	-	-	-	-	-	-
CS(1-0)/CO(1-0)	0.004	-	0.003	0.003	<0.002	-	0.004	<0.005	-	-	-	-	-	-	-
CS(2-1)/CO(2-1)	0.003	0.003	0.003	0.003	0.001	0.003	0.001	0.004	0.003	0.004	-	0.003	<0.001	0.003	-
CS(3-2)/CO(3-2)	0.002	0.002	0.001	0.001	0.002	0.001	0.002	-	-	-	0.003	<0.001	-	-	0.001
CS(4-3)/CO(4-3)	0.001	-	-	-	-	-	-	-	-	-	-	-	-	-	-
HCN(4-3)/HCN(1-0)	42.1	5.2	14.2	18.7	-	-	-	-	-	-	-	-	-	-	-
HCN(4-3)/HCN(3-2)	2.12	1.33	1.84	-	-	-	-	-	-	-	-	-	-	-	-
HCO ⁺ (4-3)/HCO ⁺ (1-0)	47.2	3.9	20.1	22.6	-	-	-	-	-	-	-	-	-	-	-
HCO ⁺ (4-3)/HCO ⁺ (3-2)	3.40	0.50	1.86	2.84	-	-	-	-	-	-	-	-	-	-	-
HCN(1-0)/HCO ⁺ (1-0)	1.23	0.77	0.55	1.39	1.33	1.40	0.83	1.15	1.64	1.04	-	1.18	1.57	2.29	>3.93
HCN(3-2)/HCO ⁺ (3-2)	0.86	1.53	0.76	-	-	-	-	-	-	-	-	-	-	-	-
HCN(4-3)/HCO ⁺ (4-3)	1.37	0.58	0.77	1.68	-	-	-	-	-	-	-	-	-	-	-
HCN(1-0)/CO(1-0)	0.047	0.033	0.024	0.059	0.047	0.087	0.023	0.056	0.014	0.091	0.042	0.016	0.018	0.040	0.025
HCN(3-2)/CO(3-2)	0.024	0.016	0.010	0.017	0.014	0.008	0.007	<0.013	-	0.020	-	0.009	-	<0.022	<0.025
HCN(4-3)/CO(4-3)	0.035	-	0.009	0.023	-	-	-	-	-	-	-	-	-	-	-
CS(1-0)/HCN(1-0)	0.082	-	0.14	0.043	0.050	-	0.18	0.084	-	-	-	-	-	-	-
CS(3-2)/HCN(3-2)	0.083	0.15	0.14	0.081	0.16	0.065	0.30	-	-	-	-	0.11	-	-	0.049
CS(4-3)/HCN(4-3)	0.024	-	-	-	-	-	-	-	-	-	-	-	-	-	-
HNC(1-0)/HCN(1-0)	0.71	0.71	0.52	0.50	0.30	0.15	0.51	0.30	0.32	0.49	-	0.36	0.60	0.28	0.78

Table 10.5: Possible components explaining CO ratios

Galaxy	low CR PDR	high CR PDR	XDR
NGC 253	very high n	very high n	y
NGC 4945	y	y	y
M 82	y	y	y
IC 342	n	n	y
Maffei 2	n	n	y
M 83	very high n	very high n	y
NGC 6946	very high n	y	y
M 51	very high n	y	y
NGC 891	y	y	y
NGC 1068	very high n	y	y
NGC 1365	y	y	y
NGC 2146	very high n	y	y
NGC 3628	y	y	y
NGC 2903	y	y	y
NGC 3079	y	y	y

One solution can be an elevated cosmic rays rate caused by greatly enhanced supernova rates in starforming regions (Suchkov et al. 1993; Bradford et al. 2003). Especially for low density gas it is then possible to obtain somewhat higher ratios (Meijerink et al. 2006a). For a cosmic ray rate of $\zeta = 5 \times 10^{-15} \text{ s}^{-1}$, corresponding to a star-formation rate of $\sim 100 M_{\odot} \text{ yr}^{-1}$, the ratio at $n = 10^3$ and $G_0 = 10^2$ increases from 5.9 to 7.5, and for $n = 10^4$ and $G_0 = 10^2$ from 7.8 to 8.4. CO ratios for high density gas ($n = 10^5 \text{ cm}^{-3}$) are not affected by a higher cosmic ray rate and ratios as high as 9.5 cannot be obtained. High (~ 64) CO(4-3)/CO(1-0) ratios still require densities of $n = 10^5 \text{ cm}^{-3}$.

XDRs models, however, easily produce ratios CO(2-1)/CO(1-0) $\sim 5.7 - 9.5$ and CO(4-3)/(1-0) $\sim 30 - 64$, and do not need extreme radiation fields and high densities. Therefore, it is very well possible that the diffuse gas component in galaxies such as NGC 253, IC 342 and Maffei 2 is dominated by X-rays. Pietsch et al. (2001) found X-ray emission from both an active nucleus and binary stars in NGC 253, and Bauer et al. (2003) found a large number of X-ray binaries in IC 342, that can account for such X-ray irradiation. In Table 10.5, we summarize which components can reproduce the line ratios of CO.

We also compared the $^{13}\text{CO}(2-1)/^{13}\text{CO}(1-0)$ and $^{13}\text{CO}(2-1)/^{12}\text{CO}(1-0)$ ratios with the Meijerink et al. (2006b) model grids, and get almost the same range of PDR and XDR models as for the CO ratios discussed above.

Note that we need to be careful in interpreting CO ratios from the large regions we consider here. The low- J CO rotational lines trace diffuse gas and are optically thick, while also large velocity gradients occur. Maloney & Black (1988) studied the effect of cloud parameters such as density, temperature and elemental abundances on the estimated H_2 mass derived from the CO emission, and already pointed this out.

10.4.2 [CI] 609 μm /¹³CO(2-1)

The observed [CI] 609 μm /¹³CO(2-1) ratios range from 9 for Maffei 2 to 115.6 for NGC 3079 (see Table 10.4). High ratios are difficult to explain with low cosmic ray PDRs. Various studies (Pineau des Fôrets et al. 1992; Schilke et al. 1993; Flower et al. 1994) postulate enhanced cosmic ray rates to reproduce these high ratios. It is indeed possible to obtain the ratio 116 for $\zeta = 5 \times 10^{-15} \text{ s}^{-1}$, density $n = 10^3 \text{ cm}^{-3}$ and impinging flux $G_0 = 10^2 - 10^4$. However, it is very questionable, whether cosmic rays remain in the galaxy center where they are produced, since their absorption cross sections are very small. A better option is an XDR model, which capable of reproducing these high ratios with moderate X-ray fluxes (Meijerink et al. 2006a). This is a direct consequence of the fact that CO, C⁺, and C co-exist to large depths in XDRs, and large columns of neutral carbon are present. In PDRs, however, there is only a small carbon layer in the C⁺/C/CO transition.

10.4.3 HCN/HCO⁺ ratios

The observed HCN(1-0)/HCO⁺(1-0) line intensity ratios, range between 0.55 for M 82 to >3.9 for NGC 3079 (see Table 10.4). Comparing this to the PDR and XDR model results, we find that both model sets give solutions. In XDRs, HCN/HCO⁺ ratios are high (> 1) in highly ionized regions, and the HCO⁺ abundance is suppressed compared to HCN due to additional recombination reactions. However, the abundances of both HCN and HCO⁺ are small (< 10⁻¹⁰) in these regions and little emission is produced. Therefore, XDR models with low densities, $\sim 10^4 \text{ cm}^{-3}$ and high radiation field, $> 10 \text{ erg s}^{-1} \text{ cm}^{-3}$ (where the ionized fraction is high all throughout the cloud), show large (> 1) integrated ratios, but are hardly detectable. Thus, observed ratios larger than unity probably correspond to a region dominated by FUV photons. For a low HCN/HCO⁺ ratio (<1), we cannot discriminate between a PDR and an XDR. However, the XDR needs a higher density than the PDR to produce the same ratio. In that case, another density tracer would give a solution. In Table 10.6, we summarize which components can reproduce the HCN/HCO⁺ line ratios.

10.4.4 HCN/CO ratios

The ratios for HCN(1-0)/CO(1-0) range from 0.014 for NGC 891 to 0.091 for NGC 1068 (see Table 10.4). Both PDR and XDR models give solutions, but the densities found for the XDR models are systematically higher.

The densities obtained from HCN/CO ratios are lower than for the HCN/HCO⁺ ratios, since the critical density $n_{cr} = 3 \times 10^3 \text{ cm}^{-3}$ for CO(1-0) is much lower than $n_{cr} = 2 \times 10^5 \text{ cm}^{-3}$ for HCO⁺. When we assume that CO traces both low and high densities, while HCO⁺ traces only the high density, we can make an estimate of the contribution of the high and low density component to the ISM in each galaxy. First, we determine from our grid the HCN/CO ratio needed to obtain the same density as for HCN/HCO⁺, and then calculate how much CO should be in the low density component to obtain this ratio. We find that 70 to 80 percent of the CO radiation should be produced by the diffuse component in each galaxy. Exceptions are NGC 1068 and M 83, for which we find 55

Table 10.6: Possible components explaining HCN/HCO⁺ ratios

Galaxy	PDR	XDR
NGC 253	y	n (only low N)
NGC 4945	y	y
M 82	y	y
IC 342	y	n (only low N)
Maffei 2	y	n (only low N)
M 83	y	n (only low N)
NGC 6946	y	y
M 51	y	n (only low N)
NGC 891	y	n (only low N)
NGC 1068	y	n (only low N)
NGC 1365	y	n (only low N)
NGC 2146	y	n (only low N)
NGC 3628	y	n (only low N)
NGC 2903	y	n (only low N)
NGC 3079	y	n (only low N)

percent, and NGC 891 and NGC 3079, for which we find 95 percent. This is consistent with the results of a more detailed analysis by Israel et al. (2006).

10.4.5 HNC/HCN ratios

All the observed galaxies show HNC(1-0)/HCN(1-0) ratios less than unity, and range from 0.15 for M 83 to 0.7 for NGC 253 and NGC 4945 (see Table 10.4). Our grid of models with fixed cloud sizes of 1 pc yield solutions only by XDR models with strong radiation fields, $F_X > 10 \text{ erg s}^{-1} \text{ cm}^{-2}$, and densities $n = 10^4 - 10^5 \text{ cm}^{-3}$. This is an acceptable answer, since galaxies such as M 82, NGC 891, and NGC2903 are typical starburst galaxies and are probably best modelled with PDR models. Further consideration shows that the total column density of the cloud is a crucial parameter in this case. In the radical regions of PDRs, the HCN abundance is much larger than the HNC abundance, but deeper in the cloud they are almost identical. As a consequence, the PDR HNC(1-0)/HCN(1-0) ratio is about unity for column densities larger than $N_H = 10^{22} \text{ cm}^{-2}$ ($\sim 5 \text{ mag}$), and less than unity, when $N_H < 10^{22} \text{ cm}^{-2}$. This is also illustrated in Fig. 27 of Meijerink et al. (2006b), where we show the cumulative intensity ratios and find that the ratios increase toward larger column densities.

Note that HNC and HCN emission lines are optically thick, and possibly also pumped by infrared emission (Aalto, private communication), which will make the interpretation of the ratios more complex than it seems now. IR pumping is mostly important for HNC since the HCN rate is down by a factor of > 100 for the same mid-infrared brightness temperature ($T_{IR} \sim 60 - 80 \text{ K}$ is needed for pumping).

10.4.6 CS ratios

For a small number of galaxies, we also have CS lines, which are also high density tracers. We compared the CS(2-1)/CS(1-0) lines with the PDR and XDR models, and obtain results consistent with the other high density tracers HCN/HCO⁺ and HCN/CO. A remarkable result is obtained for NGC 6946, which has a ratio CS(2-1)/CS(1-0)=2.67, and which can only be reproduced with an XDR ($n = 0.6 - 2 \times 10^5 \text{ cm}^{-3}$, and $F_X = 1.6 - 30 \text{ erg s}^{-1} \text{ cm}^{-2}$). To reproduce the CS ratio with a PDR model, we need a density $n < 10^3 \text{ cm}^{-3}$, independent of G_0 , but at these densities there is (almost) no CS emission produced.

10.5 Comparison to Galactic PDRs

It not clear whether the observed emission of, e.g., HCN and CO in our sample is spatially correlated, due to the lack of resolution. It is possible, however, to study the spatial distribution of emission in Galactic Giant Molecular Clouds (GMCs). Helfer & Blitz (1997), studied the I(HCN)/I(CO) and I(CS)/I(CO) ratio as a function of effective radius in the GMCs S140, Orion B, S88 and S269. In all GMCs, they find a drop in the ratios as a function of effective radius. HCN, CS and CO emission are spatially not equally distributed. HCN and CS emission is only emitted by the densest part of the cloud, while CO is also emitted by more diffuse gas. The HCN/CO ratios of 0.12-0.16 indicates a density of $n = 0.5 - 1 \times 10^5 \text{ cm}^{-3}$ in the center of the GMC going down to $n < 10^4 \text{ cm}^{-3}$ at an effective radius of 5 pc, where the ratio is between 0.02-0.03. Young Owl et al. (2000) observed the distribution of HCN and HCO⁺ emission in the Orion Bar, and compared this to that of CO. The CO emission is much more smoothly distributed than the HCN and HCO⁺ emission. Half of the CO emission is coming from the interclump medium, while this is only a small fraction for the HCN and HCO⁺ emission. The average HCN(1-0)/CO(1-0) line emission ratio is 0.11, resulting in a density of $n = 3 - 4 \times 10^4 \text{ cm}^{-3}$, while the average HCN(1-0)/HCO⁺(1-0) = 2.0 yields a density $n = 1.5 - 4 \times 10^5 \text{ cm}^{-3}$. Both papers confirm our conclusion that CO emission is partially from diffuse and partially from dense gas.

10.6 X-ray versus FIR emission

In Table 10.1, the X-ray and FIR luminosities are shown. We obtained both X-ray and FIR fluxes from the NED database and consequently converted them to luminosities for a more convenient comparison. The X-ray fluxes are observed by the Einstein and ROSAT satellites. The FIR emission are results obtained by IRAS, at rather poor resolution. The FIR luminosity is always larger than the X-ray luminosity. This is expected, however, due to the fact that FIR emission is produced throughout a galaxy, while the X-rays are mostly produced in the center. Another reason for the small X-ray/FIR luminosity ratio, is that X-rays can be absorbed by foreground gas clouds and re-emitted by dust in the FIR regime. It is therefore hard to say what contribution the X-rays make to the total emitted radiation in the center of each galaxy.

10.7 Discussion

Below we briefly discuss each galaxy separately, and especially those for which we have obtained remarkable results. Then, we conclude with some general remarks, and give a diagnostic table.

10.7.1 Individual galaxies

NGC 253

In the center of NGC 253, we find indications for both a dense PDR and a diffuse XDR component. We need very high densities to reproduce the CO and ^{13}CO ratios with the low and high cosmic ray PDR models, while XDRs with moderate densities and radiation fields easily reproduce these ratios. It is not very likely that dense highly irradiated gas has very large filling factors. It is also consistent with the fact that NGC 253 contains an AGN and an outflow emitting X-rays (Einstein: Fabbiano et al. 1992; ROSAT: Brinkmann et al. 1994). The $\text{HCN}(1-0)/\text{HCO}(1-0)^+$ ratio, however, favours a PDR model. XDR models with low column densities can reproduce the ratio, but there is not much line emission produced and thus XDRs cannot account for the observed emission from these species.

NGC 4945

The center of NGC 4945 contains an embedded active galactic nucleus, which was observed by e.g., BeppoSAX (Guainazzi et al. 2000). Both PDR and XDR models, however, reproduce the observed ratios within reasonable parameters. One problem is the resolution of our observations ($21''$) and the distance to NGC 4945 (3.9 Mpc). Therefore, a region as large as 400 kpc is observed at once, which can easily hide the very specific properties that are common to XDRs.

M 82

M 82 is a starburst galaxy, but also X-rays are observed, which are produced in an outflow (Einstein: Fabbiano et al. 1992). Low cosmic ray PDRs need quite high densities to reproduce the CO ratios, but an enhanced cosmic ray rate (which might indeed be appropriate in a starburst galaxy) gives reasonable results. XDR models also reproduce the line ratios very well.

IC 342

IC 342 shows both PDR and XDR components. The CO ratios are only properly reproduced with XDR models. PDR models reproduce the ratios for unacceptably large densities. The HCN/HCO^+ ratio is only properly reproduced with a PDR model, while the $\text{CS}(2-1)/\text{CS}(1-0)$ is again requires an XDR model. It is very likely that the diffuse component is dominated by X-rays (e.g. XMM-Newton observations Bauer et al. 2003 confirm X-ray emission), but this is not clear for the dense component of the galaxy.

Maffei 2

The CO ratios of Maffei 2 can only be reproduced by the XDR models. This would indicate that the diffuse component is dominated by X-rays. However, Maffei 2 is not detected in the X-ray regime. This is very probably caused by the large amount of extinction, which has is as large as $A_V = 7^m.3$. PDRs with an elevated cosmic ray rate would come close to the observed CO ratios. When we consider the [CI] $609\mu\text{m}/^{13}\text{CO}(2-1)$ ratio, which is consistent with a lack of X-rays, it seems very plausible that the FUV (aided by cosmic rays) photons dominate the chemical structure of the gas, and the same holds for the high density tracers.

M 83

The starburst M 83 contains X-ray emission from point sources connected to star-formation (e.g., ROSAT: Ehle et al. 1998). We again find that the CO ratios are best produced by a diffuse X-ray component, while the high density tracers are best reproduced by PDR models.

NGC 6946

The starburst galaxy NGC 6946 contains both signs of discrete sources connected to star-formation (Holt et al. 2003), but also shows indications for a hot ionized halo (Ehle 2005). Although the CO ratios can be reproduced with high cosmic ray PDR models, the CS(2-1)/CS(1-0) can only be reproduced with an XDR model.

M 51

Fukazawa et al. (2001) observed M 51 with BeppoSAX, and found evidence for a heavily obscured AGN. The CO ratios can both be reproduced by high cosmic ray PDRs or XDRs. The high density tracers, however, favour PDR models.

NGC 891

Although X-ray emission is observed from the supernova remnant SN 1986J (Bregman & Pildis 1992), there is no evidence that NGC 891 is dominated by X-rays. The diffuse component (CO lines) is easily reproduced by both PDR and XDR models, while the dense component is only reproduced by PDR models.

NGC 1068

NGC 1068 is the nearest strong Seyfert 2 galaxy, but although many people view this galaxy as a pure XDR (Einstein: Fabbiano et al 1992; ROSAT: Brinkmann et al. 1994; EXOSAT: Turner and Pounds 1989), this is not unambiguously clear from the observations. The diffuse component (CO lines) can be modelled by both (enhanced cosmic ray) PDR and XDR models. The dense component can be modelled by a PDR or a very strongly irradiated XDR. It is not very likely that a large beam is filled with very strongly

X-ray irradiated gas, since at the 14.4 Mpc distance, the area covered is 1.5 kpc in size, and the PDR model is favoured. High resolution observations of high-J CO lines, which are produced by warm CO gas, are very good indicators of an XDR (Meijerink et al. 2006a), but these emission lines can only be observed in the FIR by Herschel (HIFI). CO absorption at $4.7\mu\text{m}$ gives no sign of the presence of warm CO gas in the core of NGC 1068 (Nakagawa, private communication).

NGC 1365

Although NGC 1365 contains an X-ray nucleus, which is observed by, e.g., BeppoSAX (Risaliti et al. 2000), we find no indication in the ratios that would favour an XDR. The reason is that the $21''$ beam covers a very large region of 1.5 kpc at 13.7 Mpc.

NGC 2146

NGC 2146 is a starburst galaxy with strong diffuse hard X-ray emission (Matsumoto 2003). This could be a possible explanation for the CO ratios, especially for the ratio $^{13}\text{CO}(2-1)/^{13}\text{CO}(1-0)=12.9$. The dense component, however, is best modelled by PDRs, since very dense, highly irradiated XDRs would be needed to reproduce the $\text{HCN}(1-0)/\text{HCO}^+(1-0)$ line ratio.

NGC 3628

Dahlem et al. (1995) observed NGC 3628 with ROSAT, and find that the nuclear source is either a very low luminosity AGN or the brightest X-ray binary known. This source is not powerful, and this is also seen in the ratios. All ratios can be explained by normal PDRs over an acceptable parameter range. The very high $[\text{CI}] 609\mu\text{m}/^{13}\text{CO}(2-1)$ indicates that the diffuse part of the gas is very prominent.

NGC 2903

Tschöke et al. (2003) find hot extraplanar gas in NGC 2903, indicating a galactic superwind, which is very common in edge-on galaxies with a central starburst. We can easily fit the ratios with normal PDRs, and especially the high density tracer ratio, $\text{HCN}(1-0)/\text{HCO}^+(1-0)=2.29$, strongly hints toward a PDR chemistry.

NGC 3079

Pietsch et al. (1998) find, based on ROSAT observations, that the amount of X-rays produced in NGC 3079 is 10 times higher than for other galaxies with the same luminosity. Iyomoto et al. (2001) find with BeppoSAX that NGC 3079 contains an highly obscured AGN ($N_H \sim 10^{25} \text{ cm}^{-3}$) with high luminosity ($L_X \sim 10^{42} - 10^{43} \text{ erg s}^{-1}$). This might explain the high ratio of $[\text{CI}] 609\mu\text{m}/^{13}\text{CO}(2-1)=116$. The CO ratios are also consistent with an XDR. The ratio $\text{HCN}(1-0)/\text{HCO}^+(1-0) > 3.93$ hints in the direction of an XDR. When almost no HCO^+ is observed, it is possible that we have an highly irradiated

($F_X > 10 \text{ erg s}^{-1} \text{ cm}^{-2}$) XDR with densities between $n = 10^4 - 10^5 \text{ cm}^{-3}$. The dense part is also (maybe even better) explained by a very dense PDR.

10.7.2 General remarks

In Table 10.22, we give representative values for often observed ratios, which can also be applied to other galaxies, such as (U)LIRGS. Below we conclude with some general remarks.

1. X-rays and enhanced cosmic ray rates are crucial to explain the emission line ratios (particularly those of the CO lines) emitted by the diffuse gas component of galaxy centers.
2. The nearby galaxies in our sample often require high density PDR models to explain ratios between HCN and HCO^+ . The ratios are high density tracers, and therefore a strong indication of embedded active star-formation.
3. To velocity separate the PDR and XDR components in galaxies, we need a spatial resolution $< 40 \text{ pc}$, which will be readily obtained with ALMA.
4. Ratios that cannot be explained by our models might be due to the nature of the global velocity field (i.e., radiative transfer) and the occurrence of shocks.

Table 10.7: NGC 253

	ratio	PDR		XDR	
		n [cm ⁻³]	G ₀	n [cm ⁻³]	F _X [erg s ⁻¹ cm ⁻²]
CO(2-1)/CO(1-0)	9.1	1 – 3 × 10 ⁶	10 ⁵ – 10 ³	10 ² – 10 ⁴	0.2
				1 – 3 × 10 ⁶	1-4
CO(3-2)/CO(2-1)	3.1	2 × 10 ⁴ – 2 × 10 ⁵	10 ⁵ – 10 ²	2 × 10 ² -10 ⁴	1-0.2
CO(4-3)/CO(3-2)	2.3	1 × 10 ⁵ – 3 × 10 ⁶	10 ⁵ – 2 × 10 ³	1.5 – 10 × 10 ³	10
				10 ⁴ – 3 × 10 ^{6.5}	1-10
CO(4-3)/CO(1-0)	63.7	10 ⁵ – 3 × 10 ⁶	10 ⁵ – 10 ³	1.5 × 10 ² – 10 ⁴	1-0.3
				1 – 3 × 10 ⁶	1.6-3
¹³ CO(2-1)/ ¹³ CO(1-0)	8.8	10 ⁴ – 3 × 10 ⁶	4 × 10 ⁴ – 3 × 10 ³	10 ² – 10 ³	0.15-0.04
¹³ CO(3-2)/ ¹³ CO(1-0)	27.3	10 ⁴ – 3 × 10 ⁶	10 ⁵ – 2 × 10 ³	10 ² – 10 ³	0.3-0.15
				4 – 10 × 10 ³	0.16-0.25
[CI] 609μm/ ¹³ CO(2-1)	36.6	3 – 9 × 10 ²	10 ^{0.5} – 10 ³	4 × 10 ³ – 10 ⁴	0.16-5
				4 × 10 ⁴ – 3 × 10 ⁵	1.6-160
HCN(1-0)/HCO ⁺ (1-0)	1.23	9 × 10 ⁴ – 2 × 10 ⁵	10 ⁵ – 10 ²	10 ⁶	100
HCN(1-0)/CO(1-0)	0.047	1.5 – 2 × 10 ⁴	10 ⁵ – 10 ²	0.9 – 1.5 × 10 ⁵	1.6-160
CS(2-1)/CS(1-0)	6.6	3 – 5 × 10 ⁴	10 ² – 10 ⁵	10 ⁴ – 2 × 10 ⁵	1.6-40

Table 10.8: NGC 4945

	ratio	PDR		XDR	
		n [cm ⁻³]	G_0	n [cm ⁻³]	F_X [erg s ⁻¹ cm ⁻²]
CO(2-1)/CO(1-0)	6.7	$2 - 6 \times 10^3$	$10^4 - 10^1$	$10^2 - 10^3$	0.1-0.04
CO(3-2)/CO(2-1)	2.4	$2 - 10 \times 10^3$	$10^4 - 10^2$	$10^2 - 10^3$	1.0-0.01
¹³ CO(2-1)/ ¹³ CO(1-0)	7.4	$4 \times 10^3 - 10^4$	$10^4 - 2 \times 10^2$	$10^2 - 10^3$	0.12-0.03
¹³ CO(3-2)/ ¹³ CO(1-0)	20.2	$5 \times 10^3 - 2 \times 10^4$	$10^4 - 10^2$	$10^2 - 10^3$	0.2-0.1
HCN(1-0)/HCO ⁺ (1-0)	0.77	$5 - 5.5 \times 10^4$	$10^5 - 10^2$	5×10^5	20-160
				$5 - 10 \times 10^5$	20
				$1 - 3 \times 10^6$	20-160
HCN(1-0)/CO(1-0)	0.033	$1 - 1.5 \times 10^4$	$10^3 - 10^2$	$0.6 - 1.5 \times 10^5$	1.6-160
		$4 - 8 \times 10^3$	$10^4 - 10^1$		

Table 10.9: M 82

	ratio	PDR		XDR	
		n [cm ⁻³]	G_0	n [cm ⁻³]	F_X [erg s ⁻¹ cm ⁻²]
CO(2-1)/CO(1-0)	7.7	$8 - 10 \times 10^3$	$10^4 - 10^3$	$10^2 - 10^3$	0.15
CO(3-2)/CO(2-1)	3.3	$6 \times 10^4 - 3 \times 10^6$	$10^5 - 10^3$	$2 \times 10^2 - 10^4$	1-10
				$1 - 3 \times 10^6$	1-4
CO(4-3)/CO(3-2)	2.0	$2 \times 10^4 - 3 \times 10^5$	$10^5 - 10^2$	$10^3 - 10^4$	4-0.4
CO(4-3)/CO(1-0)	51.0	$2 \times 10^4 - 1.5 \times 10^5$	$10^5 - 10^2$	$2 \times 10^2 - 10^4$	1.0-0.1
¹³ CO(2-1)/ ¹³ CO(1-0)	8.9	$10^4 - 3 \times 10^6$	$6 \times 10^4 - 6 \times 10^3$	$10^2 - 10^3$	0.15-0.04
¹³ CO(3-2)/ ¹³ CO(1-0)	32.4	$5 \times 10^4 - 3 \times 10^6$	$10^5 - 5 \times 10^4$	$1.5 - 10 \times 10^2$	1.6-0.2
				$2.5 - 10 \times 10^3$	0.16-1
HCN(1-0)/HCO ⁺ (1-0)	0.55	$3 - 3.5 \times 10^4$	$10^5 - 10^2$	4×10^5	1.6-160
				$2 - 3 \times 10^6$	1.6-5
HCN(1-0)/CO(1-0)	0.024	$3 - 6 \times 10^3$	$10^4 - 10^3$	$0.5 - 1 \times 10^5$	1.6-160
CS(2-1)/CS(1-0)	6.6	$3 - 5 \times 10^4$	$10^2 - 10^5$	$10^4 - 2 \times 10^5$	1.6-40

Table 10.10: IC 342

	ratio	PDR		XDR	
		n [cm ⁻³]	G_0	n [cm ⁻³]	F_X [erg s ⁻¹ cm ⁻²]
CO(2-1)/CO(1-0)	9.5	$> 10^{6.5}$	$> 10^4$	$10^2 - 10^4$ $10^5 - 10^{6.5}$	0.2 1-7
CO(3-2)/CO(2-1)	3.0	$3 - 8 \times 10^4$	$10^5 - 10^2$	$4 \times 10^2 - 10^4$	1-0.3
CO(4-3)/CO(3-2)	2.1	$4 \times 10^4 - 10^6$	$10^5 - 10^2$	$10^3 - 10^4$ $2 - 3 \times 10^6$	10-2 1-2
CO(4-3)/CO(1-0)	60.0	$5 \times 10^5 - 3 \times 10^6$	$10^5 - 3 \times 10^2$	$10^2 - 10^4$ 2×10^6	1.0-0.5 1.6-3
¹³ CO(2-1)/ ¹³ CO(1-0)	11.1	-	-	$10^2 - 10^3$ $3 - 10 \times 10^4$ $10^5 - 3 \times 10^6$	0.4-0.1 0.16-0.55 1.6-6.5
¹³ CO(3-2)/ ¹³ CO(1-0)	31.1	$5 \times 10^4 - 3 \times 10^6$	$10^5 - 2 \times 10^4$	$1.5 - 10 \times 10^2$ $2.5 - 10 \times 10^3$	1.6-0.2 0.16-1
[CI] 609 μ m/ ¹³ CO(2-1)	22.2	$4.5 \times 10^2 - 2 \times 10^3$	$10^{0.5} - 10^4$	$5.5 \times 10^3 - 10^4$ $4 \times 10^4 - 2 \times 10^6$	0.16-1.5 1.6-160
HCN(1-0)/HCO ⁺ (1-0)	1.39	$1 - 2 \times 10^5$	$10^5 - 10^2$	-	-
HCN(1-0)/CO(1-0)	0.059	$2 - 2.5 \times 10^4$	$10^5 - 10^2$	$1.3 - 1.9 \times 10^5$	1.6-160
CS(2-1)/CS(1-0)	10.05	-	-	$10^4 - 3 \times 10^6$	1.6-160

Table 10.11: Maffei 2

	ratio	PDR		XDR	
		n [cm ⁻³]	G_0	n [cm ⁻³]	F_X [erg s ⁻¹ cm ⁻²]
CO(2-1)/CO(1-0)	9.4	$> 10^{6.5}$	$> 10^4$	$10^2 - 10^4$ $10^5 - 10^{6.5}$	0.2 1-7
CO(3-2)/CO(2-1)	2.9	$1 - 5 \times 10^4$	$2 \times 10^4 - 10^2$	$4 \times 10^2 - 2 \times 10^3$	1-0.1
CO(4-3)/CO(3-2)	2.3	$1 \times 10^5 - 3 \times 10^6$	$10^5 - 2 \times 10^3$	$1.5 - 10 \times 10^3$ $10^4 - 3 \times 10^{6.5}$	10 1-10
CO(4-3)/CO(1-0)	62.8	$10^5 - 3 \times 10^6$	$10^5 - 10^3$	$1.5 \times 10^2 - 10^4$ $1 - 3 \times 10^6$	1-0.3 1.6-3
¹³ CO(2-1)/ ¹³ CO(1-0)	11.0	-	-	$10^2 - 10^3$ $3 - 10 \times 10^4$ $10^5 - 3 \times 10^6$	0.4-0.1 0.16-0.55 1.6-6.5
¹³ CO(3-2)/ ¹³ CO(1-0)	1.7	$3.5 \times 10^3 - 2.5 \times 10^4$	$10^4 - 10^2$	$10^2 - 10^3$	0.18-0.08
[CI] 609 μ m/ ¹³ CO(2-1)	9.33	$7.5 - 10 \times 10^3$ $2 - 3 \times 10^4$	$10^4 - 7 \times 10^2$ $10^5 - 10^2$	$1 - 3 \times 10^6$	1.6-7
HCN(1-0)/HCO ⁺ (1-0)	1.33	$1 - 2 \times 10^5$	$10^5 - 10^2$	-	-
HCN(1-0)/CO(1-0)	0.047	$1.5 - 2 \times 10^4$	$10^5 - 10^2$	$0.9 - 1.5 \times 10^5$	1.6-160
CS(2-1)/CS(1-0)	>4.32	$> 10^4$	$10^2 - 10^5$	$10^4 - 3 \times 10^6$	1.6-160

Table 10.12: M 83

	ratio	PDR		XDR	
		n [cm ⁻³]	G_0	n [cm ⁻³]	F_X [erg s ⁻¹ cm ⁻²]
CO(2-1)/CO(1-0)	9.0	$8 \times 10^5 - 3 \times 10^6$	$10^5 - 10^3$	$10^2 - 10^4$	0.2 1-4
CO(3-2)/CO(2-1)	2.4	$2 - 10 \times 10^3$	$10^4 - 10^2$	$10^2 - 10^3$	1.0-0.01
CO(4-3)/CO(3-2)	2.0	$2 \times 10^4 - 3 \times 10^5$	$10^5 - 10^2$	$10^3 - 10^4$	4-0.4
CO(4-3)/CO(1-0)	43.2	$7 \times 10^3 - 4 \times 10^4$	$10^4 - 10^2$	$2 \times 10^2 - 2 \times 10^3$	1-0.1
¹³ CO(2-1)/ ¹³ CO(1-0)	8.9	$10^4 - 3 \times 10^6$	$6 \times 10^4 - 6 \times 10^3$	$10^2 - 10^3$	0.15-0.04
¹³ CO(3-2)/ ¹³ CO(1-0)	21.0	$6 \times 10^3 - 4 \times 10^4$	$10^4 - 10^2$	$10^2 - 10^3$	0.2-0.1
[Cl] 609 μ m/ ¹³ CO(2-1)	31.3	$4 \times 10^2 - 1.5 \times 10^4$	$10^{0.5} - 10^4$	$4.5 \times 10^3 - 10^4$	0.16-3
HCN(1-0)/HCO ⁺ (1-0)	1.40	$1 - 2 \times 10^5$	$10^5 - 10^2$	-	-
HCN(1-0)/CO(1-0)	0.087	$3 - 3.5 \times 10^4$	$10^5 - 10^2$	2×10^5	1.6-160

Table 10.13: NGC 6946

	ratio	PDR		XDR	
		n [cm ⁻³]	G_0	n [cm ⁻³]	F_X [erg s ⁻¹ cm ⁻²]
CO(2-1)/CO(1-0)	8.4	$2 - 6 \times 10^5$	$10^2 - 10^5$	$10^2 - 10^4$	0.15
CO(3-2)/CO(2-1)	1.6	$2 - 3 \times 10^2$	$10^{0.5} - 10^3$	$1 - 5 \times 10^2$	0.2-0.01
CO(4-3)/CO(3-2)	2.6	-	-	$1.5 - 8 \times 10^3$	10
				$10^4 - 1.5 \times 10^5$	2-160
CO(4-3)/CO(1-0)	34.3	$4 \times 10^3 - 2 \times 10^4$	$10^4 - 10^2$	$5 \times 10^2 - 10^3$	1-0.1
¹³ CO(2-1)/ ¹³ CO(1-0)	6.0	$1.5 - 2 \times 10^3$	$10^4 - 10$	$1 - 5.5 \times 10^2$	0.09-0.02
¹³ CO(3-2)/ ¹³ CO(1-0)	14.8	$1.5 - 10 \times 10^3$	$10^4 - 10$	$10^2 - 10^3$	0.15-0.06
[CI] 609 μ m/ ¹³ CO(2-1)	29.6	$4 \times 10^2 - 1.5 \times 10^4$	$10^{0.5} - 10^4$	$4.5 \times 10^3 - 10^4$	0.16-3
				$4 \times 10^4 - 4 \times 10^5$	1.6-160
HCN(1-0)/HCO ⁺ (1-0)	0.83	$5.5 - 6 \times 10^4$	$10^5 - 10^2$	6×10^5	30-160
				$6 \times 10^5 - 2.5 \times 10^6$	30-160
HCN(1-0)/CO(1-0)	0.023	$3 - 6 \times 10^3$	$10^4 - 10^1$	$0.5 - 1 \times 10^5$	1.6-160
CS(2-1)/CS(1-0)	2.67	$< 10^3?$	-	$5 \times 10^4 - 2 \times 10^5$	1.6-30

Table 10.14: M 51

	ratio	PDR		XDR	
		n [cm ⁻³]	G_0	n [cm ⁻³]	F_X [erg s ⁻¹ cm ⁻²]
CO(2-1)/CO(1-0)	8.7	2×10^5	$10^2 - 10^5$	$10^2 - 10^4$	0.15
CO(3-2)/CO(2-1)	3.4	$2 \times 10^5 - 3 \times 10^6$	$10^5 - 10^3$	$2 \times 10^2 - 10^4$	1-10
				$2 \times 10^5 - 3 \times 10^6$	1-6
CO(4-3)/CO(3-2)	1.1	5×10^2	$10^{0.5} - 10^3$	$1 - 7 \times 10^2$	0.3-0.01
CO(4-3)/CO(1-0)	31.3	$3 \times 10^3 - 2 \times 10^4$	$10^4 - 10^2$	$10^2 - 10^3$	1-0.1
¹³ CO(2-1)/ ¹³ CO(1-0)	9.1	$10^4 - 3 \times 10^6$	$10^5 - 2 \times 10^4$	$10^2 - 10^3$	0.15-0.04
¹³ CO(3-2)/ ¹³ CO(1-0)	27.0	$10^4 - 3 \times 10^6$	$10^5 - 2 \times 10^3$	$10^2 - 10^3$	0.3-0.15
				$4 - 10 \times 10^3$	0.16-0.25
[Cl] 609 μ m/ ¹³ CO(2-1)	19.9	$7 \times 10^2 - 3 \times 10^3$	$10^{0.5} - 10^4$	$7 - 10 \times 10^3$	0.16-1
				$6 \times 10^4 - 1.5 \times 10^6$	1.6-160
HCN(1-0)/HCO ⁺ (1-0)	1.15	$8 - 10 \times 10^4$	$10^5 - 10^2$	10^6	90
HCN(1-0)/CO(1-0)	0.056	$1.8 - 2.2 \times 10^4$	$10^5 - 10^2$	$1.2 - 1.5 \times 10^5$	1.6-160
CS(2-1)/CS(1-0)	>7.2	$> 10^4$	$10^2 - 10^5$	$10^4 - 3 \times 10^6$	1.6-160

Table 10.15: NGC 891

	ratio	PDR		XDR	
		n [cm ⁻³]	G_0	n [cm ⁻³]	F_X [erg s ⁻¹ cm ⁻²]
CO(2-1)/CO(1-0)	5.7	5×10^2	$10^{0.5} - 10^3$	$10^2 - 10^3$	0.09-0.03
CO(3-2)/CO(2-1)	1.3	$1.5 - 2 \times 10^2$	$10^{0.5} - 10^3$	$1 - 4 \times 10^4$	0.1-0.01
¹³ CO(2-1)/ ¹³ CO(1-0)	5.5	9×10^2	$10^{0.5} - 10^3$	$1 - 4.5 \times 10^2$	0.08-0.02
HCN(1-0)/HCO ⁺ (1-0)	1.64	$1.5 - 2.5 \times 10^5$	$10^5 - 10^2$	-	-
HCN(1-0)/CO(1-0)	0.014	$1.5 - 3 \times 10^3$	$10^4 - 10^1$	$2.5 - 9 \times 10^4$	1.6-160

Table 10.16: NGC 1068

	ratio	PDR		XDR	
		n [cm ⁻³]	G_0	n [cm ⁻³]	F_X [erg s ⁻¹ cm ⁻²]
CO(2-1)/CO(1-0)	8.5	7×10^4	$10^2 - 10^5$	$10^2 - 10^4$	0.15
CO(3-2)/CO(2-1)	2.2	$1 - 5 \times 10^3$	$5 \times 10^3 - 10^1$	$1.5 - 7 \times 10^2$	1-0.01
CO(4-3)/CO(3-2)	1.7	$10^3 - 10^4$	$10^4 - 10^3$	$1 - 1.5 \times 10^3$	0.15-0.01
		$1 - 4 \times 10^4$	$10^3 - 10^2$		
CO(4-3)/CO(1-0)	31.3	$3 \times 10^3 - 2 \times 10^4$	$10^4 - 10^2$	$10^2 - 10^3$	1-0.1
¹³ CO(2-1)/ ¹³ CO(1-0)	6.8	$2 - 8.5 \times 10^3$	$10^4 - 10$	$10^2 - 10^3$	0.1-0.01
¹³ CO(3-2)/ ¹³ CO(1-0)	20.8	$6 \times 10^3 - 4 \times 10^4$	$10^4 - 10^2$	$10^2 - 10^3$	0.2-0.1
[CI] 609 μ m/ ¹³ CO(2-1)	28.0	$4 \times 10^2 - 1.5 \times 10^4$	$10^{0.5} - 10^4$	$4.5 \times 10^3 - 10^4$	0.16-3
				$4 \times 10^4 - 4 \times 10^5$	1.6-160
HCN(1-0)/HCO ⁺ (1-0)	1.04	$7.5 - 9 \times 10^4$	$10^5 - 10^2$	$7 \times 10^5 - 2 \times 10^6$	70-160
HCN(1-0)/CO(1-0)	0.091	$3 - 4 \times 10^4$	$10^5 - 10^2$	$1.6 - 2 \times 10^5$	1.6-160

Table 10.17: NGC 1365

	ratio	PDR		XDR	
		n [cm ⁻³]	G_0	n [cm ⁻³]	F_X [erg s ⁻¹ cm ⁻²]
CO(2-1)/CO(1-0)	6.1	$1 - 2 \times 10^3$	$10^1 - 10^4$	$10^2 - 10^3$	0.1-0.05
CO(3-2)/CO(2-1)	3.1	$2 \times 10^4 - 2 \times 10^5$	$10^5 - 10^2$	$2 \times 10^2 - 10^4$	1-0.2
¹³ CO(2-1)/ ¹³ CO(1-0)	6.7	$1.5 - 7 \times 10^3$	$10^4 - 10$	$10^2 - 10^3$	0.1-0.01
¹³ CO(3-2)/ ¹³ CO(1-0)	20.1	$5 \times 10^3 - 2 \times 10^4$	$10^4 - 10^2$	$10^2 - 10^3$	0.2-0.1
HCN(1-0)/CO(1-0)	0.042	$1.2 - 1.6 \times 10^4$	$10^5 - 10^2$	$0.8 - 1.4 \times 10^5$	1.6-160

Table 10.18: NGC 2146

	ratio	PDR		XDR	
		n [cm ⁻³]	G_0	n [cm ⁻³]	F_X [erg s ⁻¹ cm ⁻²]
CO(2-1)/CO(1-0)	8.7	2×10^5	$10^2 - 10^5$	$10^2 - 10^4$	0.15
CO(3-2)/CO(2-1)	2.9	$1 - 5 \times 10^4$	$2 \times 10^4 - 10^2$	$4 \times 10^2 - 2 \times 10^3$	1-0.1
CO(4-3)/CO(3-2)	1.6	$10^3 - 10^4$	$10^3 - 5 \times 10^2$	$1 - 2 \times 10^3$	1.5-0.1
		$1 - 3 \times 10^4$	$6 \times 10^2 - 10^2$		
CO(4-3)/CO(1-0)	40.5	$7 \times 10^3 - 4 \times 10^4$	$10^4 - 10^2$	$2 \times 10^2 - 2 \times 10^3$	1-0.1
¹³ CO(2-1)/ ¹³ CO(1-0)	12.9	-	-	$1.5 - 10 \times 10^2$	1.6-0.16
				$2 - 10 \times 10^3$	0.16-2.0
				$5 \times 10^4 - 8 \times 10^5$	1.6-160
¹³ CO(3-2)/ ¹³ CO(1-0)	25.0	$10^4 - 3 \times 10^6$	$2 \times 10^4 - 10^2$	$10^2 - 10^3$	0.25-0.15
HCN(1-0)/HCO ⁺ (1-0)	1.18	$8.5 - 10 \times 10^4$	$10^5 - 10^2$	10^6	100
HCN(1-0)/CO(1-0)	0.016	$1.7 - 3.5 \times 10^3$	$10^4 - 10^1$	$3.2 - 10 \times 10^4$	1.6-160

Table 10.19: NGC 3628

	ratio	PDR		XDR	
		n [cm ⁻³]	G_0	n [cm ⁻³]	F_X [erg s ⁻¹ cm ⁻²]
CO(2-1)/CO(1-0)	5.7	5×10^2	$10^{0.5} - 10^3$	$10^2 - 10^3$	0.09-0.03
CO(3-2)/CO(2-1)	3.4	$2 \times 10^5 - 3 \times 10^6$	$10^5 - 10^3$	$2 \times 10^2 - 10^4$	1-10
				$2 \times 10^5 - 3 \times 10^6$	1-6
CO(4-3)/CO(3-2)	1.6	$10^3 - 10^4$	$10^3 - 5 \times 10^2$	$1 - 2 \times 10^3$	1.5-0.1
		$1 - 3 \times 10^4$	$6 \times 10^2 - 10^2$		
CO(4-3)/CO(1-0)	30.0	$3 \times 10^3 - 2 \times 10^4$	$10^4 - 10^2$	$5 \times 10^2 - 10^3$	1-0.1
¹³ CO(2-1)/ ¹³ CO(1-0)	4.4	$3 - 3.5 \times 10^2$	$10^{0.5} - 10^3$	$1 - 2.5 \times 10^2$	0.04-0.02
¹³ CO(3-2)/ ¹³ CO(1-0)	16.5	$2.5 \times 10^3 - 10^4$	$10^4 - 10^2$	$10^2 - 10^3$	0.1-0.07
[CI] 609 μ m/ ¹³ CO(2-1)	57.0	$3.5 - 5 \times 10^2$	$10^{0.5} - 10^3$	$3 - 10 \times 10^3$	0.16-10
				$3 \times 10^4 - 2 \times 10^5$	1.6-160
HCN(1-0)/HCO ⁺ (1-0)	1.57	$1.2 - 2.2 \times 10^5$	$10^5 - 10^2$	-	-
HCN(1-0)/CO(1-0)	0.018	$1.9 - 4 \times 10^3$	$10^4 - 10^1$	$3.8 - 10 \times 10^4$	1.6-160

Table 10.20: NGC 2903

	ratio	PDR		XDR	
		n [cm ⁻³]	G_0	n [cm ⁻³]	F_X [erg s ⁻¹ cm ⁻²]
CO(2-1)/CO(1-0)	6.0	$1 - 1.5 \times 10^3$	$10^4 - 10^1$	$10^2 - 10^3$	0.1-0.05
CO(3-2)/CO(2-1)	3.5	$6 \times 10^5 - 3 \times 10^6$	$10^5 - 3 \times 10^3$	$2 \times 10^2 - 10^4$	1-10
				$2 \times 10^5 - 3 \times 10^6$	1-6
¹³ CO(2-1)/ ¹³ CO(1-0)	7.3	$4 - 10 \times 10^3$	$10^4 - 2 \times 10^2$	$10^2 - 10^3$	0.12-0.03
HCN(1-0)/HCO ⁺ (1-0)	2.29	$2 - 8 \times 10^5$	$10^5 - 10^2$	-	-
		$2 - 3 \times 10^6$	$10^4 - 10^5$	-	-
HCN(1-0)/CO(1-0)	0.040	$1.2 - 1.8 \times 10^4$	$10^5 - 10^2$	$0.8 - 1.5 \times 10^5$	1.6-160

Table 10.21: NGC 3079

	ratio	PDR		XDR	
		n [cm ⁻³]	G_0	n [cm ⁻³]	F_X [erg s ⁻¹ cm ⁻²]
CO(2-1)/CO(1-0)	7.0	$3 - 9 \times 10^4$	$10^1 - 10^4$	$10^2 - 10^3$	0.1
CO(3-2)/CO(2-1)	2.5	$2 - 10 \times 10^3$	$10^4 - 10^2$	$10^2 - 10^3$	1.0-0.01
CO(4-3)/CO(3-2)	2.0	$2 \times 10^4 - 3 \times 10^5$	$10^5 - 10^2$	$10^3 - 10^4$	4-0.4
CO(4-3)/CO(1-0)	35.2	$4 \times 10^3 - 2 \times 10^4$	$10^4 - 10^2$	$10^2 - 10^3$	1-0.1
¹³ CO(2-1)/ ¹³ CO(1-0)	8.0	$1 - 3.5 \times 10^4$	$10^3 - 10^2$	$10^2 - 10^3$	0.12-0.03
¹³ CO(3-2)/ ¹³ CO(1-0)	44.4	-	-	$7 \times 10^4 - 3 \times 10^6$	1.6-20
[CI] 609 μ m/ ¹³ CO(2-1)	115.6	$2 - 3 \times 10^2$	$10^{0.5} - 10^3$	$2 \times 10^3 - 10^4$	0.16-10
				$2 \times 10^4 - 2 \times 10^5$	1.6-160
HCN(1-0)/HCO ⁺ (1-0)	3.93	$3 \times 10^5 - 2 \times 10^6$	$10^4 - 10^5$	-	-
HCN(1-0)/CO(1-0)	0.025	$3 - 6 \times 10^3$	$10^4 - 10^1$	$0.5 - 1 \times 10^5$	1.6-160

Table 10.22: Diagnostic diagram

Density [cm ⁻³]	ratio	low CR PDR	high CR PDR	XDR ($N \geq 10^{23}$ cm ⁻²)	XDR ($N \leq 10^{22}$ cm ⁻²)
$10^3 - 10^4$	CO(2-1)/CO(1-0)	6-8	7.5-9.0	8-40	-
	CO(4-3)/CO(1-0)	17-50	25-55	35-1300	-
	[CI] 609 μ m/ ¹³ CO(2-1)	12-32	15-140	10-10 ⁶	$10^2 - 10^7$
$\sim 10^5$	HCN(1-0)/HCO ⁺ (1-0)	> 1	0.5-1.0	0.1-0.25	0.1-10
	HCN(1-0)/CO(1-0) ¹	0.1-0.3	0.1-0.3	0.01-0.05	<0.02
	HNC(1-0)/HCN(1-0) ²	≤ 1.0	≤ 1.0	>1	≥ 0.5
	CO(16-15)/CO(1-0)	0.1-10	0.1-15	10-7000	>10000

¹In general, the HCN(1-0)/CO(1-0) ratio will be 3-4 times lower, since diffuse gas adds to the total CO line emission.

²The HNC(1-0)/HCN(1-0) ratio is less than unity in PDRs for column densities $N < 10^{22}$ cm⁻².

CHAPTER 11

Highlights & Outlook

In this study, we have made substantial progress in understanding the thermal and chemical balance in the centers of active galaxies. Prior to this work, only classical PDRs were applied to galactic centers. However, it turns out that the inclusion of an XDR component is necessary for a number of galaxies to understand the atomic and molecular line ratios. PDR models only consider photons in the far-ultraviolet range (FUV: $6 < E < 13.6$ eV), which are produced by O and B stars in starburst regions. XDRs are irradiated by photons with energies $E > 1$ keV, and are produced by, e.g., an accreting central black hole or intermediate-mass pre-main-sequence stars. XDRs have been imitated by using an elevated cosmic ray ionization rate in PDRs. However, as we have shown in Chapter 9, this does yield results significantly different from those obtained for XDRs. The cross sections for the absorption of X-ray photons are much lower than those for FUV photons. The variations in the thermal and chemical balance as a function of column density in an XDR are more gradual than in PDRs, where a very stratified structure is seen. For example, PDRs show a very clear $C^+ \rightarrow C \rightarrow CO$ sequence, but in XDRs these species co-exist, and large column densities of neutral carbon (unlike in PDRs) are produced. In PDRs, most ionizations are through direct absorption of a single FUV photon, which gives at most a fractional electron abundance of about 10^{-4} . Ionization in an XDR yields a very energetic electron, which can cause multiple ionizations/dissociations and excitations, and also heat the gas, resulting in a fractional electron abundance as high as ~ 0.1 . Consequently, more molecules are formed at high temperatures ($T \sim 300$ K) due to the higher ion-molecule reaction rates, leading to more rotational line radiation from high- J transitions. This is illustrated in Fig. 11.1, where we show the line intensities for the CO molecule as a function of upper rotational level at density $n = 10^5 \text{ cm}^{-3}$ and $G_0 = 10^5$ ($F_X = 160 \text{ ergs s}^{-1} \text{ cm}^{-2}$).

11.1 Identification of diagnostics

Sure: We have calculated line intensities for the atomic fine-structure lines of [SiII], [CII], [CI], [OI], [S], [FeII], and [Si]. Lines emitted by XDRs are generally brighter than those from PDRs, and the ratios obtained for the same density and impinging flux are quite different. Especially the [CI] lines are much brighter in XDRs, since neutral carbon is present throughout the cloud. As a consequence, the [CI] $609\mu\text{m}/^{13}\text{CO}(2-1)$ ratios are high as well, as they are thus a valuable diagnostic specially to distinguish between PDRs and XDRs. We have also calculated molecular rotational line intensities for CO, ^{13}CO , HCN, HNC, HCO^+ , SiO, and CS. We find

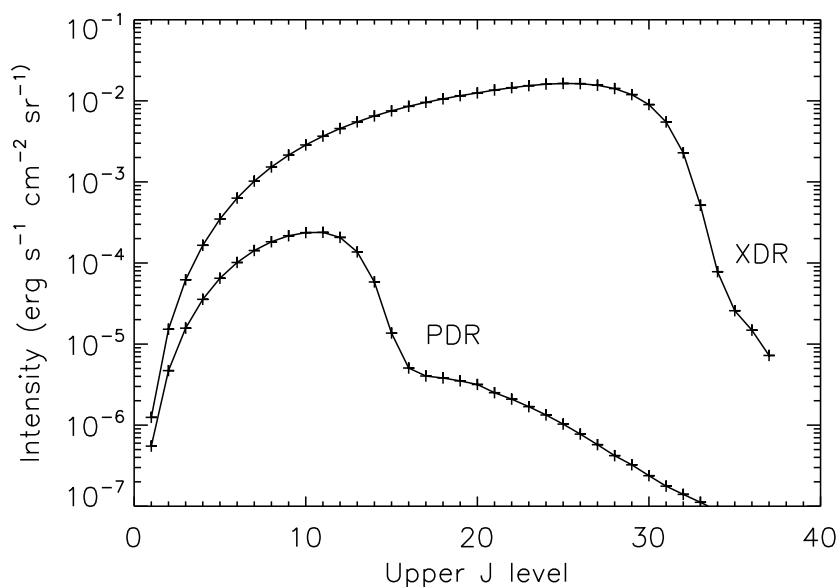


Figure 11.1: Line intensities for the CO molecule as a function of upper rotational level at density $n = 10^5 \text{ cm}^{-3}$ and $G_0 = 10^5$ ($F_X = 160 \text{ ergs s}^{-1} \text{ cm}^{-2}$)

that the HNC/HCN and HCN/HCO⁺ ratios are also very helpful in the constraining the physical properties of the dense gas part of the ISM.

Maybe: CN, CH and NO are possible diagnostics to discriminate between PDRs and XDRs. Evaluating their column density ratios relative to HCN and CO, we find that CN, CH and NO are enhanced by more than an order of magnitude. Unfortunately, it is very difficult to obtain accurate line intensities from our models, since there are no (reliable) collision rates available for these molecules. From our point of view, these are urgently needed. The transient molecules CO⁺ and CH⁺ might likewise serve as diagnostics to discriminate between PDRs and XDRs, since the column densities obtained in XDR models are much higher. The problem for these molecules, however, is not only that we have no reliable collision rates, but they are also formed and destroyed at a rate comparable to the collision rates. As a consequence the excitation of the molecule also reflects the distribution of available translational energy over its internal degrees of freedom during the formation process.

It would also be very interesting to have data for electron collisions with H₂O. This molecule has a very high dipole moment and its excitation is therefore very sensitive to collisions with electrons. This would especially affect the excitation state of H₂O in XDRs, since the electron abundances can be as high as 10⁻³ to 10⁻² where H₂O has a significant abundance.

In general, the H₂ gas is on average warmer in XDRs than in PDRs. Spitzer currently observes the pure rotational lines, e.g., S(0) 28.2 μm and 17.0 μm lines of H₂.

These emission lines should be brighter in XDRs than in PDRs, and also the ratios between the lines should differ.

Finally, it would be interesting to observe HCO (which unfortunately also does not have collisional data). HCO lines have been observed in M 82 and NGC 253, and the HCO/HCO⁺ column density ratios calculated in Chapter 8 suggest that the combination of both molecules might have diagnostic merit in discriminating between PDRs and XDRs.

Nope: Some molecules turn out to have no direct diagnostic value for several reasons. The sulfur chemistry is very uncertain due to the presence of energy barriers in the collision rates. As a consequence, line emission from molecules such as SO and SO₂ is hard to interpret in terms of excitation only. Although we find that the SiO(1-0)/CO(1-0) ratio is typically 2-3 times larger in XDRs, SiO is much more useful as a shock tracer. We have also included somewhat larger molecules in the chemical network, such as H₂CO and CH₃OH. We know, however, that their bulk is formed on grains. They typically trace hot cloud cores and very dense clouds in starforming regions. Although molecules as N₂H⁺ and HCN⁺ are enhanced in XDRs, they have very low abundances leaving even enhanced emission very weak. N₂H⁺ is also probably formed on dust grains in dense dark clouds.

In Chapter 10, some of these diagnostics have been used to interpret data and estimate impinging fluxes and densities. However, some discrepancies remain between models and observations. In the coming decade, much progress will be made in the observations of the interstellar medium in galaxies with the advent of the next generation of telescopes, such as Herschel and ALMA. The new data will contain much more detail requiring significant improvement of the models used in their interpretation. In the following sections we discuss some of the issues that can be improved upon in our models. We also summarize possible diagnostics for future observations.

11.2 Model extensions

In our modelling of the observed data, we use a convolution of two or more separate homogeneous one-sided slab PDR and/or XDR models to determine the physical properties of the gas in galactic centers. However, the distribution of the molecular clouds relative to sources of radiation (the AGN and star-forming regions) has important effects on line intensity maps. This was already discussed in papers by, e.g., Hogerheijde et al. (1995), Jansen et al. (1995) and Spaans & van Dishoeck (1997). With the advent of, e.g., ALMA it is important that models with 2/3D physical representations of the ISM are constructed to interpret the observed line intensity maps of active galaxies. This would also improve the agreement with ¹³CO/¹²CO and HNC/HCN ratios. The large optical depths in these lines found by our models would be significantly reduced when we include clumpiness. For the same column density, the effective optical depth is smaller, when a cloud consists of low and high density components, because photons penetrate deeper into the cloud and easier escape the cloud through scattering.

So far, we only considered steady state models. These kinds of models have been very successful in describing diverse ISM environments in galaxy disks, such as cold and dense clouds, quiescent diffuse and translucent clouds, and hot, photon-dominated regions. Although feedback processes such as, e.g., supernova explosions may cause local disturbances, disk cloud physics and chemistry derived from observations are well-described by time-independent models. In galactic centers, however, steady-state models are often not fully adequate to explain observed molecular line ratios. Central regions in galaxies experience frequent changes on relatively short time scales so that static equilibrium may not be an appropriate assumption. Time scales for chemical processes at low density such as H_2 formation, occurrence of star-bursts, and orbiting molecular gas in the central few hundred parsecs, turn out to be similar and of the order of $10^6 - 10^7$ years. Due to the orbital periods of $t_R = 3 - 15 \times 10^6$ years, the fast-rotating molecular clouds in the central few hundred parsecs encounter (inner spiral) shocks at least every few million years. These shocks cannot be ignored since the presence of shock-excited molecular hydrogen is already known for some time (Moorwood & Oliva 1990; Koornneef & Israel 1996), and the effects of orbital shocks on molecular chemistry have been observed in centers of spiral galaxies such as, e.g., IC 342 and NGC 253 (Meier & Turner 2005; Martín et al. 2003). To take into account these mechanical effects, the PDR/XDR code needs to be incorporated into a hydrodynamical code, and needs to be made time-dependent.

11.3 Future observatories

In Chapter 8, we have identified a number of molecules that are possible diagnostics to discriminate between PDRs and XDRs. The low- J CO lines are able to discriminate between normal PDRs on the one side, and enhanced cosmic ray rate PDRs and XDRs on the other side. High- J CO lines are much brighter, however, in XDRs compared to (elevated cosmic ray) PDRs (see Chapter 8 and 9). With the future Herschel (HIFI) telescope, it will be possible to observe these high- J CO lines. It is claimed that the CO $4.7\mu\text{m}$ absorption band has already traced warm CO gas in, e.g, the obscured AGN IRAS 08572+3915 (Shirahata et al. 2006). However, the absorption features can also be originating from atmospheres around supergiants. NGC 1068, which is viewed as a pure AGN by many people, does not show any signs of these CO $4.7\mu\text{m}$ absorption (Nakagawa, private communication).

When ALMA comes on-line, it will be possible to obtain high spatial resolution (~ 25 pc for $\sim 1''$ beam and at a distance of $D = 5$ Mpc) line intensity maps. Then, we will be able to resolve regions dominated by FUV and X-ray photons, and to better understand the scale-dependent geometry and (time-dependent) contributions of the radiation sources (star-burst versus AGN) in galactic centers. The ALMA frequency bands range from 30 to 950 GHz. It will be possible to observe rotational line emission up to $J = 9$ for CO. For galaxies at redshift $z = 1$, it is possible to observe up to $J = 18$ and to detect warm CO gas that probably indicates an XDR.

Bibliography

- Aalto, S. 2005, in IAU Symposium, ed. C. L. Dariusz, A. B. Geoffrey, & H. Eric, 261–270
- Aalto, S., Hüttemeister, S., Scoville, N. Z., & Thaddeus, P. 1999, *ApJ*, 522, 165
- Abel, N. P., Ferland, G. J., Shaw, G., & van Hoof, P. A. M. 2005, *ApJS*, 161, 65
- Agladze, N. I., Sievers, A. J., Jones, S. A., Burlitch, J. M., & Beckwith, S. V. W. 1996, *ApJ*, 462, 1026
- Alton, P. B., Bianchi, S., Rand, R. J., et al. 1998, *ApJ*, 507, L125
- Alton, P. B., Bianchi, S., Richer, J., Pierce-Price, D., & Combes, F. 2002, *A&A*, 388, 446
- Alton, P. B., Lequeux, J., Bianchi, S., et al. 2001, *A&A*, 366, 451
- Alton, P. B., Xilouris, E. M., Bianchi, S., Davies, J., & Kylafis, N. 2000, *A&A*, 356, 795
- Asplund, M., Grevesse, N., & Sauval, A. J. 2005, in ASP Conf. Ser. 336: Cosmic Abundances as Records of Stellar Evolution and Nucleosynthesis, ed. T. G. Barnes & F. N. Bash, 25–+
- Baan, W. A., Henkel, C., Schilke, P., Guesten, R., & Mauersberger, R. 1990, *ApJ*, 353, 132
- Baan, W. A. & Klöckner, H.-R. 2005, *Ap&SS*, 295, 263
- Bakes, E. L. O. & Tielens, A. G. G. M. 1994, *ApJ*, 427, 822
- Bauer, F. E., Brandt, W. N., & Lehmer, B. 2003, *AJ*, 126, 2797
- Bayet, E., Gerin, M., Phillips, T. G., & Contursi, A. 2004, *A&A*, 427, 45
- Bayet, E., Israel, F. P., Meijerink, R., & Gerin, M. 2006, *A&A*, submitted
- Beckman, J. E., Peletier, R. F., Knapen, J. H., Corradi, R. L. M., & Gentet, L. J. 1996, *ApJ*, 467, 175
- Bensch, F., Leuenhagen, U., Stutzki, J., & Schieder, R. 2003, *ApJ*, 591, 1013
- Bergin, E. A., Melnick, G. J., Stauffer, J. R., et al. 2000, *ApJ*, 539, L129
- Bertoldi, F. & Draine, B. T. 1996, *ApJ*, 458, 222
- Bianchi, S. 2004, in ASP Conf. Ser. 309: Astrophysics of Dust
- Bjorkman, J. E. & Wood, K. 2001, *ApJ*, 554, 615
- Black, J. H. & Dalgarno, A. 1976, *ApJ*, 203, 132
- . 1977, *ApJS*, 34, 405
- Black, J. H. & van Dishoeck, E. F. 1987, *ApJ*, 322, 412
- Blitz, L., Bloemen, J. B. G. M., Hermsen, W., & Bania, T. M. 1985, *A&A*, 143, 267
- Bohlin, R. C., Savage, B. D., & Drake, J. F. 1978, *ApJ*, 224, 132
- Boland, W. & de Jong, T. 1982, *ApJ*, 261, 110
- Bradford, C. M., Nikola, T., Stacey, G. J., et al. 2003, *ApJ*, 586, 891
- Braine, J., Kruegel, E., Sievers, A., & Wielebinski, R. 1995, *A&A*, 295, L55+
- Bregman, J. N. & Pildis, R. A. 1992, *ApJ*, 398, L107
- Brinkmann, W., Siebert, J., & Boller, T. 1994, *A&A*, 281, 355
- Bruzual, A. G. & Charlot, S. 1993, *ApJ*, 405, 538
- Cazaux, S. & Tielens, A. G. G. M. 2002, *ApJ*, 575, L29
- . 2004, *ApJ*, 604, 222

- Chamblaud, G., Levy, B., Millie, P., et al. 1980, *Journal of Physics B Atomic Molecular Physics*, 13, 4205
- Chini, R., Kreysa, E., Kruegel, E., & Mezger, P. G. 1986, *A&A*, 166, L8
- Chini, R., Kreysa, E., Mezger, P. G., & Gemuend, H.-P. 1984a, *A&A*, 137, 117
- Chini, R., Mezger, P. G., Kreysa, E., & Gemuend, H.-P. 1984b, *A&A*, 135, L14
- Cravens, T. E. & Dalgarno, A. 1978, *ApJ*, 219, 750
- Curran, S. J., Aalto, S., & Booth, R. S. 2000, *A&AS*, 141, 193
- Curran, S. J., Johansson, L. E. B., Bergman, P., Heikkilä, A., & Aalto, S. 2001, *A&A*, 367, 457
- Dahlem, M., Heckman, T. M., & Fabbiano, G. 1995, *ApJ*, 442, L49
- Dalgarno, A., Yan, M., & Liu, W. 1999, *ApJS*, 125, 237
- Dame, T. M., Hartmann, D., & Thaddeus, P. 2001, *ApJ*, 547, 792
- de Jong, T., Boland, W., & Dalgarno, A. 1980, *A&A*, 91, 68
- Devereux, N. A. & Young, J. S. 1990, *ApJ*, 359, 42
- . 1992, *AJ*, 103, 1536
- Diaz, A. I., Terlevich, E., Vilchez, J. M., Pagel, B. E. J., & Edmunds, M. G. 1991, *MNRAS*, 253, 245
- Draine, B. T. 1978, *ApJS*, 36, 595
- Draine, B. T. & Lee, H. M. 1984, *ApJ*, 285, 89
- Draine, B. T. & Sutin, B. 1987, *ApJ*, 320, 803
- Dufton, P. L. & Kingston, A. E. 1994, *Atomic Data and Nuclear Data Tables*, 57, 273
- Dullemond, C. P. & Dominik, C. 2004, *A&A*, 417, 159
- Dullemond, C. P. & Turolla, R. 2000, *A&A*, 360, 1187
- Dumke, M., Nieten, C., Thuma, G., Wielebinski, R., & Walsh, W. 2001, *A&A*, 373, 853
- Dunne, L., Eales, S., Edmunds, M., et al. 2000, *MNRAS*, 315, 115
- Eckart, A., Downes, D., Genzel, R., et al. 1990, *ApJ*, 348, 434
- Ehle, M. 2005, in *XMM-Newton Proposal ID #04013602*, 53–+
- Ehle, M., Pietsch, W., Beck, R., & Klein, U. 1998, *A&A*, 329, 39
- Emerson, D. T. 1995, in *ASP Conf. Ser. 75: Multi-Feed Systems for Radio Telescopes*, 309–+
- Fabbiano, G., Kim, D.-W., & Trinchieri, G. 1992, *ApJS*, 80, 531
- Ferland, G. J., Korista, K. T., Verner, D. A., et al. 1998, *PASP*, 110, 761
- Field, G. B., Goldsmith, D. W., & Habing, H. J. 1969, *BAAS*, 1, 240
- Field, G. B., Somerville, W. B., & Dressler, K. 1966, *ARA&A*, 4, 207
- Flower, D. R., Le Bourlot, J., Pineau des Fôrets, G., & Roueff, E. 1994, *A&A*, 282, 225
- Fukazawa, Y., Iyomoto, N., Kubota, A., Matsumoto, Y., & Makishima, K. 2001, *A&A*, 374, 73
- Gao, Y. & Solomon, P. M. 2004, *ApJS*, 152, 63
- García-Burillo, S., Guélin, M., & Cernicharo, J. 1993, *A&A*, 274, 123
- Garnett, D. R., Shields, G. A., Peimbert, M., et al. 1999, *ApJ*, 513, 168
- Garrett, M. A., Muxlow, T. W. B., Garrington, S. T., et al. 2001, *A&A*, 366, L5
- Glassgold, A. E. & Langer, W. D. 1973, *ApJ*, 179, L147+
- Gould, R. J. & Salpeter, E. E. 1963, *ApJ*, 138, 393
- Guainazzi, M., Matt, G., Brandt, W. N., et al. 2000, *A&A*, 356, 463
- Guélin, M., Zylka, R., Mezger, P. G., Haslam, C. G. T., & Kreysa, E. 1995, *A&A*, 298, L29+
- Guélin, M., Zylka, R., Mezger, P. G., et al. 1993, *A&A*, 279, L37
- Güsten, R., Serabyn, E., Kasemann, C., et al. 1993, *ApJ*, 402, 537
- Haas, M., Lemke, D., Stickel, M., et al. 1998, *A&A*, 338, L33
- Habing, H. J. 1969, *Bull. Astron. Inst. Netherlands*, 20, 177
- Harrison, A., Henkel, C., & Russell, A. 1999, *MNRAS*, 303, 157

- Harrison, A., Puxley, P., Russell, A., & Brand, P. 1995, *MNRAS*, 277, 413
- Helfer, T. T. & Blitz, L. 1993, *ApJ*, 419, 86
- . 1997, *ApJ*, 478, 233
- Henkel, C. & Bally, J. 1985, *A&A*, 150, L25
- Henkel, C., Mauersberger, R., Wiklind, T., et al. 1993, *A&A*, 268, L17
- Hippelein, H., Haas, M., Tuffs, R. J., et al. 2003, *A&A*, 407, 137
- Hippelein, H., Lemke, D., Haas, M., et al. 1996, *A&A*, 315, L82
- Hogerheijde, M. R., Jansen, D. J., & van Dishoeck, E. F. 1995, *A&A*, 294, 792
- Holland, W. S., Robson, E. I., Gear, W. K., et al. 1999, *MNRAS*, 303, 659
- Hollenbach, D. & McKee, C. F. 1979, *ApJS*, 41, 555
- . 1989, *ApJ*, 342, 306
- Hollenbach, D. & Salpeter, E. E. 1971, *ApJ*, 163, 155
- Hollenbach, D. J., Takahashi, T., & Tielens, A. G. G. M. 1991, *ApJ*, 377, 192
- Holt, S. S., Schlegel, E. M., Hwang, U., & Petre, R. 2003, *ApJ*, 588, 792
- Houghton, S., Whiteoak, J. B., Koribalski, B., et al. 1997, *A&A*, 325, 923
- Hubble, E. P. 1930, *ApJ*, 71, 231
- Hurt, R. L., Turner, J. L., Ho, P. T. P., & Martin, R. N. 1993, *ApJ*, 404, 602
- Hüttemeister, S. & Aalto, S. 2001, in *ASP Conf. Ser. 249: The Central Kiloparsec of Starbursts and AGN: The La Palma Connection*, ed. J. H. Knapen, J. E. Beckman, I. Shlosman, & T. J. Mahoney, 619–+
- Hüttemeister, S., Henkel, C., Mauersberger, R., et al. 1995, *A&A*, 295, 571
- Irwin, J. A. & Avery, L. W. 1992, *ApJ*, 388, 328
- Israel, F. P. 1992, *A&A*, 265, 487
- . 1997, *A&A*, 317, 65
- . 2005, *Ap&SS*, 295, 171
- . unpublished, JCMT/IRAM/SEST database
- Israel, F. P. & Baas, F. 2001, *A&A*, 371, 433
- . 2002, *A&A*, 383, 82
- . 2003, *A&A*, 404, 495
- Israel, F. P., Tilanus, R. P. J., & Baas, F. 2006, *A&A*, 445, 907
- Israel, F. P., van der Werf, P. P., & Tilanus, R. P. J. 1999, *A&A*, 344, L83
- Israel, F. P., White, G. J., & Baas, F. 1995, *A&A*, 302, 343
- Iyomoto, N., Fukazawa, Y., Nakai, N., & Ishihara, Y. 2001, *ApJ*, 561, L69
- Jackson, J. M., Paglione, T. A. D., Carlstrom, J. E., & Rieu, N. 1995, *ApJ*, 438, 695
- James, A., Dunne, L., Eales, S., & Edmunds, M. G. 2002, *MNRAS*, 335, 753
- Jansen, D. J., van Dishoeck, E. F., Black, J. H., Spaans, M., & Sosin, C. 1995, *A&A*, 302, 223
- Jaquet, R., Staemmler, V., Smith, M. D., & Flower, D. R. 1992, *Journal of Physics B Atomic Molecular Physics*, 25, 285
- Jenkins, E. B. 2004, in *Origin and Evolution of the Elements*, 339–+
- Jenness, T., Holland, W. S., Chapin, E., Lightfoot, J. F., & Duncan, W. D. 2000, in *ASP Conf. Ser. 216: Astronomical Data Analysis Software and Systems IX*, 559–+
- Jenness, T. & Lightfoot, J. F. 1998, in *ASP Conf. Ser. 145: Astronomical Data Analysis Software and Systems VII*, 216–+
- Johnson, C. T., Burke, P. G., & Kingston, A. E. 1987, *Journal of Physics B Atomic Molecular Physics*, 20, 2553
- Kamp, I. & Bertoldi, F. 2000, *A&A*, 353, 276
- Kamp, I. & van Zadelhoff, G.-J. 2001, *A&A*, 373, 641

- Katz, N., Furman, I., Biham, O., Pirronello, V., & Vidali, G. 1999, *ApJ*, 522, 305
- Kaufman, M. J., Wolfire, M. G., Hollenbach, D. J., & Luhman, M. L. 1999, *ApJ*, 527, 795
- Klöckner, H.-R., Baan, W. A., & Garrett, M. A. 2003, *Nature*, 421, 821
- Kobulnicky, H. A. & Skillman, E. D. 1998, *ApJ*, 497, 601
- Koornneef, J. & Israel, F. P. 1996, *New Astronomy*, 1, 271
- Kramer, C., Mookerjea, B., Bayet, E., et al. 2005, *A&A*, 441, 961
- Kraus, J. D. 1966, *Radio astronomy* (New York: McGraw-Hill, 1966)
- Laurikainen, E. & Salo, H. 2001, *MNRAS*, 324, 685
- Le Bourlot, J., Pineau Des Forets, G., Roueff, E., & Flower, D. R. 1993, *A&A*, 267, 233
- Le Petit, F., Le Bourlot, J., Roueff, E., & Nehmé, C. 2006, *ArXiv Astrophysics e-prints*
- Le Petit, F., Roueff, E., & Le Bourlot, J. 2002, *A&A*, 390, 369
- Le Teuff, Y. H., Millar, T. J., & Markwick, A. J. 2000, *A&AS*, 146, 157
- Lee, H.-H., Herbst, E., Pineau des Forets, G., Roueff, E., & Le Bourlot, J. 1996, *A&A*, 311, 690
- Lennon, M. A., Bell, K. L., Gilbody, H. B., et al. 1988, *Journal of Physical and Chemical Reference Data*, 17, 1285
- Lepp, S. & Dalgarno, A. 1988, *ApJ*, 335, 769
- . 1996, *A&A*, 306, L21
- Lepp, S. & Shull, J. M. 1983, *ApJ*, 270, 578
- Li, A. & Draine, B. T. 2001, *ApJ*, 554, 778
- London, R. 1978, *ApJ*, 225, 405
- Lucy, L. B. 1999, *A&A*, 344, 282
- Maloney, P. & Black, J. H. 1988, *ApJ*, 325, 389
- Maloney, P. R. 1999, *Ap&SS*, 266, 207
- Maloney, P. R., Hollenbach, D. J., & Tielens, A. G. G. M. 1996, *ApJ*, 466, 561
- Mao, R. Q., Henkel, C., Schulz, A., et al. 2000, *A&A*, 358, 433
- Martín, S., Martín-Pintado, J., Mauersberger, R., Henkel, C., & García-Burillo, S. 2005, *ApJ*, 620, 210
- Martín, S., Mauersberger, R., Martín-Pintado, J., García-Burillo, S., & Henkel, C. 2003, *A&A*, 411, L465
- Matsumoto, H. 2003, in *Workshop on Galaxies and Clusters of Galaxies*, 25—
- Mauersberger, R. & Henkel, C. 1989, *A&A*, 223, 79
- Mauersberger, R., Henkel, C., & Chin, Y.-N. 1995, *A&A*, 294, 23
- Mauersberger, R., Henkel, C., Walmsley, C. M., Sage, L. J., & Wiklind, T. 1991, *A&A*, 247, 307
- Mauersberger, R., Henkel, C., Walsh, W., & Schulz, A. 1999, *A&A*, 341, 256
- Mauersberger, R., Henkel, C., Weiß, A., Peck, A. B., & Hagiwara, Y. 2003, *A&A*, 403, 561
- Mauersberger, R., Henkel, C., Whiteoak, J. B., Chin, Y.-N., & Tieftrunk, A. R. 1996a, *A&A*, 309, 705
- Mauersberger, R., Henkel, C., Wielebinski, R., Wiklind, T., & Reuter, H.-P. 1996b, *A&A*, 305, 421
- Mauersberger, R., Henkel, C., Wilson, T. L., & Harju, J. 1989, *A&A*, 226, L5
- McCall, M. L., Rybski, P. M., & Shields, G. A. 1985, *ApJS*, 57, 1
- McLaughlin, B. M. & Bell, K. L. 1993, *ApJ*, 408, 753
- Meier, D. S. & Turner, J. L. 2004, *AJ*, 127, 2069
- . 2005, *ApJ*, 618, 259
- Meier, D. S., Turner, J. L., & Hurt, R. L. 2000, *ApJ*, 531, 200
- Meijerink, R. & Spaans, M. 2005, *A&A*, 436, 397
- Meijerink, R., Spaans, M., & Israel, F. P. 2006a, *ApJ* submitted

- . 2006b, *A&A*, submitted
- Meijerink, R., Tilanus, R. P. J., Dullemond, C. P., Israel, F. P., & van der Werf, P. P. 2005, *A&A*, 430, 427
- Mendoza, C. 1983, in *IAU Symp. 103: Planetary Nebulae*, 143–172
- Moorwood, A. F. M. & Oliva, E. 1990, *A&A*, 239, 78
- Morrison, R. & McCammon, D. 1983, *ApJ*, 270, 119
- Nakai, N. & Kuno, N. 1995, *PASJ*, 47, 761
- Neufeld, D. A. & Kaufman, M. J. 1993, *ApJ*, 418, 263
- Neufeld, D. A., Lepp, S., & Melnick, G. J. 1995, *ApJS*, 100, 132
- Nguyen, Q.-R., Jackson, J. M., Henkel, C., Truong, B., & Mauersberger, R. 1992, *ApJ*, 399, 521
- Nguyen-Q-Rieu, Nakai, N., & Jackson, J. M. 1989, *A&A*, 220, 57
- Olofsson, H. & Rydbeck, G. 1984, *A&A*, 136, 17
- Ott, J., Weiss, A., Henkel, C., & Walter, F. 2005, *ApJ*, 629, 767
- Paglione, T. A. D., Jackson, J. M., Ishizuki, S., & Rieu, N.-Q. 1995, *AJ*, 109, 1716
- Papadopoulos, P. P., Thi, W.-F., & Viti, S. 2002, *ApJ*, 579, 270
- Pascucci, I., Wolf, S., Steinacker, J., et al. 2004, *A&A*, 417, 793
- Peschke, S. B. & Schulz, B. 2002, in *ESA SP-482: Photometric Mapping with ISOPHOT using the "P32" Astronomical Observation Template*, 53–+
- Pietsch, W., Roberts, T. P., Sako, M., et al. 2001, *A&A*, 365, L174
- Pietsch, W., Trinchieri, G., & Vogler, A. 1998, *A&A*, 340, 351
- Pineau des Fôrets, G., Roueff, E., & Flower, D. R. 1992, *MNRAS*, 258, 45P
- Pirronello, V., Liu, C., Roser, J. E., & Vidali, G. 1999, *A&A*, 344, 681
- Poelman, D. R. & Spaans, M. 2005, *A&A*, 440, 559
- . 2006, *ArXiv Astrophysics e-prints*
- Popescu, C. C., Misiriotis, A., Kylafis, N. D., Tuffs, R. J., & Fischera, J. 2000, *A&A*, 362, 138
- Popescu, C. C. & Tuffs, R. J. 2003, *A&A*, 410, L21
- Popescu, C. C., Tuffs, R. J., Völk, H. J., Pierini, D., & Madore, B. F. 2002, *ApJ*, 567, 221
- Rand, R. J. 1993, *ApJ*, 410, 68
- Reynolds, J. H. 1913, *MNRAS*, 74, 132
- Risaliti, G., Maiolino, R., & Bassani, L. 2000, *A&A*, 356, 33
- Röllig, M., Abel, N., Bell, T., et al. 2006, in preparation
- Röllig, M., Ossenkopf, V., Jeyakumar, S., Stutzki, J., & Sternberg, A. 2006, *ArXiv Astrophysics e-prints*
- Rots, A. H., Crane, P. C., Bosma, A., Athanassoula, E., & van der Hulst, J. M. 1990, *AJ*, 100, 387
- Roueff, E. & Le Bourlot, J. 1990, *A&A*, 236, 515
- Sage, L. J., Henkel, C., & Mauersberger, R. 1991, *A&A*, 249, 31
- Sage, L. J. & Isbell, D. W. 1991, *A&A*, 247, 320
- Sage, L. J., Shore, S. N., & Solomon, P. M. 1990, *ApJ*, 351, 422
- Sampson, D. H., Zhang, H. L., & Fontes, C. J. 1994, *Atomic Data and Nuclear Data Tables*, 57, 97
- Sandage, A. & Tammann, G. A. 1975, *ApJ*, 196, 313
- . 1987, *A Revised Shapley-Ames Catalog of Bright Galaxies* (Carnegie Institution of Washington Publication, Washington: Carnegie Institution, 1987, 2nd ed.)
- Sanders, D. B. & Mirabel, I. F. 1996, *ARA&A*, 34, 749
- Sandqvist, A., Elfhag, T., & Jorsater, S. 1988, *A&A*, 201, 223
- Sandqvist, A., Joersaeter, S., & Lindblad, P. O. 1995, *A&A*, 295, 585
- Savage, B. D., Drake, J. F., Budich, W., & Bohlin, R. C. 1977, *ApJ*, 216, 291

- Schilke, P., Carlstrom, J. E., Keene, J., & Phillips, T. G. 1993, *ApJ*, 417, L67+
- Schöier, F. L., van der Tak, F. F. S., van Dishoeck, E. F., & Black, J. H. 2005, *A&A*, 432, 369
- Schröder, K., Staemmler, V., Smith, M. D., Flower, D. R., & Jaquet, R. 1991, *Journal of Physics B Atomic Molecular Physics*, 24, 2487
- Searle, L. 1971, *ApJ*, 168, 327
- Shirahata, M., Nakagawa, T., Goto, M., et al. 2006, *ApJ*, submitted
- Shull, J. M. 1978, *ApJ*, 219, 877
- Silk, J. 2005, *MNRAS*, 364, 1337
- Smith, H. E. 1975, *ApJ*, 199, 591
- Smith, J. 1982, *ApJ*, 261, 463
- Sodroski, T. J., Bennett, C., Boggess, N., et al. 1994, *ApJ*, 428, 638
- Sodroski, T. J., Odegard, N., Dwek, E., et al. 1995, *ApJ*, 452, 262
- Sorai, K., Nakai, N., Kuno, N., & Nishiyama, K. 2002, *PASJ*, 54, 179
- Sorai, K., Nakai, N., Kuno, N., Nishiyama, K., & Hasegawa, T. 2000, *PASJ*, 52, 785
- Spaans, M. 1996, *A&A*, 307, 271
- Spaans, M. & Silk, J. 2000, *ApJ*, 538, 115
- Spaans, M., Tielens, A. G. G. M., van Dishoeck, E. F., & Bakes, E. L. O. 1994, *ApJ*, 437, 270
- Spaans, M. & van Dishoeck, E. F. 1997, *A&A*, 323, 953
- . 2001, *ApJ*, 548, L217
- Spitzer, L. J. 1978, *JRASC*, 72, 349
- Spoon, H. W. W., Keane, J. V., Cami, J., et al. 2005, in *IAU Symposium*, ed. C. L. Dariusz, A. B. Geoffrey, & H. Eric, 281–290
- Spoon, H. W. W., Keane, J. V., Tielens, A. G. G. M., Lutz, D., & Moorwood, A. F. M. 2001, *A&A*, 365, L353
- Spoon, H. W. W., Moorwood, A. F. M., Pontoppidan, K. M., et al. 2003, *A&A*, 402, 499
- Stäuber, P., Doty, S. D., van Dishoeck, E. F., & Benz, A. O. 2005, *A&A*, 440, 949
- Stecher, T. P. & Williams, D. A. 1967, *ApJ*, 149, L29+
- Steppe, H., Mauersberger, R., Schulz, A., & Baars, J. W. M. 1990, *A&A*, 233, 410
- Sternberg, A. & Dalgarno, A. 1989, *ApJ*, 338, 197
- . 1995, *ApJS*, 99, 565
- Sternberg, A. & Neufeld, D. A. 1999, *ApJ*, 516, 371
- Stevens, J. A., Amure, M., & Gear, W. K. 2005, *MNRAS*, 357, 361
- Stevens, J. A. & Gear, W. K. 2000, *MNRAS*, 312, L5
- Stoerzer, H. & Hollenbach, D. 1998, *ApJ*, 495, 853
- Stoerzer, H., Stutzki, J., & Sternberg, A. 1996, *A&A*, 310, 592
- Strong, A. W., Moskalenko, I. V., Reimer, O., Digel, S., & Diehl, R. 2004, *A&A*, 422, L47
- Suchkov, A., Allen, R. J., & Heckman, T. M. 1993, *ApJ*, 413, 542
- Taylor, S. D., Hartquist, T. W., & Williams, D. A. 1993, *MNRAS*, 264, 929
- Tielens, A. G. G. M. & Hollenbach, D. 1985, *ApJ*, 291, 722
- Tilanus, R. P. J. & Allen, R. J. 1989, *ApJ*, 339, L57
- . 1991, *A&A*, 244, 8
- Tilanus, R. P. J., Allen, R. J., van der Hulst, J. M., Crane, P. C., & Kennicutt, R. C. 1988, *ApJ*, 330, 667
- Tine, S., Lepp, S., Gredel, R., & Dalgarno, A. 1997, *ApJ*, 481, 282
- Tschöke, D., Hensler, G., & Junkes, N. 2003, *A&A*, 411, 41
- Tuffs, R. J. & Gabriel, C. 2003, *A&A*, 410, 1075
- Tully, R. B. 1974, *ApJS*, 27, 437

- Turner, J., Kirby-Docken, K., & Dalgarno, A. 1977, *ApJS*, 35, 281
- Turner, J. L. & Ho, P. T. P. 1994, *ApJ*, 421, 122
- Turner, T. J. & Pounds, K. A. 1989, *MNRAS*, 240, 833
- van der Hulst, J. M., Kennicutt, R. C., Crane, P. C., & Rots, A. H. 1988, *A&A*, 195, 38
- van der Tak, F. F. S. & van Dishoeck, E. F. 2000, *A&A*, 358, L79
- van Dishoeck, E. F. & Black, J. H. 1986, *ApJS*, 62, 109
- . 1988, *ApJ*, 334, 771
- Verner, D. A. & Yakovlev, D. G. 1995, *A&AS*, 109, 125
- Vila-Costas, M. B. & Edmunds, M. G. 1992, *MNRAS*, 259, 121
- Voit, G. M. 1991, *ApJ*, 377, 158
- Wadehra, J. M. & Bardsley, J. N. 1978, *Physical Review Letters*, 41, 1795
- Wall, W. F. & Jaffe, D. T. 1990, *ApJ*, 361, L45
- Wall, W. F., Jaffe, D. T., Bash, F. N., & Israel, F. P. 1991, *ApJ*, 380, 384
- Wang, M., Henkel, C., Chin, Y.-N., et al. 2004, *A&A*, 422, 883
- Weingartner, J. C. & Draine, B. T. 2001, *ApJS*, 134, 263
- Werner, M. W. 1970, *Astrophys. Lett.*, 6, 81
- White, G. J., Ellison, B., Claude, S., Dent, W. R. F., & Matheson, D. N. 1994, *A&A*, 284, L23
- Wielebinski, R., Dumke, M., & Nieten, C. 1999, *A&A*, 347, 634
- Wild, W., Harris, A. I., Eckart, A., et al. 1992, *A&A*, 265, 447
- Wolfire, M. G., Hollenbach, D., & Tielens, A. G. G. M. 1993, *ApJ*, 402, 195
- Wolfire, M. G., McKee, C. F., Hollenbach, D., & Tielens, A. G. G. M. 2003, *ApJ*, 587, 278
- Xilouris, E. M., Alton, P. B., Davies, J. I., et al. 1998, *A&A*, 331, 894
- Xu, C., Lisenfeld, U., & Voelk, H. J. 1994, *A&A*, 285, 19
- Yan, M. 1997, Ph.D. Thesis, Center for Astrophysics, Harvard University
- Young, J. S., Schloerb, F. P., Kenney, J. D., & Lord, S. D. 1986, *ApJ*, 304, 443
- Young, J. S., Xie, S., Kenney, J. D. P., & Rice, W. L. 1989, *ApJS*, 70, 699
- Young Owl, R. C., Meixner, M. M., Wolfire, M., Tielens, A. G. G. M., & Tauber, J. 2000, *ApJ*, 540, 886
- Zaritsky, D., Kennicutt, R. C., & Huchra, J. P. 1994, *ApJ*, 420, 87

Nederlandse samenvatting

De bouwstenen van sterrenstelsels

Het zichtbare materiaal in een sterrenstelsel bestaat uit gas, stof en sterren. Het gas bestaat uit atomen en moleculen en het stof is samengesteld uit silicaat- en koolstofverbindingen. Sterren hebben massa's die uiteenlopen van één honderdste tot honderd maal de massa van onze zon. Ons melkwegstelsel bevat ongeveer honderd miljard sterren en zijn in totaal goed voor ongeveer negentig procent van de zichtbare massa. De andere tien procent bestaat uit gas en stof, en dit geheel wordt ook wel het Interstellair Medium (ISM) genoemd. Deze percentages kunnen verschillen in andere sterrenstelsels. Het ISM kan zich in een scala van condities bevinden. Het kan dichtheden hebben van één tiende deeltje tot tien miljard deeltjes per kubieke centimeter. Ter vergelijking: in de lucht om ons heen is de dichtheid van het gas ongeveer een miljard maal hoger dan de hoogste dichtheid in het ISM. De temperaturen in het ISM variëren van ongeveer -263 tot 10 miljoen graden Celsius. Het grootste gedeelte van de ruimte tussen sterren wordt gevuld met gas, dat een zeer lage dichtheid heeft. Het warme geïoniseerde medium (HII) heeft een dichtheid van ongeveer één tiende deeltje per kubieke centimeter, terwijl dit voor het warme neutrale medium (HI) ongeveer één tiende tot één deeltje per kubieke centimeter is. In die gebieden waar nieuwe sterren worden geboren, is het gas samengetrokken onder invloed van de zwaartekracht. Hier lopen de dichtheden uiteen tussen tienduizend en een miljoen deeltjes per kubieke centimeter. Gas met temperaturen van 10 duizend graden Celsius kan worden gevonden in een planetaire nevel. Dit vertegenwoordigt het laatste stadium in de evolutie van een middelzware ster (met een massa tussen de één en vier maal de massa van de zon), waarbij de buitendelen worden weggeblazen en zodoende een nevel ontstaat. De hoogste dichtheden worden gevonden in gas-schijven rond pas gevormde sterren, ongeveer 100 miljoen tot 10 miljard deeltjes per kubieke centimeter. Onder de juiste omstandigheden worden hieruit later planeten gevormd. Hoewel we de laatst genoemde dichtheden als hoog beschouwen in astronomische zin, is dit niet het geval voor aardse begrippen. Het beste vacuum dat we op aarde kunnen bereiken in een laboratorium is net goed genoeg om deze "hoge" dichtheden te representeren .

Stof

De variatie in de omvang van stofdeeltjes is heel erg groot, van 0.25\AA tot $0.25\mu\text{m}$, en deze kunnen daardoor zeer verschillende eigenschappen hebben. Kosmische stofdeeltjes

zijn meer dan tien maal kleiner dan het zogenaamde “fijn stof”, dat wordt geproduceerd door bijvoorbeeld dieselauto’s. Hoewel we weten dat stofdeeltjes bestaan uit silicaat- en koolstofverbindingen, is de exacte samenstelling en structuur van stof nog niet goed begrepen. Deze samenstelling verandert ook als het stof wordt blootgesteld aan verschillende omstandigheden. Ondanks het feit dat deze deeltjes slechts ongeveer 1 procent van de totale massa van het ISM vertegenwoordigen, houden zij wel het meeste zichtbare en ultraviolette licht tegen. Het blokkeren van straling wordt ook wel extinctie genoemd. Voor een bepaalde samenstelling van stof, kan er een zogenaamde extinctiekromme worden afgeleid. Deze geeft aan hoeveel licht op welke golflengte wordt tegengehouden. Omdat de samenstelling van stof nogal moeilijk te bepalen is, zijn de onzekerheden hierin vaak een factor twee, iets wat voor sterrenkundige begrippen niet eens zo ontzettend groot is. Stof zorgt er ook voor dat het gas wordt verhit. Dit kan geschieden door botsingen tussen stof- en gasdeeltjes. Bij deze botsingen wordt een gedeelte van de thermische energie van het stof overdragen. Een andere manier is door een electron te bevrijden van een stofdeeltje dat een lichtdeeltje absorbeert. Dit losgemaakte electron heeft kinetische (bewegings) energie, die dan door botsingen overgedragen kan worden aan het gas. Dit wordt foto-electrische verhitting genoemd. Stof is ook heel belangrijk voor de vorming van moleculair waterstof (H_2). Stof is bij deze reactie een soort katalysator. In de gasfase gaat de reactie voor de vorming van H_2 erg langzaam.

Gas

Gas in sterrenstelsels bestaat voor het grootste gedeelte uit waterstof (90 procent) en helium (8.5 procent). Alle zwaardere elementen, zoals koolstof, stikstof en zuurstof, zijn slechts anderhalve procent van het geheel en worden door astronomen metalen genoemd. Afhankelijk van het stralingsveld en de dichtheid, hebben gaswolken een bepaalde chemische en thermische structuur. Zij stralen allemaal verschillende zogenaamde atomaire fijn-structuur en moleculaire (zoals H_2 , CO, HCN en H_2O) rotationele en vibrationele lijnen uit. De lijnen worden als volgt geproduceerd. Eerst komt een deeltje (zeg H_2) in botsing met een ander deeltje (zeg CO). Als gevolg hiervan kan één van de deeltjes in een toestand komen die een hogere energie heeft. Zo’n deeltje kan door het uitzenden van een lichtdeeltje weer in de oorspronkelijke toestand terugkomen. Deze lichtdeeltjes worden uitgezonden op een golflengte die wij met onze ogen niet kunnen zien, namelijk in het (sub)-millimeter gebied, maar zij kunnen wel worden waargenomen met telescopen als de James Clerk Maxwell Telescope (JCMT) en de Institute de Radio Astronomie Millimétrique (IRAM) 30m telescope. Wanneer de condities verschillen, wordt ook een verschillende set lijnintensiteiten en lijnverhoudingen geproduceerd. Zij kunnen daarom gebruikt worden om de fysische eigenschappen van het gas te helpen bepalen.

Extreme omstandigheden in centra van sterrenstelsels

Ons zonnestelsel draait op een afstand van 26000 lichtjaar rond het centrum van de Melkweg. De hoeveelheid sterren per volume eenheid is erg laag in onze directe omgeving.

Proxima Centauri, de ster die het dichtste bij is, staat op een afstand van iets meer dan vier lichtjaar. De dichtheid van sterren en de gemiddelde dichtheid van het gas in het centrum van een sterrenstelsel is veel hoger dan in de omgeving van de zon. In het centrum is het daarom makkelijker om gas om te vormen naar sterren en als gevolg daarvan is de gemiddelde hoeveelheid geproduceerde straling veel hoger. Sterke stralingsvelden worden niet alleen geproduceerd door de nieuw gevormde sterren, maar ook door een zwart gat, dat vaak aanwezig is in het centrum van een sterrenstelsel en dat gas en sterren opslokt. Bij deze aanwas (accretie) van materie komt veel energie vrij. Hoewel er veel straling geproduceerd wordt, is het centrum vaak moeilijk waarneembaar met optische telescopen. De reden hiervoor is dat de grote hoeveelheid aanwezige stof het merendeel van het licht tegenhoudt. Op langere golflengtes, zoals in het sub-millimeter gebied, is de extinctie door stof veel minder. Hier straalt stof over een heel spectrum van golflengtes en atomen en moleculen op heel specifieke golflengtes, ook wel emissielijnen genoemd. Deze emissielijnen, die geproduceerd zijn door bijvoorbeeld CO, HCN en HCO^+ , kunnen als diagnostiek dienen. Deze lijnen willen we gaan reproduceren met modellen. Hierbij gaan we ervan uit dat straling de dominante factor in de bepaling van de chemische en thermische structuur is. Deze modellen heten zogenaamde foton-gedomineerde gebieden (PDRs) als de lichtdeeltjes voornamelijk ver-ultraviolette straling (FUV) betreffen, en X-ray-gedomineerde gebieden (XDRs) als het stralingsveld bestaat uit röntgen fotonen. FUV fotonen worden geproduceerd door hete zware sterren, terwijl röntgen fotonen voornamelijk worden geproduceerd door het zwarte gat. De energie van de fotonen is verschillend en heeft daardoor ook andere eigenschappen. röntgen fotonen dringen veel dieper door in wolken dan FUV fotonen, omdat atomen, moleculen en stof röntgen fotonen moeilijker kunnen absorberen. Het proces waarmee FUV and röntgen fotonen het gas verhitten is ook verschillend. Als gevolg hiervan is de thermische en chemische structuur in PDRs and XDRs anders. PDRs hebben een duidelijke gelaagdheid. Er is een duidelijke overgang van atomair naar moleculair waterstof ($\text{H} \rightarrow \text{H}_2$), als ook voor geïoniseerd koolstof naar neutral koolstof en koolstofmono-oxide ($\text{C}^+ \rightarrow \text{C} \rightarrow \text{CO}$). In XDRs is deze overgang niet zo duidelijk en bestaan deze atomen en moleculen naast elkaar. Deze eigenschappen, die worden bestudeerd in dit proefschrift, leiden tot een diagnostiek die de effecten van massieve sterren (FUV fotonen) en een zwart gat dat gas en sterren opslokt (röntgen fotonen) kan onderscheiden in de centra van sterrenstelsels.

Dit proefschrift

Dit proefschrift is opgedeeld in drie delen. In het eerste deel wordt specifiek ingegaan op de waarneming van de stofcomponent in M 51. In deel twee worden de PDR en XDR modellen gepresenteerd en vergeleken met andere beschikbare modellen. In deel drie rekenen we een groot rooster van modellen uit, dat vervolgens wordt toegepast op waarnemingen. Hieronder wordt kort ingegaan op de inhoud van de verschillende hoofdstukken.

Deel I

In hoofdstuk 2 geven we een introductie op waarnemingen van stof die zijn gedaan in sterrenstelsels. We gaan in op problemen, zoals het bepalen van de stoftemperatuur, de bepaling van de opaciteit (hoe makkelijk laat het licht door) van stof en de onzekerheden die hieruit volgen.

In hoofdstuk 3 laten we een waarneming van het melkwegstelsel M 51 zien, dat is waargenomen met de JCMT op een golflengte van $850 \mu\text{m}$. De spiraalarmen zijn duidelijk te zien op deze golflengte. De structuren van de armen komen goed overeen met de straling die is geproduceerd door koolstofmonoxide (CO) en atomair waterstof (HI). Het meest bijzondere aan deze waarneming is echter de onderliggende exponentiële schijf, die de straling op de golflengte van $850 \mu\text{m}$ domineert. Het is niet mogelijk deze schijf te verklaren met alleen een radiële gradiënt in de temperatuur. Hiervoor is ook een exponentiële verdeling van het stof nodig.

In hoofdstuk 4 gebruiken we de waarneming van M 51 op $850 \mu\text{m}$ om op een onafhankelijke manier de CO-naar- H_2 conversiefactor te bepalen. CO wordt vaak gebruikt om de hoeveelheid H_2 te bepalen. De reden hiervoor is dat H_2 met een lage temperatuur moeilijk is waar te nemen, omdat het dan bijna geen straling produceert. CO kan worden gebruikt om H_2 te traceren. De waarden die wij vinden voor deze conversiefactor komen overeen met waarden die zijn gevonden met andere methoden.

Deel II

In hoofdstukken 5 en 6 behandelen we de numerieke methodes om PDR en XDR modellen uit te rekenen, die ons in staat stelt de thermische en chemische structuur van het ISM in de centra van sterrenstelsels te bepalen. Er wordt diep ingegaan op de processen die we meenemen. Vervolgens rekenen we met beide numerieke methodes vier diepte-afhankelijke modellen uit, om hiermee een vergelijking te maken tussen de fysica in PDR en XDR modellen. We laten cumulatieve lijnintensiteiten zien voor atomaire fijn-structuurlijnen van koolstof, zuurstof, silicium en ijzer. Ook laten we cumulatieve kolomdichtheden en verhoudingen tussen kolomdichtheden van CO, H_2 , HCN, HCO^+ en HNC zien. Hierbij valt op dat de veranderingen voor de PDR modellen als functie van diepte veel groter zijn dan voor XDR modellen. Dit valt te begrijpen uit het feit dat een XDR geen gelaagde structuur heeft.

In hoofdstuk 7 worden kort de resultaten besproken van een vergelijkingstest voor PDR modellen. Het doel van deze vergelijking is om de verschillen tussen de PDR codes en de effecten op de fysische en chemische structuur te begrijpen en om te convergeren naar een eenduidige oplossing.

Deel III

In hoofdstuk 8 worden modellen berekend met de numerieke methodes die zijn gepresenteerd in hoofdstukken 5 en 6. Hiermee gaan we de fysische condities bepalen die behoren bij gaswolken die dichtbij bronnen van straling staan. Deze worden vaak gevonden

in de centra van zogenaamde actieve sterrenstelsels. Actieve sterrenstelsels worden gekenmerkt door een hoge mate van stervorming of door een aangroeiend zwart gat. Met deze modellen kunnen we dan iteratief bepalen wat de thermische en chemische structuur wordt van gas dat is blootgesteld aan röntgen of FUV straling. Dit levert een diagnostiek op die onderscheid maakt tussen XDR and PDR modellen. We kunnen concluderen dat verhoudingen tussen HCN en HCO^+ erg bruikbaar zijn in het maken van onderscheid tussen PDRs en XDRs. Deze zijn met de huidige generatie telescopen goed waar te nemen. Het beste zou echter zijn om te beschikken over CO lijnen met een hoge excitatie energie. Deze lijnen worden alleen geproduceerd in warm CO gas en dat wordt alleen gevonden in XDRs. Helaas kunnen we deze lijnen pas goed meten met de Herschel (een ver-infrarood/submillimeter satelliet, lancering 2008) en het instrument HIFI (The Heterodyne Instrument for the Far-Infrared) dat hierop is gemonteerd. Verder worden er een aantal moleculen gevonden die ook diagnostisch zijn, zoals NO, CN, CH en CH^+ . Op dit moment is het echter niet mogelijk om voor deze moleculen op een nauwkeurige manier lijnintensiteiten uit te rekenen.

In hoofdstuk 9 wordt ingegaan op de verschillen in invloed die röntgen fotonen en kosmische straling op het ISM hebben. Kosmische straling wordt voornamelijk geproduceerd in overblijfselen van Supernova's. Een Supernova is de ontploffing van een zware ster (meer dan acht maal de massa van de zon) aan het einde van zijn leven. In gebieden waar veel stervorming is, zijn veel van deze zware sterren aanwezig en wordt meer kosmische straling geproduceerd. Met een hogere intensiteit van kosmische straling kan de thermische en chemische structuur van een gaswolk veranderen. Daarom bekijken we wat er gebeurt met PDR-modellen als we de hoeveelheid kosmische straling verhogen en vergelijken dit met normale PDR-modellen en XDR-modellen. In sommige gevallen kunnen zowel PDR-modellen met een hoge intensiteit van cosmic rays als XDR modellen waargenomen verhoudingen verklaren. Onderscheid tussen beide kan echter worden gemaakt door te kijken naar de hoog energetische lijnen van CO, die met de Herschel (HIFI) kunnen worden waargenomen.

In hoofdstuk 10 schatten we de relatieve aanwezigheid van stervormingsgebieden, actieve kernen en verhoogde cosmic ray straling in de centra van sterrenstelsels met behulp van moleculaire emissie van HCN, HCO^+ , HNC, CO, ^{13}CO , CS en [CI]. Hiervoor gebruiken we het rooster van modellen dat is besproken in hoofdstuk 8. We herleiden vervolgens de aanwezige PDR (met verhoogde kosmische straling) en XDR componenten. We definiëren een diagnostisch diagram dat kan worden toegepast op andere sterrenstelsels, zoals (U)LIRGs (sterrenstelsels die veel straling produceren in het infra-rood). We zien vaak dat de lage, diffuse component kan worden verklaard door XDRs en PDRs met verhoogde cosmic ray straling. We zien ook dat het sterrenstelsel NGC 1068, dat vaak wordt gezien als een stelsel met een actieve kern (XDR), een PDR component van hoge dichtheid nodig heeft.

In hoofdstuk 11 wordt een blik op de toekomst geworpen. We bespreken mogelijke uitbreidingen voor de modellen. Deze zullen nodig zijn om waarnemingen van toekomstige telescopen, zoals Herschel en ALMA (een millimeter interferometer van ~ 50 telescopen in Chili), te kunnen begrijpen. We bespreken ook enkele diagnostische moleculen voor toekomstige waarnemingen.

Syatu pisi fu na buku in Sranan

Den bowston fu den stèrstelsel

San yu e si fu den stèrstelsel na gas, stòf nanga stèr. A gas dè fu den atoom nanga molecuul en a stòf meki nanga silicaat nanga koolstof tai. Stèr abi massa san kan de wan hondertse fu te kon miti wan hondru tron a massa fu unu son. Konmiti wan hondru miljarti stèr de na ini unu melkwegstelsel en makandra den e gi negitenti persent fu ala massa san wi e si. A tra tin persent na gas nanga stòf, en dati wi e kari na Interstellair Medium (ISM). A ISM kan de wan bradi ipi fasi. A kan abi wan dichtheid fu wan tinde pisi te kon miti tin miljard pisi ini wan kubieke centimeter. Wan ayersi: in a loktu pe wi e libi a dichtheid fu gas de wan miljard tron moro hei leki na moro hei dichtheid fu ISM. Den temperaturu na ini ISM kan waka fu -263 te 10 miljun graden Celsius. Na moro bigi pisi fu na presi na mindri den stèr lai nanga gas san abi wan tumsi lagi dichtheid. A waran medium (HII) di ioniseer abi wan dichtheid fu konmiti wan tinde pisi ini wan kubieke centimeter, pe fu na waran neutraal medium (HI) a de wan tinde te kon miti wan heri pisi na ini wan kubieke centimeter. In den presi pe nyun stèr e gebore a gas har kon makandra ondro hebi fu zwaartekracht. Dya so den dichtheid e waka fu tindusun kon miti wan miljoen pisi na ini wan kubieke centimeter. Wan eksempre pe a gas kan miti temperaturu fu wan dusun graden Celsius na wan planetaire nevel. Disi na a laatste stadium in a evolutie fu wan mindri hebi stèr (nanga massa fu wan konmiti fo tron na massa fu son) pe den dorosé pisi e bro gwe en so fasi wan nevel e kon. Wi e fini den moro hei dichtheid na ini gas-schijven lontu nyun stèr, wan 100 miljoen te kon mitit 10 miljard pisi na ini wan kubieke centimeter. Efu den kondisi de bun moro lati planeet e kmoto fu drape. Awinsi wi e denki dati den dichtheid di un kari leki laatste de hei in wan astronomisch fasi, a no de so fu wan grontapu begrip. Den “hei” dichtheid disi e tenapu gi a moro bun vacuum san wi kan kisi na grontapu ini wan laboratorium.

Stòf

A kenki ini na bigi fu den stòfpisi bigi tru, fu 0.25Å te kon miti $0.25\mu\text{m}$, en dati meki den kan habi furu difrenti maniri. Kosmische stòfpisi pikin moro leki tin tron a kon meki un taki “fini stòf” san disel oto e gi. Unu sabi dati den stòfpisi meki fu silicaat- nanga koolstof tai ma toku unu no e ferstan so bun san na a semper seti nanga strukturu fu stòf. A seti disi e kenki tu efu stòf e kon na ini difrenti kondisi. A wansi den pisi disi de konmiti wan persent nomo fu na heri massa fu ISM den e tapu na moro furu ultraviolet

faya nanga faya di wi e si. Tapu pasi gi straling we kari extinctie. Gi wan spersutu seti fu stòf un kan hari wan kon meki un taki extinctie kromme. A kromme disi e meki unu syi osortu golflengte e tapu o meni faya. Fu di a de tranga fu feni a seti fu stòf, somentron den onzekerheid de wan factor tu, wan sani di no de tumsi bigi na ini sterrekunde. Stòf e sorgu dati gas e waran. Disi kan spa bika stòf nanga gas deeltjes e boks makandra. Na den boks disi wan pisi fu na thermische energie fu stòf e djompo abra. Wan tra fasi de dati wan stòfpisi e absorbeer wan fayapisi en dan a de fri wan electron. A electron di lusu now habi kinetische (bewegings) energie san kan djompo abra tapu na gas te den boks. Disi wi e kari foto-electrische waran. Stòf de tumsi prenspari fu na meki fu moleculair watrastòf (H_2). Stòf na wan sortu katalysator na a reactie disi. Ini na gasfase a reactie te H_2 e meki de tumsi safri.

Gas

Gas na ini den sterstelsel meki fu na moro bigi pisi fu watrastòf (90 percent) nanga helium (8,5 percent). Ala moro hebi element leki korostof, stikstof nanga zuurstof de soso 1.5 percent fu ala sani. Astronoom e kari den metaal. A e anga tapu na fasi fa a stralingsveld nanga na dichtheid de fa den gaswolku e abi wan spesrutu chemische nanga termische strukturu. Den ala e seni difrenti san wi e kari atomaire fini-structuru nanga moleculaire (leki H_2 , CO, HCN, nanga H_2O) rotationele nanga vibrationele lini. Den lini e meki sofasi. Fosi wan pisi (kon un taki H_2) e boks nanga wan tra pisi (kon un taki CO). A boks disi kan meki wan fu den pisi kon na ini wan sitwasi di habi wan moro hei energie. A pisi disi efu a seni wan fayapisi go na doru a kan kisi en kmopope sitwasi baka. Den fayapisi disi e seni go na doru tapu wan golflengte san wi no kan syi nanga un ai bika a de ini na (sub)-millimeter presi, ma den telescoop leki James Clerk Maxwell Telescoop (JCMT) nanga na Institute de Radio Astronomie Millimétrique (IRAM) 30m telescope kan syi den wel. Te den kondisi e difrenti, owktu wan difrenti set lini-intensiteit nanga linihori e meki. Fu dati meki un kan gebroiki den fu jepi feni den fysische maniri fu na gas.

Extreme sitwasi ini centra fu den stèrstelsel

Unu sonstelsel e drai tapu wan distantia fu 26000 fayajari lontu na mindri fu na Melkweg. Na ini un sjatu kontren na omeni stèr na ini wan volume eenheid lagi fu tru. Proxima Centauri na moro krosbei stèr de tapu wan afstand fu moro leki fofayajari. Na dichtheid fu den stèr en na gemiddelde dichtheid fu gas in na mindri fu wan stèrstelsel de bun furu moro hei efu yu kék en na a birti fu na son. Dati meki ini na mindri a de moro makriki fu kenki gas kon tron stèr en so fasi na gemiddelde omeni straling di e meki de bun furu moro hei. Tranga stalingsveld no e kon soso fu den nyun meki stèr ma owktu ini wan blaka holo di de drape nofotron en di eswari den gas nanga stèr. A gro (accretie) fu materi e gi furu energie. A winsi furu straling e meki, a mindri de tranga fu waki nanga den optische telescoop. Dati e kon bika na bun furu stof di de e tapu na moro bigi pisi fu na faya. Na tapu moro langa golflengte so leki ini na sub-millimeter presi, na extinctie bika fu stof ede

no de so furu. Dat hede wel un kan kisi diagnostiek fu den lini di kon un taki CO, HCN nanga HCO^+ meki. Den lini disi wi wani meki baka nanga den model. Djaso wi e kruderi dati straling na a dominante factor fu feni a chemische nanga thermische strukturu. Den model disi wi e kari kon meki un taki foton gedomineerde presi (PDRs) te den fayapisi de moro furu far-ultraviolette straling (FUV) en wi e kari den X-ray gedomineerde presi (XDRs) efu na stralingsveld de fu röntgen foton. Den FUV foton e komoto fu faja hebi stèr, nadi moro furu fu den röntgen foton komoto fu blaka holo.

Na energie fu den foton de difrenti en dati meki a abi tra maniri. Röntgen foton e go bun furu moro dipi na ini den wolku leki den FUV foton, bikasi den atoom abi moro muiti fu absorbeer den molecuul nanga den stof röntgen foton. Na procesi fa FUV nanga röntgen foton é waran na gas de difrenti tu. Fu dati ede na thermisch nanga chemische strukturu ini PDRs nanga XDRs de tra fasi. PDRs habi wan krin laag tapu laag strukturu. Yu kan si wan krin abra fu atomair go na moleculair watrastof ($\text{H} \rightarrow \text{H}_2$), so leki fu korostof di ioniseer go na neutraal korostof nanga korostof mono-oxide ($\text{C}^+ \rightarrow \text{C} \rightarrow \text{CO}$). Na ini den XDR a kenki disi no de so krin en den atoom nanga molecuul disi e bestan sei makandra. Den maniri disi fu di stuka de meki na ini na proefskreft e tyari unu na wan diagnostiek di kan ondroschei den effect fu den massief stèr (FUV fotonen) nanga wan blaka holo di e swari gas nanga den stèr (röntgen foton) na ini a mindri fu den stèrstelsel.

Na proefskreft disi

Na proefskreft disi prati na ini dri pisi. In a fosi pisi we go spesrutu na ini waki fu na stofcomponent ini M 51. A di fu tu e sori unu den PDR nanga XDR model en kék den nanga tra model di un habi. Ini pisi nomru dri we reken wan bigi losi fu den model uit, dan we poti en tapu den waki di un du. Bilo we luku na inibere fu den diffrenti kapitri sjatu.

Pisi I

Ini kapitri 2 we tyari un kon na ini waki fu stof di ben du na ini den stèrstelsel. We go na ini problema so leki feni na temperaturu fu stof, feni na opaciteit fu stof en san no de seiker na ini.

Na ini kapitri 3 we sori wan waki fu na melkwegstelsel M 51, di ben waki nanga a JCMT tapu wan golflengte fu 850 μm . Tap na golflengte disi un' kan si den spiraalanu krin. A strukturu fu den anu e kruderi bun nagna na straling di korostofmonoxide (CO) nanga atomair watrastòf (HI) meki. A moro aparti fu na waki disi na a exponentiële schijf ondro den, di e basi na straling tapu na 850 μm golflengte. Un no sa man ferkrari na schijf disi soso nanga wan radiële gradient in a temperaturu. Un fanodu wan exponentieel prati fu na stòf owktu.

Na ini kapitri 4 we gebroiki a waki fu M 51 tapu 850 μm fu kan feni na conversiefactor fu CO go na H_2 tapu wan srefidensi fasi. Nofotron we gebroiki CO fu feni ofuru H_2 de. We du dati bika a tranga fu waki H_2 nanga wan lagi temperaturu, bika bijna a no e gi straling. Un' kan gebroiki CO fu feni H_2 . Den waarde di we kisi fu a conversiefactor disi e kruderi nanga den waarde di ben feni nanga tra fasi.

Pisi II

In kapitri 5 nanga 6 we broko broko den numeriek fasi fu kan bereken wan PDR nanga wan XDR model, di e meki dati unu kan feni a thermisch nanga chemisch strukturu fu na ISM ini den mindri fu den stèrstelsel. We go dipi na ini den procesi di wi e stuka. Baka dati we reken fo diepte afhankelijk model uit gi alla tu numeriek fasi fu kan meki wan kék mindri na fysica ini PDR nanga XDR model. We meki un syi den cumulatieve lini-intensiteit fu atomaire fini-strukturulini fu korostof, zuurstof, silicium nanga isri. Owktu wi e sori den cumulatieve kolomdichtheden nanga na fasi fa a kolomdichtheid fu CO, H₂, HCN, HCO⁺ nanga HNC e drai nanga den srefi. Dan a de fu syi dati, efu wi e luku a dipi, a kénki gi den PDR model de bun furu moro bigi leki den XDR model. Un kan ferstan dati, bika a de so dati wan XDR no habi wan gelaagde strukturu.

In kapitri 7 we taki syatu abra den kbapisi fu wan agersitest fu den PDR model. Na dorope fu na kék disi na fu kan ferstan den difrenti mindri den PDR code nanga de effecti tapu na fysische nanga chemische strukturu en fu kan convergeer go miti wan wanfasi lukufasi.

Pisi III

Ini kapitri 8 we bereken den numeriek model nanga den numeriek fasi di un presenteri na ini den kapitri 5 nanga 6. Nanga disi we go bepaal den fysische kondisi di e fiti den gaswolku di tenapu krosbei den bron fu straling. Somentron un' kan feni den na mindri fu den sotaki aktief stèrstelsel. Un' kan sabi den actief stèrstelsel bika den e form bunfuru stèr noso wan blaka holo san e gro. Nanga den model disi un kan bepaal iteratief san na thermische nanga chemische strukturu fu gas di opo en borsu fu kisi röntgen noso FUV straling. Sofasi we kisi diagnostiek di e meki difrenti mindri den XDR nanga PDR model. Un' konkruderi dati ratio mindri HCN nanga HCO⁺ kan meki wan tru bun difrenti mindri den PDR nanga XDR. Nanga den telescopu fu tide un kan waki den bun. A moro betre wan ben sa de fu habi CO lini nanga wan hei excitatie faya. Den lini disi e meki soso na ini waran CO gas en unu kan feni dati soso na ini den XDR. Eru un' kan marki den lini disi fosi bun nanga a Herschel (wan fara-infrarede/submilimeter satelliet di sa lanceer ini 2008) nanga a wrokosani HIFI (The Heterodyne Instrument for the Far-Infrared) di fasi na en tapu. Moro fara un' kan feni wan nomru molecuul di owktu de diagnostich, soleki NO, CN, CH nanga CH⁺. Now now so un' no man reken uit lini-intensiteit gi den molecuul disi na tap wan kweti fasi.

Na ini kapitri 9 wi e go na ini den difrenti kénki die röntgen foton nanga kosmische straling e trakti fu meki tapu na ISM. Kosmische straling e meki frunamku na ini san tan abra fu den Supernova. Wan Supernova na te wan hebi stér bos (moro aiti tron a massa fu son) na a keba fu en libi. Ini den presi pe furu stèr e form furu fu den hebi stèr disi de, en owktu moro kosmische straling e meki. Nanga wan moro hei intensiteit fu kosmische straling a thermisch nanga chemisch strukturu fu wan gaswolku kan kenki. Fu dati meki w'e luku san e pesa nanga den PDR model efu w'e opo na ofurumarki kosmische straling en owktu w'e kék dati nanga den gewoon PDR model nanga XDR model. Ini son sitwasi PDR model nanga wan hei intensiteit fu kosmische straling, soleki XDR model kan ferkrari den ratios di ben waki. Ma un kan meki difrenti mindri den tu

efu un luku den hei energetisch lini fu CO, die un kan waki nanga Herschel (HIFI).

Ini kapitri 10 we schat relatief omeni presi pe den stèr e meki de, den actief ini bere nanga den kon moro hei kosmische straling na a mindri fu den stèrstelsel nanga jepi fu moleculaire emissie fu HCN, HCO⁺, HNC, CO, ¹³CO, CS nanga [CI]. Fu disi we gebroiki a losi di un ben tja kon na fesi ini kapitri 8. Baka dati wi e herlei den PDR di de (nanga kon moro hei kosmische straling) nanga den XDR componenti. Wi e definieer wan diagnostisch diagram di un kan gebroiki owktu gi tra stèrstelsel so leki (U)LIRGs (stèrstelsel die egu furu infra-rood straling). Nofotron wi e si dati na ferkrari fu a lagi difuus component didon na ini den XDR so leki den PDR nanga kon moro hei kosmische straling. Owktu wi e si dati a stèrstelsel NGC 1068, di un kan si nofotron leki wan stelsel nanga wan actief inibere (XDR), fanodu wan hei dichtheid fu na PDR componenti.

Kapitri 11 e gi wan luku na ini futuru. W'e tja kon na fesi den bradi fu den model. Den disi sa de fanowdu fu kan ferstan den waki fu den konten telescopu leki Herschel nanga ALMA (wan millimeter interferometer fu ~ 50 telescopu na ini Chili). W'e tja kon na fesi owktu wan tu diagnostisch molecuul gi waki di un mu du ete.

Curriculum Vitae

Op 12 oktober 1978 werd ik geboren in Enschede. Na het behalen van mijn Gymnasium diploma in 1997 aan het Ichthus College in Enschede, begon ik in hetzelfde jaar met de studie Sterrenkunde aan de Universiteit Leiden. Tegelijkertijd werd ik ook lid van de roeivereniging “*K.S.R.V. Njord*” en roeide dat jaar in de Lichte Acht. Desondanks wist ik na dat jaar het propedeutisch examen te halen. In het eerste jaar van mijn doctoraal fase, werd ik praeses van studievereniging “*De Leidsche Flesch*” en tevens lid van studentenvereniging “*L.S.V. Minerva*”. Deze activiteiten en studeren waren dat jaar helaas niet te combineren met wedstrijdroeien, maar de drie volgende jaren gelukkig wel. In de laatste twee jaren van mijn studie deed ik twee onderzoeksprojecten in de Theorie-groep. Het eerste, onder leiding van prof. dr. V. Icke, ging over stralingstransport in inter-stellaire materie. Het tweede, onder leiding van dr. G. Mellema, besloeg het modelleren van de evolutie van het variabele massaverlies rond AGB sterren. Tijdens het laatste jaar van mijn studie maakte ik mijn eerste waarneemreis en nam ik 5 weken waar met de “*Dutch-telescope*” op La Silla (Chili).

Na het behalen van mijn doctoraal examen in september 2002, begon ik aan mijn promotie-onderzoek onder leiding van prof. dr. F.P. Israel en prof. dr. M.C. Spaans. Het resultaat van dit onderzoek staat beschreven in dit proefschrift. In 2003 en 2004 ben ik twee maal naar de “*James Clerk Maxwell Telescope*” geweest om waarnemingen te doen aan gas in de centra van actieve melkwegstelsels. Daarnaast heb ik deelgenomen aan conferenties in Leiden, Lunteren, Kleve (Duitsland), Zwolle, Gramado (Brazilië), Nijmegen, Vlieland, Blankenberge (België), Asilomar (USA) en Onsala (Zweden), en heb ik mijn werk mondeling of op een poster gepresenteerd. Verder was ik werkgroep assistent van prof. dr. M. Franx en dr. M.R. Hogerheijde bij het college “*Sterrenkundig praktikum 3*” en van drs. R.S. le Poole bij het college “*Astronomische waarneemtechnieken*”.

Vanaf december zal ik twee jaar als *Postdoctoral Fellow* theoretisch onderzoek doen aan proto-planetaire schijven met prof. dr. A. Glassgold aan de University of California, Berkeley (USA).

Nawoord

Het verwezenlijken van een proefschrift is niet slechts het werk van één persoon, hoewel de voorkant van dit boekje anders doet vermoeden. Op zowel het wetenschappelijke als het sociale vlak heb ik de afgelopen vier jaren de nodige ondersteuning gehad.

Ik heb de Sterrewacht als een prettige en stimulerende omgeving ervaren. Discussies met stafleden, promovendi en studenten waardeerde ik altijd zeer. De buitengewoon gerespecteerde personen, waarmee ik gezamenlijke projecten heb gedaan, staan vermeld bij ieder hoofdstuk in dit boekje. Zonder de hulp van het secretariaat - Kirsten, Jeanne, Elise, Liesbeth en Laura - en de computergroep - David, Erik, Tycho en Aart - zou mijn promotie lang niet zo soepel zijn verlopen. Ook ben ik erg erkentelijk voor de financiële ondersteuning die ik heb ontvangen van het Leids Kerkhoven-Bosscha Fonds voor het bezoeken van conferenties in onder andere Brazilië en de Verenigde Staten.

Ontspanning was er ook natuurlijk, bijvoorbeeld tijdens gesprekken bij de koffie en lunch of het sporten met Jelle, Koen, Sijme-Jan, Franco, Erik-Jan, Remko, Dominic en Inti. Ook heb ik altijd met plezier een kamer gedeeld met Inga en later Lottie en Eveline. Buiten de Sterrewacht waren er ook een hoop vrienden met een luisterend oor en veel geduld, zeker de laatste zes maanden van mijn promotie. In de eerste plaats mijn zeer gewaardeerde hofgenoten, onder andere, Joost, Rebecca, Gijs, Mark, Steven en Sigrid, maar zeker ook Sjoerd en Thijs.

Verder wil ik mijn ouders bedanken, voor het feit dat ze me hebben vrijgelaten in het maken van mijn keuzes en dat ze me altijd hebben ondersteund tijdens mijn studie. Ik ben Paul en Christina zeer erkentelijk voor het vertalen van de samenvatting in het Sranan.

Samora, ik snap af en toe niet waar ik je aan verdiend heb, zonder jou had ik het schrijven van dit proefschrift nooit voor elkaar gekregen.

